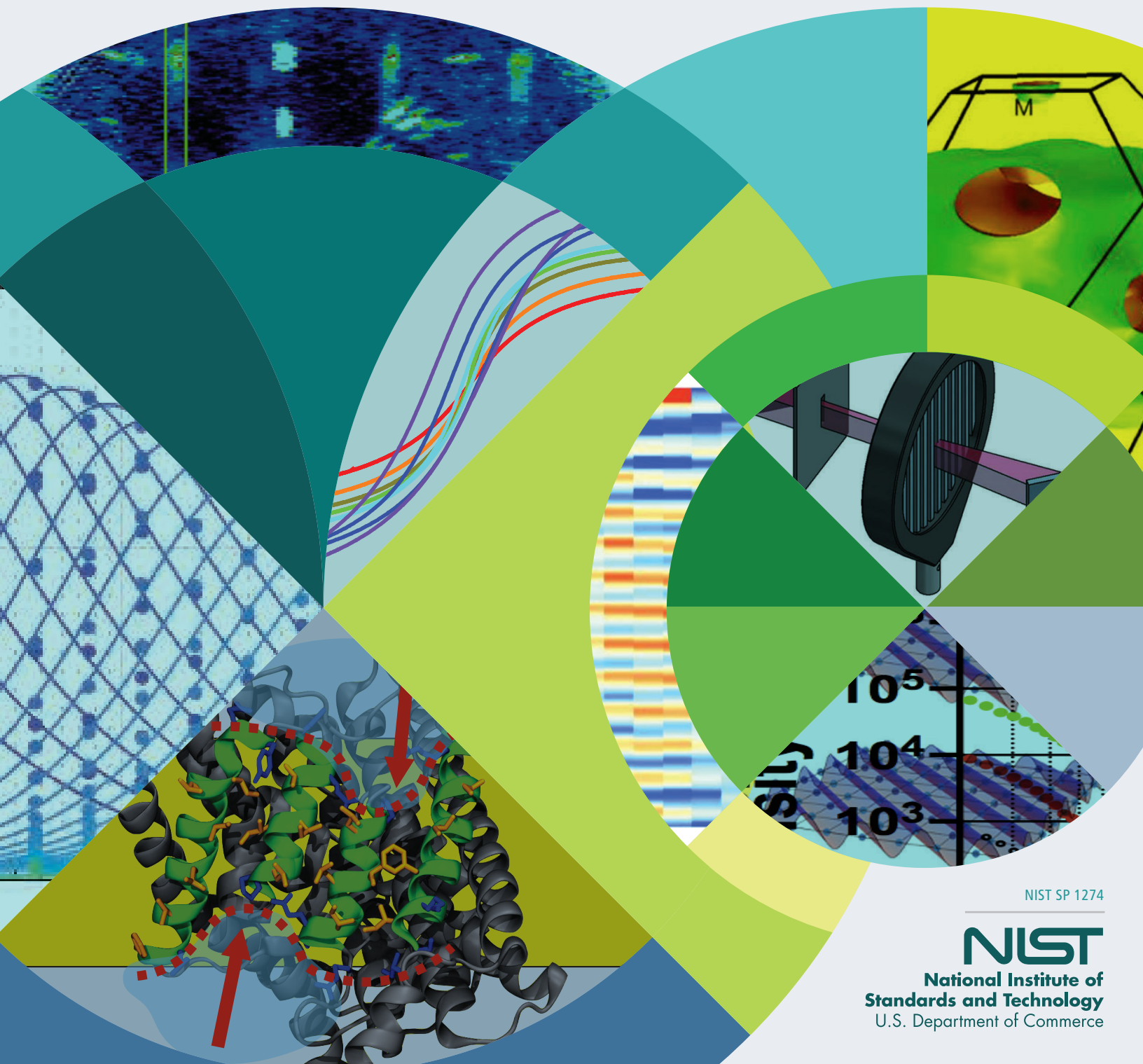
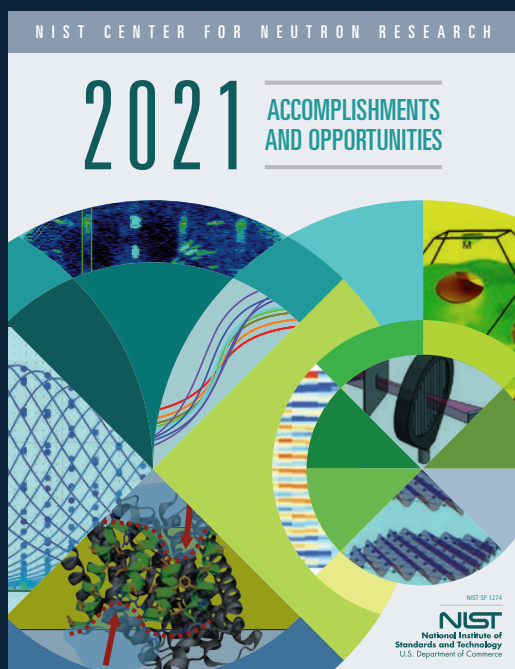


2021

ACCOMPLISHMENTS AND OPPORTUNITIES



NIST SP 1274



ON THE COVER

The NCNR's neutron source provides a valuable research tool for a wide variety of scientific fields from biological systems, engineering materials, to magnetic structures, and more. The cover features data from only a few of the experiments highlighted in this report.

NIST Special Publication 1274

2021 NIST Center for Neutron Research Accomplishments and Opportunities

Robert M. Dimeo, Director

Steven R. Kline, Editor

This publication is available free of charge from:
<https://doi.org/10.6028/NIST.SP.1274>

December 2021



U.S. Department of Commerce
Gina M. Raimondo, Secretary

National Institute of Standards and Technology
*James K. Olthoff, Performing the Non-Exclusive Functions and Duties of the Under Secretary of Commerce
for Standards and Technology & Director, National Institute of Standards and Technology*

DISCLAIMER

Certain commercial entities, equipment, or materials may be identified in this document in order to describe an experimental procedure or concept adequately. Such identification is not intended to imply recommendation or endorsement by the National Institute of Standards and Technology, nor is it intended to imply that the entities, materials, or equipment are necessarily the best available for the purpose. Throughout the text, unless otherwise stated, q (or Q) refers to the momentum transfer. Error bars in figures and uncertainties in the text represent one standard deviation unless otherwise stated.

National Institute of Standards and Technology Special
Publication 1274, 89 pages (December 2021)
CODEN: NSPUE2

This publication is available free of charge from:
<https://doi.org/10.6028/NIST.SP.1274>

Table of Contents

II FOREWORD

1 THE NIST CENTER FOR NEUTRON RESEARCH

2 NIST CENTER FOR NEUTRON RESEARCH INSTRUMENTS

BIOSCIENCES

- 4 Small-angle neutron scattering used to determine the structure of an engineered nanoparticle vaccine S. Krueger, et al. (CHRNS)
- 6 Understanding the mechanisms underlying vaping-associated lung injury M. DiPasquale, et al. (CHRNS)
- 8 Exploring pharmaceutical component incompatibility through very small-angle neutron scattering, P. H. Gilbert, et al. (CHRNS)
- 10 Membrane surface recognition by the ASAP1 PH domain and consequences for interactions with the small GTPase Arf1, O. Soubias, et al.
- 12 Small-angle neutron scattering reveals preferential solvation as a mechanism for regulating protein dimerization in membranes, J. L. Robertson, et al. (CHRNS)

CHEMICAL PHYSICS

- 14 Ambient-temperature hydrogen storage via vanadium(ii)-dihydrogen complexation in a metal-organic framework D. E. Jaramillo, et al.
- 16 Elucidating ion transport in Li-ion cells by *operando* neutron, contact potential measurements, and first-principles modeling, J. L. Weaver, et al.
- 18 On the question of dynamic tetragonal domains in the cubic phase of the photovoltaic semiconductor methylammonium lead triiodide, N. J. Weadock, et al.
- 20 Electrostatically driven selective adsorption of carbon dioxide over acetylene in an ultramicroporous metal-organic framework material, Y. Xie, et al.
- 22 Self-adjusting binding pockets enhance H₂ and CH₂ adsorption in a uranium-based metal-organic framework, D. P. Halter, et al.

CONDENSED MATTER

- 24 Time-resolved probes of magnetic monopoles in spin ice, Y. Wang, et al. (CHRNS)
- 26 Competing magnetic phases and fluctuation-driven scalar spin chirality in the kagome metal YMn₆Sn₆, N. J. Ghimire, et al.

- 28 Unraveling the unusual metal-to-metal transition in metallic nickelate, J. Zhang, et al. (CHRNS)
- 30 Surface-symmetry dependent magnetism at topological interfaces, C. Yang, et al.
- 32 Local quantum criticality in a stoichiometric semi-metal, W. T. Fuhrman, et al. (CHRNS)

NEUTRON PHYSICS

- 34 Imaging electric field with electrically neutral particles, Y.-Y. Jau, et al.
- 36 Measurement of the neutron decay electron antineutrino angular correlation by the aCORN experiment, M. T. Hassan, et al.

SOFT MATTER

- 38 Molecular view on mechanical reinforcement in polymer nanocomposites, S. Cheng, et al. (CHRNS)
- 40 Arresting bicontinuous channels with a solvent segregation driven gel, Y. Xi, et al. (CHRNS)
- 42 Dynamics and toughness in glassy polycarbonates, C. L. Soles, et al. (CHRNS)
- 44 Scaling relationships for the elastic and viscous properties of mixed lipid membranes, E.G. Kelley, et al. (CHRNS)

ADVANCES IN MEASUREMENT

- 46 Sub-micrometer neutron tomography, B. Heacock, et al.
- 47 Design of a neutron microscope based on Wolter mirrors, D. S. Hussey, et al.
- 48 New measurement capability enabled by a linear chopper for cold neutron beam activation analysis, D. J. Turkoglu, et al.

NEUTRON SOURCE OPERATIONS

51 FACILITY DEVELOPMENTS 2021

54 SERVING THE SCIENCE AND TECHNOLOGY COMMUNITY

57 THE CENTER FOR HIGH RESOLUTION NEUTRON SCATTERING (CHRNS)

63 2021 AWARDS

66 PUBLICATIONS: AUGUST 1, 2020 TO JULY 31, 2021

87 INSTRUMENTS AND CONTACTS

89 NIST CENTER FOR NEUTRON RESEARCH CONTACTS

Foreword

Serving the U.S. scientific community by providing, advanced neutron measurement tools, strong user support and a reliable source of neutrons is the heart of our mission. Unfortunately, we aren't currently fulfilling this mission due to an incident that occurred on reactor restart on February 3. Our analysis has shown that an improperly latched fuel element was the proximal cause event. NIST has identified several root causes and has developed a series of corrective actions to prevent recurrence. During the event, the primary cooling system was contaminated and NIST has developed a plan to mitigate this issue as quickly as possible. We recently presented our analysis to the Nuclear Regulatory Commission (NRC) along with our request to restart the reactor while work continues on restoring the reactor to operational readiness. As of this writing, we still have much work to do to prepare the reactor for operations, but our goal is to restart the reactor in 2022.

During the unplanned outage, we continue to work on several major facility developments. Planning continues for the 2023 outage when the H₂ cold source will be replaced with a liquid D₂ cold source, doubling the cold neutron flux at long wavelengths. This upgrade will improve the performance of all the cold neutron instruments in the guide hall. The new Neutron Spin-Echo spectrometer project continues on-schedule and promises to increase the performance by increasing the data rate by an order of magnitude for a given maximum Fourier time.

Despite the issues with the reactor, the science produced by NCNR users continues to be outstanding as you



will see in the high-quality research highlights in this report. I am delighted to share with you this impressive work as well as details on facility developments. Finally, I wish to express thanks to all those who have reached out to us in this difficult time and shown your support. It means a lot to me and all the NCNR staff. Thank you.

A handwritten signature in black ink that reads "Bob Di".

The NIST Center for Neutron Research

Neutrons provide a uniquely effective probe of the structure and dynamics of materials ranging from water moving near the surface of proteins to magnetic domains in memory storage materials. The properties of neutrons (outlined below) can be exploited using a variety of measurement techniques to provide information not otherwise available. The positions of atomic nuclei in crystals, especially of those of light atoms, can be determined precisely. Atomic motion can be directly measured and monitored as a function of temperature or pressure. Neutrons are especially sensitive to hydrogen, so that hydrogen motion can be followed in H-storage materials and water flow in fuel cells can be imaged. Residual stresses such as those deep within oil pipelines or in highway trusses can be mapped. Neutron-based measurements contribute to a broad spectrum of activities including engineering, materials development, polymer dynamics, chemical technology, medicine, and physics.

The NCNR's neutron source provides the intense, conditioned beams of neutrons required for these types of measurements. In addition to the thermal neutron beams from the heavy water moderator, the NCNR has two liquid hydrogen moderators, or cold sources which supply neutrons to three-fourths of the instruments. One is a large area moderator and the other is smaller, but with high brightness. These moderators provide long wavelength guided neutron beams for industrial, government, and academic researchers.

There are currently 30 experiment stations: 12 are

used for neutron physics, analytical chemistry, or imaging, and 18 are beam facilities for neutron scattering research. The subsequent pages provide a schematic description of our instruments. More complete descriptions can be found at <https://www.nist.gov/ncnr/neutron-instruments>. The newest instrument, a quasi-white beam neutron reflectometer (CANDOR) is currently in the commissioning stage.

The Center supports important NIST measurement needs but is also operated as a major national user facility with merit-based access made available to the entire U.S. technological community. Each year, approximately 2000 research participants from government, industry, and academia from all areas of the country are served by the facility (see pp. 54). Beam time for research to be published in the open literature is without cost to the user, but full operating costs are recovered for proprietary research. Access is gained mainly through a web-based, peer-reviewed proposal system with user time allotted by a beamtime allocation committee twice a year. For details see <https://www.nist.gov/ncnr/obtaining-beam-time>. The National Science Foundation and NIST co-fund the Center for High Resolution Neutron Scattering (CHRNS) that currently operates five of the world's most advanced instruments (see pp. 57). Time on CHRNS instruments is made available through the proposal system. Some access to beam time for collaborative measurements with the NIST science staff can also be arranged on other instruments.

Why Neutrons?

Neutrons reveal properties not readily probed by photons or electrons. They are electrically neutral and therefore easily penetrate ordinary matter. They behave like microscopic magnets, propagate as waves, can set particles into motion, losing or gaining energy and momentum in the process, and they can be absorbed with subsequent emission of radiation to uniquely fingerprint chemical elements.

WAVELENGTHS – in practice range from ≈ 0.01 nm (thermal) to ≈ 1.5 nm (cold) ($1 \text{ nm} = 10 \text{ \AA}$), allowing the formation of observable interference patterns when scattered from structures as small as atoms to as large as biological cells.

ENERGIES – of millielectronvolts, the same magnitude as atomic motions. Exchanges of energy as small as nanoelectronvolts and as large as tenths of electronvolts can be detected between samples and neutrons, allowing motions in folding proteins, melting glasses and diffusing hydrogen to be measured.

SELECTIVITY – in scattering power varies from nucleus to nucleus somewhat randomly. Specific isotopes can stand out from other isotopes of the same kind of atom. Specific light atoms, difficult to observe with x-rays, are revealed by neutrons. Hydrogen, especially, can be distinguished from chemically equivalent deuterium, allowing a variety of powerful contrast techniques.

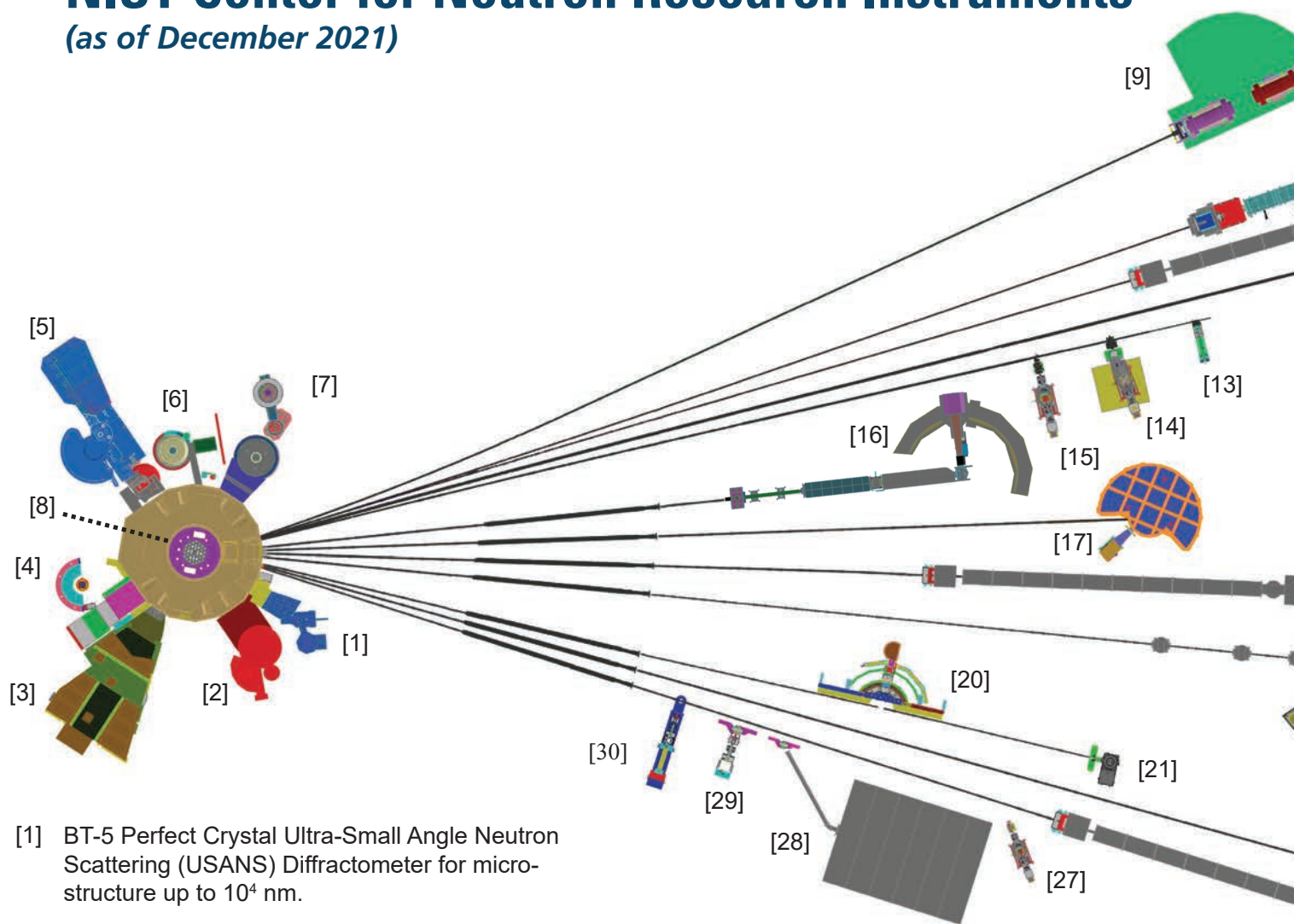
MAGNETISM – makes the neutron sensitive to the magnetic moments of both nuclei and electrons, allowing the structure and behavior of ordinary and exotic magnetic materials to be detailed precisely.

NEUTRALITY – of the uncharged neutrons allows them to penetrate deeply without destroying samples, passing through walls that condition a sample's environment, permitting measurements under extreme conditions of temperature and pressure.

CAPTURE – characteristic radiation emanating from specific nuclei capturing incident neutrons can be used to identify and quantify minute amounts of elements in samples as diverse as ancient pottery shards and lake water pollutants.

NIST Center for Neutron Research Instruments

(as of December 2021)



[1] BT-5 Perfect Crystal Ultra-Small Angle Neutron Scattering (USANS) Diffractometer for micro-structure up to 10^4 nm.

[2] BT-4 Filter Analyzer Neutron Spectrometer with cooled Be/Graphite filter analyzer for chemical spectroscopy and thermal triple axis spectrometer.

[3] BT-2 Neutron Imaging Facility for imaging hydrogenous matter in large components such as water in fuel cells and lubricants in engines, in partnership with General Motors and DOE.

[4] BT-1 Powder Diffractometer with 32 detectors; incident wavelengths of 0.208 nm, 0.154 nm, and 0.120 nm, with resolution up to $\Delta d/d \approx 8 \times 10^{-4}$.

[5] BT-9 Multi Axis Crystal Spectrometer (MACS II), a cold neutron spectrometer for ultra high sensitivity access to dynamic correlations in condensed matter on length scales from 0.1 nm to 50 nm and energy scales from 2.2 meV to 20 meV. 

[6] BT-8 Engineering Diffractometer optimized for depth profiling of residual stresses in large components.

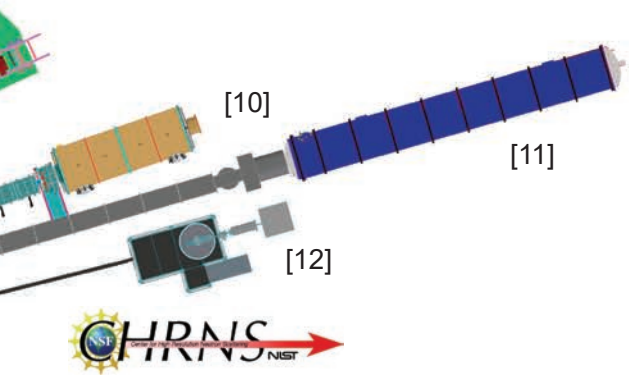
[7] BT-7 Thermal Triple Axis Spectrometer with large double focusing monochromator and interchangeable analyzer/detectors systems.

[8] VT-5 Thermal Neutron Capture Prompt Gamma-ray Activation Analysis Instrument used for quantitative elemental analysis of bulk materials including highly hydrogenous materials ($\approx 1\%$ H) such as foods, oils, and biological materials.

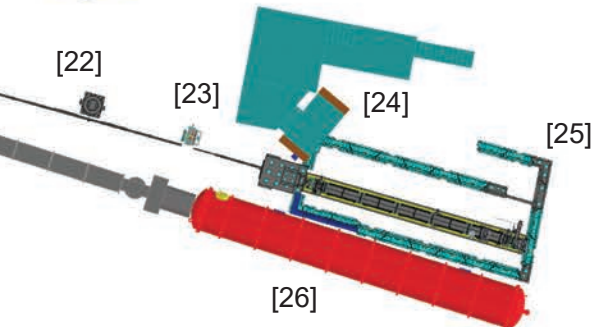
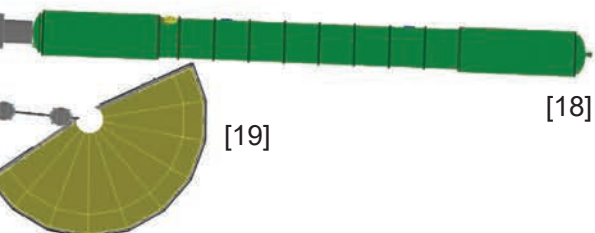
[9] NG-A Neutron Spin-Echo Spectrometer (NSE) for measuring dynamics from 5 ps to 100 ns.



[10] NG-B 10 m SANS for macromolecular structure measurements. 



The Center for High Resolution Neutron Scattering (CHRNS) is a partnership between NIST and the National Science Foundation that develops and operates neutron scattering instrumentation for use by the scientific community. The following instruments are part of the Center: 5 (MACS II), 9 (NSE), 16 (CANDOR), 17 (HFBS), and 18 (vSANS).



- [11] NG-B 30 m SANS for microstructure measurements.
- [12] NG-C Neutron lifetime experiment.
- [13] NG-D Cold neutron capture Prompt Gamma Activation Analysis, for quantitative elemental analysis of bulk materials
- [14] NG-D MAGIK off-specular reflectometer for studies of thin-film samples with in-plane structure.
- [15] NG-D Polarized Beam Reflectometer (PBR) for measuring reflectivities as low as 10^{-8} to determine subsurface structure.

- [16] NG-1 CANDOR Chromatic Analysis Diffractometer or Reflectometer, capable of high throughput measurements.
- [17] NG-2 Backscattering Spectrometer (HFBS), high intensity inelastic scattering instrument with energy resolution $< 1 \mu\text{eV}$ for studies of motion in molecular and biological systems.
- [18] NG-3 VSANS for single measurement investigation of lengths from 1 nm to 2 micron.
- [19] NG-4 Disk Chopper Time-of-Flight Spectrometer for diffusive motions and low energy dynamics. Wavelengths from $\approx 0.18 \text{ nm}$ to 2.0 nm and energy resolutions from $\approx 2 \text{ meV}$ to $< 10 \mu\text{eV}$.
- [20] NG-5 Spin-Polarized Triple Axis Spectrometer (SPINS) using cold neutrons with position sensitive detector capability for high-resolution studies.
- [21] NG-5 Cold Neutron Depth Profiling for profiling of subsurface elemental composition.
- [22] NG-6 Precision measurement of the magnetic dipole moment of the neutron.
- [23] NG-6 Precision measurement of neutron flux.
- [24] NG-6 LAND detector development, neutron source calibration, and neutron cross section measurement
- [25] NG-6 Cold Neutron Imaging Facility for imaging hydrogenous matter in large components such as water in fuel cells and lubricants in engines.
- [26] NG-7 30 m SANS for microstructure measurements, in partnership with ExxonMobil and University of Minnesota's IPrime.
- [27] NG-7 PHADES Cold neutron test station.
- [28] NG-7 Neutron Interferometry and Optics Station with perfect crystal silicon interferometer. A vibration isolation system provides exceptional phase stability and fringe visibility.
- [29] NG-7 Neutron Physics Interferometry Test Bed for quantum information science.
- [30] NG-7 Horizontal Sample Reflectometer allows reflectivity measurements of free surfaces, liquid/vapor interfaces, as well as polymer coatings.

Small-angle neutron scattering used to determine the structure of an engineered nanoparticle vaccine

S. Krueger,¹ J. E. Curtis,¹ D. R. Scott,² A. Grishaev,³ G. Glenn,² G. Smith,² and E. L. Maynard²

Nanoparticles represent a powerful and versatile platform for development of vaccines to combat deadly pathogens such as respiratory syncytial virus (RSV), influenza, and recently, SARS-CoV-2. Despite the growing number of nanoparticle-based vaccines being developed, little is known about the structural features that contribute to their immunogenicity. In this study, small-angle neutron scattering (SANS) with contrast variation and small-angle X-ray scattering (SAXS) were used to obtain key information that helped elucidate the structure of an RSV nanoparticle vaccine in solution. The work was made possible through strong collaboration between clinicians and basic scientists and demonstrates the importance of such collaborations in driving vaccine characterization and development.

RSV, an enveloped RNA virus in the *Pneumoviridae* family, is a major cause of severe lower respiratory tract infection in susceptible populations comprised of newborns, young children 6 months to 5 years old, and adults 60 and over. Repeat infections with RSV are common, making it the cause of a considerable worldwide disease burden. In spite of many attempts since the 1960s to develop an effective vaccine, no licensed vaccine for RSV currently exists. RSV infection occurs when the virus fuses to the host cell and subsequently releases its RNA into the cell (Figure 1A). This process is mediated by the RSV fusion (F) envelope glycoprotein (Figure 1B), which is present on the surface of the virus. During the fusion process, RSV F is subject to significant structural rearrangements (Figure 1C).

RSV F is a major target for vaccine development. However, like many other surface viral proteins, it is a glycoprotein with a transmembrane domain. Thus, it forms aggregates in solution unless it is stabilized by a detergent or other cell membrane mimic. Protein:detergent nanoparticles are proving to be effective platforms for vaccine development due to their size and ability to present many copies of the viral surface protein (antigen). This arrangement of surface antigens mimics that of intact viruses and their ability to trigger an immune response [1].

Novavax has produced an RSV nanoparticle vaccine that is being studied in clinical trials as a potential candidate for the protection of infants via maternal immunization during

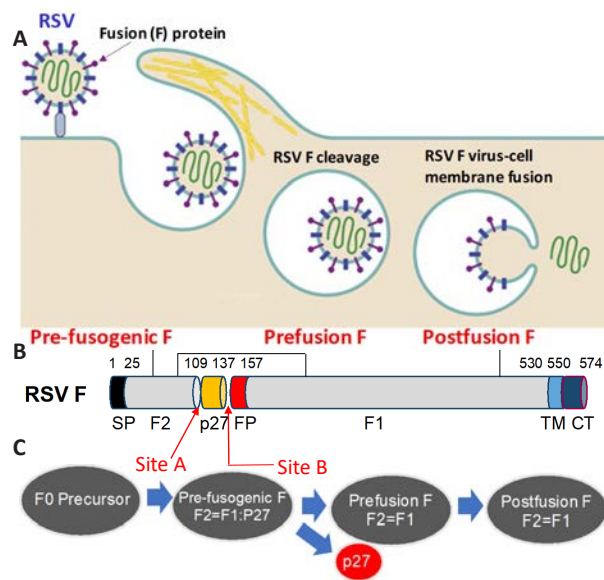


FIGURE 1: (A) Cartoon representation of RSV infection. Adapted from [2]. (B) Linear diagram of the RSV fusion (F) glycoprotein consisting of two subunits, F1 and F2, and two furin cleavage sites (Site A and Site B). RSV F also contains a p27 peptide and a fusion peptide (FP), as well as a transmembrane (TM) region and a cytoplasmic tail (CT) region. (C) During infection the precursor fusion glycoprotein (F0) is cleaved by furin (Site A) forming a fusion inactive F2-p27F1 intermediate (Pre-fusogenic F). A second furin cleavage (Site B) releases a p27 peptide to form the metastable prefusion F. Fusion of viral and cellular membranes is driven by a major structural rearrangement that results in the formation of a postfusion F. Credit: Novavax, Inc., Gaithersburg, MD. Used with Permission.

pregnancy (ClinicalTrials.gov identifier: TCT02624947) [3]. It consists of an engineered, near full-length pre-fusogenic RSV F glycoprotein trimer, importantly with an intact membrane domain, formulated into a micellar complex with polysorbate 80 (PS80) detergent. In animal and clinical studies, the RSV F:PS80 nanoparticle vaccine has been shown to induce broadly neutralizing antibodies [4]. To understand the observed efficacy of the vaccine, its structural and hydrodynamic properties were studied in solution using SANS, along with SAXS, analytical ultracentrifugation, dynamic light scattering (DLS) and transmission electron microscopy (TEM) [5]. The SANS experiments, performed using a technique known as contrast variation, proved essential in constructing a model of the

¹ NIST Center for Neutron Research, National Institute of Standards and Technology, Gaithersburg, MD 20899

² Novavax, Inc., 21 Firstfield Road, Gaithersburg, MD 20878

³ National Institute of Standards and Technology, Institute for Bioscience and Biotechnology Research, Rockville, MD 20850

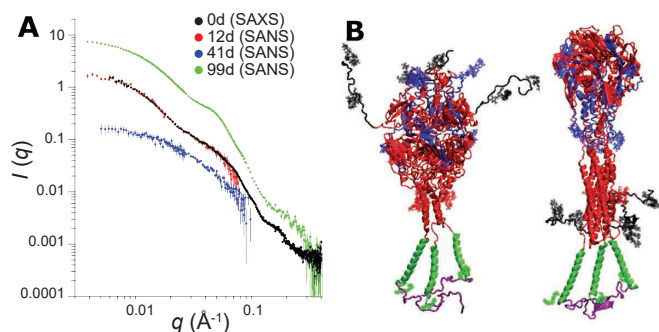


FIGURE 2: (A) SANS and SAXS data from the RSV F:PS80 nanoparticle. The percent D₂O in the buffer is indicated in the figure legend. The values range from 0d = 0 % D₂O to 99d = 99 % D₂O. The 12 % D₂O SANS data were scaled to the 0 % D₂O SAXS data to show that their shapes are the same. (B) All-atom models of the prefusion (left) and postfusion (right) RSV F trimers with the same protein sequence as in the Novavax nanoparticle vaccine. The F2 subunit is shown in blue and the F1 subunit ectodomain is shown in red. The TM (green) and CT (purple) domains, p27 peptide (black), glycans (red, blue and black, shown as spheres) and fatty acids (green, shown as spheres) were added to the RSV F trimer prefusion and postfusion ectodomain X-ray crystal structures using modern molecular dynamics techniques [5].

nanoparticle structure that described its overall shape and the spatial relationship between the RSV F protein and the PS80 detergent.

SANS and SAXS data were obtained for the RSV F:PS80 nanoparticles (Figure 2A), with the SANS data being obtained in buffers containing different ratios of H₂O:D₂O. Due to the widely different neutron scattering properties of hydrogen and deuterium, varying the H₂O:D₂O ratio in the buffer changed the scattering contrast between the RSV F protein and the buffer and between the PS80 detergent and the buffer in different ways. Thus, the scattering from RSV F:PS80 in 99 % D₂O buffer contained contributions from both RSV F and PS80, whereas that in 41 % D₂O buffer contained a contribution only from PS80 and that in 12 % D₂O buffer contained a contribution only from RSV F. This allowed for the separation of the scattering from the two components in the RSV F:PS80 nanoparticle and for the calculation of the molecular weights of the individual components [5], providing key information for constructing structural models of the nanoparticle.

All-atom models of the RSV F trimer used in the nanoparticle vaccine were constructed (Figure 2B) using available X-ray crystal structures of RSV F trimer prefusion and postfusion ectodomains (lacking the TM and CT regions) as starting structures [5]. The SANS contrast variation data and molecular weight analysis showed that the nanoparticle vaccine consisted of five RSV F trimers ordered around a cylindrical-shaped PS80 core that is assumed to stabilize the TM regions of the trimers. A hybrid all-atom and coarse-grained model of the RSV F:PS80 nanoparticle was constructed that was consistent with the SAXS and SANS data (Figure 3A). The five-trimer model also explains the TEM images (Figure 3B), which are projections of the 3-D structure (Figure 3C).

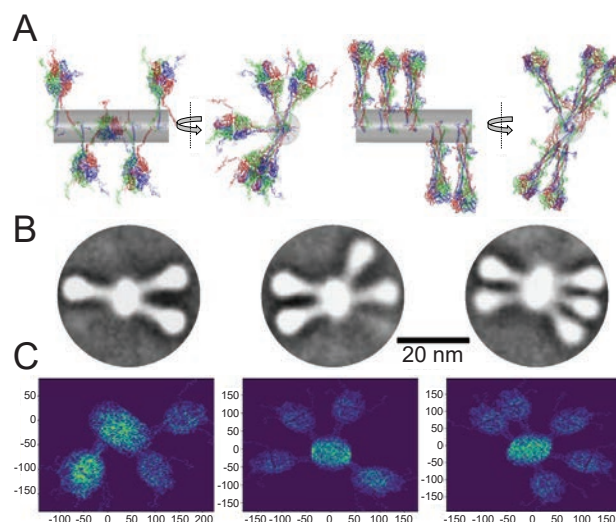


FIGURE 3: Adapted from [5]. (A) Representative five-trimer RSV F:PS80 nanoparticle model structures constructed from the prefusion (left) and postfusion (right) trimer ectodomain starting structures. The cylinder represents the region where the PS80 resides and stabilizes the TM domains of the trimer. (B) TEM 2-D class-averaged images of the RSV F:PS80 nanoparticle. (C) 2-D projections of representative five-trimer (prefusion) RSV F:PS80 nanoparticle model structure showing that a single population of five-trimer nanoparticles can result in 2-D images that are consistent with the TEM data. Axes are in Angstroms.

SANS data provided critical information that, when combined with those obtained from other techniques, provided a consistent picture of the structure of the RSV F:PS80 nanoparticle vaccine in solution. The resultant structure explains how the size of the nanoparticle is modulated by the ratio of protein to detergent, suggesting linear growth along the long axis of the PS80 cylindrical core and stabilization by controlling the amount of detergent available at a given protein concentration. The arrangement of RSV F in the nanoparticle is not closely packed, which helps explain why a diverse range of antibodies can bind the vaccine and thus elicit the observed robust immune response. This work outlines a general strategy that can be extended to the characterization of other colloidal vaccines and drug delivery systems in solution.

References

- [1] H. G. Kelly, S. J. Kent, A. K. Wheatley, *Expert Review of Vaccines* **18**, 269 (2019).
- [2] C. Griffiths, S. J. Drews, D. J. Marchant, *Clin Microbiol Reviews* **30**, 277 (2017).
- [3] A. August, G. M. Glenn, E. Kpamegan, S. P. Hickman, D. Jani, H. Lu, D. N. Thomas, J. Wen, P. A. Piedra, L. F. Fries, *Vaccine* **35**, 3749 (2017).
- [4] N. Patel, M. J. Massare, J.-H. Tian, M. Guebre-Xabier, H. Lu, H. Zhou, E. Maynard, D. Scott, L. Ellingsworth, G. Glenn, G. Smith, *Vaccine* **37**, 6112 (2019).
- [5] S. Krueger, J. E. Curtis, D. R. Scott, A. Grishaev, G. Glenn, G. Smith, L. Ellingsworth, O. Borisov, E. L. Maynard, *Mol. Pharmaceutics* **18**, 359 (2021).

Understanding the mechanisms underlying vaping-associated lung injury

M. DiPasquale,¹ O. Gbadamosi,¹ M. H. L. Nguyen,¹ S. R. Castillo,¹ E. G. Kelley,² M. Nagao,^{2,3,4} and D. Marquardt^{1,5}

There is increasing evidence that vaping causes lung injury known as e-cigarette/vaping associated lung injury (EVALI)—an epidemic affecting mostly youths and individuals under 35 years old [1]. EVALI is a condition with symptoms ranging from shortness of breath to chronic lung damage. The cause of EVALI is not well understood, but among the factors that link EVALI to lung dysfunction, vitamin E acetate (VitEAc) has emerged as a critical mediator [2]. VitEAc is safe when ingested as a supplement or used in topical applications. Strikingly, its use in vape mixtures implicate its direct inhalation with toxic effects: VitEAc is the primary toxicant found in the bronchoalveolar lavage fluid of EVALI patients [2], but how it may induce alveolar dysfunction is currently unknown. The use of small angle neutron scattering (SANS) and neutron spin-echo spectroscopy (NSE) indicates that VitEAc can significantly alter the properties of the inner lining of the lungs, the pulmonary surfactant.

The pulmonary surfactant monolayer is a key structure for the proper function of the lungs, and as such, needs to maintain very strict physical and mechanical properties. For example, the pulmonary surfactant monolayer should have an area compressibility of < 0.01 mN/m for proper lung function, indicative of two-dimensional membrane elasticity. If this compressibility increases, the alveoli may be prone to collapse, thus resulting in many of the symptoms observed in those suffering from EVALI. By way of NSE, we were able to measure the 2D elastic properties of two pulmonary surfactant mimic systems. The first being the commonly used single-lipid mimic of dipalmitoylphosphatidylcholine (DPPC, the most prevalent phospholipid in lung surfactant) and a more complex surfactant-mimic containing the most abundant lipid components in natural lung surfactant: DPPC, palmitoyloleoylphosphatidylcholine, palmitoyloleoylphosphatidylglycerol, and cholesterol [3].

NSE data collected on the NG-A neutron spin-echo spectrometer located at the NCNR show a softening of the both membrane system mimics upon the addition of VitEAc (Figure 1a). Interestingly, it was found that increasing vitamin E acetate concentration nonlinearly increased membrane

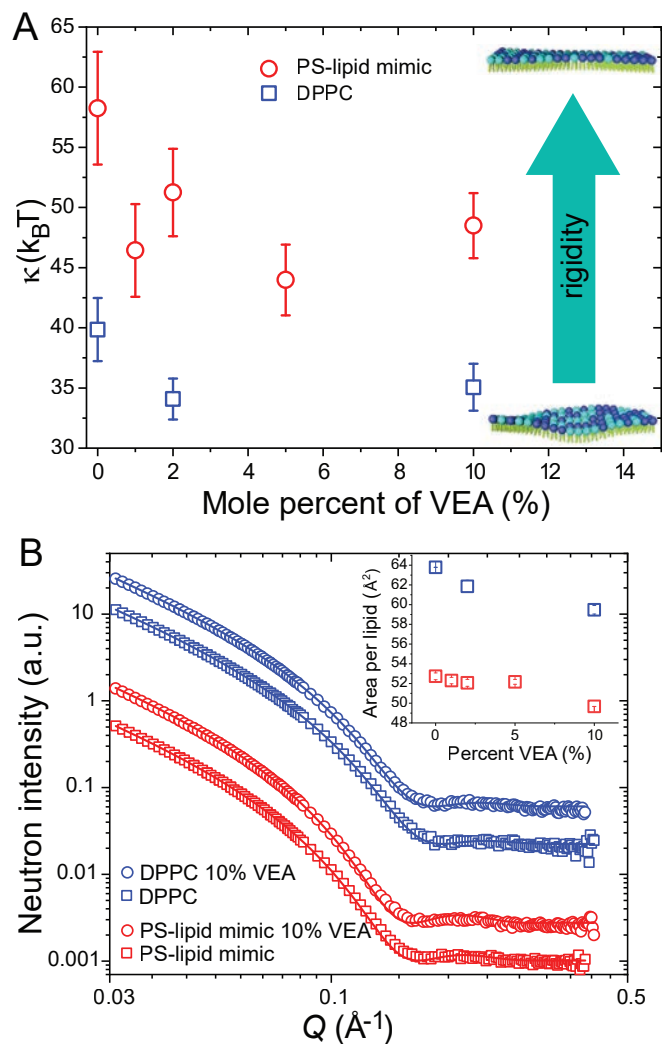


FIGURE 1: (A) Bending moduli (κ) for DPPC at 45 °C (\square) and PS-lipid mimic at 37 °C (\circ) with increasing amounts of vitamin E acetate (VEA) measured with NSE. (B) SANS curves for DPPC (blue) without VEA (\square) and with $\chi = 0.10$ VEA (\circ) and PS lipid mimic (red) without VEA (\square) and with $\chi = 0.10$ VEA (\circ). Data are offset for improved visibility. Optimized model fits are represented by solid lines using [5]. The inset shows the area per lipid (AL) for DPPC (\square) and PS-lipid mimic (\square) as a function of vitamin E acetate content. Figure adapted from DiPasquale et al. [6].

¹ Department of Chemistry and Biochemistry, University of Windsor, Windsor, Ontario, Canada N9B 3P4

² NIST Center for Neutron Research, National Institute of Standards and Technology, Gaithersburg, MD 20899

³ Indiana University, Bloomington, IN 47408

⁴ University of Delaware, Newark, DE 19716

⁵ Department of Physics, University of Windsor, Windsor, Ontario, Canada N9B 3P4

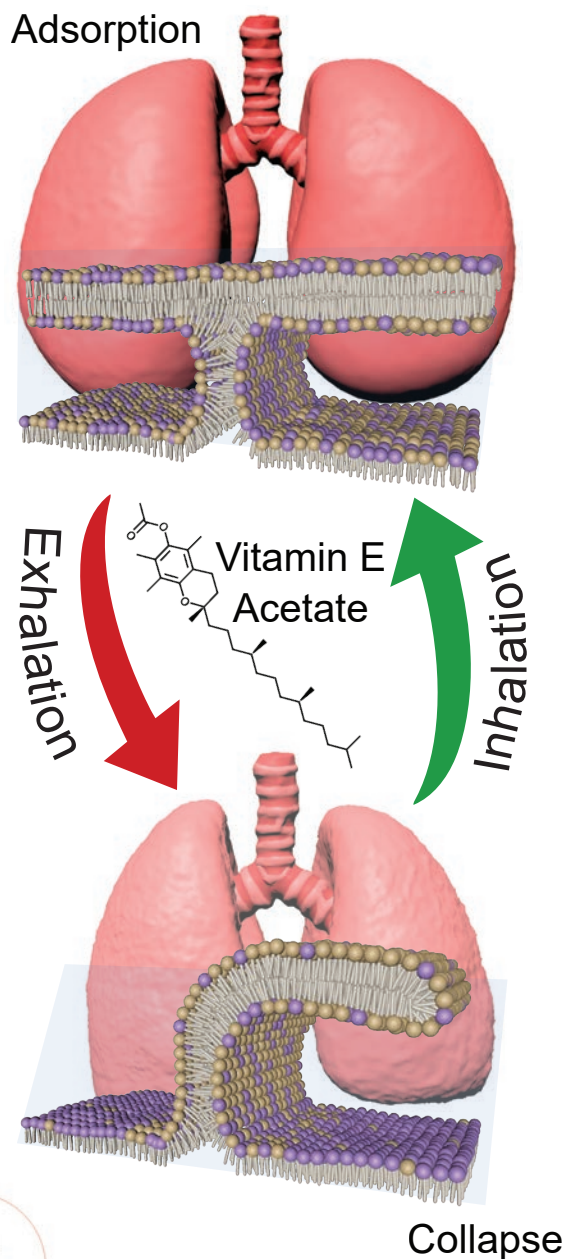


FIGURE 2: Addition of vitamin E acetate to pulmonary surfactant produces a membrane with softer mechanical properties. Softer monolayer systems promote adsorption to interfaces at the low surface tensions of inhalation but will subsequently collapse when exposed to the high surface tensions of exhalation.

softness; nevertheless, softer membranes would promote adsorption to the air–liquid interface during inhalation as well as collapse from the interface during exhalation.

Further, structural information, namely the hydrocarbon thickness of the monolayer, was determined from SANS measurements (Figure 1b) taken on the NGB-30m SANS instrument. The hydrocarbon thickness of the monolayer directly impacts the key membrane elastic property of area compressibility, which is crucial to the respiration process. By combining our NSE and SANS data, we observed a significant increase in the area compressibility. In fact, an increase in compressibility of approximately 20 % was observed, which would interfere with surfactant monolayer stability

at high surface tensions. Based on the classical mechanism of pulmonary surfactant, we suspect that VitEAc-induced membrane softening promotes monolayer collapse at end expiration, thereby offering a mechanical explanation for lung dysfunction and linking the physical chemistry of VitEAc to disease pathology (Figure 2).

The data support the notion that a shortness of breath and pneumonitis-like pathology of EVALI [4] stem from a failure of pulmonary surfactant at end expiration. This failure occurs due to a physical interaction between vitamin E acetate and the PS. Although more evidence is required to confirm this theory, the effects of vitamin E acetate on the PS lipid mimics studied here could provide a multifaceted mechanical basis for prolonged lung dysfunction that makes e-cigarette/vaporizer users significantly more susceptible to complications involving respiratory distress, particularly those caused by infections [1].

The biological function of the pulmonary surfactant relies on a precarious balance of adsorption and film stability. To date, we have employed NSE spectroscopy to characterize the elastic behavior of two lipid mimics of pulmonary surfactant. We further tested the elastic behavior upon the addition of vitamin E acetate to our mimetic systems and observed an increase in compressibility of approximately 20 % that could interfere with pulmonary surfactant stability at high surface tensions. From this we speculate that vitamin E acetate-induced membrane softening can promote pulmonary surfactant failure at end exhalation, thereby offering a mechanical explanation for lung dysfunction.

Though it remains unclear that vitamin E acetate is the sole culprit of EVALI, neutrons have provided a link between biophysics and pathology that suggests vitamin E acetate can affect the elastic properties of the pulmonary surfactant that play a vital role in breathing.

References

- [1] B. A. King, C. M. Jones, G. T. Baldwin, P. A. Briss, N. Engl. J. Med. **382**, 689 (2020).
- [2] B. C. Blount, et al., (2020) N. Engl. J. Med. **382**, 697 (2020).
- [3] Y. Y. Zuo, R. A. Veldhuizen, A. W. Neumann, N. O. Petersen, F. Possmayer, *Biochim. Biophys. Acta, Biomembr.* **1778**, 1947 (2008).
- [4] Y. M. Butt, M. L. Smith, H. D. Tazelaar, L. T. Vaszar, K. L. Swanson, M. J. Cecchini, J. M. Boland, M. C. Bois, J. H. Boyum, A. T. Froemming, A. Koor, I. Mira-Avendano, A. Patel, and B. T. Larsen, N. Engl. J. Med. **381**, 1780 (2019).
- [5] A. Lewis-Laurent, M. Doktorova, F. A. Heberle, D. Marquardt, ChemRxiv. doi.org/10.26434/chemrxiv.14454645.v1 (2021).
- [6] M. DiPasquale et al., *Chem. Res. Toxicol.*, **33**, 2432 (2020).

Exploring pharmaceutical component incompatibility through very small-angle neutron scattering

P. H. Gilbert,^{1,2} Z. Zhang,^{1,2} K. K. Qian,³ D. P. Allen,³ N. J. Wagner,¹ and Y. Liu^{1,2}

Successful pharmaceutical formulations must maintain product stability and efficacy during storage and delivery. Stability of an injectable pharmaceutical is inextricably linked to the interactions among its individual components: protein, surfactant, preservative, etc. Incompatibility between any of these formulation constituents can result in undesired phase separation or aggregation, which may reduce or even negate the therapeutic effect of a pharmaceutical product. It is well known that some anti-microbial preservatives, specifically phenolic preservatives, are not compatible with common surfactants, like polysorbates [1], which sometimes results in increased aggregation, and eventually solution turbidity [2]. However, despite the popular use of both components in injectable pharmaceuticals, there has not been a conclusive investigation on the underlying mechanism of surfactant/preservative solution turbidity. It is thus of critical interest to reveal the root causes of incompatibility between non-ionic surfactants and phenolic preservatives.

Biopharmaceutical formulations such as monoclonal antibody and fusion protein solutions typically contain a surfactant component for stability. A common choice is polysorbate 80 (PS80), a nonionic surfactant that plays a key role in stabilizing protein solutions by protecting protein surfaces and preventing protein adsorption to container walls. At pharmaceutically relevant concentrations in aqueous solution, PS80 molecules self-assemble into ellipsoidal micelles. These micelles are stable in solution and have an aggregation number of ≈ 89 with a radius of gyration, R_g , of ≈ 3.0 nm [3].

Antimicrobial preservatives, such as m-cresol, maintain the sterility of injectable pharmaceutical products by preventing unwanted microbial growth. Inclusion of m-cresol allows for multiple doses to be housed in a single vial. At concentrations below the solubility limit, aqueous m-cresol is clear and does not assemble into micelles. Thus, PS80 and m-cresol separately produce clear stable solutions at room temperature.

However, the combination of PS80 and m-cresol may result in a turbid formulation, which is unacceptable in drug products. The onset of turbidity is sometimes delayed, requiring days or even weeks to become apparent to the eye. To understand the nature of this undesired turbidity, very small-angle neutron

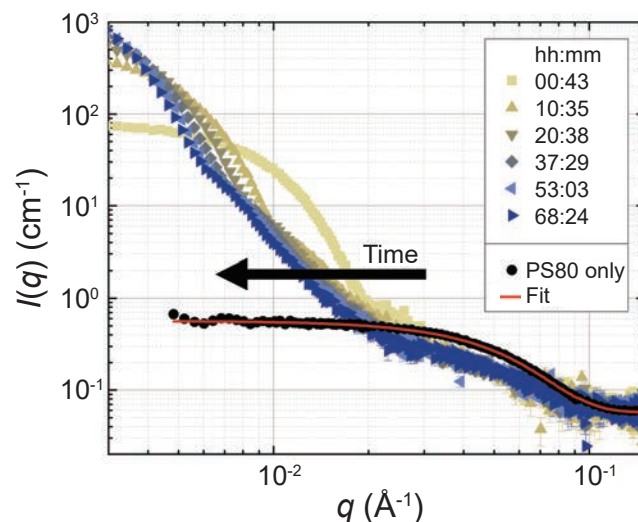


FIGURE 1: Scattering intensity curves measured on vSANS for solutions of 1 mg/mL PS80 with and without 3.15 mg/mL m-cresol in D_2O at 22 °C showing the increasing aggregate size with time after m-cresol addition, where the ellipsoidal model fit for the time-invariant PS80 only solution is presented along with the data. Error bars denote one standard deviation.

scattering (vSANS) is used to explore the morphology of nanostructures such as micelles that form and aggregate over time. By simultaneously covering a wide range of the scattering vector, q , with multiple detectors, vSANS is well-suited for revealing the kinetics of morphological changes across a broad range of length scales. Figure 1 provides an example of vSANS data for both a nonaggregating PS80-only solution (black) and an aggregating PS80/m-cresol solution (brown/blue). For a solution of 1 mg/mL PS80 and 3.15 mg/mL m-cresol, the intensity curve shifts left and up at low- q over time, consistent with aggregate growth. Increased scattering intensity at low- q corresponds to larger aggregate size that causes greater solution turbidity [4]. These aggregates continuously grow over time, where no stable aggregate size is reached during the ≈ 70 h experimental period.

The radius of gyration, R_g , is extracted from scattering patterns in Figure 1 to produce Figure 2a, where R_g is plotted versus time, t , for each measurement temperature. Figure 2a confirms that increasing turbidity is caused by progressive growth of

¹ Department of Chemical and Biomolecular Engineering, Center for Neutron Science, University of Delaware, Newark, DE 19716

² NIST Center for Neutron Research, National Institute of Standards and Technology, Gaithersburg, MD 20899

³ Eli Lilly and Company, Indianapolis, IN 46225

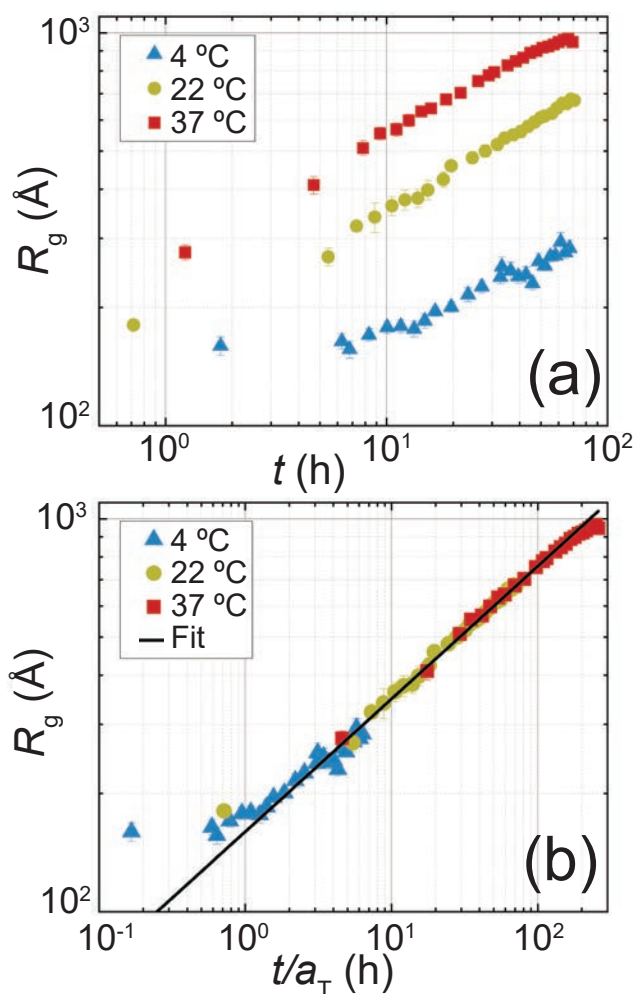


FIGURE 2: R_g (Å) versus t (h) a) plot of unbuffered 1.0 mg/mL PS80 and 3.15 mg/mL m-cresol solution in D_2O at $T = 4$ °C, 22 °C and 37 °C and b) time-shifted master curve at $T = 4$ °C ($a_T = 10.6$), 22 °C ($a_T = 1$) and 37 °C ($a_T = 0.267$) along with power-law fit, $R_g = 154(t/a_T)^{0.349}$, corresponding to a fractal dimension $d_f = 2.865$. Error bars denote one standard deviation.

aggregates in solution. Furthermore, warmer measurement temperatures accelerate aggregate growth resulting in larger aggregates. Interestingly, each of the three curves in Figure 2a can be collapsed onto a single master curve in Figure 2b. The master curve reveals that the aggregation mechanism is not altered by temperature changes. The evolution of R_g over t follows a power-law relationship after an initial growth stage. This power-law coalescence of smaller aggregates into larger ones is reminiscent of diffusion-limited colloidal aggregation (DLCA) kinetics.

When PS80 and m-cresol are combined in the presence of a 5 mmol/L citrate buffer, the solution becomes turbid more rapidly than in unbuffered solution. This unexpected effect of solution buffering is quantitatively examined by analyzing the vSANS to extract the Porod coefficient, K , as shown in Figure 3, where $K \propto S/V$, S is aggregate surface area and V is aggregate volume. Higher K correlates to a Figure 3 reveals that including a citrate buffer accelerates aggregate growth by many orders of magnitude, where the open symbols (buffered solutions) represent aggregates that are much larger than those of the

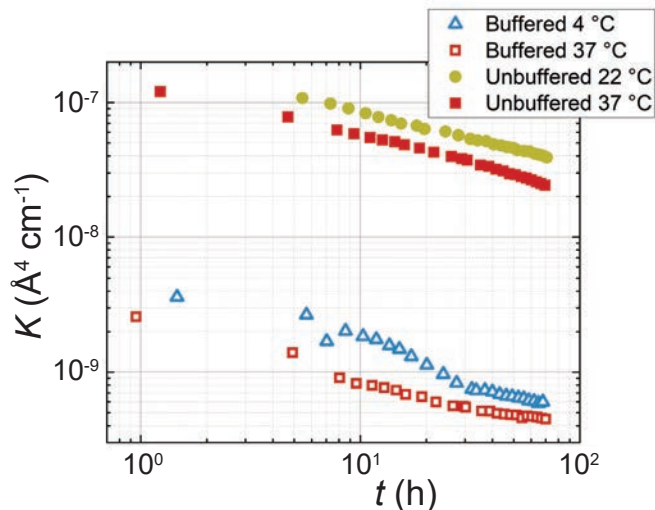


FIGURE 3: Porod plot of buffered (open) and unbuffered (filled) 1.0 mg/mL PS80 and 3.15 mg/mL m-cresol solution in D_2O at $T = 4$ °C, 22 °C and 37 °C showing decrease in surface area to volume ratio with time. Error bars denote one standard deviation.

closed symbols (unbuffered solutions).

This vSANS study reveals that PS80/m-cresol incompatibility results in progressive aggregate growth that eventually causes increased solution turbidity. Because these aggregates continually grow over time, the sample eventually experiences macroscopic phase separation at long time. The kinetics of aggregation, coalescence and eventual phase separation are affected by both temperature and buffer conditions. These observations contribute to a deeper understanding of PS80/m-cresol solution incompatibility and reveal the structural origins of aggregation, allowing for a more systematic approach to combating this formulation challenge.

References

- [1] R. C. Rowe, P. J. Sheskey, M. E. Quinn, Handbook of Pharmaceutical Excipients, 6th ed., Pharmaceutical Press, London and American Pharmacists Association: Washington 5837 (2009).
- [2] S. Shi, Z. Chen, J. M. Rizzo, et al., J. Anal. Bioanal. Tech. **6**(3), 1000245 (2015).
- [3] J. Nayem, Z. Zhang, A. Tomlinson, et al., J. Pharm. Sci. **109**(4), 1498 (2020).
- [4] P. H. Gilbert, Z. Zhang, K. K. Qian, et al., J. Pharm. Sci. **110**(6), 2395 (2021).

Membrane surface recognition by the ASAP1 PH domain and consequences for interactions with the small GTPase Arf1

O. Soubias,¹ S. Pant,^{2,3} F. Heinrich,^{4,5} Y. Zhang,¹ N. S. Roy,⁶ J. Li,¹ X. Jian,⁶ M. E. Yohe,⁷ P. A. Randazzo,⁶ M. Lösche,^{4,5} E. Tajkhorshid,^{2,3} and R. A. Byrd¹

Cell membrane signaling and trafficking are fundamental properties of living organisms supporting cell communication, function, and growth. Cell signaling pathways also lay at the center of many diseases such as cancer and are a prime target for medical intervention. Many aspects of cell membrane signaling and trafficking are regulated by the assembly of dynamic multi-component protein platforms, which associate with cell membrane surfaces in a lipid-dependent fashion [1]. Phosphatidylinositol phosphates (PIPs) are a component of lipid membranes and a common target for lipid-binding domains of signaling proteins. Although present in cell membranes at relatively low concentrations, PIPs may cluster to form nanoscale domains. Pleckstrin homology (PH) domains are among the most common membrane-binding domains

and bind PIPs. Our work focuses on the PH domain of the Arf GTPase (guanine triphosphatase)-activating protein (GAP) ASAP1 [2]. ASAP1 affects cell behaviors such as proliferation, invasion, and metastasis of cancer cells. Its function depends on interacting with a member of the Ras superfamily, adenosine diphosphate-ribosylation factor-1 (Arf1) [3].

The ASAP1 PH domain binds to phosphatidylinositol 4,5-bisphosphate (PI(4,5)P₂)-containing membranes. Recently, a crystal structure of ASAP1 PH in complex with isolated PI(4,5)P₂ was solved, providing structural evidence for the presence of two PI(4,5)P₂ headgroup-binding sites in a single domain. This result suggests that PI(4,5)P₂ lipids cooperate to promote membrane association, potentially switching GAP activity

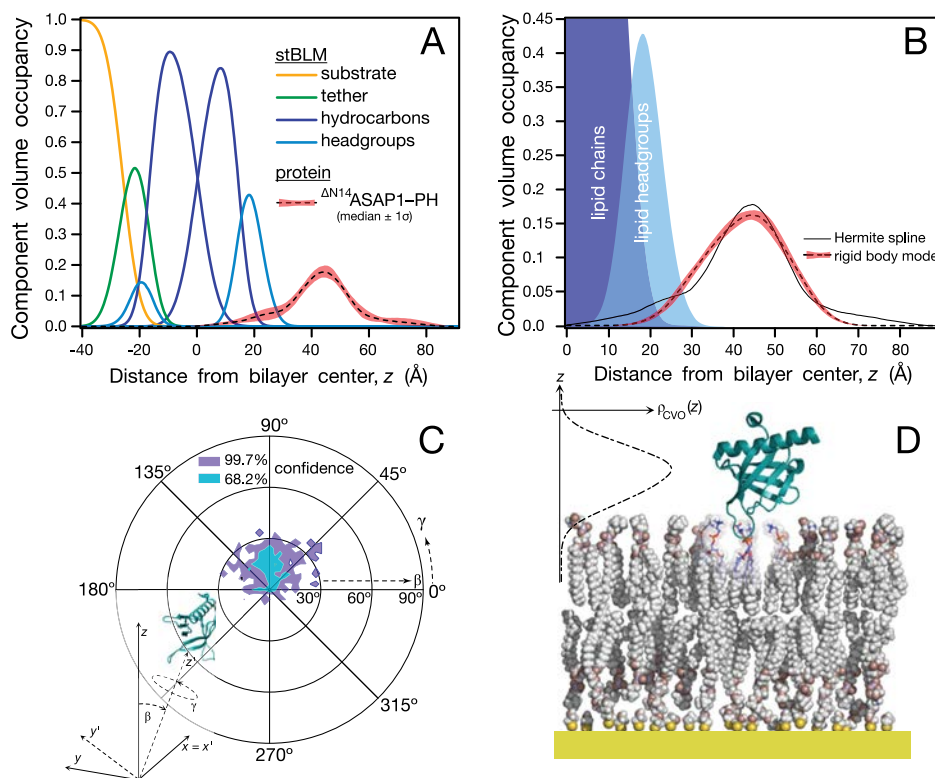


FIGURE 1: Docking geometry of the ASAP1 PH domain on a PI(4,5)P₂-containing surface-tethered lipid membrane by NR. (A) CVO profiles of a lipid bilayer with the surface-bound ASAP1 PH parameterized as a Hermite spline. The protein distribution is indicated with its median (black dashed line) and 68.2% confidence region. (B) Best-fit rigid-body modeling with the crystal structure of ASAP1 PH to determine the protein orientation (PDB: 5C79) and comparison with the free-form model shown in (A). (C) Distribution of orientations of ASAP1 PH at the membrane parameterized in terms of two Euler angles, as indicated in the inset. (D) Visualization of the ASAP1 PH crystal structure on the surface-tethered membrane in a configuration (orientation and insertion depth) on the membrane at the center of the 68.2% probability region shown in (C). Phospholipids and substrate are only schematically displayed, but lipids are shown at the same scale as the protein. The CVO profile at the left shows the same data as in (B).

¹ Structural Biophysics Laboratory, Center for Cancer Research, National Cancer Institute, Frederick, MD 21702
² NIH Center for Macromolecular Modeling and Bioinformatics, Bethesda, MD 20892
³ Department of Biochemistry, Center for Biophysics and Quantitative Biology, University of Illinois at Urbana-Champaign, Urbana, IL 61801
⁴ Department of Physics, Carnegie Mellon University, Pittsburgh, PA 15213
⁵ NIST Center for Neutron Research, National Institute of Standards and Technology, Gaithersburg, MD 20899
⁶ Laboratory of Cellular and Molecular Biology, National Cancer Institute, National Institute of Health, Bethesda, MD 20892
⁷ Pediatric Oncology Branch, National Cancer Institute, National Institute of Health, Bethesda, MD 20892

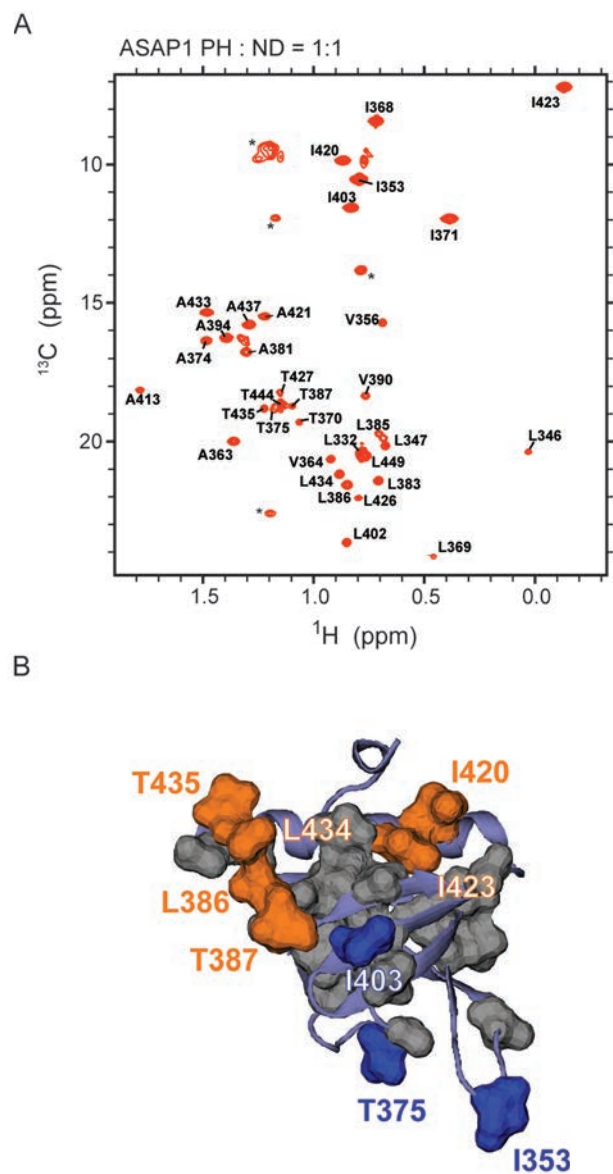


FIGURE 2: PI(4,5)P₂ triggered conformational switch identified by NMR. (A) Methyl-TROSY HMQC NMR spectrum of I, L, V, A, T-¹³CH₃ methyl labeled, perdeuterated ASAP1-PH reveals residue-specific chemical shift perturbations (CSPs) upon binding to PC:PI(4,5)P₂ NDs. (B) Methyl residues that show significant CSP differences, which are not located in the PI(4,5)P₂ binding sites, and suggest an allosteric conformational change triggered by PI(4,5)P₂ binding are plotted in orange on the crystal structure. Residues in the PI(4,5)P₂ binding sites are plotted in dark blue.

within a narrow range of PIP concentrations. Neutron scattering techniques such as reflectometry are particularly suited to validate this hypothesis by structurally probing the association of such proteins with intrinsically disordered membranes, albeit at low spatial resolution. An interdisciplinary collaboration between NIST, the National Cancer Institute, Carnegie Mellon University, and the University of Illinois at Urbana-Champaign has determined the membrane-bound structure of the PH domain using neutron reflectometry (NR), nuclear magnetic resonance (NMR) and molecular dynamics (MD) simulations.

Figure 1A shows the results from fitting the NR data measured after exposing a sparsely-tethered bilayer lipid membrane to ASAP1 PH in solution. In this approach, the protein component volume occupancy (CVO) profile is modeled using a nearly bias-free monotonic Hermite spline. Uncertainties on all model parameters are obtained from evaluating the posterior probability distribution function obtained from a Monte Carlo Markov Chain-based global parameter optimizer. Panel B shows how such a protein CVO compares to a crystal structure of ASAP1 PH for various orientations of the protein with respect to the lipid membrane. We demonstrated that only a narrow range of orientations is supported by the NR data (Figure 1C). Figure 1D shows a to-scale representation of the crystal structure positioned on the bilayer in agreement with the experimental data.

NMR experiments were performed using small membrane mimetics in the form of nanodiscs (ND) [4] containing PI(4,5)P₂ in a background of other essential lipids. NMR monitors the binding interactions between the ASAP1 PH and PI(4,5)P₂ at atomic resolution. Analysis of both amide ¹⁵N and methyl ¹³C spectra revealed the location of the PI(4,5)P₂ binding sites and the binding affinity (Figure 2). Further NMR experiments using paramagnetic relaxation enhancement revealed which portions of the ASAP1 PH were inserted into the membrane. The NMR data collectively suggested a conformational change of ASAP1 PH at the membrane, and they provided restraints of the protein's orientation. Molecular dynamics (MD) simulations permitted an atomistic sampling of binding events between the membrane and ASAP1 PH beyond the detail provided by NR and NMR. A correlation of the NMR results with MD trajectories identified individual residues involved in binding PI(4,5)P₂. MD simulations in detail characterized the ensemble of ASAP1 PH orientations at the membrane, which was found to be in excellent agreement with the NR data.

NR, NMR, and MD simulations collectively let us identify the orientation of ASAP PH at the membrane surface and the residues that interact with PI(4,5)P₂ lipids. We found that binding multiple PI(4,5)P₂ molecules triggers a functionally relevant allosteric conformational switch and maintains ASAP1 PH in a well-defined orientation, allowing critical contacts with an Arf1 mimic to occur. Our model [5] provides a framework to understand how binding of the ASAP1 PH domain to PI(4,5)P₂ at the membrane may play a role in the regulation of Arf1.

References

- [1] J. Cherfils, *Curr. Opin. Struct. Biol.* **29**, 67 (2014).
- [2] M. T. Brown, J. Andrade, et al., *Mol. Cell. Biol.* **18**, 7038 (1998).
- [3] E. Sztul, P.-W. Chen, et al., *Mol. Biol. Cell* **30**, 1249 (2019).
- [4] I. G. Denisov, S. G. Sligar, *Chem. Rev.* **117**, 4669 (2017).
- [5] O. Soubias, S. Pant, et al., *Sci. Adv.* **6**, eabd1882 (2020).

Small-angle neutron scattering reveals preferential solvation as a mechanism for regulating protein dimerization in membranes



J. L. Robertson,¹ E. G. Kelley,² S. C. M. Teixeira,^{2,3} and J. D. Faraldo-Gómez⁴

Lipid membranes are self-assembling macromolecular structures that encapsulate a cell's interior, separating it from the external world. Membranes can be formed by a large variety of lipid types, with many other kinds of greasy molecules found therein, and so membranes have apparently infinite possibilities of chemical composition. In addition to acting as a barrier, the lipid bilayer also provides an environment that houses membrane proteins; for example, transport proteins that facilitate the import and export of essential biological components, such as water, protons, ions, nutrients and waste.

How might the lipid membrane influence membrane proteins? Previous studies demonstrated that membrane protein activity can be affected by structural changes in the lipid bilayer, specifically by the mechanism of hydrophobic mismatch [1]. In this event, either the membrane itself, or the proteins within, adopt conformations to minimize this mismatch. However, these conformational biases come with a cost. On a macroscopic level, the membrane behaves much like a spring, with an associated free-energy minimum and defined work required to stretch or compress it. One way around this is to alter the global thickness of the membrane by altering the lengths of the lipid chains comprising the membranes. Thus, membranes thickness can be controlled by the lipid composition, and this can alter the conformational distribution of proteins directly.

While experimental studies of model systems show that there is a clear connection of membrane thickness to membrane protein assembly, in nature, the hydrophobic thickness of the membrane is generally set to be around 35 Å, regardless of natural variations in lipid composition. This suggests that other mechanisms may be required if physiological lipid compositions are to influence membrane protein structure and function. To investigate this, we studied whether membrane protein dimerization equilibrium in membranes is sensitive to lipid composition. Our group previously demonstrated that the homodimeric CLC-ec1 chloride/protein antiporter (Figure 1A,B) demonstrates reversible, equilibrium dimerization in lipid

bilayers using single-molecule photobleaching microscopy [2]. This method allows for the measurement of full equilibrium binding isotherms in a synthetic mimic of the *E. coli* polar lipid composition containing 16-carbon palmityl, and 18-carbon oleoyl, acyl-chains (PO lipids). The measured free energy is -11 kcal/mol, relative to the 1 subunit/lipid standard state, implying that if two CLC-ec1 subunits were expressed in an *E. coli* cell, they would be observed to be dimeric 90% of the time. Thus, from a biological perspective, this represents a stable association, yet the mechanism conferring such stability remained unknown.

The CLC-ec1 dimerization interface is large and significantly greasy but appears to be curved and shorter in the center, offering a clue that hydrophobic mismatch may be a factor. To quantify this, we carried out a computational analysis of the membrane structure in monomeric and dimeric states by coarse-grained molecular dynamics simulations [5]. While the dimer is appropriately matched to the surrounding membrane, the monomeric state reveals a change in the membrane structure, with a pronounced 8 Å thinning at the dimerization interface, i.e. about a quarter of the hydrophobic thickness. Thus, it appears as though the dimerization interface of CLC-ec1 is poorly solvated and non-bilayer like in 16/18 chain biological lipids.

Based on this, we hypothesized that the energetic penalty that is introduced by this membrane defect surrounding the monomeric state is a major driving force for dimerization. If true, then we would expect that adding in shorter chain lipids, such as di-lauryl lipids containing 12 carbon chains (DL lipids), would act as better solvents for this interface and thus shift equilibrium to the monomeric state (Figure 1C). Experimentally, the protein showed no change in function in membranes with (0 to 20) % DL, and a gradual decrease in transport rates for DL > 20 %. Yet, when we examined dimerization, we observed a two-phase shift in dimerization with a 1.5 kcal/mol destabilization for DL < 1 %, with an additional 0.8 kcal/mol destabilization for every 10 % increase in DL. Thus, the addition of short-chain lipids shifted the equilibrium completely to the

¹ Biochemistry and Molecular Biophysics, Washington University School of Medicine, St. Louis, MO 63110

² NIST Center for Neutron Research, National Institute for Standards and Technology, United States, Gaithersburg, MD 20899

³ Center for Neutron Science, Chemical and Biomolecular Engineering, University of Delaware, Newark, DE 19716

⁴ Theoretical Molecular Biophysics Laboratory, National Heart, Lung and Blood Institute, National Institutes of Health, Bethesda, MD 20824

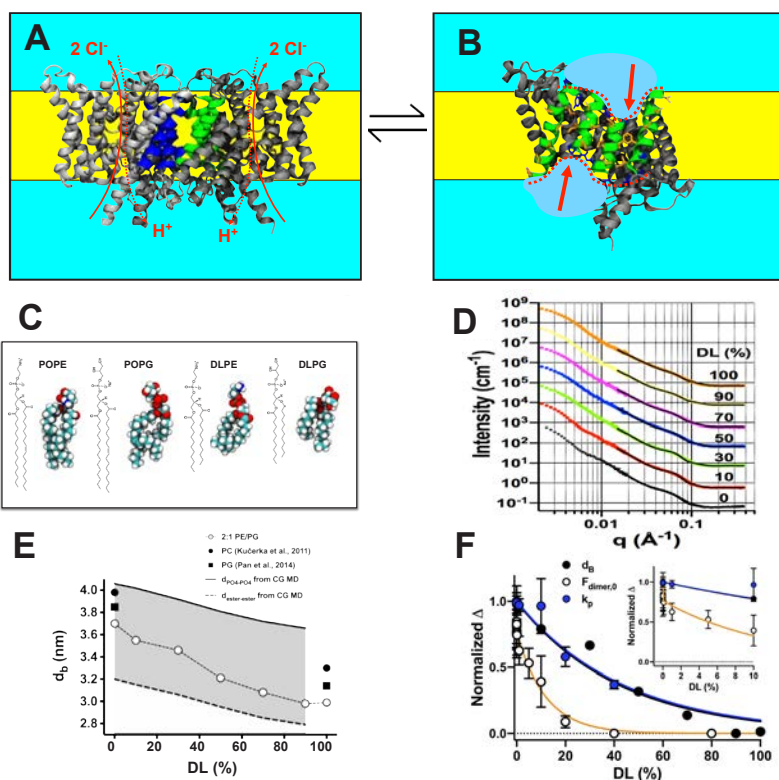


FIGURE 1: Dimerization of CLC-ec1 in lipid bilayers depends on lipid composition by the mechanism of preferential solvation. (A) CLC-ec1 dimer and (B) monomer with dimerization interface shown in green and blue. Non-polar side-chains are highlighted orange with red arrows indicating a region of hydrophobic mismatch. (C) Structures of C16:0,18:1 palmityl-oleoyl (PO) phosphatidylethanolamine and phosphatidylglycerol lipids, as well as C12:0 di-lauryl (DL) phosphatidylethanolamine and phosphatidylglycerol lipids used in this study. (D) SANS spectra as a function of DL (%) at 25 °C from 100 nm extruded vesicles. Spectra are offset from the 0 % condition for visualization. Solid lines represent best fit of the $q > 0.015 \text{ \AA}^{-1}$ regions using the multilamellar form factor model. The broad shoulder at $q \approx (0.06\text{--}0.7) \text{ \AA}^{-1}$ is due to the presence of a small population of multi-lamellar vesicles. (E) Bilayer thickness (d_b) as a function of DL (%), white circles). Reference SANS data is shown for PC (solid circle [3]) and PG (solid square [4]). (F) Change in membrane transport rate (Δk_p), and dimerization ($\Delta F_{dimer,0}$) compared to the change in bilayer thickness (Δd_b). Inset shows that there are two phases to the change in dimerization, occurring before changes in bilayer thickness supporting the mechanism of preferential solvation.

monomeric form while maintaining the protein's function. While this observation supported the original hypothesis, the mechanism remained unknown.

Determining this required quantitative information about the bilayer structure, and so we carried out small angle neutron scattering (SANS) experiments of the mixed membranes examining (0 to 100) % DL (Figure 1D,E). The SANS data demonstrated that the membranes become thinner with increased DL, reaching an 8 Å decrease in thickness that is expected to hydrophobically match the thinned defect at the CLC-ec1 dimerization interface. However, comparing the change in bilayer thickness with changes in transport activity and dimerization indicated that there are different ways that the membrane is linking to the structure and function of the protein (Figure 1F). Thus, this suggests that dimerization equilibrium is linked to the membrane, but by a mechanism that is distinct from hydrophobic matching.

Examining the full titration of dimerization with DL provided a clue. In the lower DL range, the change in free energy depends on the logarithm of DL in the membrane. Classically, this type of response has been well known in the study of the stability of soluble proteins and indicates a mechanism of preferential solvation [6]. This explains how salts, sugars, glycerol and denaturants can alter the stability and solubility of many proteins that are solvated by water. While this has been proposed to be a plausible effect in membranes [7], it had not yet been observed experimentally. To further validate this idea we carried out additional computations investigating the solvation distributions of DL and PO around the CLC-ec1 monomer in these mixed membranes. The analysis

demonstrated that while the non-bilayer defect is still present, the DL lipids become enriched around the dimerization interface, acting as a better solvent.

In summary, this study demonstrates that differential energetics in membrane solvation drive the dimerization of the homodimeric CLC-ec1 transporter. While hydrophobic matching is a means of modulating protein reactions, our findings demonstrate that the membrane can modulate the protein when there are no macroscopic changes in membrane structure. When the lipid composition changes at low levels within the membrane, reactions between proteins are affected by preferential solvation, presenting a new and physiological plausible mechanism of regulation within the membrane.

References

- [1] O. S. Andersen, R. E. Koeppe, *Annu Rev Bioph Biom.* **36**, 107 (2007).
- [2] R. Chadda, V. Krishnamani, K. Mersch, et al., *Elife.* **5**:e17438 (2016).
- [3] N. Kučerka, B. W. Holland, C. G. Gray, et al., *J Phys Chem B.* **116**, 232 (2011).
- [4] J. Pan, D. Marquardt, F. A. Heberle, et al., *Biochim Biophys Acta.* **1838**, 2966 (2014).
- [5] R. Chadda, N. Bernhardt, E. G. Kelley, et al., *Elife.* **10**:e63288 (2021).
- [6] C. Tanford, *J Mol Biol.* **39**, 539 (1969).
- [7] D. Marsh, *Biophys J.* **69**, 1191 (1995).

Ambient-temperature hydrogen storage via vanadium(II)-dihydrogen complexation in a metal–organic framework

D. E. Jaramillo,^{1,2} H. Z. H. Jiang,^{1,2} H. A. Evans,³ R. Chakraborty,^{1,4} H. Furukawa,^{1,2} C. M. Brown,^{3,5} M. Head-Gordon,^{1,4} and J. R. Long^{1,2,6}

The widespread implementation of hydrogen as a transportation fuel is hindered by the high pressures and cryogenic temperatures required to store sufficient gas to achieve reasonable driving ranges. As an alternative to compressed gas storage, the realization of solid adsorbent materials capable of strongly and reversibly binding H₂ at ambient temperatures and moderate pressures could transform the transportation sector and expand the adoption of fuel cells in other applications. Porous metal–organic frameworks (MOFs) have emerged as leading candidates in this context given their extremely high surface areas and atomic-level tunability. MOFs featuring coordinatively unsaturated, Lewis-acidic metal sites able to polarize and bind H₂ have been the focus of research in recent years; however, none of these materials exhibits H₂-binding enthalpies within the optimal range of –15 kJ/mol to –25 kJ/mol for ambient-temperature storage. Here, we describe the hydrogen storage properties of V₂Cl_{2.8}(btdd) (Fig. 1; H₂btdd, bis(1*H*-1,2,3-triazolo[4,5-*b*],[4',5'-*i*])dibenzo[1,4]dioxin), a framework exhibiting an H₂-binding enthalpy of –21 kJ/mol and usable hydrogen capacities greater than can be achieved with compressed H₂ under the same conditions [1].

The remarkable H₂-storage properties of V₂Cl_{2.8}(btdd) derive from the high density of exposed vanadium(II) sites (Fig. 1a, inset), which can engage in orbital-mediated interactions with weak π acids, as previously demonstrated for N₂ [2]. This framework engages in back-bonding interactions with H₂, as characterized via a range of techniques including variable-temperature *in situ* infrared spectroscopy, electronic structure calculations, and neutron powder diffraction. Structural models of guest-free and D₂-dosed V₂Cl_{2.8}(btdd) (Fig. 1b) were made possible through *in situ* neutron powder diffraction data collected at the NCNR using a custom-built gas delivery setup.

Deuterium was used for these experiments due to its favorable neutron scattering cross section relative to H. Because vanadium has a small neutron-scattering cross section, X-ray powder diffraction data were collected under the same conditions to obtain refined vanadium positions and thermal parameters. The ‘superatom’ approach was used to approximate the bound D₂ molecule as a single D-atom [3].

The refined structural model of V₂Cl_{2.8}(btdd) dosed with D₂ shows that the equatorial V–Cl bonds contract upon D₂ binding (Fig. 1b) while the Cl–V–Cl bond angle decreases slightly from 175.8(6)° to 167.9(7)°. These changes lead to a slight shift of the vanadium center out of the equatorial ligand plane, presumably to enhance metal orbital overlap with D₂. A similar structural change occurs when V₂Cl_{2.8}(btdd) is exposed to N₂ [2]. An analysis of the change in the weighted-profile R-factor with varying D-superatom positions led to a V–D centroid distance of 1.966(8) Å [1], which is the shortest metal–H₂ distance characterized in a MOF to date. In tandem with *in situ* infrared spectroscopy data and electronic structure calculations, these data indicate that back-bonding from vanadium(II) to H₂ is key to the stabilization of bound H₂ in the framework.

Because of the strong orbital-mediated interaction between H₂ and vanadium(II) in V₂Cl_{2.8}(btdd), the framework adsorbs appreciable hydrogen at ambient temperatures and low pressures. For example, at 1.2 bar and 298 K, the material achieves an H₂ capacity of 0.26 mmol/g, corresponding to a 10% vanadium(II)-site occupancy. Quantitative analysis of low-pressure adsorption data obtained for V₂Cl_{2.8}(btdd) at 298 K, 286 K, and 273 K revealed an H₂-binding enthalpy of –21 kJ/mol, which lies within the optimal range for ambient-temperature H₂ storage [5]. Hydrogen uptake in V₂Cl_{2.8}(btdd) was also examined at ambient temperatures and higher pressures near target conditions for on-board H₂ storage. At and above 40 bar, 100% of the vanadium(II) sites are occupied with hydrogen compared to only 33% of the nickel(II) sites in Ni₂(*m*-dobdc). Significantly, at 298 K and 100 bar, the total volumetric hydrogen uptake in V₂Cl_{2.8}(btdd) (based on the framework density from diffraction data) is 10.7 g/L; this is 38% more than that achievable with compressed H₂ under identical conditions (Fig. 2a). Further, considering operation at 298 K between 5 bar and 100 bar, the usable volumetric capacity of V₂Cl_{2.8}(btdd) is 30% more than that achievable with compressed H₂ under the same conditions (Fig. 2b).

In summary, we have shown that the coordinatively unsaturated vanadium(II) sites in V₂Cl_{2.8}(btdd) are capable of back-bonding interactions with H₂, as characterized using *in situ* variable-

¹ Department of Chemistry, University of California, Berkeley, CA 94720

² Materials Sciences Division, Lawrence Berkeley National Laboratory, Berkeley, CA 94720

³ NIST Center for Neutron Research, National Institute of Standards and Technology, Gaithersburg, MD 20899

⁴ Chemical Sciences Division, Lawrence Berkeley National Laboratory, Berkeley, CA 94720

⁵ Department of Chemical and Biomolecular Engineering, University of Delaware, Newark, DE 19716

⁶ Department of Chemical and Biomolecular Engineering, University of California, Berkeley, CA 94720

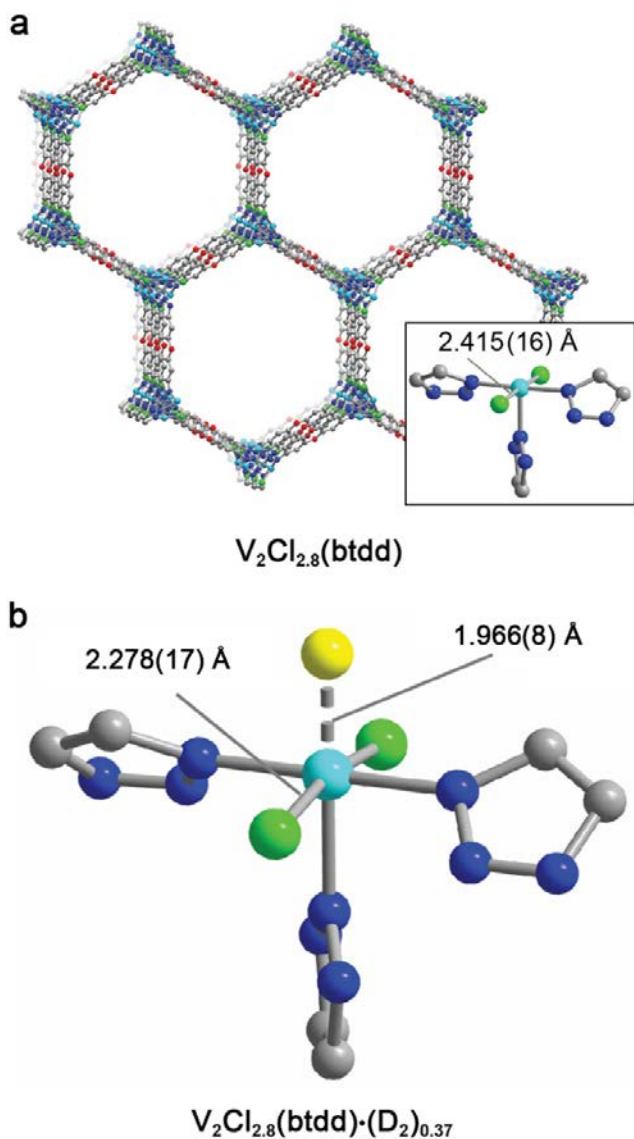


FIGURE 1: (a) A portion of the structure of $V_2Cl_{2.8}(btdd)$ determined from X-ray powder diffraction. In this material, 60% of the metal sites are coordinatively unsaturated vanadium(II) and 40% are coordinatively saturated vanadium(III). (Inset) Structure of the primary vanadium(II) coordination sphere in activated $V_2Cl_{2.8}(btdd)$ determined from neutron powder diffraction data. (b) Structure of the primary vanadium(II) coordination sphere in $V_2Cl_{2.8}(btdd)$, dosed with 0.75 equivalents of D_2 , determined in this work from Rietveld refinement of powder neutron diffraction data collected at 100 K. Cyan, green, blue, red, and grey spheres represent V, Cl, N, O, and C, atoms, respectively, while the yellow sphere represents the centroid of an adsorbed D_2 molecule.

temperature infrared spectroscopy, electronic calculations, and neutron powder diffraction, which also enabled the first structural characterization of the $V^{II}-H_2$ interaction. This orbital-mediated interaction gives rise to strong H_2 binding with an associated enthalpy of -21 kJ/mol, well within the optimal range for ambient storage. Significantly, usable H_2 capacities achieved with this material are greater than those of compressed H_2 under a range of conditions. Ultimately, this work suggests that pursuit of MOFs featuring coordinatively unsaturated metal sites capable of back-bonding interactions with H_2 is a promising strategy toward the continued optimization of adsorbents for hydrogen storage near room temperature.

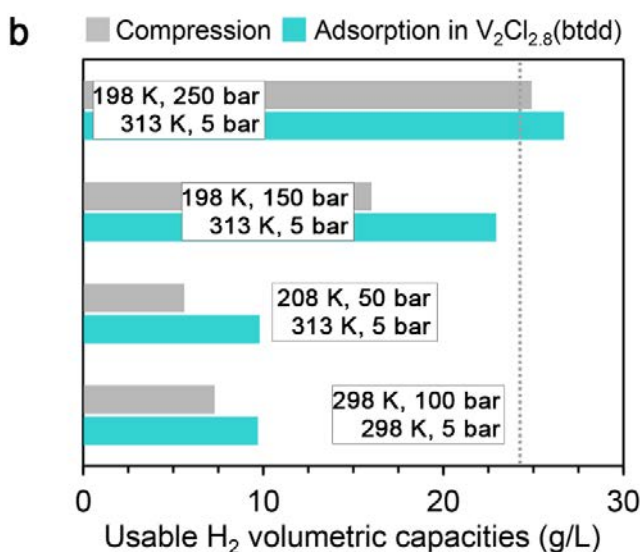
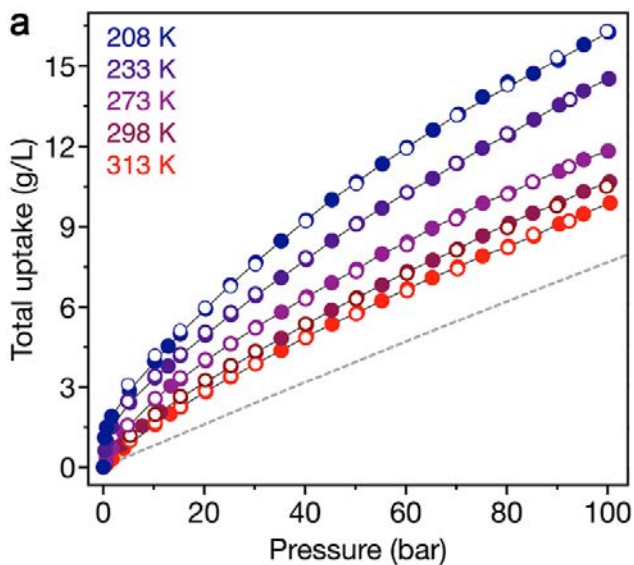


FIGURE 2: (a) High-pressure H_2 isotherms obtained for $V_2Cl_{2.8}(btdd)$ at the indicated temperatures. Filled and open circles represent adsorption and desorption, respectively. Solid lines indicate fits to a dual-site Langmuir-Freundlich model. The gray dashed line represents the volumetric density of compressed hydrogen at 298 K. (b) Comparison of usable volumetric H_2 capacities using $V_2Cl_{2.8}(btdd)$ and compression under four different loading/discharging conditions (indicated in the white boxes). The dotted gray line indicates usable volumetric capacity for 350 bar compressed storage at 298 K.

References

- [1] D. E. Jaramillo et al., *J. Am. Chem. Soc.* **143** (16), 6248 (2021).
- [2] D. E. Jaramillo et al., *Nat. Mater.* **19** (5), 517 (2020).
- [3] R. A. Pollock et al., *J. Phys. Chem. C.* **118** (31), 18197 (2014).
- [4] M. T. Kapelewski et al., *Chem. Mater.* **30** (22), 8179 (2018).
- [5] M. D. Allendorf et al., *Energy Environ. Sci.* **11** (10) 2784 (2018).

Elucidating ion transport in Li-ion cells by *operando* neutron, contact potential measurements, and first-principles modeling

J. L. Weaver,¹ E. Strelcov,^{2,3} E. J. Fuller,⁴ M. W. Swift,^{5,6} J. D. Sugar,⁴ A. Kolmakov,² N. Zhitenev,² J. J. McClelland,² Y. Qi,^{5,7} J. A. Dura,⁸ and A. A. Talin³

Predicting potential distributions in solid-state electrochemical systems such as solid-state batteries (SSB) and electrochemical random-access memory are challenging due to metrological constraints but are key to controlling mechanisms that drive capacity fade and limit a cell's performance. Measurement obstacles can be overcome by merging *operando* cold neutron depth profiling (NDP) and Kelvin probe force microscopy (KPFM) data to map otherwise difficult to quantify Li distributions and corresponding local electric potential differences, respectively [1]. The contributions from ions, electrons, and interfaces to the measured KPFM contact potential difference (CPD) have been deconvolved by correlating CPD with Li-concentration determined by NDP and confirmed by internal energy diagrams calculated from first-principles models for a fully functioning Si-LiPON-LiCoO₂ SSB. New insights into the interface and bulk layer chemical evolution of these cells during early charge/discharge cycles have been gained through the combination of these techniques.

Kelvin probe force microscopy provides real-time information on the contact potential difference of a sample surface (Fig. 1 and Fig. 2c, e, g). While the CPD reflects changes in solid-state batteries *operando*, it cannot quantify the underlying variations in Li⁺ concentration that causes the contact potential difference to change [2]. NDP can quantitatively measure the movement of the Li using ⁶Li(*n*,³H,⁴He) neutron capture reaction (Fig. 1 and Fig. 2d, f, h) and has previously had many successful applications to the study of Li diffusion (e.g., [3]). It is also nominally non-destructive, allowing for *operando* or *in situ* measurements, and has a depth resolution similar to Kelvin probe force microscopy. NDP and KPFM contrast in that KPFM is performed on a cleaved surface under vacuum while NDP can be performed under real-world operating conditions. Successful correspondence of NDP to KPFM reveals that the necessary surface exposure does not significantly alter the electrochemistry of the cell.

The solid-state batteries studied here consist of thin layers

of Cu, Si (*n*-type, anode), LiPON (electrolyte), LiCoO₂ (LCO, cathode) and Pt. Details of cell creation can be found in [1]. Cells of a similar chemistry were modeled using first-principles calculations [4]. The model further connects KPFM with NDP through the construction of internal energy diagrams for the coupled ionic and electronic degrees of freedom. DFT-calculated materials properties of Li_{*m*}Si (with *m* ranging from 0.0 at full discharge to 3.75 at full charge), the solid electrolyte Li₃PO₄ (a proxy for LiPON), and Li_{*n*}CoO₂ (*n* ranging from 1 at full discharge to 0.5 at full charge) were used in these calculations. The need to model crystalline Li₃PO₄ as a proxy for the complex amorphous LiPON is a limitation of the model and highlights the importance of combining theory with experimental techniques when studying complex Li-ion cell chemistries.

Associating NDP and KPFM results began with analysis of the as-manufactured, pristine cells, where the Si anode and Cu current collectors were observed to include Li (Fig. 2d). This is an interesting result as past investigations have assumed the as-fabricated Si anodes to be Li free. Inclusion of the Li (measured by NDP) supported the finding that the layers had higher than expected contact potential differences (measured by KPFM) than unlithiated Si and Cu.

A similar discrepancy in anticipated Li content (NDP) and contact potential difference (KPFM) was observed in the LiPON/LCO region of the pristine cell. SEM imaging implies this was the result of physical intermixing between the layers (Fig. 2a, b). Li was observed to predominately be removed from this intermixed region and shifted to the interface region between the Si anode and LiPON during the first half of charging during the first cycle (Fig. 2d). The NDP data correlates with an ≈ 200 nm-wide drop in the contact potential difference along the LiPON/LCO interface. This indicates that interfacial chemistry, which is key to understanding a cell's capacity fade, is substantially altered on a cell's first charging cycle. Complete charging resulted in a more uniform depletion of Li across the LCO layer and an increase in Li in the Si anode with a higher Li concentration at the Si/Cu interface. Li and CPD profiles for

¹ Material Measurement Laboratory, National Institute of Standards and Technology, Gaithersburg, MD 20899

² Physical Measurement Laboratory, National Institute of Standards and Technology, Gaithersburg, MD 20899

³ Maryland NanoCenter, University of Maryland, College Park, MD 20742

⁴ Sandia National Laboratories, 7011 East Ave. Livermore, CA 94550

⁵ Department of Chemical Engineering and Materials Science, Michigan State University, East Lansing, MI 48824

⁶ Center for Computational Materials Science, US Naval Research Laboratory, Washington, DC 20375

⁷ School of Engineering, Brown University, Providence, RI 02912

⁸ NIST Center for Neutron Research, National Institute of Standards and Technology, Gaithersburg, MD 20899

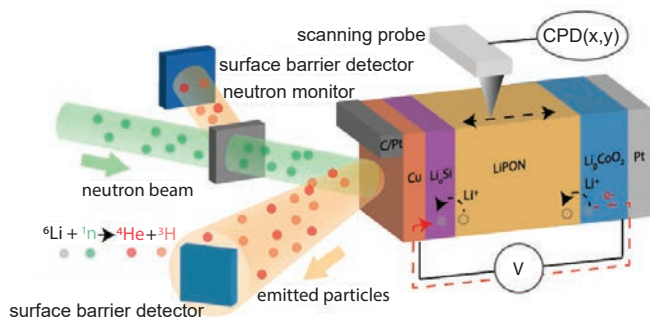


FIGURE 1: Schematic of Kelvin probe force microscopy and neutron depth profiling measurements (done separately)

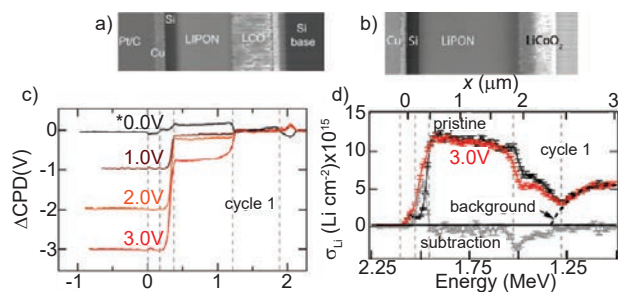


FIGURE 2: (a), (b) SEM micrographs of the cross-sections of the SSBs measured using KPFM and NDP, respectively. (c, d) $CPD(x)$ and $\Delta CPD(x)$ and the Li concentration profiles measured by NDP for similar as-prepared solid-state batteries. Gray and black dashed lines correspond to estimated interface locations and NDP profile backgrounds, respectively. NDP uncertainties are reported to 1σ based on experimental counting statistics.

the remainder of the cycles were similar, except for the noted exception below, to those measured during the second half of the first charging and subsequent discharging. Reproduction of the cycling behavior past the first cycle indicates that the first charge/discharge cycle plays an important role in forming stabilized electrode/electrolyte interfaces. Experimentation with more cycles is needed to investigate how long this evolved chemistry will be retained and whether deviation from it is an indicator of cell failure.

A slight gradient in Li content and CPD was found to form across the LiPON layer increasing over the course of all cycles measured. Net Li content calculations for the layer from the NDP profiles reveals that the total amount of Li in the LiPON was consistent throughout all cycles (Fig 2 c). This alludes to a structural change (e.g., density) within the layer over the course of repeat cycling. Further research with neutron reflectometry [5] is needed to pinpoint the source of this variation.

A stronger connection between NDP and KPFM was made through first-principles modeling (Fig. 3). The model calculated similar changes in both magnitude and direction of Li content and electrochemical potential as determined by NDP and KPFM. However, the model did not predict all experimental observations. It did not forecast the lithium variability at the LCO/LiPON interface observed by NDP and inferred from the KPFM data. It also could not predict the Li/CPD gradient detected in the LiPON upon repeat cycling as it treated this layer as a conductor of lithium ions and a static

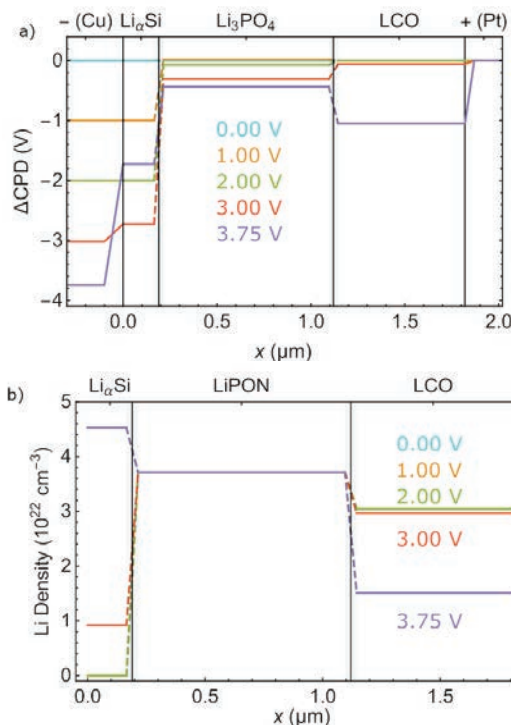


FIGURE 3: Simulated $\Delta CPD(x)$ (a) and Li concentration (b) at OCV = 0 V through 3.75 V.

electronic insulator.

Utilization of NDP with KPFM and first-principles modeling has enabled deeper insight into the ways Li ion cells chemically develop during operation while filtering out other effects that hinder data interpretation for these techniques. This study shows that the composition and density along with the electrochemical potentials of Li ion cells can change at both the interfaces and within the bulk of the layers within the first and first few charge/discharge cycles, respectively. Findings from this work reiterate the importance of early cycling processes to the formation of a stabilized cell that can withstand repeat electrochemical cycles. These factors may be key to developing faster-charging and longer lasting Li-ion cells, fundamental goals of battery manufacturers. Additionally, the methodology could be refined for use in early capacity fade detection – a metric that can be employed industrially to extend a cell's service life through data-driven maintenance planning.

References

- [1] E. J. Fuller, et al., under review, (2021).
- [2] E. Strelcov, et al., ECS Mtg. Abs. **5**, 1024 (2020).
- [3] S. C. Nagpure, et al., Electrochim. Acta. **56** (13), 4735 (2011).
- [4] M. W. Swift, Y. Qi, Phys. Rev. Lett. **122** (16), 167701 (2019).
- [5] E. D. Rus, J. A. Dura, ACS Appl. Mater. Interfaces, **11** (50), 47553 (2019).

On the question of dynamic tetragonal domains in the cubic phase of the photovoltaic semiconductor methylammonium lead triiodide

N. J. Weadock,¹ P. M. Gehring,² A. Gold-Parker,³ I. C. Smith,³ H. Karunadasa,^{3,4} and M. F. Toney¹

Hybrid organic-inorganic metal halide perovskites (HOIPs) are a novel class of semiconductor with promising optoelectronic properties for solar absorbers, light-emitting diodes, and spintronics. The HOIP family exhibits significant dynamical disorder that arises in part from weak bonding and the rotational degrees of freedom of the organic cation. The dynamical disorder correlates to the structural phase transitions in the prototypical HOIP, $\text{CH}_3\text{NH}_3\text{PbI}_3$ (MAPI), which transforms from orthorhombic to tetragonal to cubic symmetry at 162 K and 327.5 K, respectively. These transitions are marked by the appearance of additional Bragg peaks on cooling and result from the successive freezing of various tilt modes of the lead-iodide octahedra, which oscillate cooperatively in the cubic phase. The octahedral-tilting transition from the cubic to the tetragonal phase proceeds as a condensation of the soft, transverse acoustic R -point phonon, becoming the Γ point (zone center) of the tetragonal phase. X-ray inelastic scattering measurements of the cubic-phase phonon dispersions reveal quasielastic scattering (centered at zero energy transfer) at the cubic R -point, leading to predictions that small, dynamic, tetragonal domains exist within the cubic phase. This hypothesis has been used to explain why the optoelectronic properties of MAPI-based devices differ little between the cubic and tetragonal phases [1]. The X-ray inelastic scattering measurements did not have sufficient energy resolution to confirm or refute the prediction of dynamic domains; therefore we performed neutron inelastic scattering measurements, which provide up to 10 times better energy resolution, on the SPINS and BT4 triple-axis spectrometers at the NIST Center for Neutron Research to test these claims [2]. We find that the domains appear static within our best experimental resolution and are most likely a manifestation of the famous neutron central peak phenomenon.

The prediction of dynamic domains is not unique to HOIPs. Many materials that exhibit soft-mode-driven structural transitions often display quasielastic “critical scattering” from finite-sized regions that fluctuate between the minority and majority phases near the critical temperature T_C [3]. The lifetime, τ , of these dynamic domains is related to the energy linewidth (half-width at half-maximum, HWHM) of the scattering through the Heisenberg uncertainty principle,

$\tau \propto \hbar/\text{HWHM}$. As the system nears T_C , the minority phase lifetime diverges towards infinity, and the energy linewidth narrows until it is limited by the spectrometer resolution. Similarly, the Q width of the nascent Bragg peak narrows as the domain size of the minority phase diverges. The scattering intensity also diverges as the system approaches T_C . Critical scattering behavior has been investigated in many other perovskite compounds including SrTiO_3 , KMnF_3 , RbCaF_3 , CsPbCl_3 , CsPbBr_3 , and MAPbCl_3 .

Neutron inelastic scattering studies of soft-mode transitions have found that, for certain materials, no critical narrowing of the quasielastic scattering is observed; instead, the energy linewidth is always resolution-limited. This suggests that the origin of the scattering is static and has no dynamic component. First reported for SrTiO_3 by Riste *et al.* in 1971 [4], this phenomenon is known as the neutron central peak (CP). The origin of the CP is still under debate. Proposed origins include anharmonic renormalization of the soft-mode phonons or static domains nucleating about defects within the material.

We used high-resolution neutron spectroscopy to characterize the cubic R -point scattering in deuterated MAPI (to avoid the incoherent scattering from H) as a function of temperature. Data obtained from constant- Q scans (E scans), in which the energy transfer $\hbar\omega$ is varied at a fixed wave vector Q , and elastic Q -scans, where Q is varied with $\hbar\omega = 0$, were compared to models based on the dynamic-domains and CP hypotheses. A summary of these results is presented in Fig. 1. Figure 1(a) shows the cubic-phase R -point scattering at 340 K as a function of four different instrumental resolutions. The scattering linewidth decreases with resolution linewidth and is resolution-limited in each case, consistent with the CP phenomenon. E scans and Q scans were performed at different temperatures with a resolution HWHM = 0.095 meV, the narrowest linewidth that still provided sufficient dynamic range. The results, plotted in Fig. 1(b) and 1(c), show an increasing intensity on cooling towards T_C . At 327 K, just below T_C , the intensity diverges because the sample has transformed to the tetragonal phase.

The energy linewidths in Fig. 1(b) remain resolution-limited as the sample approaches T_C , providing further evidence that the

¹ University of Colorado, Boulder, Boulder, CO 80303

² NIST Center for Neutron Research, National Institutes of Standards and Technology, Gaithersburg, MD 20899

³ Department of Chemistry, Stanford University, Stanford, CA 94305

⁴ Stanford Institute for Materials and Energy Sciences, SLAC National Accelerator Laboratory, Menlo Park, CA 94025.

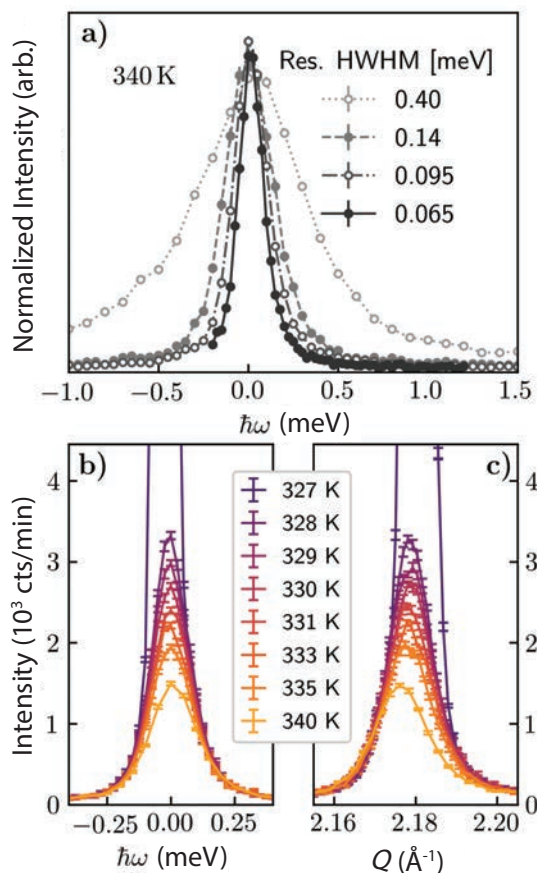


FIGURE 1: Scattering at the cubic R -point $Q = \frac{1}{2}(1,3,3)$ in deuterated MAPI measured with thermal and cold neutrons. In (a), the scattering linewidth matches the resolution energy linewidth. Data were collected at 340 K on BT4 (dotted) and SPINS (dash, dash-dot, solid). The (b) energy and (c) wave-vector (at $\hbar\omega = 0$) dependence as a function of temperature measured with an instrumental energy resolution HWHM of 0.095 meV.

scattering is a manifestation of the neutron CP. One could argue, however, that dynamic domains with sufficiently long lifetimes would manifest as resolution-limited scattering. We therefore established a minimum bound on the lifetime of any dynamic domains by constructing a highest posterior density interval (HPDI) from the log likelihood that the E scans are described by a narrow, resolution broadened scattering linewidth (see [2] for details). The results, plotted as a function of reduced temperature ($T-T_c$) in Fig. 2(a) yield a minimum bound of $\tau = 17$ ps at 340 K to $\tau = 47$ ps at 328 K. For the narrowest resolution linewidth of HWHM = 0.065 meV, the minimum bound on the lifetime increases to 36 ps at 340 K. This is significantly longer than the ≈ 1 ps lifetimes proposed in the literature [5].

The peak area obtained from fits of the E scans to both dynamic domain and CP models is plotted as a function of reduced temperature in Fig. 3(b). In the framework of critical scattering from dynamic domains, the peak area should diverge near T_c with a power law dependence. Instead, we observe a weak temperature dependence above T_c followed by a jump in the tetragonal phase. This behavior further supports the validity of the CP model and indicates that the cubic-to-tetragonal phase transition in MAPI is at least weakly first order.

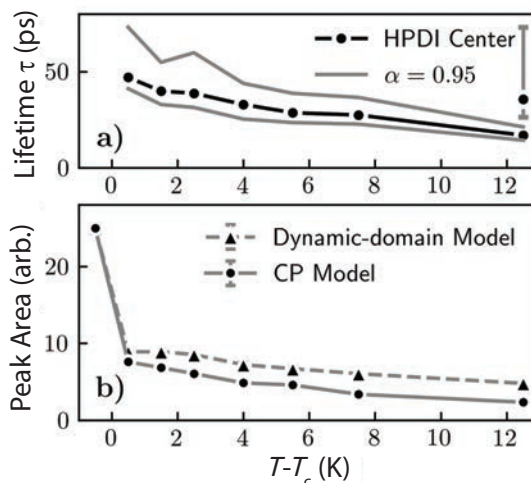


FIGURE 2: (a) Minimum lifetime τ (with 95% confidence interval α) of the proposed tetragonal domains determined from maximum likelihood estimation. The temperature-dependent τ are determined from E scans with a resolution HWHM of 0.095 meV. The data point at $T - T_c = 12.5$ K corresponds to an E scan measured with the best energy resolution HWHM of 0.065 meV. (b) Peak areas obtained from fits of E scans to dynamic domain and CP models. Error bars are $\pm 1 \sigma$ and may be smaller than the corresponding marker.

The lineshape and peak area of the Q scans (Fig. 1[c]) were also fit to the dynamic domain and CP models. As with the E scans, the peak area and correlation length (derived from the linewidth in Q) do not diverge with temperature [2]. This behavior is hard to reconcile with critical scattering from dynamic domains but is fully consistent with the CP phenomenon. The lineshape of the Q scans is consistent with the picture of static domains nucleating about point defects. We find that these domains are 10 Å to 18 Å in size and may originate from iodide vacancies in the lattice.

In summary, we report neutron inelastic scattering experiments on MAPI through the cubic-tetragonal phase transition and find that the R -point scattering is a manifestation of the CP phenomenon rather than critical scattering from dynamic domains. Our data set a lower bound on the lifetime of any dynamic domains of 36 ps at 340 K. While we do not determine the physical origin of the CP scattering, a defect-based origin is likely. This work highlights the importance of understanding the nature of defects in HOIPs and how they affect optoelectronic properties.

References

- [1] L. T. Schelhas et al., ACS Energy Lett. **1**, 1007 (2016).
- [2] N. J. Weadock et al., Phys. Rev. Lett. **125**, 075701 (2020).
- [3] W. G. Stirling and S. C. Perry, Critical Scattering, in Introduction to Neutron Scattering (1996), pp. 86–102.
- [4] T. Riste et al., Solid State Communications **9**, 1455 (1971).
- [5] C. Quarti, E. Mosconi, J. M. Ball, V. D’Innocenzo, C. Tao, S. Pathak, H. J. Snaith, A. Petrozza, and F. D. Angelis, Energy & Environmental Science **9**, 155 (2016).

Electrostatically driven selective adsorption of carbon dioxide over acetylene in an ultramicroporous metal–organic framework material

Y. Xie,¹ H. Cui,¹ H. Wu,² R.-B. Lin,¹ W. Zhou,² and B. Chen¹

Acetylene, C_2H_2 , is the simplest alkyne and an important raw material in the chemical industry. It is mainly manufactured by partial combustion of methane or the cracking of long-chain hydrocarbons. Carbon dioxide, CO_2 , is a major impurity in the crude product and must be removed to produce high purity acetylene. However, the similarities between the two molecular sizes, shapes, and physical properties (boiling point, dipole moment, polarizability, etc.) make C_2H_2/CO_2 separation a great challenge. Compared with conventional approaches (solvent extraction or cryogenic distillation), adsorptive separation using porous materials is environmentally friendlier, more energy efficient, and thus considered a promising future separation technology.

Extensive research has been devoted to developing porous solids for adsorptive separations. Depending on the binding preferences for the two gas molecules, the adsorbents can be either C_2H_2 -selective or CO_2 -selective. Most relevant adsorbents are C_2H_2 -selective because they feature certain functional sites that preferentially bind the relatively acidic and polarizable C_2H_2 molecule. The performance of C_2H_2 -selective adsorbents relies on the strength of adsorbent–adsorbate interactions, ranging from non-electrostatic interactions to hydrogen bonding and π -complexation. By incorporating basic moieties such as open oxygen and fluoride sites as hydrogen-bonding acceptors, we have developed several C_2H_2 -selective adsorbents that show exclusive C_2H_2 adsorption with high adsorption enthalpy [1,2].

Adsorbents that selectively adsorb CO_2 over C_2H_2 are rarely reported, not only because CO_2 is less polarizable but also because no clear separation mechanism exists to help identify potential adsorbents. In practice, CO_2 -selective separation is a more efficient and feasible purification process than C_2H_2 -selective separation since pure C_2H_2 can be produced directly in a single adsorption stage. Motivated by the complementary electrostatic interaction that determines the binding orientation of a variety of biological molecular recognitions, like protein folding and substrate binding, we reasoned that the dramatically different charge distributions of the two molecules, which have oppositely signed quadrupole moments ($-13.4 \times 10^{-40} \text{ C m}^2$ for CO_2 and $+20.5 \times 10^{-40} \text{ C m}^2$ for C_2H_2), could be exploited to recognize CO_2 or C_2H_2 exclusively through a similar mechanism. In a large pore space, CO_2 and C_2H_2 can find their own optimal binding configurations in

different orientations; this makes it impossible to differentiate the molecules by their charge distributions. But restricting the molecular orientations in a rigid, confined space makes a charge-distribution-recognition mechanism possible.

Recently, we successfully developed such a material: cadmium nitroprusside $Cd[Fe(CN)_5NO]$, or Cd-NP, a metal-organic framework compound of the Prussian blue family [3]. This compound exhibits a narrow pore aperture of 3.2 \AA connecting quasi-discrete ellipsoidal cavities that resemble the molecular shapes of CO_2 and C_2H_2 , and the open Cd sites at the pore extremity provide an electrostatic potential field that is well-suited for CO_2 binding (Figure 1a). Gas adsorption and column breakthrough experiments show that CO_2 can be captured in Cd-NP ($58.0 \text{ cm}^3 \text{ g}^{-1}$, at 1 bar and 298 K) with a significant preference over C_2H_2 ($9.7 \text{ cm}^3 \text{ g}^{-1}$), giving a new benchmark CO_2/C_2H_2 selectivity of ≈ 85 at room temperature.

Each Cd^{II} atom in Cd-NP is coordinated by five nitrogen atoms from different cyanide groups, whereas the Fe^{II} atoms are octahedrally coordinated by the five carbon atoms of these cyanide groups and one nitrogen atom of a nitrosyl group, which piles up in an antiparallel fashion along the b -axis creating a three-dimensional (3D) network (Fig. 1). Cd-NP consists of a 3D-pore system with a void ratio of 27.2 % in which the quasi-discrete cavities (size: $6.1 \text{ \AA} \times 4.5 \text{ \AA} \times 4.5 \text{ \AA}$) are interconnected through narrow windows surrounded by cyanide linkers and nitrosyl groups (aperture size: 3.2 \AA). The cavity and aperture size matches well with the molecular dimensions of CO_2 and C_2H_2 . In addition, the Cd atoms are exposed to the cavity as unsaturated metal centers. We calculated the electrostatic potential (ESP) of the pore surface in the cavity of Cd-NP using density functional theory (Figure 1b), where strong positive potentials (denoted as α and β) are found on the vertex of the ellipsoidal cavity near the Cd center and the nitrogen atom in the nitrosyl group, respectively, as well as a weak negative potential (denoted as γ) near the nitrogen atom of the cyanide groups surrounding the center of the ellipsoid. Apparently, the ESP of the pore surface in Cd-NP is well-matched to that of CO_2 but not with that of C_2H_2 (Figure 1c).

To understand the adsorption behavior of CO_2 and structurally characterize the host–guest interaction, high-resolution

¹ University of Texas at San Antonio, San Antonio, TX 78249

² NIST Center for Neutron Research, National Institute of Standards and Technology, Gaithersburg, MD 20899

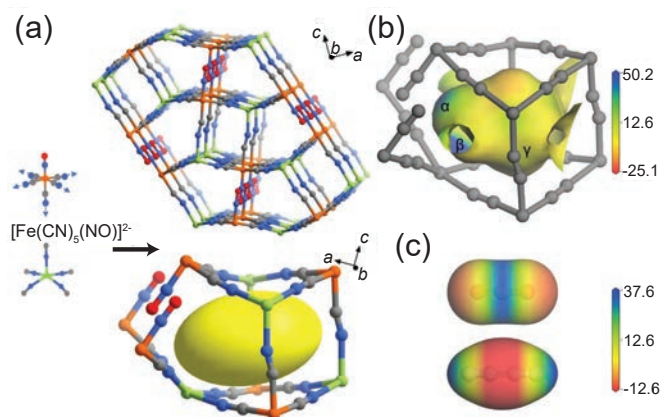


FIGURE 1: (a) Top: Crystal structure of Cd-NP viewed along the b-axis. Bottom: Side view of the ellipsoidal cavity unit. Cd light green, Fe orange, C gray, N blue. (b) The electrostatic potential of Cd-NP mapped onto the Connolly surface with a probe radius of 1.2 Å. (c) Molecular electrostatic potential of the CO₂ and C₂H₂ molecule mapped onto 0.015 e⁻ Å⁻³ electron density isosurfaces.

neutron powder diffraction (NPD) measurements were carried out at NCNR to determine the binding site of CO₂. From a sample loaded with CO₂ and equilibrated at room temperature and 1 bar, a single type of CO₂ binding configuration was identified. It is located at the ellipsoidal cavity (Fig. 2a and 2b). The CO₂ molecules are well confined within the narrow ellipsoidal cavity through Cd^{δ+}...O^{δ-} interactions (3.017 Å) and by van der Waals interactions with the two cyanide ligands positioned symmetrically (N^{δ-}...C^{δ+} 3.854 Å). As shown in Fig. 2c, the negative and positive potential regions of the CO₂ molecule are mainly stabilized by attractive interactions with the positive potential region near the Cd center and the negative potential region near the cyanide groups, respectively, which validates the electrostatic matching between Cd-NP and CO₂. In addition, comparing the structure of bare Cd-NP to that of Cd-NP⊃CO₂, the unit cell expansion and conformation change are negligible, indicating the rigidity of Cd-NP framework and its pore structure.

We also performed Grand Canonical Monte Carlo simulations of C₂H₂ and CO₂ adsorption. The calculated CO₂ binding configuration is fully consistent with the NPD data. In addition, the calculated binding interaction between the Cd-NP framework and the CO₂ molecule (Cd^{δ+}...O^{δ-} 3.187 Å, N^{δ-}...C^{δ+} 3.796 Å) is energetically favorable, whereas the C₂H₂ binding (Cd^{δ+}...H^{δ+} 2.867 Å, N^{δ-}...C^{δ-} 3.767 Å -3.910 Å) is electrostatically unfavorable (Fig. 2d).

To evaluate the practical CO₂/C₂H₂ separation performances of Cd-NP, column breakthrough experiments were carried out where CO₂/C₂H₂ (equal volume) gas mixtures flowed over a packed column of activated Cd-NP at a flow rate of 0.002 L min⁻¹ at 298 K. Complete separation of CO₂ from the mixture was demonstrated at ambient conditions. C₂H₂ was eluted from the outlet with no detectable CO₂, showing a high purity of 99.9%, whereas CO₂ was retained in the column until the uptake capacity of Cd-NP was saturated, giving a dynamic C₂H₂ productivity of 2.342 mol/L sorbent. Multiple cycling breakthrough experiments under the same conditions showed the same retention time of CO₂ and C₂H₂ productivity,

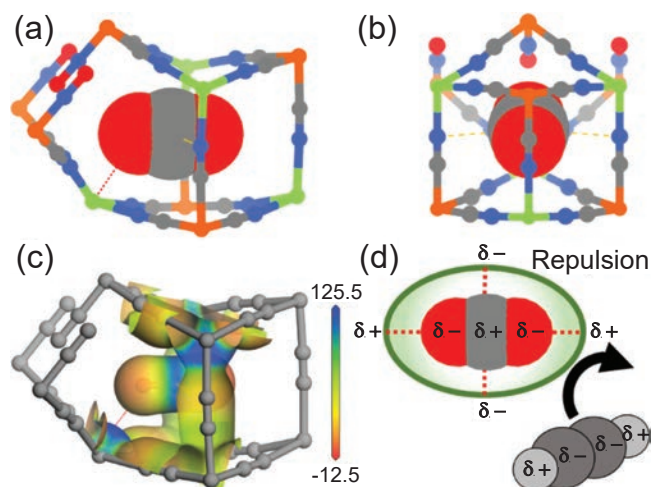


FIGURE 2: (a-b) Crystal structure of Cd-NP⊃CO₂ from neutron diffraction. Guest molecules are represented as space-filling ellipsoids. (c) Electrostatic potential of Cd-NP⊃CO₂ mapped onto the 0.15 e⁻ Å⁻³ electron density isosurface. (d) Schematic diagram of the electrostatically-driven separation mechanism towards CO₂ and C₂H₂ molecules.

indicating that the adsorption capability of Cd-NP is well retained under dynamic capturing.

In summary, we have realized the inverse CO₂/C₂H₂ separation in the ultramicroporous, metal nitro-prusside compound Cd-NP. The high separation selectivity is enabled by a pore sieving and confinement effect as well as an electrostatically compatible pore surface. We believe that this new electrostatically driven selective adsorption mechanism may be applicable to other challenging gas separation processes.

References

- [1] R.-B. Lin, L. Li, H. Wu, H. Arman, B. Li, R.-G. Lin, W. Zhou, B. Chen, *J. Am. Chem. Soc.* **139**, 8022 (2017).
- [2] Q. Dong, X. Zhang, S. Liu, R.-B. Lin, Y. Guo, Y. Ma, A. Yonezu, R. Krishna, G. Liu, J. Duan, R. Matsuda, W. Jin, B. Chen, *Angew. Chem. Int. Ed.* **59**, 22756 (2020).
- [3] Y. Xie, H. Cui, H. Wu, R.-B. Lin, W. Zhou, B. Chen, *Angew. Chem. Int. Ed.*, **60**, 9604 (2021).

Self-adjusting binding pockets enhance H₂ and CH₄ adsorption in a uranium-based metal–organic framework

D. P. Halter,^{1,2} R. A. Klein,^{3,4} M. A. Boreen,^{1,5} B. A. Trump,⁴ C. M. Brown,^{4,6} and J. R. Long^{1,2,7}

Hydrogen and natural gas are two alternative fuels central to the global push to combat anthropogenically accelerated climate change. A key barrier to the widespread adoption of these gases as fuel sources is the low storage capacities of current technologies at operationally relevant temperature-pressure conditions. One possible solution is to boost storage capacities by adsorbing gases within porous adsorbents. Among suitable porous adsorbents, metal–organic frameworks (MOFs) stand out as extremely promising gas-storage candidates, in part because their physical properties can be fine-tuned by molecularly precise material design [1, 2]. MOFs are composed of metal nodes connected by organic linkers, both of which can be modified to create tailored materials with large internal surface areas for gas adsorption and a high affinity for the target gas. For a MOF to be a useful H₂-storage candidate, the storage capacity must exceed the DOE-defined target at temperatures and pressures relevant to the application. So far, no materials come close to meeting these requirements. Hence, new gas-storage candidates are sought [3].

An important parameter to optimize when designing new adsorbents with better performance is the isosteric heat of adsorption, Q_{st} . This parameter describes the thermodynamic affinity of a gas molecule to adsorb at a specific surface site in the material at a given temperature. Higher isosteric heats of adsorption correspond to stronger interactions during gas storage and, in turn, require higher temperatures to desorb the gas from the framework for gas delivery. To store H₂ near room temperature, the sweet spot for Q_{st} is hypothesized to be between -15 kJ/mol and -25 kJ/mol [4]. To date, two dominant structural design motifs have emerged from the effort to achieve Q_{st} values in this optimal range. These are: (i) to include metal centers with open coordination sites at which the gas molecules can be adsorbed [5], or (ii) to synthesize MOFs with tailor-made adsorption pockets into which the gas molecule fits snugly [6]. For the latter strategy, it is important to optimize the geometric fit between the gas molecule and the binding pockets of the MOF—a difficult synthetic challenge when designing such materials.

In this work [7], we attempted to facilitate the second design motif by obviating the painstaking need to tailor and synthesize a new adsorbent material with an individualized fit for each different gas and end use requirement. The idea was to design a flexible porous material that could dynamically self-adjust the size and shape of its binding pockets to optimize the fit automatically for different target gases, thereby enhancing gas storage performance.

To test this idea, we designed uranium bis(1,4-benzenedicarboxylate), U(bdc)₂, a new MOF comprised of very large U⁴⁺ cations—that are known for ionic bonding with little orbital-overlap-induced geometry preferences in their coordination compounds—paired with organic linkers capable of bridging four of the metal centers at once. This combination was predicted to produce a flexible, porous MOF that might be able to self-adjust its binding pocket geometry upon interaction with different gases or guest molecules. The material was synthesized using a depleted uranium precursor, and a subsequent structural analysis of U(bdc)₂ revealed that this new MOF indeed features two confined pockets in each pore (illustrated as blue spheres in Fig. 1) that could serve as adsorption pockets for gas molecules.

Next, we sought to test the flexibility in this material. We conducted in situ gas dosing neutron powder diffraction experiments with D₂ and CD₄ using the high-resolution powder diffractometer BT-1 located at the NIST Center for Neutron Research. Neutron powder diffraction measurements are well suited to gas-adsorption studies of porous materials, particularly for lighter elements like hydrogen for which the coherent X-ray scattering cross section is close to zero. In contrast to X-rays, the coherent neutron scattering cross section for hydrogen and deuterium are large enough that the positions of these gases can be identified at an atomic scale during powder diffraction experiments. The incoherent scattering from hydrogen is also quite large, and this gives rise to a rolling background in the powder neutron diffraction pattern. Deuterium does not have a large incoherent scattering cross section, so deuterated gases like D₂ and CD₄ are well suited for the intended measurements.

¹ Department of Chemistry, University of California, Berkeley, CA 94720

² Materials Sciences Division, Lawrence Berkeley National Laboratory, Berkeley, CA 94720

³ Chemistry and Nanoscience Department, National Renewable Energy Laboratory, Golden, CO 80401

⁴ NIST Center for Neutron Research, National Institute of Standards and Technology, Gaithersburg, MD 20899

⁵ Chemical Sciences Division, Lawrence Berkeley National Laboratory, Berkeley, CA 94720

⁶ University of Delaware, Newark, DE 19716

⁷ Department of Chemical and Biomolecular Engineering, University of California, Berkeley, CA 94720

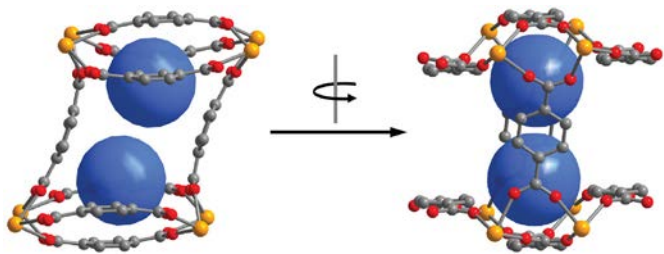


FIGURE 1: Illustration of the two binding pockets (blue spheres) in each pore of $U(bdc)_2$.

A Rietveld refinement of the diffraction data can then produce the crystal structure of the gas-dosed MOF, yielding precise atomic-scale information about the nature of gas adsorption within the framework.

Neutron powder diffraction measurements were performed with pure $U(bdc)_2$ under vacuum to obtain reference data for comparison with diffraction patterns obtained after gas dosing. From these initial measurements, we found that the *as-synthesized* $U(bdc)_2$ framework with residual water in its pores has a different crystal structure than the fully desolvated structure of so-called *activated* $U(bdc)_2$, from which all water was removed by heating the material under vacuum. This first result confirms that the framework changes shape in response to water being present as a guest molecule inside the pores. We then conducted neutron powder diffraction measurements on activated $U(bdc)_2$ with varying stoichiometric amounts of D_2 gas dosed into the framework, corresponding to 0.3, 0.7, 1.5, and 2.5 molar equivalents of D_2 per U ion per formula unit of the material. Analogously, neutron diffraction data were obtained for activated $U(bdc)_2$ dosed with 0.7 and 1.5 molar equivalents of CD_4 per U ion. In addition, we conducted X-ray powder diffraction measurements of $U(bdc)_2$ solvated with dimethylformamide (DMF) at the Advanced Photon Source at Argonne National Laboratory. Together, these three probe molecules with significantly different sizes span a range of kinetic diameters from 2.9 Å, 3.8 Å, and 5.5 Å for H_2 , CH_4 , and DMF, respectively, enabling us to study the self-adjusting behavior of the binding pockets in $U(bdc)_2$ in response to differently sized guest molecules.

Corresponding crystal structures for the MOF with the different guest molecules at varying concentrations were then extracted from the diffraction experiments described above. The structural analysis confirmed that upon adsorption of hydrogen, methane, and DMF in $U(bdc)_2$, the binding pockets of the material conform to fit the different molecules by bending the sidewalls of the pocket towards the guest molecules (Fig. 2).

As expected, the degree of this distortion was more pronounced for the smaller guests than for the larger guests (indicated by the purple arrows in Fig. 2) such that the binding pockets fit each guest molecule optimally. The geometries of the self-adjusted pockets in the presence of the three probe molecules differ distinctly from one another as well as from the geometry of the empty binding pockets in the activated

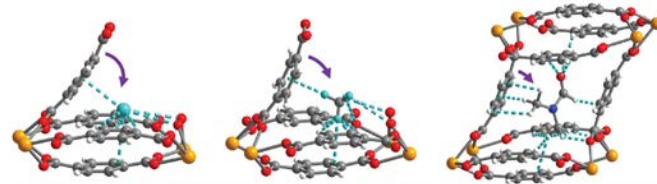


FIGURE 2: Neutron powder diffraction structures of $U(bdc)_2$ with adsorbed D_2 (left) CD_4 (middle) and DMF (right). Framework–guest interactions are depicted as aquamarine dashed lines. For clarity in (a) and (b), the pore is truncated and cut in half diagonally, showing only one of the two adsorption pockets of the pore. Orange, red, grey, blue, aquamarine, and white spheres represent U, O, C, N, D, and H atoms, respectively.

material. Upon adsorption, the framework flexes to adjust its pores to fit the guest molecules, like a baseball glove adapting its pocket to catch a small golf ball (H_2), a medium-sized baseball (CH_4), or a large softball (DMF).

Finally, we characterized the performance of the material using gas adsorption isotherm measurements, which revealed competitively large isosteric heats of adsorption for hydrogen and methane (-8.6 kJ/mol for H_2 and -25 kJ/mol for CH_4) due to the snugly-fitting, self-adjusted pockets of $U(bdc)_2$. In rigid materials with static adsorption pockets, there can generally only be a tight fit and enhanced adsorption strength for H_2 or CH_4 , but not both guest molecules.

These results illustrate that it is possible to synthesize materials that adapt their shape to optimize adsorption of multiple different gas adsorbates, validating our new synthetic design concept to boost isosteric heats of adsorption in porous adsorbents without open metal sites. While uranium-containing MOFs will probably not be adopted for use in the fuel tanks of light-duty vehicles, perhaps the next generation of gas storage materials will be based on self-adjusting porous adsorbents inspired by $U(bdc)_2$.

References

- [1] L. J. Murray, M. Dincă, J. R. Long, *Chem. Soc. Rev.* **38**, 1294 (2009).
- [2] H.-C. Zhou, J. R. Long, O. M. Yaghi, *Chem. Rev.* **112**, 673 (2012).
- [3] A. Züttel, *Mater. Today*. **6**, 24 (2003).
- [4] S. K. Bhatia, A. L. Myers, *Langmuir*. **22**, 1688 (2006).
- [5] M. T. Kapelewski, T. Runčevski, J. D. Tarver, H. Z. Jiang, K. E. Hurst, P. A. Parilla, A. Ayala, T. Gennett, S. A. FitzGerald, C. M. Brown, Long, J. R. *Chem. Mater.* **30**, 8179 (2018).
- [6] Z. Hulvey, B. Vlaisavljevich, J. A. Mason, E. Tsivion, T. P. Dougherty, E. D. Bloch, M. Head-Gordon, B. Smit, J. R. Long, C. M. Brown, *J. Am. Chem. Soc.* **137**, 10816 (2015).
- [7] D. P. Halter, R. A. Klein, M. A. Boreen, B. A. Trump, C. M. Brown, J. R. Long, *Chem. Sci.*, **11**, 6709 (2020).

Time-resolved probes of magnetic monopoles in spin ice

Y. Wang,^{1,2} T. Reeder,¹ Y. Karaki,³ J. Kindervater,¹ T. Halloran,¹ N. Maliszewskyj,² Y. Qiu,² J. A. Rodriguez,^{2,4} S. Gladchenko,² S. M. Koohpayeh,^{1,5} S. Nakatsuji,^{1,6,7,8} and C. Broholm^{1,2,5}

Our best knowledge of magnetic interactions and dynamics stems from experiments and theory on long-range ordered magnets. Protected by symmetry-breaking, magnetic excitations form spin waves with a dispersion relation that reflects the underlying interactions. This scenario, however, breaks down in frustrated magnets, where long-range order is destabilized by competing interactions. To understand and use the unique properties of frustrated magnets, new experimental methods that are sensitive to their unique magnetic excitations are needed. In this work, we introduce a time-resolved neutron scattering technique to investigate magnetic excitations in strongly frustrated $\text{Ho}_2\text{Ti}_2\text{O}_7$. This so-called spin ice material supports topological excitation known as magnetic monopoles. Combining time-domain neutron scattering and frequency-domain susceptibility measurements, the experiments span ten orders of magnitude in time scale to distinguish the distinct relaxation processes associated with monopoles and dipoles.

Fig.1 summarizes the time-dependent neutron scattering spectrum measured in the (HHL) reciprocal lattice plane of cubic $\text{Ho}_2\text{Ti}_2\text{O}_7$ at $T = 0.95$ K. Reflecting the absence of long-range orders and the local noncolinear spin alignments, the momentum-dependent scattering $S(Q)$ (Fig. 1A) has no magnetic Bragg peaks but consists solely of diffuse scattering that surrounds high-symmetry points on the Brillouin zone boundary, such as (001) , (003) , and $(3/2 \ 3/2 \ 3/2)$. We applied a square pulse sequence of magnetic field alternating between 25 mT and zero-field with a 20 s period (Fig. 1B). The time-dependent magnetic scattering signal is collected by recording the time of arrival of scattered neutrons relative to the field pulses. This allows us to probe atomic scale magnetic correlations on time scales covering eight orders of magnitude from 0.1 ms to hours.

Extracting Q -independent intensity from the diffuse scattering, the 25 mT field induces resolution limited ferromagnetic (FM) Bragg peaks (Fig. 1C-E). This indicates that the magnetization arises from aligning uncorrelated point-like defects within the spin-ice state along the applied field. The complete lack of

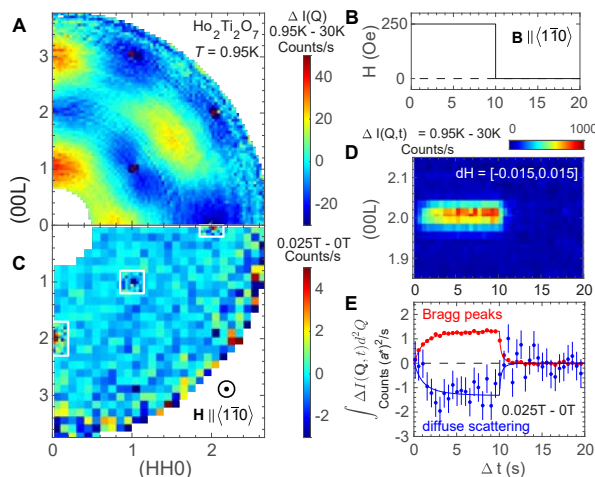


FIGURE 1: Time-resolved diffuse neutron scattering for $\text{Ho}_2\text{Ti}_2\text{O}_7$. (A) Zero-field elastic neutron scattering in the (HHL) plane at $T = 0.95$ K. (B) The time-varying magnetic field was applied along the $\langle 110 \rangle$ direction perpendicular to the scattering plane. (C) The difference in diffuse scattering induced by a 25 mT magnetic field, which concentrates around Bragg points within the white frames. (D) The time-dependent intensity at (002) . (E) The compensating time dependence of diffuse and coherent magnetic scattering induced by the time dependent field.

momentum dependence in the difference between the diffuse scattering in field and out of field indicates these defects are uncorrelated in the scattering plane and that magnetization of spin ice arises from the displacement of magnetic defects along the field direction.

The associated time scale is obtained from the time-dependent magnetic Bragg intensity $I(t)$ at (002) (Fig. 2A). Upon heating from 0.6 K to 1.3 K, this time scale decreases over six order of magnitudes, which shows thermal excitation facilitates relaxation. AC susceptibility measurements in the higher frequency and temperature range reveals two distinct characteristic frequencies at elevated temperatures ($T = 1.5$ K in Fig. 2B). This contrast with the single-mode response observed at low-temperatures (Fig. 2A and 2B) and documented in the literature [1, 2].

¹ Institute for Quantum Matter and Department of Physics and Astronomy, Johns Hopkins University, Baltimore, MD 21218
² NIST Center for Neutron Research, National Institute of Standards and Technology, Gaithersburg, MD 20899
³ Faculty of Education, University of the Ryukyus, Nishihara, Okinawa 903-0213, Japan
⁴ Department of Materials Science and Engineering, University of Maryland, College Park, MD 20742
⁵ Department of Materials Science and Engineering, Johns Hopkins University, Baltimore, MD 21218
⁶ Institute for Solid State Physics, University of Tokyo, Kashiwa, Chiba 277-8581, Japan
⁷ Department of Physics, University of Tokyo, Hongo, Bunkyo-ku, Tokyo 113-0033, Japan
⁸ Trans-scale Quantum Science Institute, University of Tokyo, Hongo, Bunkyo-ku, Tokyo 113-0033, Japan

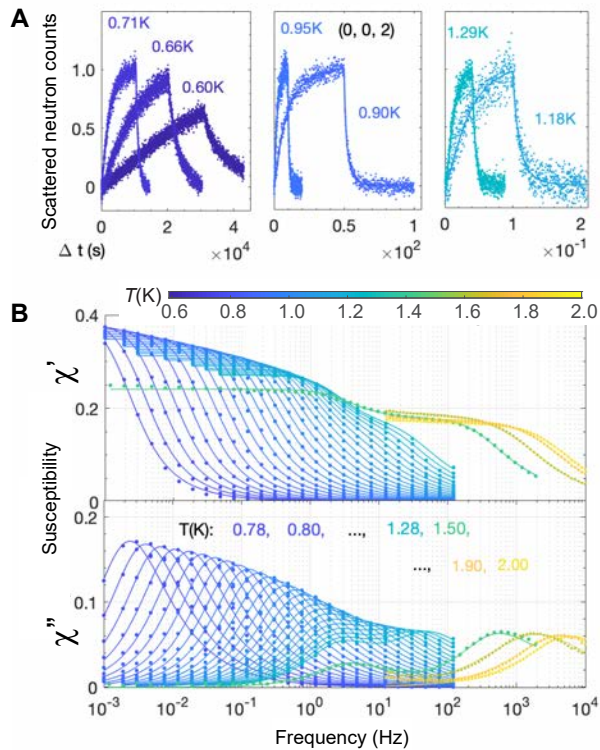


FIGURE 2: Selected curves of time-dependent neutron diffraction at (002) (A) and frequency-dependent susceptibility (B), spanning more than nine decades of timescales. The magnetic field amplitude is 10 mT in A and below 0.2 mT in B. Solid lines represent fits by the stretched exponential form in the time-domain and its Fourier transform in the frequency domain.

The bimodal relaxation can be quantitatively described by a superposition of two Cole-Davidson response functions

$$\chi(\omega = 2\pi f) = \chi_l + \chi_h = \frac{\chi_{0l}}{(1+i\omega\tau_l)^{\beta_l}} + \frac{\chi_{0h}}{(1+i\omega\tau_h)^{\beta_h}}, \quad (0 < \beta_l, \beta_h \leq 1).$$

Here, the labels l and h refer to the response that dominates at low- and high-temperatures respectively, with χ_0, τ, β each characterizing the static susceptibility, relaxation time scale and the distribution of time scales. Fig. 3A shows the thermal crossover of χ_{0l} and χ_{0h} , with $\beta_l = 0.8$ and $\beta_h = 0.5$. Fig. 3B shows τ -T curves that can be described by the Arrhenius form $\tau(T) = \tau_0 \exp(\Delta/T)$ with microscopic attempt time scales $\tau_{0l} \sim 10^{-7}$ s and $\tau_{0h} \sim 10^{-9}$ s. Finding β_l closer to one than β_h and τ_{0l} two orders of magnitude larger than τ_{0h} , suggest distinct microscopic relaxation processes: A coherent slow process at low T and an incoherent fast process at high T . We associate them with magnetic monopoles and spin dipoles respectively, as illustrated in Fig. 3C-E and described below.

The diffuse scattering in Fig. 1A indicates short range spin order that satisfies a two-in-two-out constraint driven by ferromagnetic interactions between Ising spins on the vertices of a corner-sharing network of tetrahedra (Fig. 3C) [3]. An elementary spin-flip out of this spin ice ground state costs energy and creates a pair of 3-in-1-out and 3-out-1-in defects. These can either remain bound as a spin dipole (Fig. 3D) or become separated as independent magnetic monopoles through successive spin-flips that cost no energy (Fig. 3E). Coexisting as thermally excited defects, spin dipoles and magnetic monopoles can be magnetized through single-site

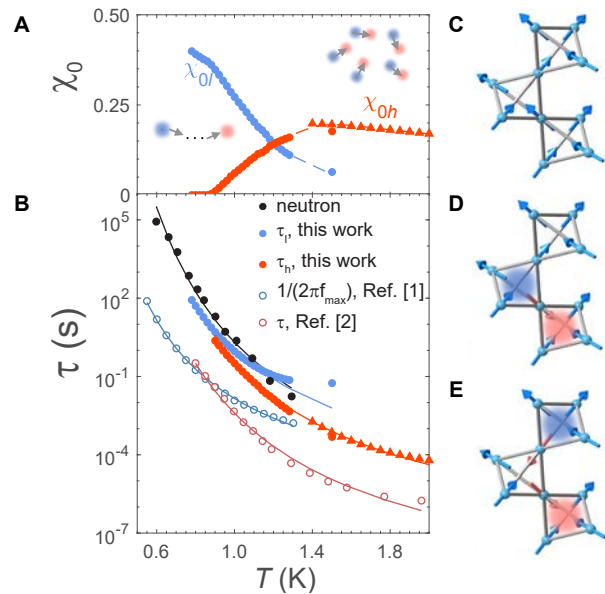


FIGURE 3: Magnetic relaxation mediated by monopoles and spin dipoles in $\text{Ho}_2\text{Ti}_2\text{O}_7$. (A-B) Temperature-dependence of χ_0 (A) and τ (B) for low- (blue) and high-temperature modes (red). (B) also shows the time constants from neutron scattering (black) and from Refs. [1, 2] (open circles). Solid lines represent best fits to the Arrhenius law. (C-E) Spin configurations with and without monopoles. The spin ice manifold has two spins pointing in and two pointing out of every tetrahedron (C). A pair of three-in-one-out (red cloud) and three-out-one-in (blue cloud) defects can remain bound as a spin dipole (D, inset of A on the right) or be separated as two monopoles (E, inset of A on the left).

spin-flips and multiple-site hopping respectively. Long-range monopole hopping requires a uniform spin ice manifold and is undermined by the increasing density of spin-flip defects at elevated temperatures. This qualitatively explains the crossover to dipolar relaxation at higher T shown in Fig. 3A. The experiment reconciles an apparent inconsistency in previous works [1, 2] (Fig. 3B, open symbols), and demonstrates that the reduced disorder in the ultra-pure crystals used in this work slows the dynamics by 3 to 4 orders of magnitude (Fig. 3B).

By probing magnetism in a new time domain with neutron scattering and AC susceptibility measurements, we have distinguished the magnetic relaxation associated with an exotic magnetic quasiparticle, namely the magnetic monopole, from that of conventional dipolar relaxation. The fact that monopole dynamics in classical spin ice can be pushed to the Debye regime (β_l close to 1) at low- T suggests that quantum coherent dynamics may be possible in analogous materials with quantum spins. The exceptionally sensitivity to disorder demonstrated here, could become a tool to control the motion of topological excitation in quantum magnets.

References

- [1] J. A. Quilliam, et. al., Phys. Rev. B **83**, 094424 (2011).
- [2] A. B. Eyvazov, et. al., Phys. Rev. B **98**, 214430 (2018).
- [3] S. T. Bramwell, et. al., Science **294**, 1495-1501 (2001).
- [4] Y. Wang, et. al., Sci. Adv. 2021; **7**: eabg0908 (2021).

Competing magnetic phases and fluctuation-driven scalar spin chirality in the kagome metal YMn_6Sn_6

N. J. Ghimire,^{1,2} R. L. Dally,³ L. Poudel,^{3,4} D. C. Jones,^{1,2} D. Michel,^{1,2} P. Siegfried,^{1,2} N. Thapa Magar,¹ M. Bleuel,^{3,4} M. A. McGuire,⁵ J. S. Jiang,⁶ J. F. Mitchell,⁶ J. W. Lynn,³ and I. I. Mazin^{1,2}

The topological Hall effect (THE) reflects the existence of an underlying topologically protected magnetic configuration.

This type of protection results in robust states of matter which are difficult to perturb, making the host materials promising for device applications. The THE is observed when charge carriers in a material interact with a particular type of fictitious magnetic field generated by the Berry phase. The Berry phase is picked up by the charge carriers as they move through a spatially varying spin configuration, and this results in an additional term in Hall measurements, the THE. The required spin configuration for the THE has traditionally been understood as originating from a non-coplanar magnetic structure where the positive and negative chirality—or handedness—of the spin winding does not cancel. This non-null *static* scalar spin chirality can be found in skyrmion hosting materials which are commonly lacking inversion symmetry (*i.e.* non-centrosymmetric). Recently, we have proposed that the non-null spin chirality need not be *static* but can originate from an imbalance in the positive and negative chiral magnetic fluctuations, or magnons [1]. The theory stems from work on the centrosymmetric system, YMn_6Sn_6 , where the static scalar spin chirality is null in the nearly room-temperature THE regime. By discovering this new THE mechanism, this combined neutron diffraction, transport, and theoretical study has expanded the known search criteria for THE host materials.

The crystal structure of YMn_6Sn_6 consists of Mn planes that are strongly coupled ferromagnetically but with different spacer layers (Fig. 1a). This results in weak magnetic exchange couplings of the Mn moments between layers that strongly compete. The frustration leads to a complicated helimagnetic ground state that is incommensurate along the *c*-axis. Due to the delicate balance of the competing interactions, the change in energetics to the system that comes with temperature (*T*) variation and the application of an in-plane external magnetic field ($\mu_0 H$) leads to the rich $\mu_0 H$ -*T* phase diagram shown in Fig. 1b [1, 2]. Our bulk transport and magnetic susceptibility measurements identified that the THE coincided with only one of these phases, and only at elevated temperatures between ≈ 100 K and up to about room temperature, with the peak

effect at 4 T and 245 K. Small angle neutron scattering work confirmed that no skyrmions were present, and the origin of the THE was a mystery.

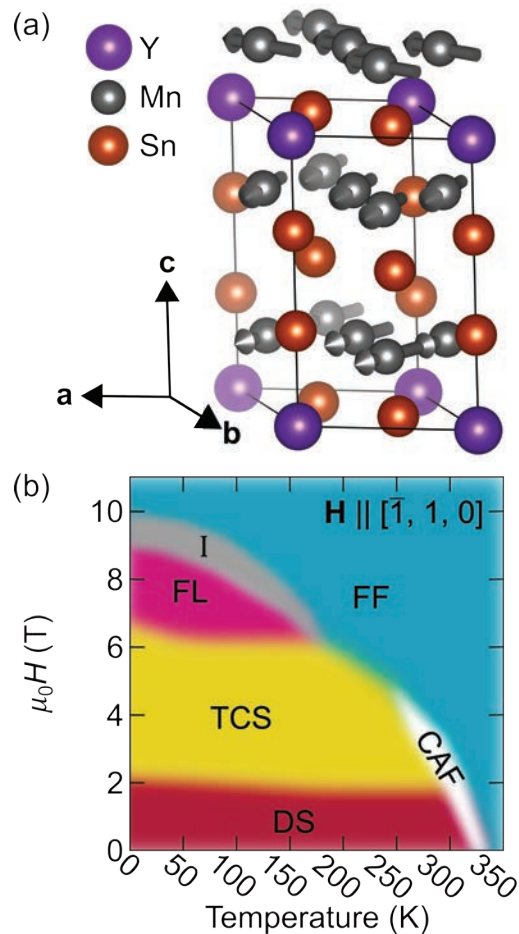


FIGURE 1: (a) Crystal structure of YMn_6Sn_6 , belonging to space group $P6/mmm$ (191). The moments of the zero-field incommensurate helimagnetic ground state are depicted by the arrows on the Mn atoms. The moments rotate in a double spiral about the *c*-axis. (b) Magnetic structure phase diagram for the applied field, *H*, in-plane. The phases DS, TCS, FL, CAF, I, and FF correspond to distorted spiral, transverse conical spiral, fanlike, canted antiferromagnet, phase I, and forced ferromagnetic, respectively.

¹ Department of Physics and Astronomy, George Mason University, Fairfax, VA 22030
² Quantum Science and Engineering Center, George Mason University, Fairfax, VA 22030
³ NIST Center for Neutron Research, National Institute of Standards and Technology, Gaithersburg, MD 20899
⁴ Department of Materials Science and Engineering, University of Maryland, College Park, MD 20742
⁵ Materials Science and Technology Division, Oak Ridge National Laboratory, Oak Ridge, TN 37831
⁶ Materials Science Division, Argonne National Laboratory, 9700 South Cass Avenue, Lemont, IL 60439

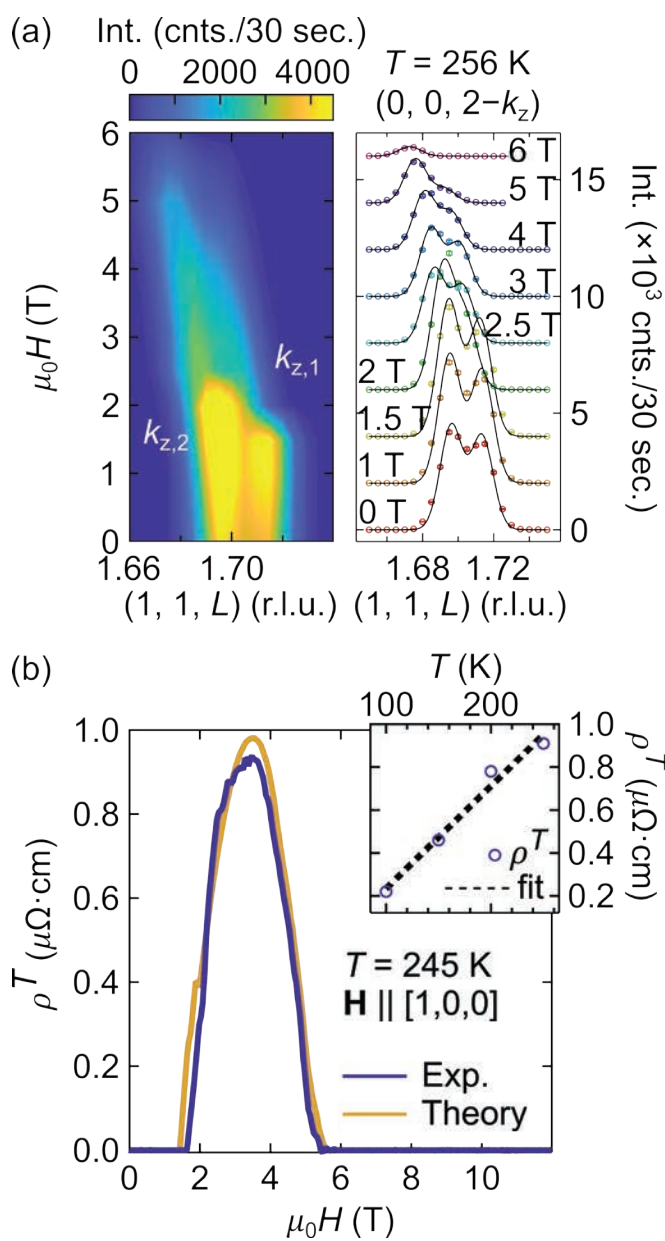


FIGURE 2: (a) Magnetic field dependence of two closely spaced incommensurate magnetic Bragg peaks $(0, 0, 2 - k_z)$ at $T = 256$ K with an applied field in-plane. The solid black lines in the right-hand panels are Gaussian fits to the data, and an offset of 100 counts/30 s was added between individual L scans for clarity. (b) Experimental and theoretical topological Hall resistivity as a function of external magnetic field at 245 K. The inset shows the temperature variation of the THE at 4 T below 250 K. The dashed line is a linear fit to the experimental data.

Through a series of neutron diffraction studies combined with detailed theoretical predictions, all the various magnetic structures in the Fig. 1b phase diagram were determined, with the magnetic structure in the THE phase being a transverse conical spiral (TCS). The evolution from the zero-field ground state helimagnetic structure to the TCS phase is marked by a spin-flop transition at ≈ 2 T which can readily be observed in the neutron diffraction data as a sharp drop in intensity of the incommensurate magnetic Bragg peaks (Fig. 2a) as well as a shift in the two propagation vectors present ($k_{z,1}$ and $k_{z,2}$).

Intriguingly, although the TCS magnetic structure is non-coplanar, it has a null static scalar spin chirality, and the elevated temperatures at which the THE occurs implied that thermal fluctuations play a key role given that the TCS phase extends down to the lowest temperatures measured. The fluctuation-driven chirality can be explained as follows: of all possible magnons, there are some that generate positive chirality, but, by crystallographic symmetry, for each such magnon, there is a partner with the same energy and opposite chirality. These two partners will be thermally excited with the same probability, and their effect will cancel each other, in the absence of an external field. However, in an applied field, a nonzero chiral susceptibility is created. The THE was calculated via this theory and was shown to match the experimental Hall data remarkably well (Fig. 2b).

In addition to identifying the THE and all the associated magnetic structures in Fig. 1b, we used polarized neutron diffraction in the zero-field helimagnetic state to investigate chiral magnetic domains [2]. We found a surprising imbalance in the right and left-chiral domains. Such a spiral phase in a centrosymmetric system is not expected to show handedness as there should be no energetic preference for either domain.

YMn_6Sn_6 is one of a large class of materials exhibiting coupled electronic and magnetic properties, yet it is the first identified material to host a fluctuation-driven spin chirality leading to the THE. The elevated temperatures at which the THE occurs is particularly desirable for potential device applications which rely on the robustness of topologically protected states. It's believed that other materials where the THE origins are currently unexplained due to the absence of a static scalar spin chirality are examples for this mechanism as well, and the inclusion of more types of centrosymmetric crystal structures greatly expands the range of THE materials for potential applications.

References

- [1] N. J. Ghimire, R. L. Dally, L. Poudel, D. C. Jones, D. Michel, N. Thapa Magar, M. Bleuel, M. A. McGuire, J. S. Jiang, J. F. Mitchell, J. W. Lynn, and I. I. Mazin, *Sci. Adv.* **6**, eabe2680 (2020).
- [2] R. L. Dally, J. W. Lynn, N. J. Ghimire, D. Michel, P. Siegfried, and I. I. Mazin, *Phys. Rev. B* **103**, 094413 (2021).

Unraveling the unusual metal-to-metal transition in metallic nickelate

J. Zhang,^{1,2} D. Phelan,¹ A. S. Botana,³ Y.-S. Chen,⁴ H. Zheng,¹ M. Krogstad,¹ S. G. Wang,⁴ Y. Qiu,⁵ J. A. Rodriguez-Rivera,^{5,6} R. Osborn,¹ S. Rosenkranz,¹ M. R. Norman,¹ and J. F. Mitchell¹

Nickelates—nickel oxides—have diverse applications, including insulating magnets, semiconductors, and superconductors. However, for stoichiometric nickelates, as well as some late transition metal nickel oxides, the norm is insulating behavior. Exceptions include an unconventional paramagnetic metal, LaNiO_3 , and layered Ruddlesden-Popper phases, $\text{R}_4\text{Ni}_3\text{O}_{10}$ ($\text{R} = \text{La}, \text{Pr}, \text{Nd}$). We have conducted experimental and modeling studies of the latter class of compounds owing to its unusual metal-to-metal transition [1]. The precise mechanism of this transition, which has been a mystery for nearly 25 years [2], is revealed to be due to an incommensurate density wave with both charge and spin character.

In the crystal structure of the $\text{La}_4\text{Ni}_3\text{O}_{10}$, the unit cell contains two trilayer perovskite-like blocks that are related through the B-centering operation of the $Bmab$ space group (Figure 1). Measurements on this crystal at temperatures from >0 K to 300 K showed that the in-plane resistivity falls with decreasing temperature, indicating metallic behavior and a metal-to-metal transition at approximately 140 K. At this transition temperature, the in-plane magnetic susceptibility was found to decrease dramatically, consistent with the behavior of previous materials showing charge density wave order, such as one-dimensional $\text{K}_{0.3}\text{MnO}_3$ [3].

Our experimental studies with single-crystal $\text{La}_4\text{Ni}_3\text{O}_{10}$, grown using a high-pressure furnace [4], included synchrotron X-ray diffraction and neutron diffraction analyses. In X-ray diffraction patterns produced at the Advanced Photon Source of Argonne National Laboratory (Figure 2), we observed charge superlattice peaks below the metal-to-metal transition appearing at an incommensurate propagation vector q . These charge superlattice reflections have intensities typically four orders of magnitude weaker than the strongest fundamental Bragg reflections, which explains why others who worked with polycrystalline samples had not earlier detected them. The single-crystal neutron diffraction data collected at the NIST Center for Neutron Research revealed the presence of a spin density wave concomitant with the charge density wave.

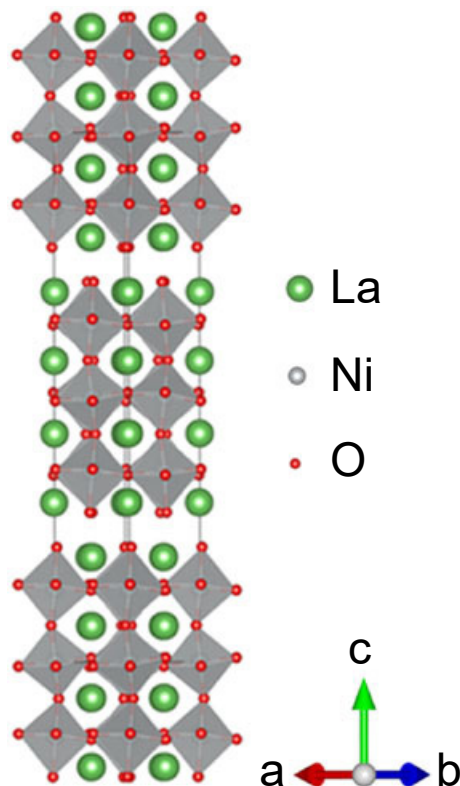


FIGURE 1: Crystal structure of $\text{La}_4\text{Ni}_3\text{O}_{10}$. The unit cell contains two trilayer perovskite-like blocks that are related by symmetry.

Figure 3 shows the magnetic superlattice reflections resulting from this spin density modulation. Neither X-ray nor neutron data show harmonics of the fundamental superlattice reflection, implying a sinusoidal nature for both density waves.

Combining the X-ray and neutron diffraction data for the $\text{La}_4\text{Ni}_3\text{O}_{10}$, we found that both the charge and spin superlattice reflections below the metal-to-metal transition indicate incommensurate propagation vectors, as expected for a system with a Fermi surface nesting-induced density wave, with the period for the spin density wave twice that of the charge

¹ Materials Science Division, Argonne National Laboratory, Lemont, IL 60439
² Institute of Crystal Materials, State Key Laboratory of Crystal Materials, Shandong University, 250100 Jinan, Shandong, China
³ Department of Physics, Arizona State University, Tempe, AZ 85287
⁴ ChemMatCARS, The University of Chicago, Lemont, IL 60439
⁵ NIST Center for Neutron Research, National Institute of Standards and Technology, Gaithersburg, MD 20899
⁶ Department of Materials Science, University of Maryland, College Park, MD 20742

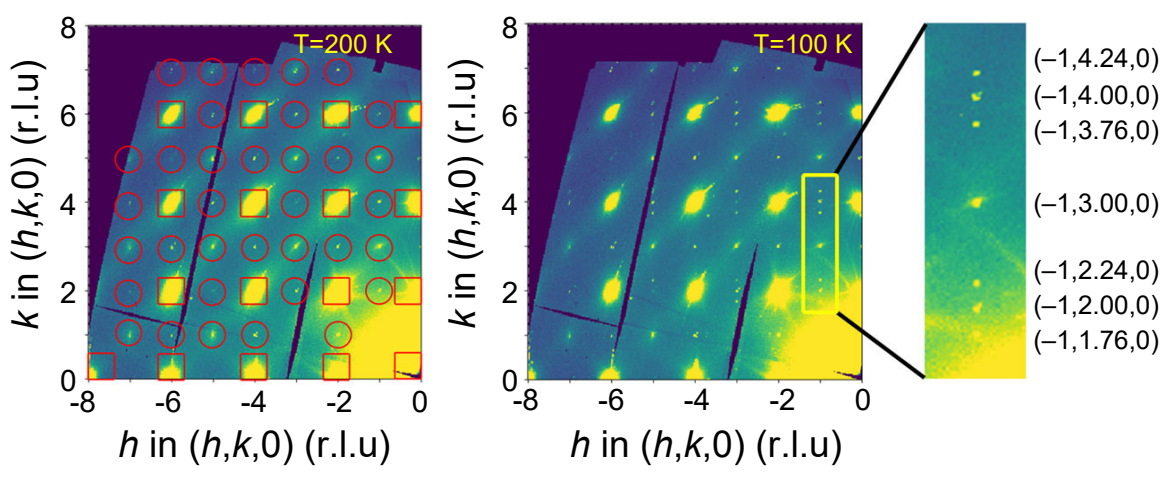


FIGURE 2: X-ray diffraction patterns for $hk0$ plane above and below the 140 K transition temperature: (left) 200 K and (right) 100 K, showing superlattice reflections from the incommensurate charge density wave. Hollow squares, fundamental Bragg peaks from high symmetry $Bmab$; hollow circles, Bragg peaks resulting from monoclinic distortion to $P2_1/a$.

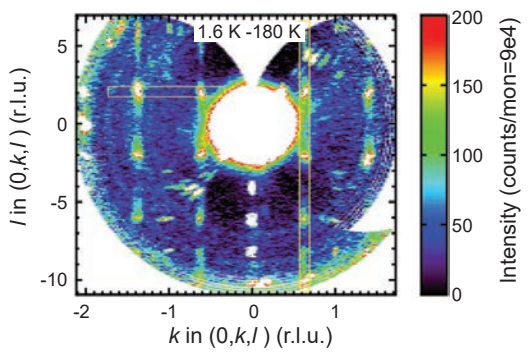


FIGURE 3: Neutron diffraction of $0kl$ plane showing superlattice reflections from the incommensurate magnetic structure.

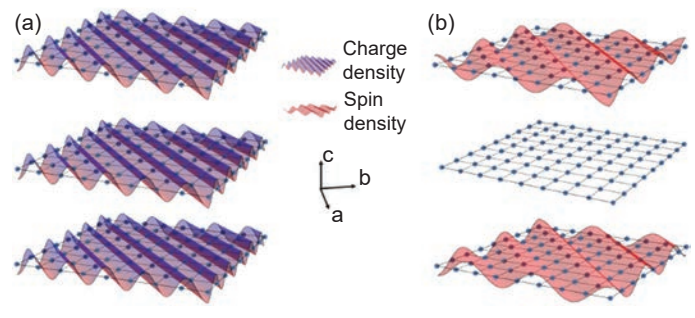


FIGURE 4: Schematic of charge (a) and spin (b) density waves in a single trilayer based on analysis of scattering patterns

density wave. Indeed, first principles calculations implicate Fermi surface nesting as the driving mechanism for the intertwined density waves.

The distinctive patterns of the superlattice reflections led us to propose models of the sinusoidal modulations in the charge and spin sectors within a trilayer of the structure. Figure 4 shows the results from model simulations for charge density waves (a) and spin density waves (b) as plotted in the a - b plane. Notably, the charge modulations are in phase within a trilayer, while the spin modulations are out of phase.

Further analysis of the data revealed that the incommensurate density wave associated with the metal-to-metal transition in $\text{La}_4\text{Ni}_3\text{O}_{10}$ lies closer in its behavior to the metallic density wave seen in chromium metal than the insulating stripes typically found in the homologous single-layer insulating nickelates, like $\text{La}_{2-x}\text{Sr}_x\text{NiO}_4$. The quasi-2D $\text{La}_4\text{Ni}_3\text{O}_{10}$ thus appears to be the missing link between the charge and spin order of 3D perovskites (e.g., LaNiO_3) and 2D insulating nickelates. From further studies of various transition metal nickelates, it should be possible to build a unified understanding of this exceptional group of quantum materials.

References

- [1] J. Zhang, D. Phelan, A. S. Botana, Y.-S. Chen, H. Zheng, M. Krogstad, S. G. Wang, Y. Qiu, J. A. Rodriguez-Rivera, R. Osborn, S. Rosenkranz, M. R. Norman, J. F. Mitchell, *Nature Commun.* **11**, 6003 (2020).
- [2] H. Yoshizawa, T. Kakeshita, R. Kajimoto, T. Tanabe, T. Katsufuji, Y. Tokura, *Phys. Rev. B* **61**, R854 (2000).
- [3] M. Greenblatt, *Chem. Rev.* **88**, 31 (1988).
- [4] J. Zhang, H. Zheng, Y.-S. Chen, Y. Ren, M. Yonemura, A. Huq, J. F. Mitchell, *Phys. Rev. Mater.* **4**, 083402 (2020).

Surface-symmetry dependent magnetism at topological interfaces

C. Yang,¹ L. Pan,¹ A. J. Grutter,² H. Wang,³ X. Che,¹ Q. L. He,^{1,4} Y. Wu,¹ D. A. Gilbert,^{2,5} P. Shafer,⁶ E. Arenholz,^{6,7} H. Wu,¹ G. Yin,¹ P. Deng,¹ J. A. Borchers,² W. Ratcliff II,^{2,8} and K. L. Wang^{1,9,10}

Topological insulators (TIs) are an exciting new class of materials which are insulating in the bulk of the material but host symmetry-protected conductive electron states on the surface [1]. Due to their unique properties, these surface states are ideal for realizing exciting quantum phenomena such as the quantum anomalous Hall (QAH) effect, in which lossless quantized edge conduction occurs in the film without the application of an external magnetic field. To stabilize the QAH effect, time-reversal symmetry is broken in the TI through the introduction of a net magnetization in the vicinity of the surface state [2]. In this work, we examine heterostructures of the TI $(\text{Bi,Sb})_2\text{Te}_3$ and the non-collinear antiferromagnet CrSe using a combination of electrical transport, polarized neutron reflectometry (PNR), neutron diffraction, X-ray spectroscopy, and theoretical calculations [3]. This combined characterization approach reveals proximity-induced magnetic order in the $(\text{Bi,Sb})_2\text{Te}_3$ which is incredibly sensitive to the surface termination of the CrSe, providing a new approach for controlling magnetism at the interface between TIs and antiferromagnets.

In order to use an antiferromagnet, which has zero net magnetization in the bulk, to induce a magnetization in the adjacent TI layer, one of two things must happen. First, an antiferromagnet with the right spin structure may have spin-polarized planes at the surface, so that an adjacent layer experiences an exchange interaction which simulates a ferromagnetic interaction at the interface. Alternatively, either through thin film growth or spin reconfigurations at the surface, a small net magnetization may develop in the antiferromagnet at the interface, allowing direct ferromagnetic coupling between the TI and the antiferromagnet. As shown in Figure 1(a), CrSe films exhibited a temperature-dependent (201) diffraction peak indicative of relatively bulk-like magnetism [4]. The extracted ordering temperature was found to be approximately 270 K, only slightly suppressed relative to the bulk value of 300 K. We conclude therefore that the CrSe

films exhibit a slightly defective version of the bulk “umbrella” magnetic structure which yields a net spin-polarization at the surface of the (001) planes along the growth axis. Further, as shown in Fig 1(b), our CrSe films are highly insulating, so that they represent the ideal candidate in which to explore antiferromagnetic proximity effects in TI heterostructures.

We therefore used molecular beam epitaxy to grow thin film heterostructures of CrSe and $(\text{Bi,Sb})_2\text{Te}_3$ with three different geometries:

1. CrSe (5 nm) / $(\text{Bi,Sb})_2\text{Te}_3$ (6 nm) – “Bottom Bilayer”
2. $(\text{Bi,Sb})_2\text{Te}_3$ (6 nm) / CrSe (5 nm) – “Top Bilayer”
3. CrSe (5 nm) / $(\text{Bi,Sb})_2\text{Te}_3$ (6 nm) / CrSe (5 nm) – “Sandwich”

where the samples are labeled based on the position of the CrSe layer(s) relative to the TI. Initial characterization of the magnetic properties was performed using anomalous Hall effect (AHE) measurements (Figure 1b-d), which allows rapid screening of the different geometries for the presence of a net magnetization consistent with induced magnetism in the TI. Interestingly, while both the Top Bilayer and Sandwich exhibit nonlinear, hysteretic AHE responses, the Bottom Bilayer Hall effect is purely linear with field. This suggests a net magnetization emerges in some samples, but that the outcome depends strongly on the symmetry of the underlying structure. The next important question is whether the emergent magnetic signal is confined to the interface, as expected. We therefore performed polarized neutron reflectometry (PNR) measurements to extract a depth-dependent picture of the structure and magnetization within a Top Bilayer. Thanks to the intrinsic spin of the neutron, a spin-polarized neutron beam will experience different scattering length density profiles in a magnetized film, so that the reflectivity expected from a spin-up ($\uparrow\uparrow$) neutron beam is different from that of a spin-down ($\downarrow\downarrow$) neutron beam. As shown in Figure 2(a), which plots the spin-up and spin-down non spin-flip reflectivities, the magnetic splitting associated with a weak induced interface magnetization is very small. Fitting

¹ Department of Electrical and Computer Engineering, University of California, Los Angeles, CA 90095

² NIST Center for Neutron Research, National Institute of Standards and Technology, Gaithersburg, MD 20899

³ College of Physics and Material Science, Henan Normal University, Xinxiang 453007, China.

⁴ International Center for Quantum Materials, School of Physics, Peking University, Beijing 100871, China.

⁵ University of Tennessee, Knoxville, TN 37996

⁶ Advanced Light Source, Lawrence Berkeley National Laboratory, Berkeley, CA 94720

⁷ Cornell High Energy Synchrotron Source, Ithaca, NY 14853

⁸ University of Maryland, College Park, MD 20742

⁹ Department of Materials Science and Engineering, University of California, Los Angeles, CA 90095

¹⁰ Department of Physics and Astronomy, University of California, Los Angeles, CA 90095

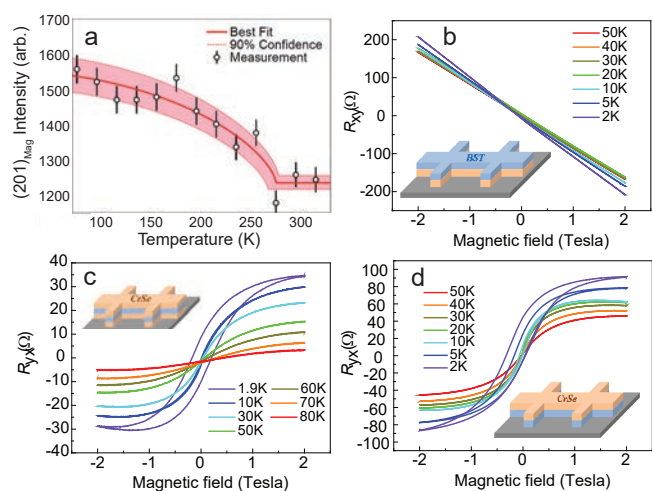


FIGURE 1: (a) Integrated intensity of the (201) CrSe neutron diffraction peak as a function of temperature, along with the best-fit to the data. Field and temperature-dependent Hall effect measurements of the (b) Bottom Bilayer (c) Sandwich, and (d) Top Bilayer sample geometries.

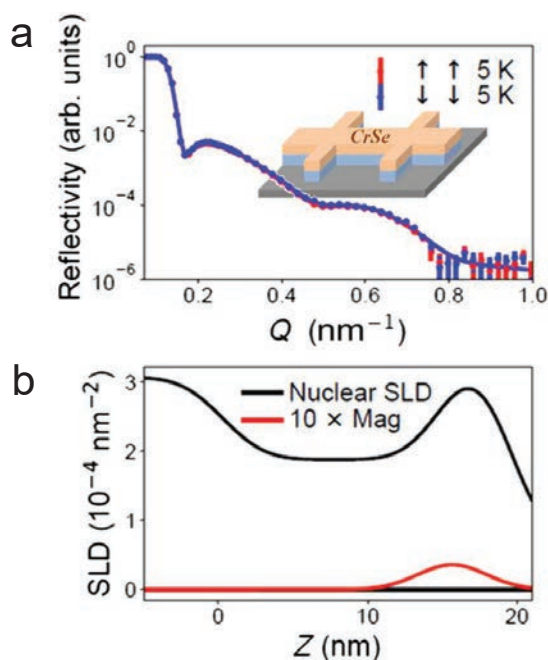


FIGURE 2: (a) Spin-dependent neutron reflectivity and (b) Structural and magnetic depth profiles used to generate the fits shown. Measurements taken at 5 K in an applied field of 700 mT.

the PNR data with a theoretical curve generated by the nuclear and magnetic scattering length density (SLD) profiles, where the magnetic SLD is proportional to the magnetization along the field, shown in Figure 2(c) yields an excellent description of the data. In the depth profile shown, a net magnetization does indeed appear at the interface, apparently biased slightly towards the CrSe side. However, the PNR data is insufficiently precise to allow a detailed distribution of the moment across the interface to be extracted.

By tuning a spin-polarized X-ray beam to the absorption edges of Cr and Sb and measuring the X-ray absorption (XAS) as a function of alternating applied magnetic fields and polarization, it is possible to determine the net magnetization associated

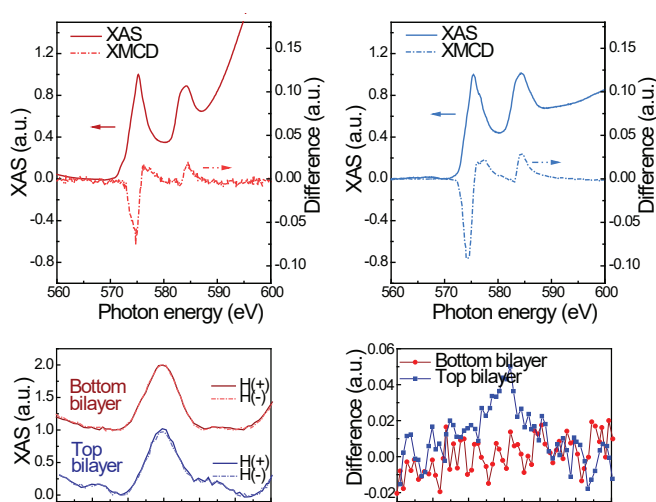


FIGURE 3: XAS and XMCD measurements at the Cr L-edge for a (a) Bottom Bilayer and (b) Top Bilayer. (c) XAS measurements at the Sb L₅-edge for both Bottom and Top bilayers. Measurements offset for clarity. (d) XMCD measurements associated with XAS curves in (c). Measurements performed at 10 K in ± 4 T steps.

with the Cr atoms in CrSe and the Sb atoms in $(\text{Bi,Sb})_2\text{Te}_3$. Although the details of this analysis are well beyond the scope of this writeup, one may understand the essentials by simply remembering that the difference between the H(+) and H(-) states (termed the XMCD) scales linearly with the net magnetization associated with that element. In Figure 4(a-b), we show the Cr XAS and XMCD for Top and Bottom Bilayers, revealing a weak net magnetization in both samples, with a stronger signal in the Top Bilayer. Similarly, Figure 4(c-d) shows the Sb-edge XAS and XMCD for the same samples, where only the Top Bilayer exhibits a net XMCD signal in the Sb.

We therefore conclude that a moment emerges in the Cr at the surface through defect-related interface reconstructions. This interaction is stronger in the Top Bilayer, which theoretical calculations indicate is due to preferential termination of the CrSe surface with Cr in this structure, strengthening the magnetizing interaction. The Bottom Bilayer, on the other hand, is terminated by nonmagnetic Sb at the interface, so that the interaction between magnetic Cr and the $(\text{Bi,Sb})_2\text{Te}_3$ layer is weakened. The combination of larger magnetization and Cr-termination induced a net magnetization the neighboring $(\text{Bi,Sb})_2\text{Te}_3$ of the Top Bilayer, while the $(\text{Bi,Sb})_2\text{Te}_3$ remains unmagnetized in the Bottom Bilayer. These results demonstrate the critical importance of interface symmetry and surface termination details in the resulting magnetic state and suggest new routes towards engineering functional TI-based magnetic heterostructures.

References

- [1] M. Z. Hasan, C. L. Kane, Colloquium: Topological insulators, *Rev. Mod. Phys.* **82**, 3045 (2010).
- [2] C.-Z. Chang, et al., *Science* **340**, 167 (2013).
- [3] C.-Y. Yang, et al., *Sci. Adv.* **6**, eaaz8463 (2020).
- [4] L. M. Corliss, et al., *Physical Review* **122**, 1402 (1961).

Local quantum criticality in a stoichiometric semi-metal

W. T. Fuhrman,¹ A. Sidorenko,² J. Hänel,² H. Winkler,² A. Prokofiev,² J. A. Rodriguez-Rivera,^{3,4} Y. Qiu,⁴ P. Blaha,⁵ Q. Si,⁶ C. L. Broholm,^{1,4,7} and S. Paschen^{2,6}

Red hot iron is paramagnetic and will not stick to your refrigerator (don't even try). At lower temperatures though, magnetized domains grow larger and reorient more slowly until below a *critical* temperature of 770 °C, the ferromagnetic refrigerator magnet is restored. Magnetic criticality also occurs in CeRu₄Sn₆ but the critical temperature curiously equals the absolute zero temperature ($T = 0$ K) so the phase transition simply cannot be traversed by cooling. We explore this unique “quantum critical” [1, 2] state of CeRu₄Sn₆ whose very existence without “tuning” stoichiometry, pressure, or field presents an intriguing mystery [3].

The centered tetragonal crystal structure of CeRu₄Sn₆ is shown in Fig. 1A. The magnetism is associated with Ce within asymmetric Ru₄Sn₈ polygons. Their lack of inversion symmetry plays an important role in the electronic band structure. Fig. 2 shows the wave vector (Q) dependence of inelastic magnetic neutron scattering from CeRu₄Sn₆ as measured at low temperature (1.8 K) on the MACS spectrometer [4]. The inelastic magnetic scattering takes the form of broad ridges through Q -space. These indicate that magnetic moments of cerium atoms fluctuate with correlations only amongst the very nearest neighboring sites, particularly those in neighboring **a-b** planes. Fig. 1B shows the so-called Fermi surface that is formed by the momenta of electrons (fermionic quasi-particles) at the chemical potential, which determine the thermodynamic and transport properties of the material. The Fermi surface reflects the electronic band structure, which was calculated using density functional theory treating cerium $4f^1$ electrons as part of the localized atomic core. The ridge-like features in Fig. 2 match wave vectors that connect large areas of the Fermi-surface in Fig. 1B especially those perpendicular to the four-fold c-axis. This indicates that correlations between cerium moments are mediated by magnetic (spin exchange) interactions with conduction electrons as they travel between near neighbors, especially those in neighboring **a-b** planes. Such “RKKY” interactions are generally associated with rare earth inter-metallics and long-range magnetic ordering below a finite critical temperature is a typical outcome. For CeRu₄Sn₆, however, the Ce based magnetic moments remain in

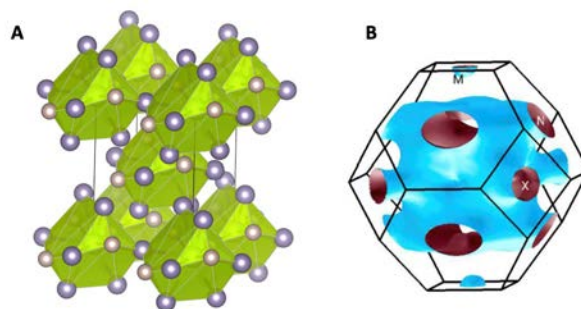


FIGURE 1: A) Crystal structure of the intermetallic CeRu₄Sn₆. Despite the magnetic nature of Ce at the center of the Ru₄Sn₈ polygons, there is no magnetic order but a fluctuating quantum critical state that persists to the absolute zero temperature. B) shows the calculated Fermi surface that controls the magnetic interactions between cerium magnetic moments. The local character of the critical fluctuations indicates these may be fluctuations of the entire Fermi surface rather than a magnetic order parameter.

a fluctuating short range correlated state down to the lowest temperature accessed (0.1 K) and are unable to form long range order.

To understand this state of affairs, consider Fig. 3, which shows the spectrum of magnetic fluctuations at the top of one of the ridges of scattering, specifically near the $Q = (100)$ point in reciprocal space (Fig. 2). Data acquired at multiple temperatures below 10 K form a consistent scaling form. Specifically, the scaling form observed indicates the magnetic susceptibility, which is related to the magnetic neutron scattering intensity through the fluctuation dissipation theorem, takes the form:

$$\chi(Q, \omega, T) \propto \frac{1}{f(Q) + (-i\hbar\omega + ck_B T)^\alpha}$$

The key feature in this expression is the scaling exponent α , which controls the energy and temperature dependence of magnetism in the low temperature limit. The data collapse on the scaling plot in Fig. 3A reveals that $\alpha = 0.6(1)$ for CeRu₄Sn₆. In addition, $f(Q)$ follows the wave vector dependence of the RKKY interactions and is small on the intense ridges, while a is a dimensionless constant. Fig. 3B shows that in the low field limit the conventional uniform magnetic susceptibility of

¹ Institute for Quantum Matter and Department of Physics and Astronomy, Johns Hopkins University, Baltimore, MD 21218
² Institute of Solid State Physics, Vienna University of Technology, Wiedner Hauptstr. 8-10, 1040 Vienna, Austria
³ Department of Materials Sciences, University of Maryland, College Park, MD 20742
⁴ NIST Center for Neutron Research, National Institute of Standards and Technology, Gaithersburg, MD 20899
⁵ Institute of Materials Chemistry, Vienna University of Technology, 1040 Vienna, Austria
⁶ Department of Physics and Astronomy, Rice Center for Quantum Materials, Rice University, Houston, TX 77005
⁷ Department of Materials Science and Engineering, Johns Hopkins University, Baltimore, MD 21218

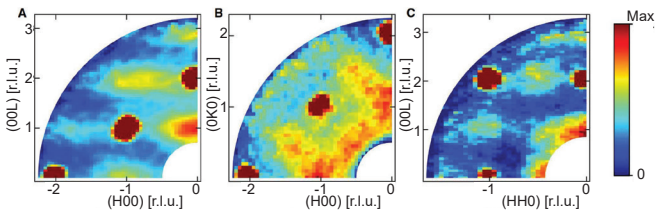


FIGURE 2: (A-C) Energy-integrated neutron scattering intensity at 1.5 K in the (H0L), (HK0), and (HHL) reciprocal lattice planes, respectively. Maxima for $H+K+L=\text{even}$ arise from nuclear Bragg scattering. Ridges of intensity indicate short range magnetic correlations. The ridge locations match wave vectors that span the Fermi-surface in Fig. 1B, which indicates they result from Ce-Ce interactions mediated by conduction electrons.

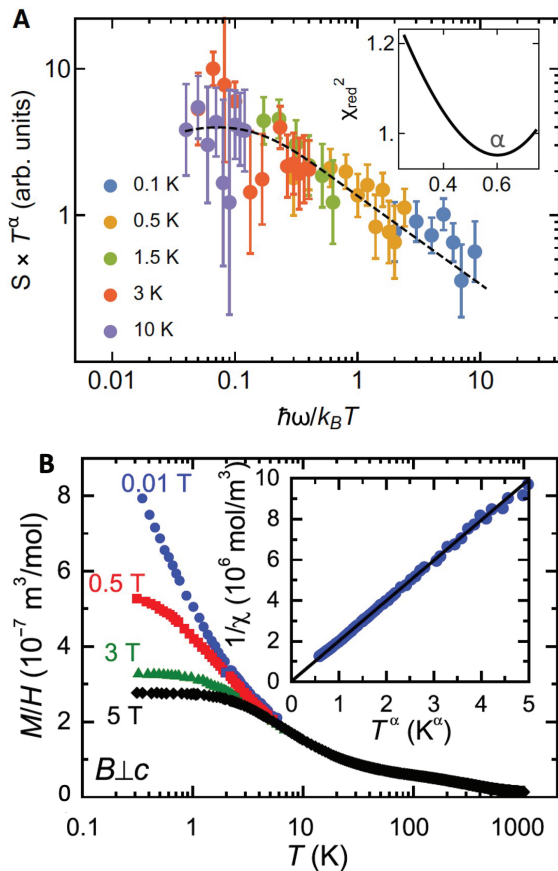


FIGURE 3: A) Scaling plot of the spectrum of magnetic neutron scattering based on measurements from 0.1 K to 10 K. These data are related to the generalized magnetic susceptibility through the fluctuation dissipation theorem. From the data collapse, a critical exponent of $\alpha = 0.6(1)$ is inferred. B) Uniform magnetic susceptibility data measured with the applied field in the basal plane. In the lowest applied field, the data follow a scaling form (inset) from which an exponent $\alpha_{\perp} = 0.50(1)$ is derived. For fields parallel to c the exponent is $\alpha_{\parallel} = 0.78(3)$.

CeRu₄Sn₆ also follows a power-law temperature dependence. While the exponent depends on the field direction within this anisotropic material, the relevant comparison to the neutron scattering data, which probes fluctuations in the plane perpendicular to momentum transfer Q , is to the average

$$\bar{\alpha} = \frac{1}{2}(\alpha_{\perp} + \alpha_{\parallel}) = 0.64(2)$$

The presence of power law scaling of the magnetic response function signals a quantum critical state of matter wherein the

absolute temperature T is the only energy scale and materials specific properties recede. The consistent power-law scaling from the uniform DC susceptibility measured in a SQUID magnetometer ($Q = 0, \omega = 0$) to broad swaths of the Brillouin zone (Fig. 2) and the THz frequency range, confirm that we are dealing with a homogeneous critical state. This sharply contrast with conventional critical phenomena where low frequency fluctuations are concentrated at a single critical wave vector Q . The experimental evidence points to a “local” quantum critical state that is associated with each cerium atom rather than with the critical fluctuations of an impending spatially coherent magnetic order [5]. The deviation of $\alpha = 0.6(1)$ from the value of 1 associated with the Landau theory of conventional critical phenomena, shows that the local quantum criticality of CeRu₄Sn₆ belongs in a separate universality class. This conclusion is reinforced by the scaling exponents measured from thermodynamic quantities (Fig. 3b) and their relations [3]. Rather than criticality associated with the specific critical wave vector of a proximate long range ordered state, the criticality in CeRu₄Sn₆ may be associated with fluctuations of the Fermi surface proper (Fig. 1B). Fluctuations between a state where the cerium 4 f electron is localized within its Ru₄Sn₈ polygon or becomes itinerant and part of an expanded Fermi-surface (Fig. 1).

While local quantum criticality has been identified in other materials including CeCu_{5.9}Au_{0.1} and YbRh₂Si₂ in an applied magnetic field, in both these cases the stoichiometric compound undergoes a conventional magnetic phase transition at zero applied field. CeRu₄Sn₆ on the other hand appears to be critical in the stoichiometric state in zero field and at zero temperature. This could be a coincidence, with the quantum critical point fortuitously located near the ambient condition. A more natural possibility is that the emergence of the quantum criticality goes hand in hand with the development of the semi-metallic nature of the strongly correlated ground state in CeRu₄Sn₆, which density functional theory suggests may be associated with topologically protected band crossings and the lack of inversion symmetry (Fig. 1A). The tantalizing prospect that quantum criticality is inherent to metallic systems with reduced charge carrier concentration, along with the anomalous critical exponents, provide new challenges and exciting opportunities for theory. Neutron scattering experiments in the presence of tuning parameters such as pressure and field will be important to explore this hypothesis and better understand the unique character of local quantum critical matter.

References

- [1] S. Sachdev, “Quantum Phase Transitions,” Cambridge University Press (2000).
- [2] S. Paschen, Q. Si, Nat. Rev. Phys. **3**, 9 (2021).
- [3] W. T. Fuhrman et al., Sci. Adv. **7**, eabf0134, (2021).
- [4] J. A. Rodriguez et al., Meas. Sci. Technol. **19** 034023 (2008).
- [5] Q. Si, S. Rabello, K. Ingersent, J. L. Smith, Nature **413**, 804 (2001).

Imaging electric field with electrically neutral particles

Y.-Y. Jau,¹ D. S. Hussey,² T. R. Gentile,² and W. C. Chen²

It has generally been thought impossible to determine/measure electric fields inside a physically isolated volume, especially inside an electrically shielded space, because a conventional electric-field sensor can only measure electric field at the location of the sensor. When an electric-field source is screened by conductive materials, no leakage electric field can be detected. For the first time, we have experimentally demonstrated that electrically neutral particles, neutrons, can be used to measure/image an electric field behind a physical barrier [1]. This work enables a new measurement capability that can visualize electrical properties inside a studied sample or detection target for scientific research and engineering applications.

The underlying working mechanism of this new penetrative imaging technology takes advantage of the interaction between neutrons and an electric field while neutrons are moving through an electric field region. A neutron has a magnetic moment (like a bar magnet) aligned to its spin. From electromagnetic theory [2], moving neutrons see an effective magnetic field $B_{\text{eff}} = -\mathbf{v} \times \mathbf{E}/c^2$ for $|\mathbf{v}| \ll c$, where \mathbf{v} is the neutron velocity vector, \mathbf{E} is the electric field vector, and c is the speed of light. The neutron spins precess about this effective magnetic field with a rate that is proportional to the electric-field amplitude. For a simplified scenario, the interaction duration is l/v , where l is the path length of the electric-field region. After neutrons pass through the electric-field region, we find the total spin precession angle θ_E to be $-\gamma_n El/c^2$, where $\gamma_n = -1.83 \times 10^8 \text{ rad s}^{-1}$ is the gyromagnetic ratio of the neutron. Thus, the electric field can be determined by measuring the spin precession angle. As we can see, the measured electric field is independent of neutron velocity, a nice feature that allows us to use a high-fluence, polychromatic neutron source for electric-field imaging. Mathematically, different neutron velocities, probing trajectories, polarization orientations, and analyzing directions can be employed to retrieve full vector information of electric field.

In our proof-of-concept experiment, we used the Neutron Guide 6 end station (NG6e) beam line at the U.S. National Institute of Standards and Technology (NIST) Center for Neutron Research. The experimental configuration is sketched in Fig. 1. Neutrons are spin polarized before being delivered to the electric-field sample, which is a parallel-plate capacitor with plates separated and enclosed by perfluoroalkoxy (PFA) material

and connected to a high-voltage source. To detect the very small neutron spin precession angle, we have developed a simple but sensitive neutron polarimetry scheme [3] that allows us to measure the change in spin rotation angle down to the micro-radian range. The left panel in Fig. 2 illustrates the typical transmission neutron image of the electric-field sample. From the picture, one can see the electrical cables, the rectangular electrodes (dark), and the PFA body and the dielectric layer between the electrodes. By engaging the neutron polarimetry and taking images with and without the high voltage, we obtain the difference image by subtracting the “OFF” state from the “ON” state with sufficient statistics, and we find the electric-field image as shown in the right panel in Fig. 2. The blue-color region on the image reveals the signal of the electric field inside the dielectric layer.

For a quantitative study, we find that the contrast signal defined in Eq. (5) in Ref. [1] (the normalized difference image/signal using the intensity background) is equal to the product of the neutron polarization P_n , analyzing power A , and the spin precession angle θ_E . This allows us to quantitatively compare the measured signals and the calculated signal strengths under different experimental conditions. In this experimental study, we used two electric-field samples, short and long versions. For the long version, the electrodes are 5 cm wide and 6.35 mm thick, $l = 11.4 \text{ cm}$, and the electrode spacing $d = (400 \pm 50) \mu\text{m}$. For the short version, the electrodes are 5 cm wide and 6.35 mm thick, $l = 5.7 \text{ cm}$, and the electrode spacing $d = (500 \pm 50) \mu\text{m}$. We measured the signal contrasts from the dielectric area on the images with several driving voltages from -35 kV to 35 kV on the short-version sample, 36 kV on the long-version sample, and 35 kV on the short-version sample with an iron shim (neutron depolarizer) in front of the sample. The results are summarized in Fig. 3. The slope of a linear fit to the data yields 1.01 ± 0.02 ; hence, the results are consistent with expectations. We see zero signal contrast with the shimmed case as proof of the need for polarized neutrons for electric field imaging. We find the minimum detectable voltage on the short-version sample is about 500 V (electric field of 10^6 V/m) using the 1172-averaged contrast images. In the future, we estimate that using multiple strategies including beam focusing [4] could provide another 2 orders of magnitude improvement, yielding a total detected neutron fluence up to the order of 10^{12} cm^{-2} in a day. For this level, we find the

¹ Sandia National Laboratories, Albuquerque, NM 87123

² National Institute of Standards and Technology, Gaithersburg, MD 20899

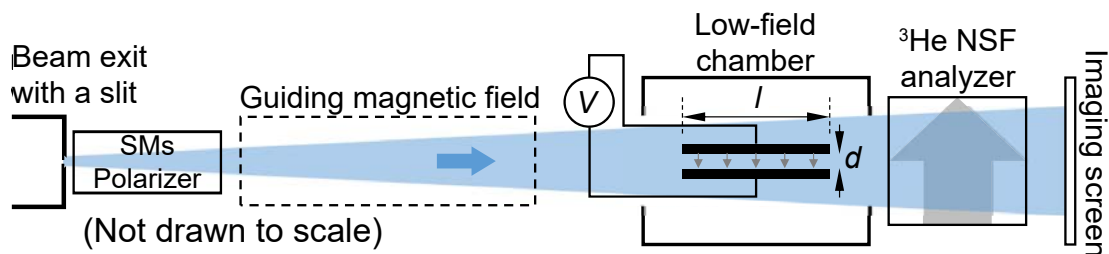


FIGURE 1: A schematic of the electric-field imaging experiments with polarized neutrons. The blue arrow represents the polarization of the neutron beam before arriving at the electric-field region (small gray arrows), which exists in between the two parallel electrodes driven by a voltage source. The gray big arrow denotes the analyzing direction of neutron spins at the analyzer. NSF denotes neutron spin filter.

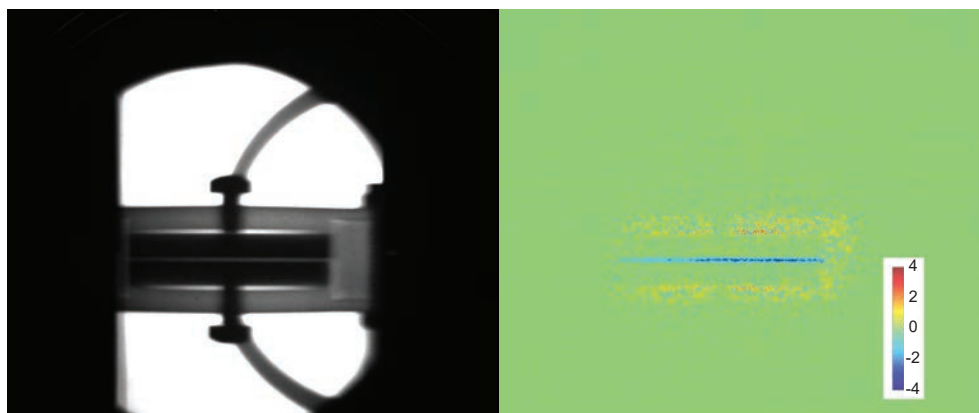


FIGURE 2: Left: A normal neutron transmission image of an electric-field sample. Right: Image of electric field in the dielectric layer of the sample using averaged difference images ($V_{-35kV} - V_{0kV}$) with "Jet" color scheme. Inside the sample, the voltage across the electrodes is -35 kV, which leads to a negative signal as the blue-color region.

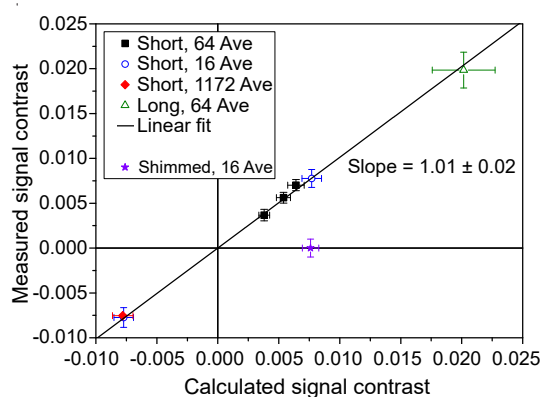


FIGURE 3: Measured signal contrasts vs calculated contrasts calculated "Short" and "Long" represent the data points from the short- and long-version E samples. "Shimmed" represents the data point using depolarized neutrons. The horizontal error bars are set by the machining uncertainty on the PFA membrane thickness, which is 50 μm , and the vertical error bars are limited by the imaging statistics. Also shown is a linear fit to the data, which yields a slope of 1.01 ± 0.02 .

minimum detectable electric-field strength for 1 cm^3 volumetric resolution to be about 5×10^4 V/m (equivalent to 500 V across 1 cm distance) and 1 mm^3 volumetric resolution to be about 5×10^6 V/m (equivalent to 5000 V across 1 mm distance). As we can see, trading sensitivity for higher volumetric resolution is inevitable. We believe this kind of sensitivity is sufficient for several image diagnostics applications for targets like high-voltage electronics, which usually contain capacitors with internal electric-field strengths $> 10^7$ V/m, dielectric materials

with externally applied very high electric field, and ferroelectric materials, which usually have spontaneous electric polarization with equivalent E strength $> 10^8$ V/m.

Before this work, visualizing electric fields within an occupied diagnostic space was not feasible. In addition, owing to the great penetration capability of neutrons through metals, this neutron-based electric field imaging technology can also measure the electric field that is inside a shielded space, which cannot be achieved by any other existing sensing technology. Our work enables provides a new diagnostic for the structure of electric potential, electric polarization, charge distribution, and dielectric constant inside an investigated target by visualizing spatially dependent electric field from a distance.

References

- [1] Y.-Y. Jau, D.S. Hussey, T.R. Gentile, W.C Chen, Phys. Rev. Lett. **125**, 110801 (2020).
- [2] J. D. Jackson, Classical Electrodynamics (Wiley, New York, 1999).
- [3] Y.-Y. Jau, W. C. Chen, T. R. Gentile, D. S. Hussey, Rev. Sci. Instrum. **91**, 073303 (2020).
- [4] D. S. Hussey, H. Wen, H. Wu, T. R. Gentile, W. Chen, D. L. Jacobson, J. M. LaManna, B. Khaykovich, J. Imaging Sci. **4**, 50 (2018).

Measurement of the neutron decay electron-antineutrino angular correlation by the aCORN experiment

M. T. Hassan,¹ W. A. Byron,¹ G. Darius,¹ C. DeAngelis,¹ F. E. Wietfeldt,¹ B. Collett,² G. L. Jones,² A. Komives,³ G. Noid,⁴ E. J. Stephenson,⁴ F. Bateman,⁵ M. S. Dewey,⁵ T. R. Gentile,⁵ M.P. Mendenhall,⁵ and J. S. Nico⁵

The free neutron decays into a proton, electron, and antineutrino via the weak nuclear force, the simplest example of nuclear beta decay. In contrast to beta decay of nuclei, the dynamics of neutron decay are undisturbed by complicated nuclear structure effects, so experimental observables can be directly related to fundamental parameters in the theory. As a result, neutron decay is an excellent laboratory for precision studies of the weak force and searches for new physics beyond the Standard Model of particle physics. Neutron-decay observables include the decay lifetime and the angular correlations between the momenta of the final state particles and the neutron spin. The aCORN (*a* CORrelation in Neutron decay) experiment measures the dimensionless "*a*-coefficient" in the neutron electron-antineutrino angular correlation: $1+a(v/c)\cos\theta_{e\nu}$. Here (v/c) is the beta electron velocity divided by the speed of light, and $\theta_{e\nu}$ is the angle between the beta electron and antineutrino momenta. The value of the *a*-coefficient is sensitive to the presence of hypothetical scalar and tensor weak forces, which are not present in the Standard Model but could be introduced by new physical phenomena such as supersymmetry. In this way, precision low-energy experiments such as aCORN explore the same physical frontier as the highest energy particle colliders e.g. the Large Hadron Collider at CERN.

The aCORN apparatus is depicted in Fig. 1. A highly uniform 36.3 mT axial magnetic field is produced by a stack of 24 water-cooled copper coils and an array of 76 axial and horizontal trim coils, each independently supplied and computer controlled. In the center of the tower is an electrostatic mirror, a region of free space surrounding the cold neutron beam that contains a uniform axial electric field of 70 V/cm. When a neutron decays in this region, if the beta-electron momentum lies within the acceptance defined by the magnetic field and the electron collimator located below the decay region, then the electron is transported to the beta spectrometer at the bottom of the tower, and its kinetic energy is measured. The associated recoil proton is directed upward by the electric field, and, if the proton momentum lies within the acceptance defined by the magnetic field and the proton collimator located above the decay region, it is detected by a silicon surface barrier detector. For each neutron-decay event where both the beta electron

and proton are detected, the beta energy and proton time-of-flight (TOF), the time between electron and proton detection, are recorded. The beta spectrometer uses a plastic scintillator detector to measure energy, and there is a 5% probability for the beta electron to backscatter from the scintillator without depositing its full energy, causing an incorrect energy to be measured. The spectrometer contains an array of "veto" detectors that identify such backscattered electrons with high efficiency and suppress those events.

The aCORN coincidence events, proton TOF vs. beta energy, form the characteristic "wishbone" plot shown in Fig. 2a. While the neutron-decay antineutrinos are not detected directly, conservation of energy and momentum identifies the upper branch of the wishbone (slow protons) with decays where $\cos\theta_{e\nu} < 0$ and the lower branch (fast protons) with decays where $\cos\theta_{e\nu} > 0$. For a given vertical slice of beta energy, the asymmetry in the number of upper branch and lower branch events $X(E) = \frac{N^I - N^{II}}{N^I + N^{II}}$ is proportional to the *a*-coefficient. Figure 2b shows a background-subtracted wishbone plot of 100 hours of aCORN data collected at the NG-C end position. Figure 3 shows the resulting measured *a*-coefficient vs. beta energy from a set of the NG-C data.

aCORN first ran at the NCNR on the NG-6 end position for 1,900 beam hours from 2013-2014. This run produced the first result that was reported in 2017 [1]: $a = -0.1090 \pm 0.0030(\text{stat}) \pm 0.0028(\text{sys})$. When the new guide hall was commissioned, the aCORN apparatus was moved to the new high-flux neutron physics end position on the supermirror guide NG-C, where it ran again for 3,760 beam hours from 2015-2016. This led to the second, more precise, result published this year [2]: $a = -0.10758 \pm 0.00136(\text{stat}) \pm 0.00148(\text{sys})$. Because the two results are in good agreement, we may combine them to present an overall aCORN result: $a = -0.10782 \pm 0.00182$ (statistical and systematic uncertainties in quadrature), for an overall relative precision of 1.7%.

Until recently, the experimental precision of the *a*-coefficient has lagged those of other neutron-decay observables, such as the beta asymmetry (*A*-coefficient), which has been measured to 0.18%, and it was the limiting uncertainty in a number

¹ Tulane University, New Orleans, LA 70118

² Hamilton College, Clinton, NY 13323

³ DePauw University, Greencastle, IN 46135

⁴ Indiana University, Bloomington, IN 47408

⁵ National Institute of Standards and Technology, Gaithersburg, MD 20899

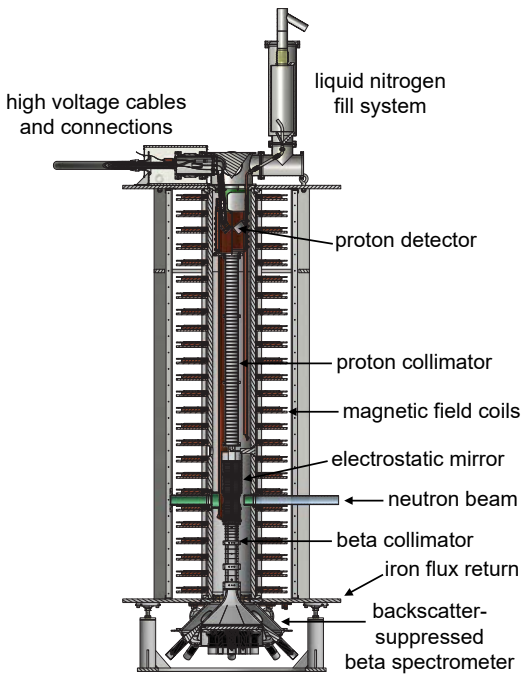


FIGURE 1: A cross section view of the aCORN tower showing the arrangement of major components. The neutron beam passes through from right to left.

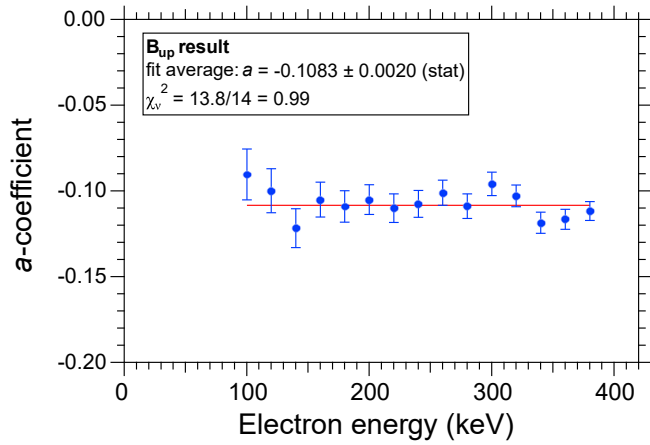


FIGURE 3: The a -coefficient determined from the aCORN wishbone asymmetry for a subset of the NG-C data.

of important Standard Model tests. The latest results from aCORN and the Institute Laue-Langevin (ILL) [3] have reduced the overall relative uncertainty of the a -coefficient from 4% to 0.7% over the past five years. While this has greatly improved Standard Model tests, it has also produced a discrepancy among neutron-decay observables. The aCORN result agrees well with other measurements, but the ILL result differs by 3-sigma. The upcoming new a -coefficient experiment Nab at the Spallation Neutron Source, and a possible future aCORN run at the NCNR, may shed further light on this problem.

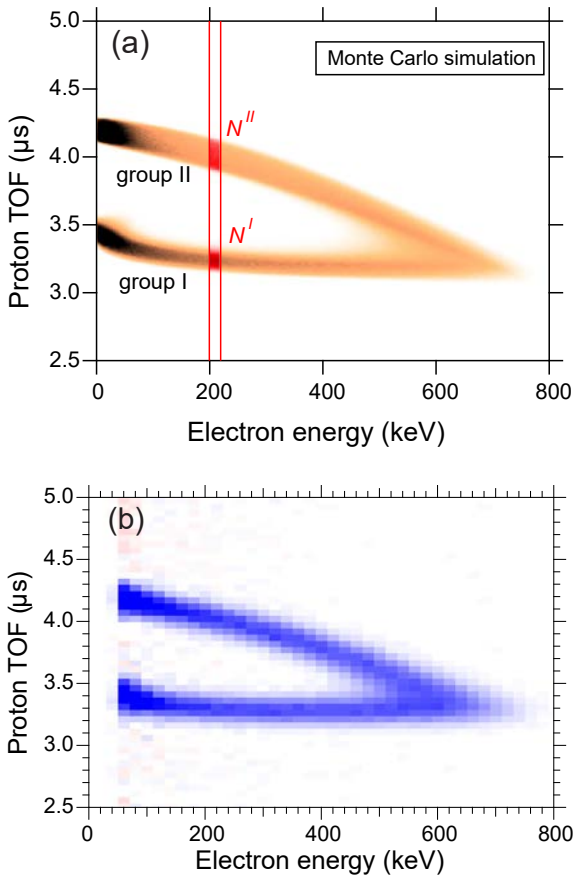


FIGURE 2: (a) A Monte Carlo simulation of aCORN data. Neutron-decay events form a characteristic "wishbone" plot with a fast-proton branch (group I) and a slow-proton branch (group II). For a given vertical slice of beta-electron energy, the asymmetry in the events N^I and N^{II} gives the a -coefficient. (b) A wishbone plot of 100 hours of aCORN data. Blue points are positive and red are negative (due to background subtraction).

References

- [1] G. Darius, W. A. Byron, C. R. DeAngelis, M. T. Hassan, F. E. Wietfeldt, B. Collett, G. L. Jones, M. S. Dewey, M. P. Mendenhall, J. S. Nico, H. Park, A. Komives, and E. J. Stephenson, *Phys. Rev. Lett.* **119**, 042502 (2017).
- [2] M. T. Hassan, W. A. Byron, G. Darius, C. DeAngelis, F. E. Wietfeldt, B. Collett, G. L. Jones, A. Komives, G. Noid, E. J. Stephenson, F. Bateman, M. S. Dewey, T. R. Gentile, M.P. Mendenhall, and J. S. Nico, *Phys. Rev. C* **103**, 045502 (2021).
- [3] M. Beck, F. Ayala Guardia, M. Borg, J. Kahlenberg, R. Muñoz Horta, C. Schmidt, A. Wunderle, W. Heil, R. Maisonnobe, M. Simson, T. Soldner, R. Virost, and O. Zimmer, M. Klopff, G. Konrad, S. Baeßler, F. Glück, and U. Schmidt, *Phys. Rev. C* **101**, 055506 (2020).

Molecular view on mechanical reinforcement in polymer nanocomposites

S. Cheng,¹ Y. Wang,² R. Sun,¹ Y. Liu^{3,4}

Polymer nanocomposites (PNCs) exhibit many superior macroscopic properties than their individual components, namely the matrix polymer and the nanoparticle (NP). However, the molecular mechanism leading to the strong enhancement of the macroscopic properties remains largely unresolved. Early studies argued the enhancement arises from matrix polymer deformations necessary to accommodate the non-deformable NP phase in PNCs [1]. Although the concept of strain amplification is widely used by the PNC community, microscopic experiments intended to confirm its existence have been inconclusive and controversial. Our recent work [2] helps to shed light on this longstanding problem.

Small-angle neutron scattering (SANS) is an excellent tool for characterizing the structural anisotropy of deformed polymers. With proper polymer deuteration, the average scattering length density (SLD) of the matrix polymer can be matched with that of the NP phase. At this match point, also called the zero-average-contrast (ZAC) point, the total scattering from the PNC is proportional to the single-chain structure factor of the polymer, $S(Q)$ [3]. For deformed PNCs, the single-chain structure factor describes the anisotropy of the matrix polymer on different length scales. A careful analysis of $S(Q)$ can therefore provide a quantitative understanding of the influence of NPs on the deformation of the matrix polymer. For instance, the molecular anisotropy of the polymer phase has been analyzed through the differences in the polymer radii of gyration along and transverse to the stretching direction. However, such an analysis is limited to the structural anisotropy at the chain level and is incapable of providing a full description of the polymer deformation at smaller length scales.

Recently, a spherical harmonic expansion analysis has been introduced to quantify the structural anisotropy of deformed polymers [4]. For deformed polymers under uniaxial extension, $S(Q)$ can be expressed as:

$$S(Q) = \sum_{l:\text{even}} S_l^0(Q) Y_l^0(\theta, \phi)$$

where $S_l^0(Q)$ is the expansion coefficient, $Y_l^0(\theta, \phi)$ is the spherical harmonic function, θ is the polar angle (the sample stretching direction), and ϕ is the azimuthal angle. The

expansion coefficients are useful for quantifying the degree of deformation as $S_0^0(Q)$ accounts for the isotropic contribution which typically dominates the scattering, and $S_2^0(Q)$ is the leading term describing the structural anisotropy.

Figure 1a presents the stress-elongation curves and the SANS data from a model PNC consisting of poly(methyl methacrylate) and silica nanoparticles [(PMMA)/SiO₂] and from pristine PMMA. At an 8% volume fraction, the NPs with a radius of $R_{\text{NP}} = 8$ nm are well dispersed in the PMMA matrix. The PMMA is a mixture of fully deuterated PMMA (molecular weight, $M_w = 217$ kg/mol, and polydispersity index, PDI = 1.27) and fully hydrogenous PMMA ($M_w = 194$ kg/mol and PDI = 1.08) with an H/D ratio of 0.59/0.41 to match the SLD of the SiO₂. The PNC exhibits a significantly higher tensile stress than the pristine matrix polymer according to rheological measurements. In contrast, no enhanced structural anisotropy is observed from SANS measurements up to $\lambda = 2.1$. A quantitative analysis of the anisotropic single-chain structure factor using a spherical harmonic expansion is given in Figure 1b. The inset shows that the isotropic expansion coefficients S_0^0 of the deformed PNC are almost identical to those of the deformed pristine polymer at $\lambda = 1.2, 1.5, 1.8,$ and 2.1 , which is consistent with the ZAC condition of the experiments. Moreover, the leading anisotropic coefficients of the deformed PNC and the pristine PMMA are also similar: they are almost identical at $\lambda = 1.2$ and 1.5 , and the magnitude of S_2^0 in PNC is only slightly smaller at $\lambda = 1.8,$ and 2.1 . These observations hold over a wide Q range of $(0.008\text{-}0.065) \text{ \AA}^{-1}$, covering a length scale from R_g to the statistical segmental length of the polymer. In other words, no enhanced structural anisotropy in the PNC is observed, at any length scale, despite the much higher tensile stress of the PNC.

To examine the contributions of the NP-NP interactions to the mechanical reinforcement of PNCs, we further carried out stress relaxation experiments (Figure 2a). The PMMA/SiO₂ and PMMA show similar stress relaxation dynamics up to 1.0τ with τ being the terminal relaxation time of the polymer. Moreover, the almost complete stress relaxation at 1.0τ for both PMMA/SiO₂ and PMMA suggests the stress contribution from the NP-NP interaction is negligible, and the high stress of the PNC originates from the polymer deformation.

¹ Department of Chemical Engineering and Materials Science, Michigan State University, East Lansing, MI 48824

² Center for Nanophase Materials Sciences, Oak Ridge National Laboratory, Oak Ridge, TN 37831

³ NIST Center for Neutron Research, National Institute of Standards and Technology, Gaithersburg, MD 20899

⁴ Department of Chemical and Biomolecular Engineering, University of Delaware, Newark, DE, 19716

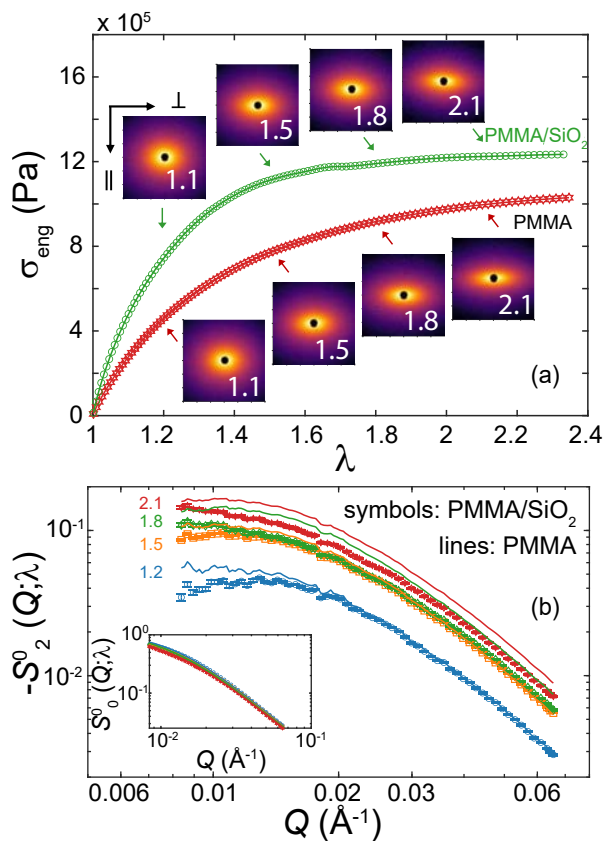


FIGURE 1: (a) Stress-elongation curves measured for a poly(methyl methacrylate) (PMMA)/SiO₂ PNC and the pristine PMMA. The inset shows the SANS spectra at different stages of deformation. (b) The $-S_2^0$ of the deformed PMMA/SiO₂ and the pristine PMMA at stretching ratios $\lambda=1.2, 1.5, 1.8,$ and 2.1 . The inset presents the corresponding S_0^0 .

SANS experiments during stress relaxation (at $t_{\text{relax}}=0.01, 0.03, 0.1, 0.3,$ and 1.0τ) provide further insight into the relationship between polymer deformation and macroscopic stress. The inset of Figure 2b presents the normalized anisotropy coefficient $S_2^0(Q, t)/S_2^0(Q, 0)$ of the deformed PNC (symbols) and the matrix polymer (lines). The PNC exhibits similar relaxation behavior in structural anisotropy as the matrix polymer over the entire Q range. Moreover, the relaxation of polymer structural anisotropy of both the PMMA/SiO₂ and pristine PMMA follows a previously reported scaling relation [5], indicating the inclusion of NPs does not fundamentally alter the slow relaxation dynamics of the deformed matrix polymer.

In summary, the combination of SANS and rheology demonstrates that polymer deformation dominates the stress response of PNCs. Despite a substantial mechanical reinforcement in the deformed PNC, a lack of molecular overstraining in the polymer phase has been identified [2]. This observation cannot be explained by the NP-NP contribution, but is consistent with the hydrodynamic effect of particles where a redistribution of the strain field in the polymer matrix is envisioned. This finding helps to clarify the molecular origin of the mechanical reinforcement in deformed PNCs and provides a new perspective for understanding the influence of NPs on the structure and dynamics of their surrounding polymer phase.

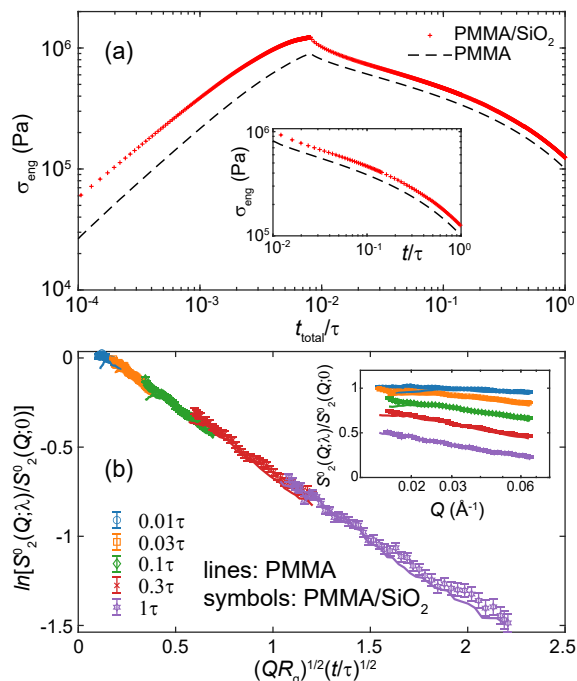


FIGURE 2: (a) Stress relaxation of the PMMA/SiO₂ and the pristine PMMA after a step deformation of $\lambda=1.8$. (b) The scaling of the normalized polymer structural anisotropy of deformed PMMA/SiO₂ and pristine PMMA during stress relaxation. The inset shows the normalized polymer structural anisotropy at different stages of stress relaxation.

References

- [1] L. Mullins, N. R. Tobin, *J. Appl. Polym. Sci.*, **9**, 2993 (1965).
- [2] R. Sun, et al., *Phys. Rev. Lett.*, **126**, 117801 (2021).
- [3] J. T. Koberstein, *J. Polym. Sci., Polym. Phys. Ed*, **20**, 593 (1982).
- [4] Z. Wang, et al., *Physical Review X*, **7**, 031003 (2017).
- [5] C. N. Lam, et al., *Phys. Rev. Lett.*, **121**, 117801 (2018).

Arresting bicontinuous channels with a solvent segregation driven gel

Y. Xi,^{1,2} R. S. Lankone,³ L.-P. Sung,³ and Y. Liu^{1,2,4}

The high specific surface area and interconnected channels of bicontinuous structures are promising for a wide range of applications from energy storage to biomaterials. One widely studied approach is to stabilize structures formed through spinodal decomposition by jamming submicrometer-sized particles at the interface of two-phase separating components in a binary solvent [1]. However, making these Bijels (bicontinuous interfacially jammed emulsion gels), requires a nontrivial treatment of particle surfaces so that both solvent components wet the surface equally [1, 2]. Moreover, the required fast quenching makes it challenging to prepare samples on a large scale [1, 3]. To overcome these limitations, we have developed a different method to arrest the growth of domains in bicontinuous structures by jamming particles within one of the two solvent domains [4, 5]. We term these materials solvent segregation driven gels (SeedGel). A SeedGel addresses the drawbacks of Bijels using a different physical mechanism to stabilize the structure, resulting in a general and scalable method. SeedGels are thermally reversible, forming highly reproducible and tunable structures which display unexpected optical properties.

The realization of a SeedGel is demonstrated using a model system that consists of highly charged silica nanoparticles and a binary solvent mixture of water and lutidine [4, 5]. By changing temperature, microscopic solvent phase separation is induced, which drives the transition of the sample from a liquid state to a solid gel state (SeedGel). The bicontinuous channels of a SeedGel consist of alternating particle domains and solvent domains. The nanoparticles are jammed within the particle domain that percolates throughout the sample providing mechanical strength.

Ultra-small angle neutron scattering (uSANS) was used to probe the structure of a model SeedGel having a transition to a gel state at ≈ 26 °C. The sample is a liquid for $T < 26$ °C, consistent with the featureless uSANS patterns shown in Figure 1(a). However, for $T > 26$ °C, the increased scattering intensity with a well-defined shoulder at around $1.7 \times 10^{-4} \text{ \AA}^{-1}$ indicates the formation of μm -sized channels. The fits using the Teubner-Strey model [6] reveal an inter-channel spacing of approximately $3 \mu\text{m}$. Interestingly, the bicontinuous structures are thermally

reversible (Figure 1(b)). By repeatedly cycling the sample between low temperature (4 °C) and high temperature (30 °C), the domain structures can be dissolved (low temperature) and reformed (high temperature).

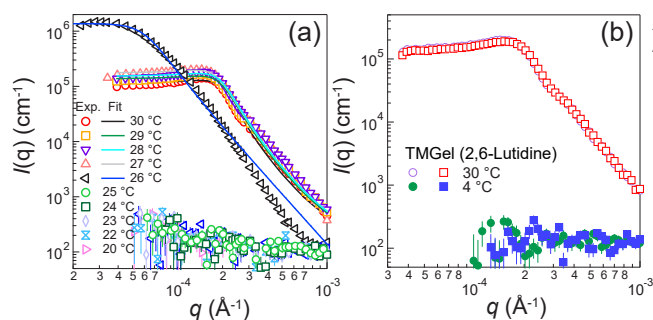


FIGURE 1: (a) Ultra-small angle neutron scattering (uSANS) profiles of SeedGel recorded at varied temperatures. The data is fit with the Teubner-Strey model. (b) uSANS profiles of SeedGel cycled between low temperature (liquid state) and high temperature (gel state).

Due to the large scattering length density (SLD) differences between particles and the solvent, the uSANS results are mainly sensitive to the domain structures formed by the nanoparticles. To probe the solvent properties inside the particle domain, the contrast variation method is used. Figure 2 (a) shows data from small angle neutron scattering (SANS) experiments obtained by mixing the appropriate amounts of H_2O and D_2O so that the SLD of water is equal to that of nanoparticles. The intensity of the inter-particle distance scattering peak at $q \approx 0.02 \text{ \AA}^{-1}$ is reduced by more than five times when the sample transitions from the liquid state (20 °C) to the gel state (30 °C). This indicates that water and particles largely share the same domain which results in the silica nanoparticles being almost “invisible” to the neutrons. In contrast, the sample prepared with only H_2O in Figure 2(b) shows comparable peak intensity between the liquid state (20 °C) and gel state (30 °C). The shifts of the peak position towards high- q upon the SeedGel formation is due to the reduced interparticle distance in the particle domain. As SANS is quite sensitive to the local particle packing, Figure 2 also shows that the local structures of the SeedGel are reproducible. Combining the information obtained from Figure 1 and Figure 2, it is clear that the particles and

¹ NIST Center for Neutron Research, National Institute of Standards and Technology, Gaithersburg, MD 20899

² Department of Chemical & Biomolecular Engineering, University of Delaware, Newark, DE 19716

³ Engineering Laboratory, National Institute of Standards and Technology, Gaithersburg, MD 20899

⁴ Department of Physics & Astronomy, University of Delaware, Newark, DE 19716

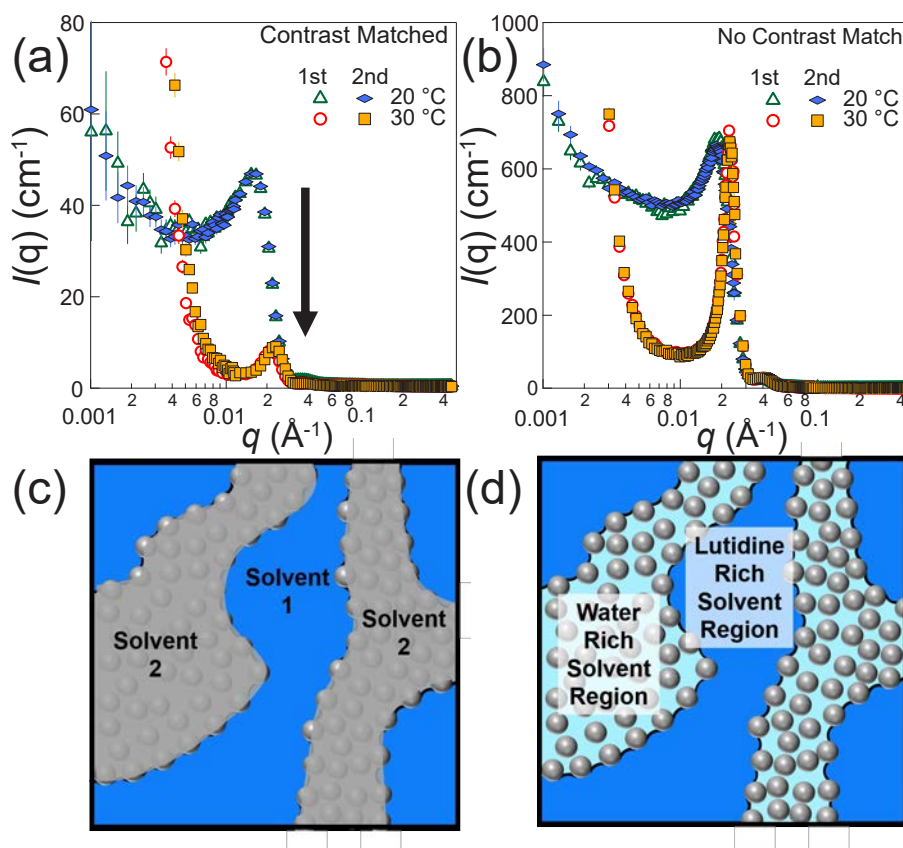


FIGURE 2: SANS profiles of SeedGel cycled between 20 °C and 30 °C. The scattering length density (SLD) of water is matched to that of the particles by mixing H₂O and D₂O in (a), while only H₂O is used in (b) for comparison. (c) and (d) show the schematic drawing of structures in (a) and (b), respectively.

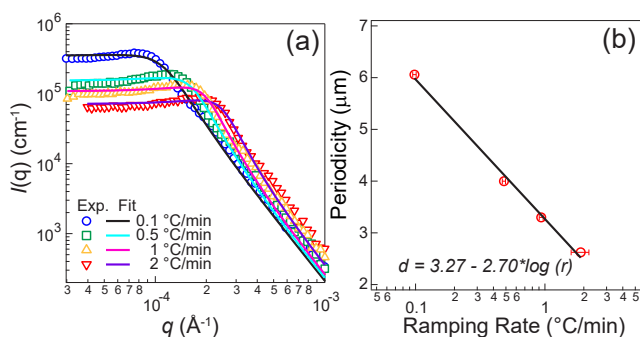


FIGURE 3: (a) uSANS results of SeedGel prepared with different ramping rate to 30 °C. (b) The fitted periodicity using Teubner-Strey model as a function of ramping rate.

solvents reversibly form bicontinuous structures in our SeedGel.

An advantage of SeedGel is that the gel is formed over a wide range of temperature ramping rates, including slow ones, making it a great technique for large-scale production. Furthermore, the ramping rate provides a robust control of the size of the bicontinuous channels. Figure 3 shows uSANS patterns of a SeedGel prepared with different temperature ramping rates. By analyzing the uSANS patterns, the periodicity, which is proportional to the domain size, is extracted. A linear dependence of the periodicity on the ramp rate is observed in the semi-log scale, which can be used as a guideline to design soft materials with a desired domain size. Very interestingly,

even with micrometer sized domains, some SeedGels are transparent at certain temperatures.

In summary, SeedGels provide a new approach to form a solid gel with a desired bicontinuous structure. The scalability, structural reproducibility, and interesting optical properties render SeedGels useful for a wide range of applications. uSANS and SANS provide the critical structural information necessary to reveal the underlying physical mechanism of how this novel bicontinuous structure is stabilized.

References

- [1] E. M. Herzig, K. A. White, A. B. Schofield, W. C. K. Poon, P. S. Clegg, *Nat. Mater.*, **6** (12), 966 (2007).
- [2] D. Cai, P. S. Clegg, *Chem. Commun.*, **51** (95), 16984 (2015).
- [3] M. Reeves, A. T. Brown, A. B. Schofield, M. E. Cates, J. H. Thijssen, *J. Phys. Rev. E*, **92** (3), 032308 (2015).
- [4] Y. Xi, R. S. Lankone, L.-P. Sung, Y. Liu, *Nat. Commun.*, **12** (1), 910 (2021).
- [5] Y. Xi, J. B. Leão, Q. Ye, R. S. Lankone, L.-P. Sung, Y. Liu, *Langmuir*, **37** (6), 2170 (2021).
- [6] M. Teubner, R. J. Strey, *J. Chem. Phys.*, **87**, 3195 (1987).

Dynamics and toughness in glassy polycarbonates

C. L. Soles¹ and M. Tyagi^{2,3}

Amorphous polymers are amazing and intriguing materials. In the glassy state, their mechanical properties can vary from low-strength brittle solids, synonymous with derogatory phrases like “cheap plastics,” to the high-performance engineering resins with amazing toughness. This diversity in their mechanical behavior has always intrigued polymer scientists. In the 1970’s, the polymers community surmised that collective molecular relaxations were important for dissipating energy and increasing mechanical toughness. Numerous studies sought to correlate the mechanical properties of polymers with their relaxation behavior using characterization techniques such as dynamic mechanical analysis, dielectric spectroscopy, and solid-state nuclear magnetic resonance spectroscopy. These are powerful methods for characterizing relaxation processes on the time scales of seconds to microseconds. Through this paradigm, the community was able to establish empirical correlations between the relaxation processes in the glassy state and the materials impact strength. However, there has always been a huge disconnect in the time and length scales of the characterization techniques used to quantify these anelastic processes and the molecular mechanisms that are responsible for the toughness. Bond or group-specific molecular vibrations can be readily identified using techniques such as Fourier Transform Infra-Red (FTIR) or Raman spectroscopy, but these high-frequency optical modes, which occur on the femtosecond time scale, fail to correlate with toughness. Measurements that characterize molecular relaxation processes in the window between femtoseconds and microseconds are critical to understand the origins of toughness in polymer glasses. They are critical to understand the difference between cheap brittle plastics and high-performance impact resistant resins.

Inelastic and quasi-elastic neutron scattering (INS and QENS) are well-suited to address this challenge. Somewhere within this picosecond to nanosecond window, the high-frequency vibrations evidenced by optical spectroscopies collectively couple and evolve into the many atom relaxations that have been shown at the microsecond and slower time scales to correlate with toughness. INS and QENS have the requisite sensitivity to better understand these processes. To establish this connection, we embarked upon a series of INS and QENS measurements on a series of polycarbonate glasses. Polycarbonate is a classic

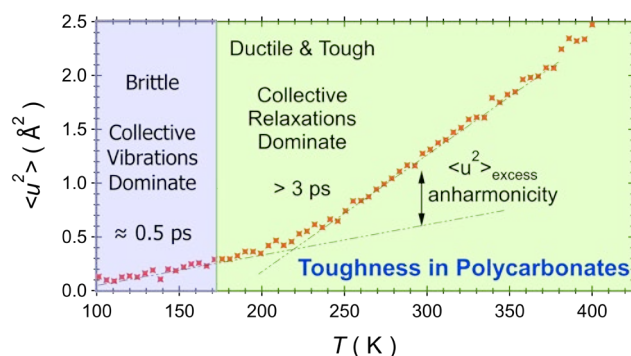


FIGURE 1: The red stars show the dependence of $\langle u^2 \rangle$ with T for a polycarbonate copolymer, showing the onset of anharmonicity in the dynamics above 175 K and how $\langle u^2 \rangle_{\text{excess}}$ quantifies this anharmonicity. The transition from the purple to green regions corresponds to the brittle-to-ductile transition. Full inelastic neutron scattering spectra confirm that this transition also corresponds to an evolution from sub-picosecond vibrations to quasielastic relaxations with a time scale of 3 picoseconds or longer.

example of a high impact strength polymer that is routinely used in mission critical applications such as aircraft canopies, bullet proof windows, and safety glass lenses. Modifications were made to the polycarbonates, through copolymerization schemes or non-reactive diluents, to systematically increase or decrease the materials impact strength. Two spectrometers at the NIST Center for Neutron Research were used to assess how these modifications changed the dynamics of the polycarbonate in the glassy state. Fixed window scans were performed on the High Flux Backscattering Spectrometer (HFBS) and were used to characterize the level of anharmonicity of the dynamics in the nanosecond time scale while the full inelastic spectra as a function of temperature were collected on the Disc Chopper Spectrometer (DCS) to characterize the relaxation processes on the picosecond time scale.

The Q -dependent elastic scattering intensities from the fixed window scans measured on the HFBS spectrometer were analyzed in terms of a harmonic oscillator to calculate the mean-square atomic displacement $\langle u^2 \rangle$ as a function of temperature, as shown in Figure 1 for one of our synthetically modified polycarbonate copolymers [1]. Starting at the lowest temperatures, $\langle u^2 \rangle$ evolves linearly with T , consistent with a harmonic oscillator. Just below 200 K a discontinuity occurs, and

¹ Materials Science & Engineering Division, National Institute of Standards and Technology, Gaithersburg, MD 20899

² NIST Center for Neutron Research, National Institute of Standards and Technology, Gaithersburg, MD 20899

³ Department of Materials Science and Engineering, University of Maryland, College Park, MD 20742

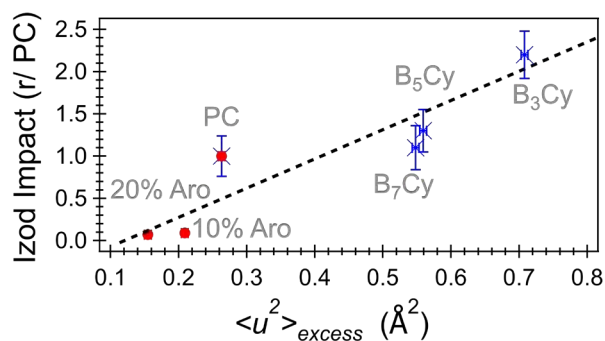


FIGURE 2: A plot of the room temperature Izod impact strength versus $\langle u^2 \rangle_{\text{excess}}$ for a homologous series of polycarbonate glasses.

the dynamics become anharmonic (non-linear) with temperature. This level of anharmonicity is defined as $\langle u^2 \rangle_{\text{excess}}$, or the difference between measured $\langle u^2 \rangle$ and value extrapolated from the low temperature linear harmonic regime.

Superimposed on Figure 1 is a map of the mechanical deformation mechanisms for this polycarbonate copolymer, previously reported elsewhere [2]. When polycarbonate is cooled to low temperatures, the material loses toughness and deforms catastrophically in a brittle manner (shaded in purple). Upon heating there is a brittle-to-ductile transition near 175 K, after which the deformation becomes ductile (shaded in green) and the polycarbonate regains toughness. It is striking that this onset of ductility and toughness corresponds to the onset of anharmonicity in terms of $\langle u^2 \rangle_{\text{excess}}$. From the energy resolution of the HFBS spectrometer, we know that the motions responsible for this $\langle u^2 \rangle_{\text{excess}}$ occur on a time scale of approximately 1 ns or faster.

To explore the time scale of the dynamics in this transition region in greater detail, we collected full inelastic neutron scattering spectra as a function of temperature on the DCS spectrometer. While we do not show the spectra here (refer to our recent publication¹), two modes were present in the scattering. At the low temperatures the spectra were dominated by the Boson Peak (BP), an inelastic vibration common to glassy materials that is understood to engulf hundreds or thousands of atoms vibrating collectively with a sub-picosecond characteristic time scale. At higher temperatures these motions are accompanied by a slower quasielastic scattering (QES) mode with a characteristic relaxation time of approximately 3 picoseconds. Our measurements reveal that this onset of $\langle u^2 \rangle_{\text{excess}}$ and toughness in the mechanical response correspond to the temperature where the intensity of the QES peak exceeds the BP peak. The toughness and ductility of polycarbonate appear to be tied with the ability of the material to parlay collective vibrations on the sub-picosecond time scale into slower collective relaxations that dissipate energy.

To test this hypothesis, we extended these measurements to a series of polycarbonates where their mechanical toughness, characterized by their Izod impact strength, was systemically varied. These variations including incorporating cyclohexylene linkages into the polycarbonate backbones to enhance molecular mobility, or blending small amounts of Aroclor, a small molecule

diluent that is known to embrittle polycarbonate. Across this homologous series of polycarbonates, we performed a series of fixed window scans on the HFBS spectrometer to quantify how these modifications affect $\langle u^2 \rangle$. In Figure 2 we plot the resulting correlation between the normalized Izod impact strength of the material against $\langle u^2 \rangle_{\text{excess}}$ at room temperature [3]. Once again, the results are striking. There appears to be a strong correlation between $\langle u^2 \rangle_{\text{excess}}$ and toughness across a range of materials, strongly implicating these collective relaxations on a time scale of 3 picoseconds as the mechanism by which polycarbonates dissipate energy and increase toughness under impact. We are currently in the process of extending these measurements to a broader class of materials, including epoxy and dicyclopentadiene networks, with our latest results indicating that these initial observations are quite general.

This is, to the best of our knowledge, the first direct evidence based on physical measurements that shows relaxations on picosecond time scale, and length scale of just a few cubic nanometers, influence the yield and deformation mechanisms. These insights are seminal because they give polymer scientists a powerful tool to interrogate toughness and provide molecular level information that can be used to design new and improved materials. Furthermore, the time and length scales of these measurements directly overlap those accessed by fully atomistic molecular dynamic (MD) simulations. The potential to bridge MD simulations with mechanical toughness via QENS is an exciting prospect for the design of new polymers with improved toughness. This has the potential to be a paradigm shift for the community.

References

- [1] C. L. Soles, A. B. Burns, K. Ito, E. P. Chan, J. F. Douglas, J. H. Wu, A. F. Yee, Y. T. Shih, L. P. Huang, R. M. Dimeo, and M. Tyagi, *Macromolecules* **54** (5), 2518 (2021).
- [2] C. J. G. Plummer, C. L. Soles, C. Xiao, J. Wu, H. H. Kausch, and A. F. Yee, *Macromolecules* **28** (21), 7157 (1995).
- [3] C. L. Soles, A. B. Burns, K. Ito, E. Chan, J. W. Liu, A. F. Yee, and M. S. Tyagi, *Macromolecules* **53** (15), 6672 (2020).

Scaling relationships for the elastic and viscous properties of mixed lipid membranes

E.G. Kelley,¹ P.D. Bulter,^{1,2,3} and M. Nagao^{1,2,4}

The macroscopic mechanical properties of soft materials often are determined by their molecular composition. From small molecule surfactants to high molecular weight polymers, small changes in the molecular composition can have considerable effects on the rigidity and viscosity of the materials, and 'short' and 'long' molecules often are blended to engineer the properties of their mixtures. Short-tail and long-tail surfactants can be blended to soften worm-like micelles often used in household and personal care products [1], and high-molecular weight (long) and low-molecular weight (short) polyolefins are blended to enhance the mechanical properties while maintaining the processability of polymers in commercial applications [2]. In each case, the macroscopic properties of the soft materials are tuned by the microscopic molecular composition.

Here we use the same framework to shed light on how cell membranes, composed of a large variety of lipids, sterols, and other components, can alter their mechanical properties to accommodate the ever-changing requirements of their various functions. By mixing long- and short-tailed lipids, we show that small changes in the molecular composition can significantly impact the elastic and viscous properties of the bilayers and make the membrane softer and more dynamic than predicted with simple mixing rules. While the properties of the mixed lipid membranes could not be predicted from the known quantities for the corresponding pure component membranes, we take advantage of the unique insights provided by the combined structural and dynamical neutron scattering measurements to show that the enhanced dynamics are directly linked to changes in the membrane structure and instead follow simple scaling relationships [3].

This work studies membranes composed of binary mixtures of a short-tail (dimyristoylphosphatidylcholine, 14:0 PC, DMPC) and long-tail (distearoylphosphatidylcholine, 18:0 PC, DSPC) lipid. These lipids have the same phosphatidylcholine headgroup, but differ in hydrophobic tail length by four carbons. The four extra carbons in the acyl tails make a DSPC lipid membrane ≈ 0.8 nm thicker than a pure DMPC lipid membrane, and as such, mixing these two lipids should be a convenient means of tuning the bilayer thickness (d_B). In particular, it is often assumed that the properties of mixed lipid membranes can be

predicted from the constituent single component lipid membrane properties using simple mixing rules i.e. $d_{B,mix} = \sum x_i d_{B,i}$; however, small angle neutron scattering (SANS) studies of the structure of mixed DMPC/DSPC membranes showed that this assumption is not always true.

Shown in Figure 1 is the bilayer thickness as a function of the mole fraction of the long-tailed DSPC lipid (x_{DSPC}) in the membrane. The measured values for the mixtures fall below the line calculated using simple mixing rules and are $\approx 5\%$ to 7% thinner than expected if the single component bilayer thicknesses were additive. Complementary densitometry measurements showed that there was no change in lipid volume upon mixing, i.e. $\Delta V_{mix} = 0$, and as such, the decrease in bilayer thickness corresponds to an increase in the area per lipid (A_L) where $A_L = 2V_{lipid}/d_B$. The area per lipid is a measure of the lateral organization of the membrane, suggesting that the effective 'size' of the molecules in the membrane increases more than expected when long- and short-tail lipids are mixed, and consequently, the mixed bilayers are less ordered than the single component membranes.

Neutron spin echo spectroscopy (NSE) measurements also showed that the mixed long- and short-tailed lipid membranes were more dynamic and softer than predicted from simple mixing rules, and in fact, even softer than either of the pure component membranes. Incorporating a mole fraction of 30% short tail DMPC lipids into a majority DSPC membrane ($x_{DSPC} = 0.7$) reduced the bending rigidity (κ) by almost a factor of 2 compared to the pure DSPC membrane. Similarly, NSE measurements of the collective thickness fluctuations showed that these dynamics also are enhanced in mixed DMPC/DSPC lipid membranes. The increase in the thickness fluctuation amplitude indicated that mixing the lipids decreased the membrane compressibility modulus (K_A), while the increase in relaxation rate suggested that the mixed lipid membranes also had a lower viscosity (η_m) than the pure component membranes.

Taken together, the NSE data show that the mixed lipid membranes are easier to bend and compress and are less viscous than either of the single component membranes. These enhanced dynamics are surprising without context; however, taking a holistic view of the neutron scattering data reveals that

¹ NIST Center for Neutron Research, National Institute of Standards and Technology, Gaithersburg, MD 20899

² University of Delaware, Newark, DE 19716

³ The University of Tennessee, Knoxville, TN 37996

⁴ University of Maryland, College Park, MD 20740

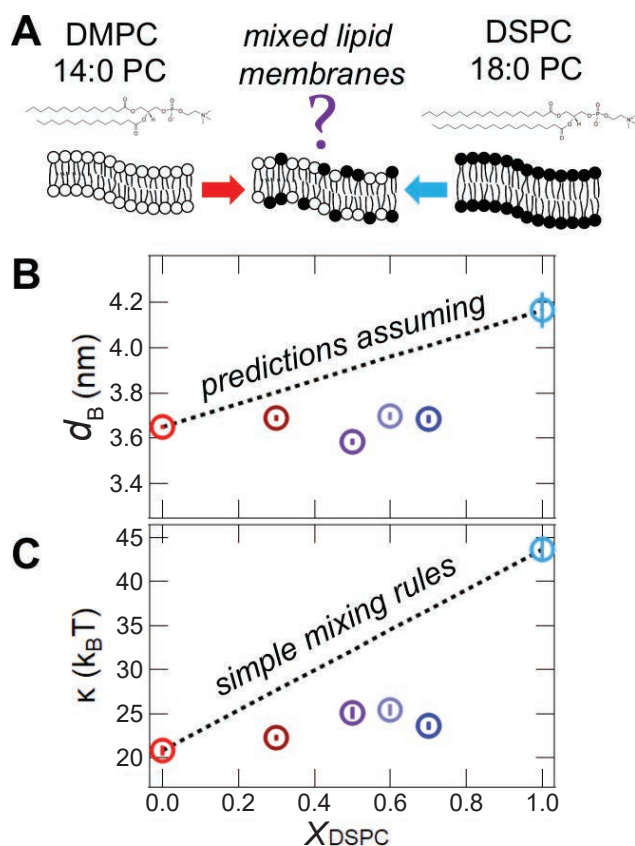


FIGURE 1: (A):Molecular structures of the DMPC and DSPC lipids mixed to study the effects of membrane composition on the structure and dynamics of mixed lipid membranes. (B) Membrane thicknesses determined using SANS as a function of mole fraction of long-tailed DSPC lipid (X_{DSPC}) in the membrane (points) and predicted from the constituent pure lipid membrane properties assuming simple mixing rules (dashed line). SANS data were collected at the same temperature relative to the phase transition temperature, T_m , of $T - T_m = 20$ °C (C) Membrane bending modulus determine from NSE measurements of the mixed lipid membranes (points) and predictions using simple mixing rules (dashed line). NSE data were collected at $T - T_m = 20$ °C.

the changes in both the membrane structure and dynamics show similar trends with the composition of the mixed lipid membranes and suggests that they are directly linked. The direct link between the membrane structure and dynamics are exemplified in Figure 2, in which κ , K_A , and η_m determined from the NSE data for all lipid compositions across a wide range of temperatures can be collapsed onto their respective master curves, in which the dynamic property directly scales with the area per lipid, A_L .

These scaling relationships provide a simple framework for understanding the role of lipid composition in controlling the elastic and viscous properties of biological membranes. While linking the complex and highly regulated lipid diversity to the membrane physical properties has been a long-standing challenge in biophysics, the neutron scattering studies show that any changes in membrane composition that disrupt the lipid packing and make the membrane less ordered, such as by incorporating unsaturated lipids with kinked hydrophobic tails, will make the membrane softer and more dynamic.

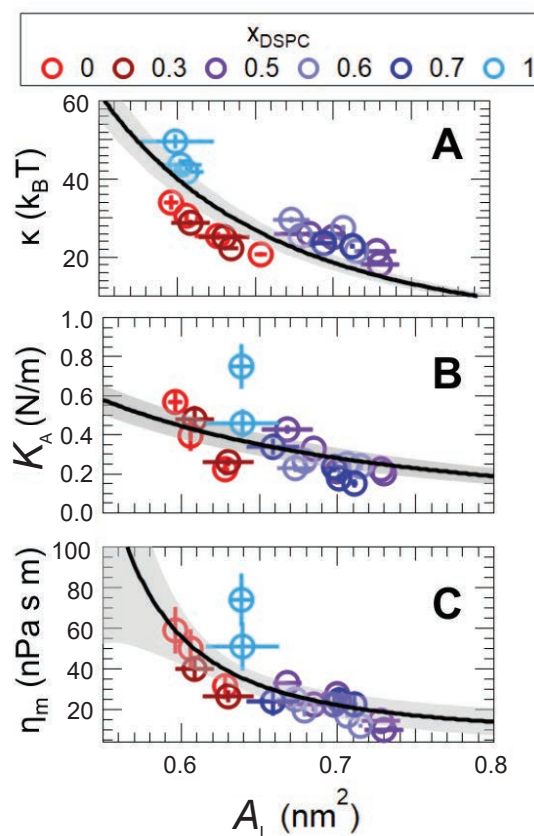


FIGURE 2: Scaling relationships for the elastic and viscous properties of DMPC and DSPC lipid membranes with area per lipid (A_L) over a range of concentration and wide range of temperatures. (A) bending modulus (κ) determined from NSE measurements of the collective membrane bending fluctuations and (B) area compressibility modulus (K_A) and (C) membrane viscosity (η_m) determined from NSE measurements of the collective thickness fluctuations. The symbols are the measured data, and the solid lines are the corresponding theoretically predicted scaling relationships with A_L [3].

The results in mixed lipid membranes also parallel finding in surfactants, liquid crystals, and polymers, and importantly, show that the same approach of blending molecules can be used to manipulate the physical properties of lipid mixtures.

References

- [1] C. Oelshlaeger and N. Willenbacher, *Colloids Surf., A* **406** 31 (2012).
- [2] F. P. Alt, L.L. Böhm, H.-F. Endler, J. Berthold, *Macromol. Symp.* **163** (1) 134 (2001).
- [3] E.G. Kelley, P.D. Butler, R. Ashkar, R. Bradbury, M. Nagao, *PNAS* **117** (38) 23365 (2020).

Sub-micrometer neutron tomography

B. Heacock,^{1,2} D. Sarenac,³ D. G. Cory,^{3,5} M. G. Huber,⁶ J. P. W. MacLean,^{3,4} H. Miao,⁷ H. Wen,⁷ and D. A. Pushin^{3,4}

Neutron imaging and tomography is a rapidly expanding field in studying materials, working devices, archeological and meteorological artifacts, and fundamental physics. Recent advances in neutron detector technologies are pushing detector resolution to a few micrometers. However, the typical neutron resolution is only a few tens of micrometers. This resolution usually defines the resolution of the tomographic reconstructions. Often the experiments and materials dictate the need for higher resolution of micrometer or less while studying "internal" bulk properties with neutrons.

We have demonstrated [1] a resolution of 300 nm could be achieved using neutron diffraction patterns generated from periodic/quasi-periodic materials/devices combined with phase-retrieval and computed tomography techniques. In [1] we used 2.4 μm periodic silicon phase grating [2, 3] as a sample under investigation (see Fig. 1 (a)) where the incoming neutron beam (wavelength $\lambda = 4.4 \text{ \AA}$) passes through perfect Si crystal monochromator and Cd entrance slit. The grating sample diffract neutrons and diffraction orders were analyzed using a 2nd Si crystal. Neutron intensities vs monochromator rotation (θ) are recorded using a ³He integrating counter. For phase retrieval and computed tomography, we repeated these procedures at different sample angle (β) orientations (see Fig. 1 (a)). Fig. 2 (b) shows how position space image reconstructed from diffraction data. We repeated this experiment for gratings with different profiles and heights. The summary of these studies is shown in Fig. 2 where the left column shows pictures obtained by scanning electron microscopy (SEM), the middle column is reconstructed profile from neutron experiments and the right column is an overlay of both measurements for comparison. Both data (SEM and neutron) are in a good agreement and we can see the grating structures with resolution about 300 nm. Expansion of this technique is possible into 3D tomography and, most importantly, allows for sub-micron resolution neutron imaging.

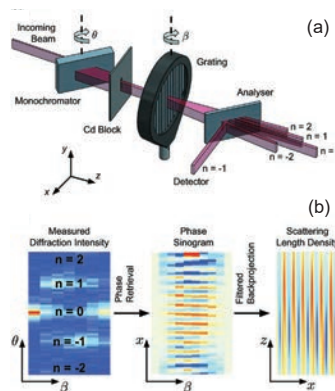


FIGURE 1: (a) The experimental setup. A neutron beam passes through a monochromator crystal, then through a phase grating whose effect is measured by an analyzer crystal and a ³He proportional counter. (b) From the measured diffraction intensity, the position-space phase is retrieved, providing the phase sinogram, which is then used to reconstruct the scattering-length density of the grating.

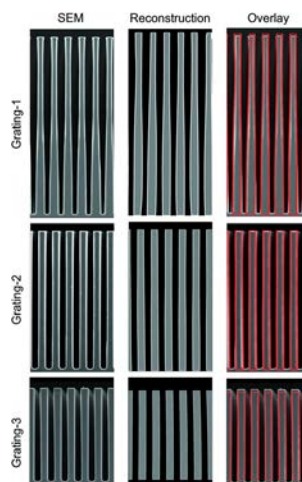


FIGURE 2: SEM micrographs of the phase gratings (left column) compared with their neutron tomographic reconstructions (middle column). Also shown is an overlay (right column) of the outline of the reconstruction over the SEM. The walls of Grating-2 and Grating-3 are shown to be very straight, while the sloped walls of Grating-1 appear in both the SEM micrograph and the reconstruction. Edge highlights are added to the reconstructions for clarity.

References

- [1] B. Heacock et al., *IUCrJ* **7**, 893 (2020).
- [2] D. A. Pushin et al., *Phys. Rev. A*, **95**, 043637 (2017).
- [3] D. Sarenac et al., *Phys. Rev. Lett.* **120**, 113201 (2018).

¹ North Carolina State University, Raleigh, NC 27695
² Triangle Universities Nuclear Laboratory, Durham, NC 27708
³ Institute for Quantum Computing, University of Waterloo, Waterloo, Ontario, Canada N2L3G1
⁴ Department of Physics, University of Waterloo, Waterloo, Ontario, Canada N2L3G1
⁵ Department of Chemistry, University of Waterloo, Waterloo, Ontario, Canada N2L3G1
⁶ National Institute of Standards and Technology, Gaithersburg, MD 20899
⁷ Biophysics and Biochemistry Center, National Heart, Lung and Blood Institute, National Institutes of Health, Bethesda, MD 20892

Design of a neutron microscope based on Wolter mirrors

D. S. Hussey,¹ M. Abir,^{2,3} J. C. Cook,⁴ D. L. Jacobson,¹ J. M. LaManna,¹ K. Kilaru,^{5,6} B. D. Ramsey,⁵ B. Khaykovich²

We have designed a novel neutron microscope (Fig. 1) that is anticipated to achieve time and spatial resolution comparable to that of an early generation synchrotron X-ray imaging beamline [1]. The design is analogous to Hooke's microscope and is expected to realize 3 μm spatial resolution with a time resolution that is about 20,000 times faster than that of a conventional neutron imaging beamline.

For neutrons, the refractive index of materials is nearly one. Therefore, they are difficult to focus, as focal lengths are on the order of hundreds of meters. However, neutrons possess critical reflection angles that are large enough to create reflective, achromatic lenses with meter-long focal lengths. This was shown by the pioneering experiments of M. Gubarev and B. Khaykovich who demonstrated that one can apply X-ray telescope technology to create neutron image-forming mirrors [2, 3]. X-ray telescopes (and the neutron microscope) are based on Wolter optics, [4] which involve axisymmetric mirrors composed of two confocal conic sections (hyperbolas, parabolas, ellipses).

A neutron lens is attractive for neutron imaging for the same reason that a regular lens is for visible light. To obtain high spatial resolution images, one must use small apertures and place the sample as close to the neutron camera as possible. Apertures with diameters of a few millimeters strongly reduce the neutron flux, making it impractical to use geometric magnification to improve spatial resolution. A neutron microscope removes these limitations.

The neutron microscope that we have designed is composed of two Wolter optics; one serves as a condenser lens and the other as an objective lens. The condenser optic is similar to an X-ray telescope, where the first conic section is a parabola and the second section is a hyperbola. The condenser is comprised of 6 such shells with a total length of 600 mm and intersection radii (the radius where the two conic sections meet) that range from about 25 mm to 45 mm. This geometry focuses about 7% of the neutrons exiting the upgraded NG6 guide (80 mm x 60 mm) onto a sample area that is about 5 mm x 5 mm in size and 1000 mm downstream of the condenser. The objective optic has 5 nested mirror pairs that

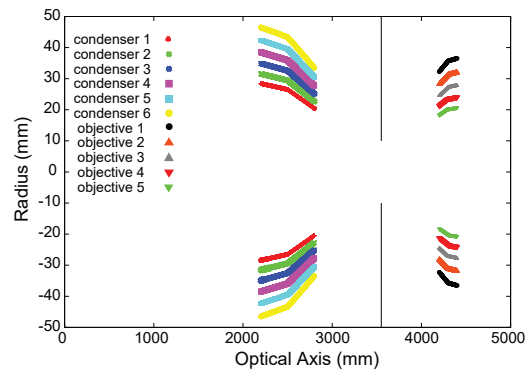


FIGURE 1: The design of the NIST neutron microscope based on Wolter mirrors shown in radial profile as a function of distance from the end of the neutron guide.

are made of an elliptical section and a hyperbolic section with a total length of 200 mm and intersection radii that range from about 20 mm to 35 mm. The objective lens is located 750 mm from the sample and magnifies the neutron image by a factor 10, so that the detector is 7500 mm downstream of the optic. The objective optic can focus approximately 10% of the flux from the condenser optic to the detector, resulting in an effective flux at the sample of about $10^{10} \text{ cm}^{-2} \text{ s}^{-1}$. The comparable conventional imaging setup for 3 μm spatial resolution would provide a flux of about $5 \times 10^5 \text{ cm}^{-2} \text{ s}^{-1}$. The NIST neutron microscope will thus be able to perform tomography at a spatial resolution of 3 μm with an acquisition time of order minutes [5].

References

- [1] D. S. Hussey, et al., Nucl. Instruments Methods Phys. Res. Sect. A Accel. Spectrometers, Detect. Assoc. Equip. **987**, 164813 (2021).
- [2] B. Khaykovich, et al., Nucl. Instruments Methods Phys. Res. Sect. A Accel. Spectrometers, Detect. Assoc. Equip. **631**, 98 (2011).
- [3] D. Liu, et al., Appl. Phys. Lett. **102**, (2013).
- [4] H. Wolter, Ann. Phys. **445**, 286 (1952).
- [5] P. Jorba, et al., J. Magn. Magn. Mater. **475**, 176 (2019).

¹ Physical Measurement Laboratory, National Institute of Standards and Technology, Gaithersburg, MD 20899

² Nuclear Reactor Laboratory, Massachusetts Institute of Technology, Cambridge, MA 02139

³ North Star Imaging (NSI), Rogers, MN 55374

⁴ NIST Center for Neutron Research, National Institute of Standards and Technology, Gaithersburg, MD 20899

⁵ NASA Marshall Space Flight Center, Huntsville, AL 35805

⁶ Cymer, San Diego, CA 92127

New measurement capability enabled by a linear chopper for cold neutron beam activation analysis

D. J. Turkoglu¹ and H. H. Chen-Mayer²

When a neutron is absorbed by a nucleus, it gives off gamma rays, either immediately (prompt gamma), or following a certain decay half-life. The energies of these gamma rays are characteristic of the absorbing nucleus, and therefore useful for multi-elemental compositional analysis. Instrumental neutron activation analysis (INAA), the spectroscopy which is used to measure these gamma rays, has been a definitive technique for the certification of Standard Reference Material (SRM) for nearly six decades. INAA is conventionally performed by shooting samples into the reactor core to be irradiated. The irradiated samples are then retrieved to a remote laboratory for data acquisition. This process involves sample transfer, which limits the observable decays to those which are no shorter than a few minutes. To overcome this limitation, we have developed a programmable chopper to perform in-beam INAA, lowering the measurable half-life of short-lived radionuclides from a few minutes to below 100 ms.

To enable these measurements, a chopper has been installed at the prompt gamma activation analysis (PGAA) station located at NGD. This chopper allows us to achieve irradiation and decay counting in predetermined duty cycles with prompt gamma emission eliminated when the neutron beam is turned off, leaving only the decay gamma rays. This process can be repeated for hours resulting in thousands of precisely timed cycles to boost counting statistics. Thus, the chopper allows us to measure prompt and/or delayed gammas in the same geometry with the same detector.

Figure 1 illustrates the chopper design and installation. The chopper consists of a ¹⁰B-Al shutter driven by an electrical linear motor for precise positional timing. The chopper transit time depends on the distance it traverses, designed to be 4 cm for the full coverage of the 2 cm neutron guide, including the acceleration and deceleration zones (Fig. 1d). Therefore, the neutron beam is turned on or off in less than 20 ms, or 40 ms per cycle. The system's dwell time can be programmed for each chopper position, thereby delivering periodic pulses of neutrons to the target sample, creating "on-off" phases with any desired duty cycle. During the beam-off phase, only the decay gamma rays are emitted, and the signal acquisition begins after the chopper transition time (40 ms), a capability currently relying on ultra-fast transport systems available in few facilities worldwide. Additionally, compared to

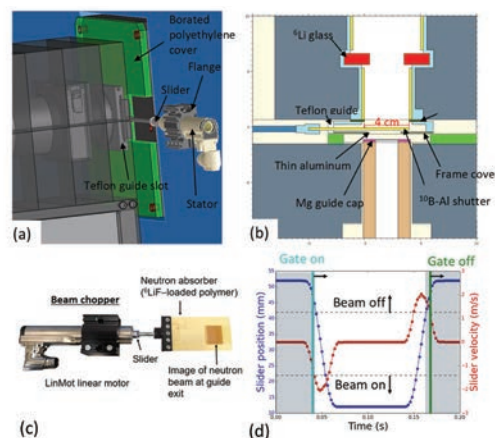


FIGURE 1: (a) A 3-D engineering drawing of the linear shutter inserted through the guide slot. (b) Geometry model for Monte Carlo simulation. (c) Photograph of the fast shutter. The ⁶LiF polymer shutter bears the imprint of the size of the neutron beam. The ⁶LiF polymer was subsequently replaced by ¹⁰B-Al to reduce fast neutron productions. (d) Measured slider position and velocity during shutter transitions with indicated gate signals for sorting collected data.

rotational disk choppers which have fixed duty cycles, a linear chopper can be programmed to have arbitrary on-off ratios according to measurement needs. Test samples containing ⁷⁷Se ($T_{1/2} = 17.36$ s) and ^{175m}Yb ($T_{1/2} = 68.2$ ms) were used to derive a calibration curve for the sensitivity of detection under different chopper settings [1]. Theoretical calculations based on the experimental parameters were in good agreement with observed results. In addition, this measurement system enables separation of overlapping energy peaks of different decay half-lives: the decay events can be recorded in the form of time-stamped list mode data. Another test sample containing ^{175m}Yb ($T_{1/2} = 0.0682$ s) and ^{165m}Dy ($T_{1/2} = 75.4$ s), both have a decay peak close to 515 keV and cannot be resolved even with the high-resolution HPGe detector in the normal histogram mode but can be time-resolved by their half-lives in the list mode. Measurements of elements of interest with a short half-lives are anticipated in the future.

Reference

- [1] D. J. Turkoglu; H. H. Chen-Mayer, IEEE Transactions on Nuclear Science, DOI: 10.1109/TNS.2021.3080682.

¹ NIST Center for Neutron Research, National Institute of Standards and Technology, Gaithersburg, MD 20899 (Current address: USNC-Tech, Seattle, WA 98199)
² Material Measurement Laboratory, National Institute of Standards and Technology, Gaithersburg, MD 20899

Neutron Source Operations

The Reactor Incident of February 3, 2021

On February 3, 2021, shortly after commencing a normal reactor startup, the reactor which provides neutrons to the NCNR, experienced a rapid power drop. This was followed by one of the radiation monitors in the building stack exceeding its set point, causing the reactor to automatically shut-down. During the event all reactor safety systems functioned as designed and at no point was there any danger to either NCNR workers or the public.

Shortly afterwards we engaged a nuclear services contractor to investigate the reactor core with special radiation hardened underwater cameras. It was quickly established that one of the fuel elements had not been properly latched in place allowing it to depart from the hole in the lower grid plate through which cooling water is provided to the fuel element (Figure 1). Based on the observations, it was also concluded that the element had been damaged through significant overheating. This was reported to the U.S. Nuclear Regulatory Commission (NRC).

A radiation survey of the reactor plant indicated that the entire primary coolant loop of the reactor had become contaminated, with dose rates peaking in areas where the flow is low, or eddy-like, such as the blind extensions of plumbing manifolds.

After the technical diagnosis was completed, all fuel elements, except the damaged one and its two immediate neighbors, were removed from the core and placed in the storage pool. In addition, a tool was inserted that allowed the hole belonging to the damaged element to be covered from the reactor top (Figure 2). Then, after cleaning debris off the bottom of the damaged element, we were able to transport it to the storage pool, where it now resides in the vicinity of an oversized ion exchange system, which makes sure that any leaching of radioactive ions into the storage pool are removed right away.

It is important to note that no damage to other reactor core components such as the lower grid plate was observed. Further cleanup of the system will consist of removing debris from the upper and lower grid plates and then filtering the primary system using custom designed filters to be placed in the core, which – from the outside – look just like a fuel element. Then, using the main primary pumps, we will try to gather the primary system debris into the filters.

Shortly after the event, a technical working group was convened to identify the root causes of the event. In May, the NCNR reactor oversight committee, the Safety Evaluation Committee, formed a subcommittee to review the root causes identified by the technical working group and to evaluate the NCNR response to the event. Both groups found that there were inadequacies in training, procedure compliance, refueling equipment, and management oversight and this was also reported to NRC.

In response to these findings, nineteen Corrective Action and Reactor Recovery Items (CARRI) teams were formed consisting of staff from Reactor Operations and Engineering, NCNR Health Physics, and NCNR Safety. These teams developed and began to implement corrective actions and recommended program improvements. In addition to the above reviews, NIST management has requested a NIST-wide review of the incident by external consultants.

The CARRI teams are shepherding a fundamental change in the way we approach operating and maintaining the reactor, strengthening the safety culture throughout the organization. Corrective actions are ongoing, with the goal to restart the reactor as soon as NRC permits, and we determine that the reactor and staff are ready for restart.

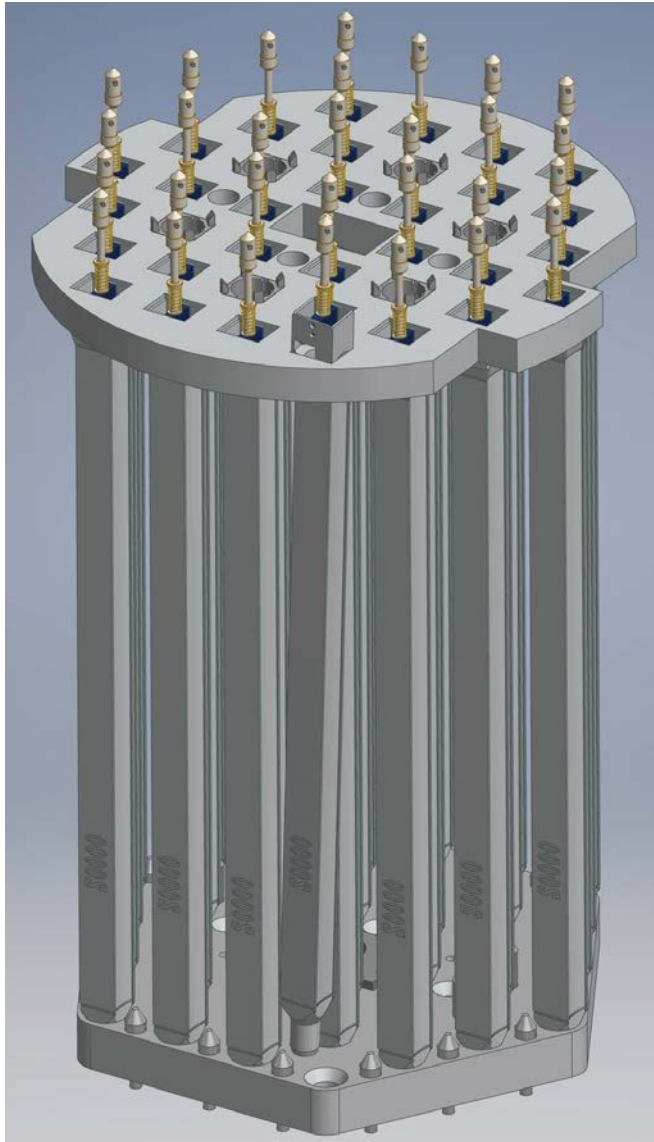


FIGURE 1: The damaged element in the as-found position. The element is parked against its nearest neighbors and the hole in the lower grid plate is uncovered. Obviously, no flow through the damaged element is possible in this configuration.

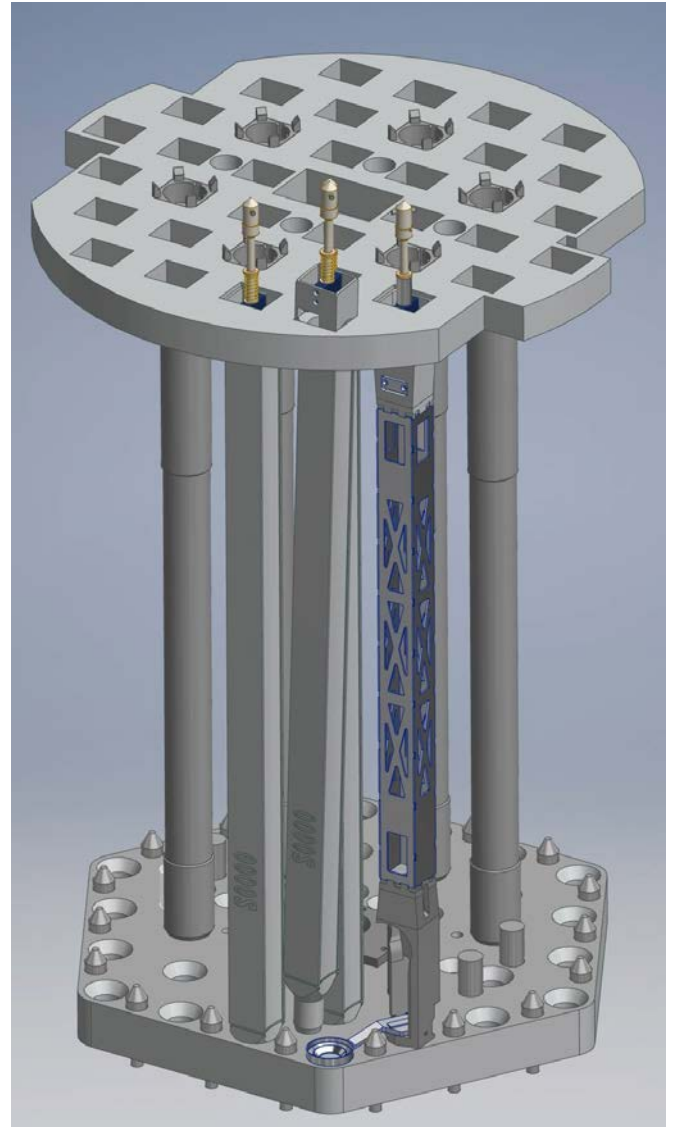


FIGURE 2: The damaged element in the as-found position with its nearest neighbors still in place. The hole in the lower grid plate is covered by a tool that has been inserted in the third nearest neighbor position.

Facility Developments 2021

Progress on D₂ Cold Source Outage Work

An extended reactor outage is planned for 2023 to replace the current "Unit 2" liquid hydrogen cold source with a new liquid deuterium cold source. This upgraded moderator is a significant gain for the scientific community, as it will boost the data rate of guide hall instruments by an average factor of 1.6. Construction of the new D₂ cold source is currently in progress. Two prototype cold source cryostats are being built to validate the design.



FIGURE 1: Deuterium cold source cryostat prototype fabrication.

Preparations are underway for the handling of Unit 2, which will be challenging due to significant neutron activation. A conceptual procedure has been completed for removal, transport, and storage of this element that is consistent with both engineering and radiation safety requirements. In addition, a detailed mockup of the reactor face has been constructed, that will allow staff to "cold practice" installation of the new D₂ cold

source, and other outage evolutions involving activated material. A new helium/deuterium condenser heat exchanger has been delivered to the NCNR and is being prepared for fit-up to the reactor face mockup. The cold source refrigerator has already been replaced with a 7 kW model that will support the new source, but the old 3.5 kW refrigerator cold box still needs to be removed from the confinement building. The cold box has been weighed, and a plan has been developed for its removal.

This outage will be further exploited by upgrading neutron guides NG5, NG6, and NG7, as well as replacing the in-pile optics serving NG1-NG4. The current ⁵⁸Ni-coated guides 5-7, which are 30 years old, will be replaced with modern supermirror guides, providing significant flux gains for all instruments served by these guides. Progress on the guide upgrades over the past year has primarily involved design, fabrication, and acquisition of key components. Figure 2 shows new elements that will be installed within the confinement building. Fabrication of the in-pile helium jackets that will go into the reactor face at CTC and CTE is complete, and testing and alignment is underway. The design is complete, and contracts have been awarded for fabrication of the 5-7 common casing, the pre-shutter vacuum jackets, primary shutters, and post-shutter penetration vacuum jackets.

CHRNS vSANS High Resolution Detector Upgrade

The CHRNS vSANS is designed to use multiple detectors to simultaneously map out different regions of reciprocal space. The instrument's original high-resolution detector used for the lowest wavevector transfers was essentially a neutron camera. Early operation showed that this technology was not ideally suited to the task, as readout calibration and associated artifacts were a consistent issue. We have developed a plan to replace this camera with a more conventional, high resolution 20 cm x 20 cm ³He area detector that is already available in-house. The manufacturer has provided a design for retrofitting the detector to operate in vacuo (*i.e.* in a SANS vessel), and will optimize the gas balance for vSANS resolution needs. Installation is planned for early 2022.

Next Generation Timestamping

CHRNS is supporting an Initiative for Non-Equilibrium Structure of Materials (see the CHRNS Section, p.57) that will enable more sophisticated time resolved neutron measurements at the NCNR. This effort will utilize the

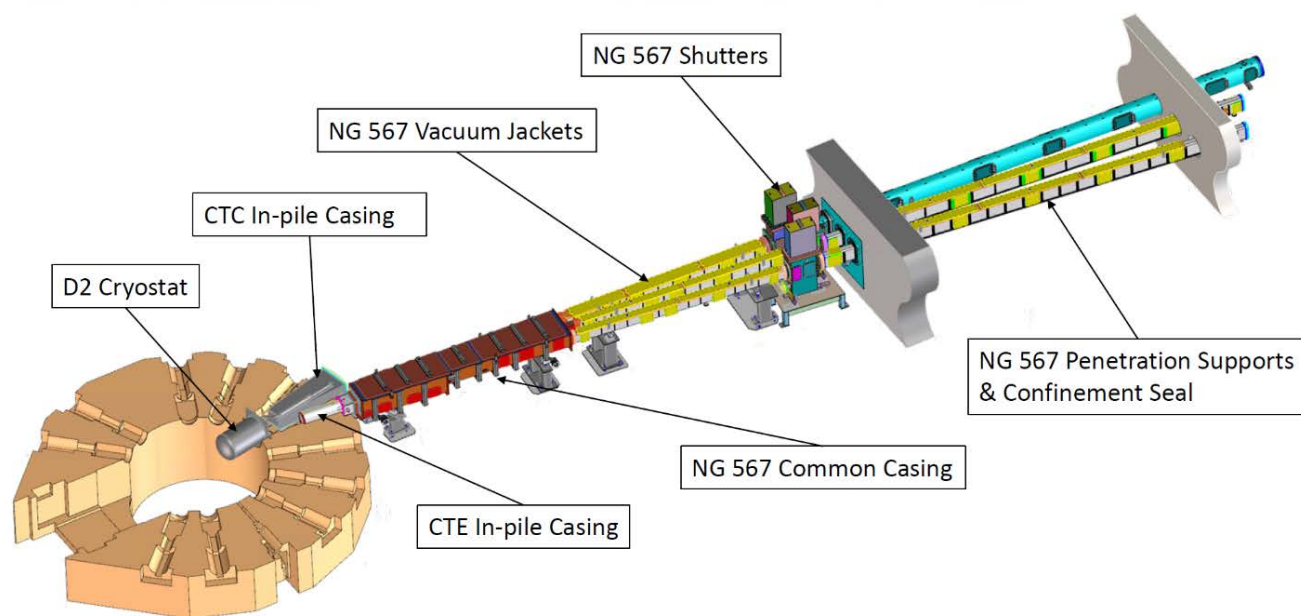


FIGURE 2: Guide elements that will be replaced during the 2023 outage.

ADARA time streaming protocol developed at the Spallation Neutron Source. ADARA describes a network packet structure that associates neutron events and metadata with an absolute timestamp using the Precision Time Protocol (PTP) (IEEE 1588). This protocol will be used in new data acquisition electronics that NCNR is procuring to timestamp neutron events for three CHRNS instrument - vSANS, CANDOR, and MACS.

The refactored version of the NCNR VIPER motor control application will produce timestamped motor position metadata using the same absolute times. Additionally, Labview virtual instrument libraries have been written to enable sample environment equipment to generate timestamped values of process variables (temperature, magnetic field, etc).

Motor Control Upgrades

The system software for VIPER, the NCNR's standard motor control system, has been massively reworked. The old program was a large TCL script, and is no longer sufficient in terms of speed or stability for newer instruments with large numbers of controlled axes of motion. The new program is a compiled application written using the cross-platform Qt toolkit. With this rewrite, not only does VIPER gain speed and robustness of operation, but it also accommodates new features such as the ability to produce IEEE 1588 absolute timestamps of motor position data.

We have also concluded a program of upgrades to stepper motor drivers facility-wide. The new drivers consume less current and subject the motors and stages to less associated heating than the previous generation.

BT-8 Residual Stress Diffractometer Upgrade

A multi-year project to overhaul the BT-8 Residual Stress Diffractometer is now complete. Earlier work included implementation of a new area detector, and a 3-wavelength monochromator that improved the data rate by a factor of 20, and the Octo-Strain and shearing load frames that enable the study of multi-axial deformation. The final element was the recent installation of a new instrument table, goniometer, and detector arm that rolls on a metal track atop a new epoxy floor. This assembly, referred to as the "bucket" is shown in Figure 3.

The robust new sample table can handle a load of up to 250 kg, necessary to accommodate very large samples, or the Octo-Strain load frame. The new detector housing features a much bigger opening to fully utilize the new area detector, and it includes a modular snout and slit system to allow for a wide range of sample sizes and experiment setups. The bucket also has a fixture for a dedicated laser scanner arm used to assist with sample alignment.

Data Acquisition Software

Features and upgrades continue to be made to the New Instrument Control Environment (NICE), as the software is adopted by more instruments across the NCNR. Most recently, NICE has been deployed on the CHRNS MACS spectrometer. Both high-level and low-level control of motors and other hardware have been successfully tested. NICE is expected to be running on MACS full-time in early 2022. The NICE sample alignment system has been replaced with a more advanced version. The new system streamlines the common way most samples are aligned on triple-axis spectrometers such as BT-7

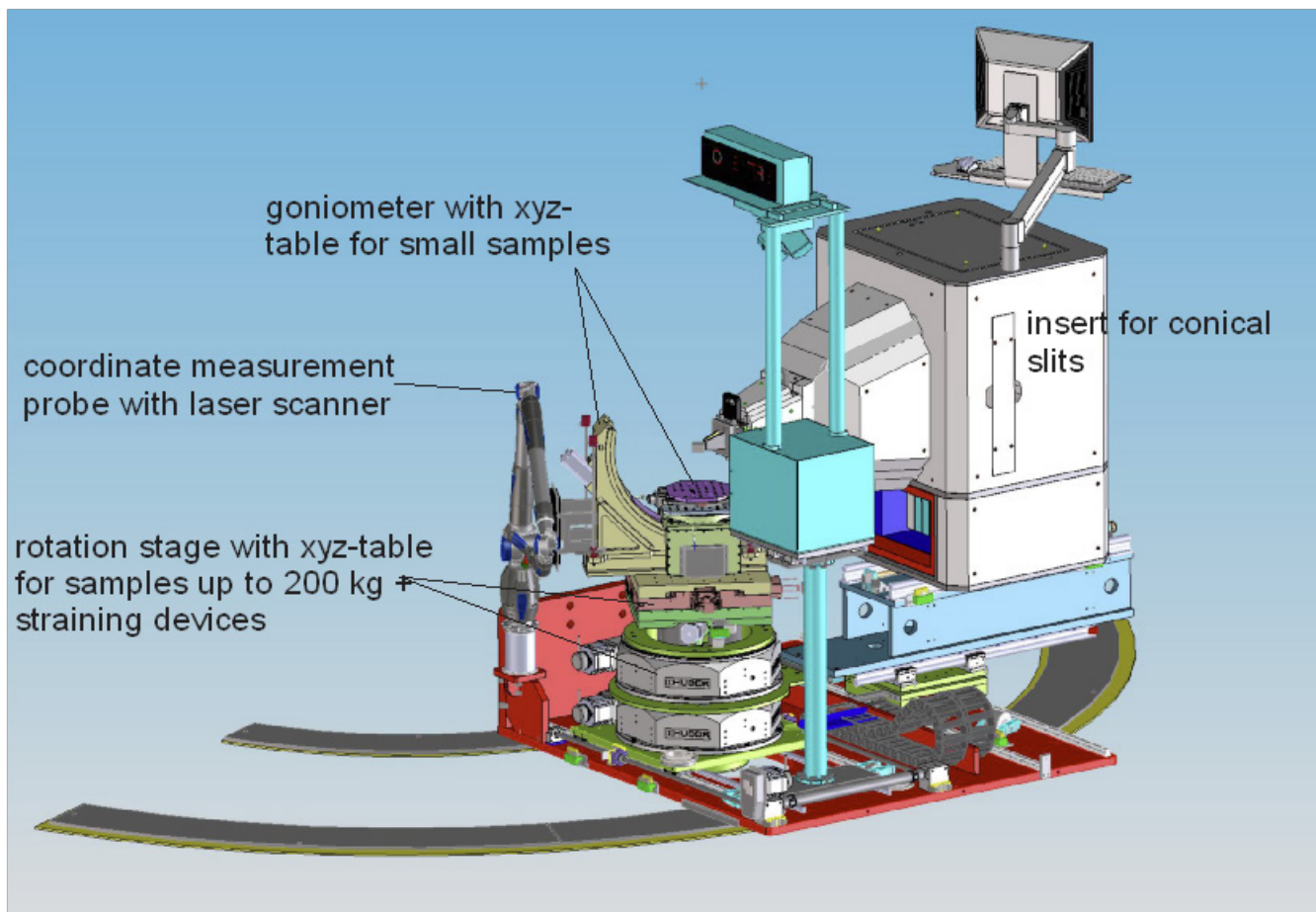


FIGURE 3: New BT-8 "Bucket."

and MACS. This code has been successfully tested, without neutrons, by simulating a virtual crystal sample on both of those instruments. CHRNS is supporting ongoing work to update NICE with metadata features consistent with the FAIR (findability, accessibility, interoperability, and reusability) principles of scientific data management. Initial features have been successfully tested and implemented.

10 m Sans Detector Upgrade

A new area detector has been installed at the *n*Soft 10 m SANS instrument. Where the old detector was a monolithic multiwire

proportional counter, the new detector is an array of linear position sensitive proportional counters grouped in modular units of 8 tubes. 14 such modules are laid out to form an active area of 1 m × 1.1 m. The sensitivity is 75% for 5 Å (3.27 meV) neutrons. The event discrimination and position encoding electronics are located on each module so the count rate over the entire detector is specified to exceed two million counts per second. Additionally, should any tubes experience a fault, the modules may be rearranged on the frame without removing the entire detector from service.

Serving the Science and Technology Community

The mission of the NIST Center for Neutron Research is to assure the availability of neutron measurement capabilities to meet the needs of U.S. researchers from industry, academia, and other U.S. government agencies. To carry out this mission, the NCNR uses several different mechanisms to work with participants from outside NIST, including a competitive proposal process, instrument partnerships, and collaborative research with NIST.

Proposal System

Most of the beam time on NCNR instruments is made available through a competitive, peer-review CHRNS proposal process. The NCNR issues calls for proposals approximately twice a year. Proposals are reviewed at several different levels. First, expert external referees evaluate each proposal on merit and provide us with written comments and ratings. This is a very thorough process where several different referees review each proposal. Second, the proposals are evaluated on technical feasibility and safety by NCNR staff. Third, we convene our Beam Time Allocation Committee (BTAC) to assess the reviews and to allocate the available instrument time. Using the results of the external peer review and their own judgment, the BTAC makes recommendations to the NCNR Director on the amount of beam time to allocate to each approved experiment. Approved experiments are scheduled by NCNR staff members in consultation with the experimenters.

The current BTAC members are:

- Pinar Akcora (Stevens Institute of Technology)
- Andrew Allen (NIST Materials Measurement Laboratory)
- Jeffrey Allen (Michigan Technological University)
- Collin Broholm (The Johns Hopkins University)
- Leslie Butler (Louisiana State University)
- Sara Callori (California State University San Bernardino)
- Mark Dadmun (University of Tennessee)
- Kendra Elk (Purdue University)
- Kushol Gupta (University of Pennsylvania)
- John Heron (University of Michigan)
- Michael Hore (Case Western Reserve University)
- Hubert King (ExxonMobil - Retired)
- Valery Kiryukhin (Rutgers University)
- Kai Liu (Georgetown University)
- Martin Mourigal (Georgia Institute of Technology)
- James Neilson (Colorado State University)
- Olivier Soubias (National Institute of Health)
- Stephen Wilson (University of California Santa Barbara)

Partnerships

The NCNR may form partnerships with other institutions to fund the development and operation of selected instruments. Partnerships are negotiated for a fixed period and may be renewed if there is mutual interest and a continued need. These partnerships have proven to be an important and effective way to expand the research community's access to NCNR capabilities.

Collaboration with NIST

Some time on all instruments is available to NIST staff in support of our mission. This time is used to work on NIST research needs, instrument development, and promoting the widespread use of neutron measurements in important research areas, particularly by new users. As a result of these objectives, a significant fraction of the time available to NIST staff is used collaboratively by external users, who often take the lead in the research. Access through such collaborations is managed through written beam time requests. In contrast to proposals, beam time requests are reviewed and approved internally by NCNR staff. We encourage users interested in exploring collaborative research opportunities to contact an appropriate NCNR staff member.

Research Participation and Productivity

The NCNR continued its strong record of serving the U.S. research community this year. Over the 2021 reporting year, the NCNR served 2576 researchers. (Research participants include users who come to the NCNR to use the facility as well as active collaborators, including co-proposers of approved experiments, and co-authors of publications resulting from work performed at the NCNR.) As the number of participants has grown, the number of publications per year has also increased.

2019 NCNR Proposal Program

In response to the last two calls for proposals (calls 40 and 41) for instrument time, we received more than 723 proposals, of which 396 were approved and received beam time. The following table shows the statistics for several instrument classes. The oversubscription, *i.e.*, the ratio of days requested on all proposals to the days available, was 2.3 on average. Proposal demand has grown substantially since the NCNR first began accepting proposals in

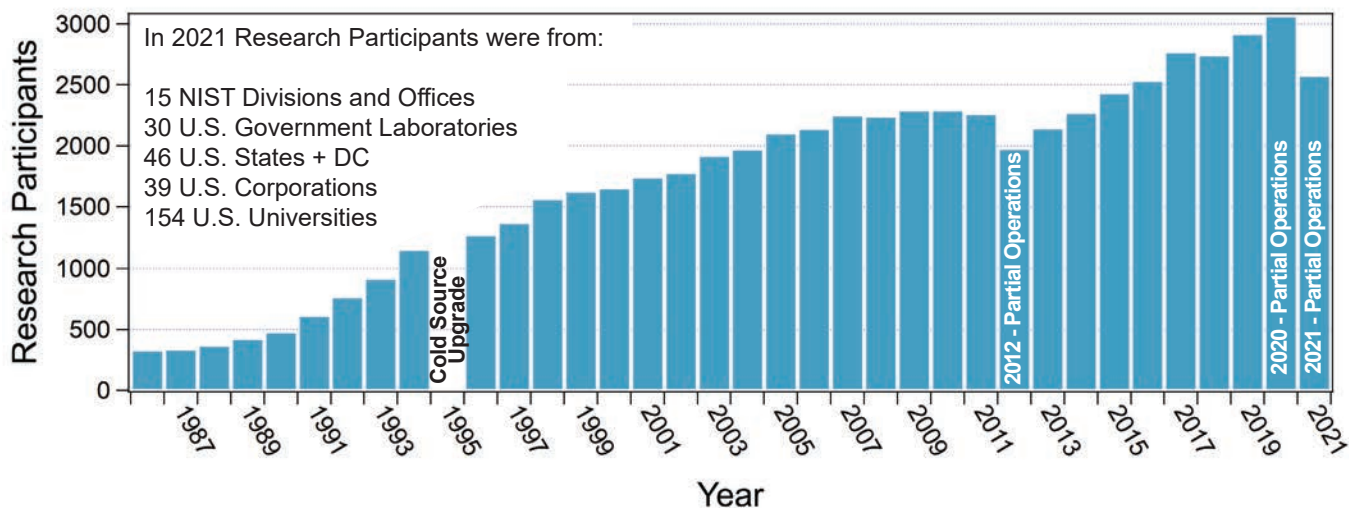


FIGURE 1: Research participants at the NCNR from 1986 to 2021. Fewer operational days in 2020 and 2021 due to COVID-19 closures and an unplanned shutdown resulted in reduced numbers of research participants.

1991. Note that the experiments for call 41 will be run immediately following the current shutdown. (Note that Imaging results from call 41 are not included in the totals.)

Instrument class	Proposals	Days requested	Days allocated
SANS	274	999	487
Reflectometers	100	648	288
Spectrometers	297	1938	757
Diffraction	32	104	57
Imaging	20	92	38
Total	723	3781	1627

Users Group

The NCNR Users Group (NUG) provides an independent forum for all facility users to raise issues to NCNR management, working through its executive officers to carry out this function. All members of the Executive Committee (EC) are elected by NCNR users. The current members of the NUG Executive Committee are Claire White (Chair, Princeton University), Michael Hore (Vice Chair, Case Western University), John Riley (The Dow Chemical Company), Malin Zackrisson Oskolkova (Novo Nordisk), Nairiti Sinha (Student/Postdoc Member, University of California Santa Barbara), and Stephen Wilson (CHRNS Liaison, University of California Santa Barbara).

The EC regularly solicits user feedback via a variety of means. The User Group held a well-attended meeting at the virtual American Conference on Neutron Scattering (ACNS) in July 2020 and plans to have another meeting at the ACNS in 2022. The EC also administers a brief email survey that is sent to users approximately one week after the completion of their

experiment. Issues identified by the EC are regularly discussed with the NCNR and CHRNS management teams with a focus on resolving those requiring immediate action. The EC also conducted a comprehensive user survey in the winter of 2020. There were more than 160 responses, the majority of whom are CHRNS users. The results from the 2020 survey are posted on the NUG website (<https://ceem.indiana.edu/lens/nug/nug.php>). Working closely with NUG, the NCNR and CHRNS management teams is in the process of developing a comprehensive response/action plan to the 2020 survey designed to make the user experience more productive and enjoyable (Refer to [https://ceem.indiana.edu/lens/nug/NCNRResponse to 2020survey Preamble%20final.pdf](https://ceem.indiana.edu/lens/nug/NCNRResponse%20to%2020survey%20Preamble%20final.pdf)).

Panel of Assessment

The major organizational components of NIST are evaluated annually for quality and effectiveness by the National Research Council (NRC), the principal operating agency of both the National Academy of Sciences and the National Academy of Engineering. A panel appointed by the NRC convened virtually on July 20 - 22, 2021. The panel members included Cherry Murray (University of Arizona, Harvard University - emerita, chair), Simon Billinge (Columbia University, Brookhaven National Laboratory), Olivia Graeve (University of California San Diego), Andrew Harrison (Diamond Light Source), Andrew Jackson (European Spallation Source), Dale Klein (University of Texas at Austin), Tonya Kuhl (University of California, Davis), Emilia Morosan (Rice University), Ann Salamone (Rochal Industries), Andrew Stephen (Frederick National Laboratory for Cancer Research), and Michael Tsapatsis (Johns Hopkins University). The report from the 2018 Panel of Assessment entitled "An Assessment of the National Institute of Standards and Technology Center for Neutron Research: Fiscal Year 2018" is available at <https://www.nap.edu/catalog/25282/an-assessment-of-the-center-for-neutron-research-at-the-national-institute-of-standards-and-technology>.

The Center for High Resolution Neutron Scattering (CHRNS)

CHRNS is a national user facility that is jointly funded by the National Science Foundation and the NCNR. Its primary goal is to maximize access to state-of-the-art neutron scattering instrumentation for the research community. It operates five neutron scattering instruments at the NCNR, enabling users from around the nation to observe dynamical phenomena involving energies from ≈ 30 neV to ≈ 10 meV, and to obtain structural information on length scales from ≈ 0.1 nm to ≈ 10 μ m. A more detailed account of CHRNS activities may be found on pp 57 of this report.

Partnerships for Specific Instruments

NG-7 SANS Consortium

A consortium that includes NIST, the ExxonMobil Research and Engineering Company, and the Industrial Partnership for Research in Interfacial and Materials Engineering (IPRIME) led by the University of Minnesota, operates, maintains, and conducts research at the 30m SANS instrument located on NG7. Twenty-five percent of the beam time on this instrument is allocated to the general scientific community through the NCNR's proposal system. Consortium members conduct independent research programs primarily in the area of large-scale structure in soft matter. For example, ExxonMobil has used this instrument to deepen their understanding of the underlying nature of ExxonMobil's products and processes, especially in the fields of polymers, complex fluids, and petroleum mixtures.

The nSoft Consortium

Formed in August 2012, the nSoft Consortium allows member companies to participate with NIST in the development of advanced measurements of materials and manufacturing processes and develop their own expertise in state-of-the-art measurement technologies to include in their analytical research programs. nSoft develops new neutron-based measurement science for manufacturers of soft materials including plastics, composites, protein solutions, surfactants, and colloidal fluids. Members receive access to leading expertise and training support in neutron technology and soft materials science at NIST. Contact: Ron Jones, nSoft Director, rjones@nist.gov, 301-975-4624.

NIST / General Motors – Neutron Imaging

An ongoing partnership and collaboration between General Motors and NIST, which also includes Honda Motors through GM's partnership with Honda, continues to yield exciting results using neutron imaging. Neutron imaging has been employed to visualize the operation of fuel cells for automotive vehicle applications. Neutron imaging is an ideal method for visualizing hydrogen, the fuel of electric vehicle engines. These unique, fundamental measurements provide valuable material characterizations that will help improve

the performance, increase the reliability, and reduce the time to market introduction of the next generation electric car engines. 25% of the time on the BT-2 Neutron Imaging Facility is made available to the general scientific community through peer-reviewed proposals.

Interagency Collaborations

The Smithsonian Institution's Nuclear Laboratory for Archaeological Research is part of the Anthropology Department at the National Museum of Natural History. It has had a longstanding and productive partnership with the NCNR, during which time it has chemically analyzed over 43,100 archaeological artifacts by Instrumental Neutron Activation Analysis (INAA), drawing extensively on the collections of the Smithsonian, as well as on those of many other institutions in this country and abroad. Such chemical analyses provide a means of linking these diverse collections together in order to study continuity and change involved in the production of ceramic and other artifacts.

DENIM

The Smithsonian Institution's Nuclear Laboratory for Archaeological Research is part of the Anthropology Department at the National Museum of Natural History. It has had a longstanding and productive partnership with the NCNR, during which time it has chemically analyzed over 43,100 archaeological artifacts by Instrumental Neutron Activation Analysis (INAA), drawing extensively on the collections of the Smithsonian, as well as on those of many other institutions in this country and abroad. Such chemical analyses provide a means of linking these diverse collections together to study continuity and change involved in the production of ceramic and other artifacts.

The Center for Food Safety and Applied Nutrition, U.S. Food and Drug Administration (FDA), maintains laboratory facilities at the NCNR providing agency-wide analytical support for food safety and food defense programs. Neutron activation and low-level gamma-ray detection techniques yield multi-element and radiological information about foods and related materials and provide a metrological foundation for FDA's field investigations and for radiological emergency response planning.

The Center for High Resolution Neutron Scattering (CHRNS)

The Center for High Resolution Neutron Scattering (<https://www.nist.gov/ncnr/chrns>) is a national user facility jointly funded by the National Science Foundation through its Division of Materials Research (grant number DMR-2010792) and by NIST. The CHRNS agreement was renewed for five years beginning on September 1, 2020. The mission of CHRNS is fourfold: (i) to develop and operate neutron scattering instrumentation, with broad application in materials research, for use by the general scientific community; (ii) to promote the effective use of the CHRNS instruments by having an identifiable staff whose primary function is to assist users; (iii) to conduct research that advances the capabilities and utilization of CHRNS facilities; and (iv) to contribute to the development of human resources through educational and outreach efforts. Simply put, CHRNS primary aim is "Maximizing access for the scientific community to transformative neutron scattering instrumentation." A 2½ minute video, *Getting Great Data with CHRNS* (https://www.ncnr.nist.gov/staff/dimeo/CHRNS_Animation_Final.mp4), highlights and summarizes CHRNS' focus on advancing neutron scattering measurement capabilities and its prominent role in expanding, educating, and diversifying the community of researchers who use neutron methods.

The scientific community provides essential input through a variety of mechanisms including post-experiment feedback and user surveys, the most recent of which was administered by the NCNR User Group Executive Committee (EC) in the winter of 2021. The EC also led a well-attended discussion for neutron users at the recent virtual American Conference on Neutron Scattering (ACNS) held on July 13-16, 2020. Another meeting of the User Group is anticipated to be held during the next ACNS meeting on June 5 – 9, 2022 at the University of Colorado Boulder. Users are also encouraged to provide input by directly contacting the CHRNS Director, Associate Director, NCNR Director, and/or members of the EC.

Initiative for Non-Equilibrium Structure of Materials

As part of the current agreement, CHRNS is pursuing a new initiative that aims to provide the scientific community powerful new tools for probing materials out of equilibrium. The goals of the program are to enhance the nation's capabilities for using neutrons to study the time evolution of materials *in operando*, under processing conditions, *etc.*, such as the charge and discharge cycles of batteries, the non-equilibrium structures of complex fluids under shear,

the kinetics of reactions, and the formation of biomolecular complexes.

Specifically, CHRNS is in the process of implementing a systematic methodology for the absolute time-stamping of instrument and sample environment data. The aim is to couple the event-mode scattering data, collected with the NICE data acquisition software, with new sample environment capabilities (such as stopped-flow mixing) that are integrated with the same master clock. Since this initiative will also produce complex data sets that can be explored during and after the experiments, CHRNS is developing the data structures, hardware, and software required for facile manipulation and analysis of the data.

During to the unplanned reactor shutdown, CHRNS staff has made significant progress on advancing this project toward its goals. To date, detailed computer network diagrams have been developed, and some hardware procurements have been submitted, with several computer systems already delivered. A proof-of-principle stopped-flow apparatus with ≈ 3 second time resolution has been designed and constructed for pilot measurements on vSANS. Preliminary visualization software has also been written for vSANS where ranges of relative times can be summed/histogrammed easily with a mouse click and drag, with automatic handling of data fetching and file-naming. Using a commercial automatic pipetting device, colleagues in the *nSoft* consortium have developed a robot system to for micellar multi-phase boundary determinations and are currently working on integrating AI algorithms for automatic measurements. For hard matter applications, MACS is close to having NICE deployed for data acquisition and the MSlice reduction software within the DAVE package has already been upgraded to read neutron event data from the future data acquisition hardware. The eventual goal is to enable a continuous data collection mode for data accumulation that will significantly reduce data acquisition times.

An additional aim of CHRNS is to expand the scope of the data management within the context of FAIR principles. These principles emphasize that data should be Findable, Accessible, Interoperable and Reusable to increase their value to the scientific community. The current policies for data management at the NCNR reflect a long-standing commitment to open data principles. Specifically, the data are created immediately and are permanently accessible

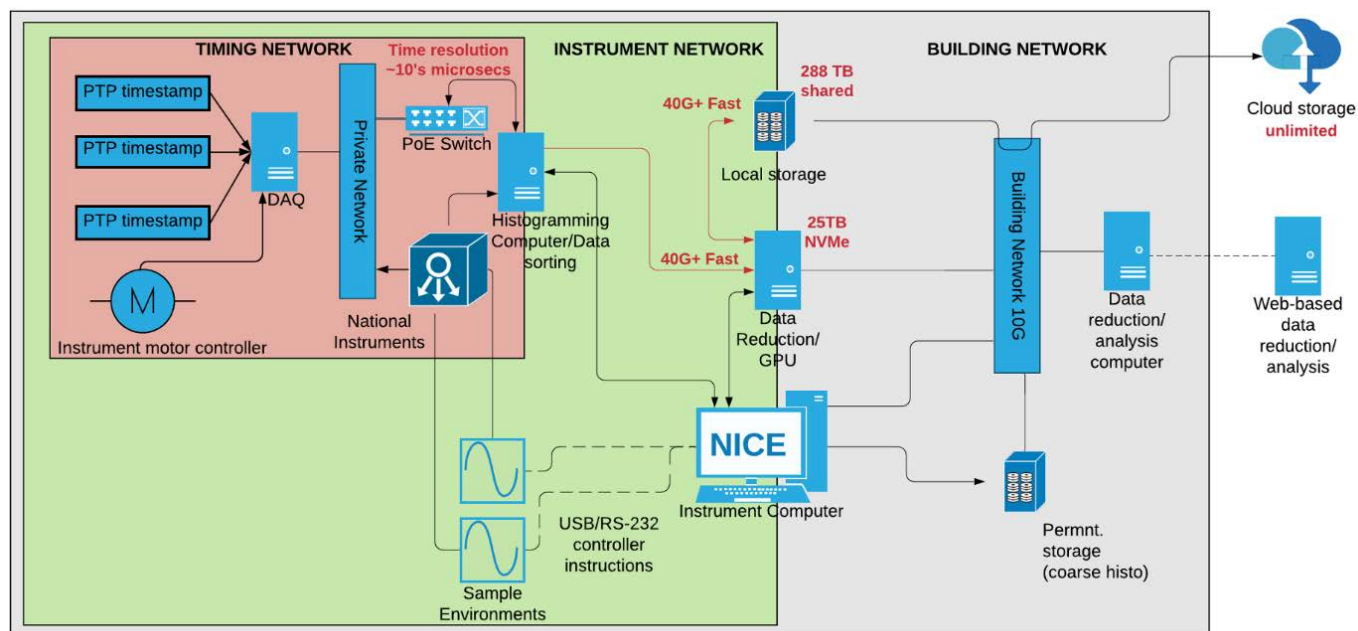


FIGURE 1: Networking diagram for time-resolved neutron scattering capabilities for CHRNS. The CHRNS instrument network has a sub-network dedicated to the time-stamped data acquisition and is self-contained to allow for robust instrument operations independent of the NCR building network.

(with limited exceptions) from an external repository. As an extension of these policies, short term goals of this effort include generation of a permanent DOI identifier for CHRNS raw data/metadata and support for ORCID identifiers. Improvements are planned for metadata capture and searchability, as well as for implementing standard, traceable workflows for data reduction with automatic handling of classifications between backgrounds, empty cells, and data etc. The time-dependent measurements should benefit from these FAIR data management efforts as they are anticipated to generate a large volume of data.

Scattering Instruments

From July through December of 2020, CHRNS provided robust user operations on the following premier neutron scattering instruments: a backscattering spectrometer (HFBS), the Multi-Axis Crystal Spectrometer (MACS), a neutron spin echo (NSE) spectrometer, and a very small angle neutron scattering instrument (vSANS). In addition, CHRNS supported the launch of an innovative white beam neutron reflectometer (CANDOR) with a unique multiplexing detector bank. An ultra-small angle neutron scattering instrument (uSANS) was phased out in the fall of 2020 as CANDOR completed its commissioning phase. Combined, CHRNS instruments can provide structural information on a length scale of 0.1 nm to ≈ 3 microns, and dynamical information on energy scales from ≈ 30 neV to ≈ 10 meV.

The unique strengths of these premier instruments are complementary by design. Specifically, HFBS can resolve motions with characteristic times of order a few nanoseconds. Since it offers the highest count rate with sub- μ eV resolution in the US, it is an ideal choice for high resolution, quasi-elastic scattering studies of low-energy dynamics in polymers and biomolecules.

MACS boasts the world's highest monochromatic cold-neutron flux and routinely is featured in transformative investigations of quantum magnetism. With its 20-detector analyzer array, MACS is well suited for surveys of large regions of reciprocal space, leveraging its exceptional polarized beam capabilities that incorporate a unique toroidal ^3He spin filter. As part of the Non-Equilibrium Initiative in the CHRNS agreement, efforts are underway to implement the ABCD (Always Be Collecting Data) approach on MACS which involves continuous sweeping of various angles and recording the position each time a neutron is counted. Compared with step scanning, this approach will substantially increase the data rate, particularly for strongly scattering samples.

The NSE instrument provides the highest energy resolution of any neutron spectrometer in North America. It relies upon the Larmor precession of neutrons' magnetic moments as an internal "clock" attached to each neutron allowing measurements of the final polarization of the neutrons to be directly correlated with the speed of the neutron. This modality results in data being obtained in the time domain rather than in the frequency domain. Fourier times as long as 300 ns (roughly corresponding to an energy resolution of 0.01 μ eV) have been achieved for investigations of slow diffusive processes in a range of soft materials notably including polymer nanocomposites, biomembranes, and biopharmaceuticals. A complete upgrade of the NSE is underway with funding received by the University of Delaware, in collaboration with NIST, from the NSF Mid-Scale Research Infrastructure program. The new primary coils and detector will increase the maximum Fourier time achievable at a given wavelength by $> 2.5x$ and reduce count times by as much as a factor of 10 for a given Fourier time. For soft matter and magnetic structure characterization, the innovative vSANS instrument is meeting the emerging

needs of the CHRNS user community. vSANS has a variety of front-end optics choices including three choices of wavelength resolution in addition to the traditional velocity selector and slit collimation as well as the standard pinhole geometry. Three separate, adjustable detectors yield an extended Q range from 0.002 nm^{-1} to 7 nm^{-1} in a single instrument setting. The flexible sample area opens possibilities for sophisticated sample environments ranging from capillary rheometers to Peltier temperature blocks to superconducting magnets. The 45m instrument can also be readily configured for GISANS (Grazing Incidence Small Angle Neutron Scattering) experiments. All these features can be used with full polarization analysis. These elements together provide unprecedented possibilities not only for structural characterization of materials, but also for time-dependent studies of complex hierarchical structures.

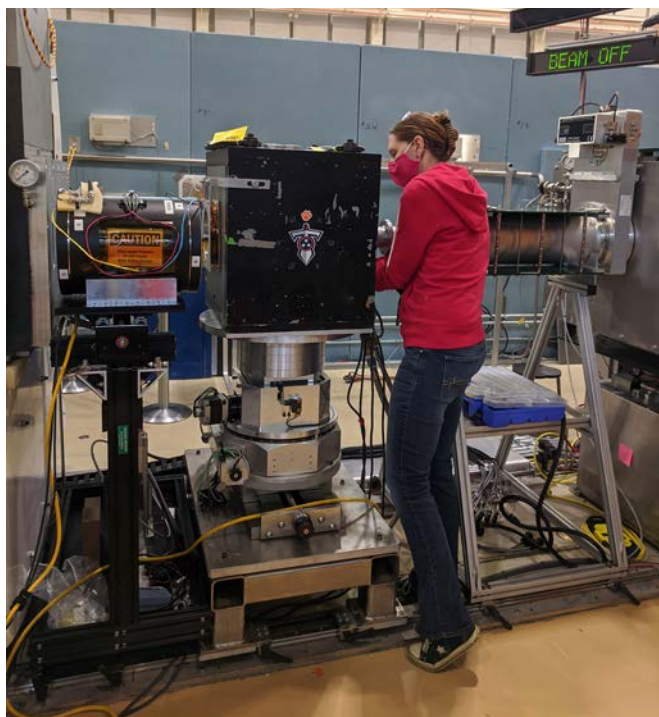


FIGURE 2: CHRNS scientist Kathryn Krycka sets up a mail-in vSANS experiment with ^3He polarization analysis.

A significant addition to the CHRNS instrument suite is CANDOR, which was included for the first time in the Call for Proposals in November of 2020. The novelty of CANDOR lies in its use of a bank of state-of-the-art “energy-dispersive” detectors, which permits a polychromatic beam to impinge on the sample for measurements of either specular and non-specular reflectivity with or without polarized beams. A gain of ≈ 20 compared to the previous generation of neutron reflectometers in service at the NCNR has been realized, and reflectivities as low as 10^{-8} have been measured. Data reduction is provided by *Reductus* which allows users to access and reduce their data anywhere they have a web connection. This exceptional performance will enable unprecedented structural and kinetic characterization of complex materials from the nanoscale to the mesoscale.

Research

The wide range of instrument capabilities available in CHRNS support a very diverse scientific program, allowing researchers in materials science, chemistry, biology, geosciences, and condensed matter physics to investigate materials such as polymers, metals, ceramics, magnetic materials, colloids, fluids and gels, rocks, and biomaterials. The research community can obtain access to the state-of-the-art CHRNS instrumentation using the NCNR’s proposal system. Proposals to use the CHRNS instruments are reviewed on the basis of scientific merit and/or technological importance and broader impacts. In the most recent Call for Proposals in November of 2020, 311 instrument-days were awarded of the 887 days requested on the CHRNS instruments. These experiments will be run immediately following the current shutdown. More than $\frac{1}{3}$ of NCNR publications (see the “Publications” section on p. 66), are based at least in part on research performed using these instruments. This report contains several highlights of CHRNS publications. See the labeled highlights in the table of contents.

Scientific Support Services

CHRNS provides scientific support in the critical areas of sample environment and chemical laboratories. Specifically, CHRNS offers eight well-equipped and well-supplied user laboratories, including a Guide Hall Laboratory which provides a safe environment for CHRNS users to handle activated samples. The laboratory staff continues to ensure that the required equipment and/or supplies are available for users for their experiments.

The CHRNS sample environment staff ensures that CHRNS users have the equipment and training needed to make neutron measurements under external conditions of temperature, pressure, magnetic field, humidity, and fluid flow. From mK dilution refrigeration systems to a 1600°C furnace, the equipment spans a large temperature range. Beyond precise temperature control, CHRNS users have access to a variety of flow systems, rheometers, gas-loading systems, two superconducting magnets with fields of up to 11 Tesla, leak detectors, and other complex equipment to control parameters such as pressure, humidity, and electric fields. From July 2020 through December 2020, CHRNS sample environment staff set up and operated a diverse range of complex sample environment equipment for more than 85 experiments on CHRNS instruments, many using multiple pieces of equipment for the same experiment. This total includes six ultra-low temperature experiments in a dilution fridge or ^3He insert, of which three were in a superconducting magnet. The majority of the experiments (> 11) on MACS and HFBS used either an ILL cryostat or closed cycle refrigerator, while NSE ran four high temperature experiments (above 325 K) during this time period. Three experiments on vSANS included complex sample environments such as the standard and capillary rheometers. In addition, ten experiments involved electromagnets with seven that utilized the polarized incident beam and three of which also employed the ^3He spin filter analyzer.

The procurement, development, and commissioning of sample environment is an essential part of the duties of the CHRNS sample environment staff. Recently, the 100 mm cryostat used on MACS was equipped with new liquid helium and liquid nitrogen level sensing capabilities and a digital pressure gauge for precise needle valve adjustments. A new serial port interface extender for automatization was purchased along with a new high-capacity liquid nitrogen trap dewar with level sensing capabilities for a dilution refrigerator. The temperature control was upgraded for the cryostat housing the 11 T magnet providing precise measurements at ultra-low temperature. A new, lightweight closed-cycle refrigerator was purchased for CANDOR that can cool to 3 K. In addition, a new CHRNS high-pressure clamp cell was commissioned. The clamp cell can achieve 2 GPa using Fluorinert or d-ethanol/d-methanol as a pressure medium in the temperature range between 300 K and 300 mK. A new sample cell was designed for HFBS so that electric fields can be applied to powders. Finally, a low background sample holder made of boron nitride was designed for thin films in vacuum for use up to 800 K in closed cycle refrigerators.

The capillary μ RheoSANS, originally developed by nSoft, is now in routine usage on the CHRNS vSANS instrument. This simple and cost-effective system maximizes the scattering signal with coiled, fused silica capillaries that create an approximate 30 mm diameter sample. The flexibility of the coils allows for both straight and sequential coiling to understand any effect of coiling. Capillary RheoSANS provides a means to measure the rheology and nanostructure of complex fluids at shear rates that are three orders-of-magnitude higher than traditional rheometers.

Broadening Participation in STEM

Since direct outreach has proven to be an effective means to attract users, CHRNS pursues many avenues for engaging institutions that serve diverse groups. Specific activities include PREM and CREST partnerships. Specifically, a partnership with the Interdisciplinary Materials Research and Education Laboratory (IMREL) at Fayetteville State University (FSU) was established in August 2018 through the NSF PREM (Partnerships for Research and Education in Materials) program (Agreement No. DMR-1827731). The PREM supports cutting-edge materials research as the context for producing motivated and skilled members of those groups most underrepresented in materials research as future professional leaders. This partnership is organized around a common theme of structure-processing-property correlations of nanomaterials to support student training in research using neutron scattering.

Recent accomplishments of this PREM partnership include the publication of three peer-reviewed articles that feature neutron scattering measurements performed as part of the collaboration among CHRNS and FSU researchers. These articles included data obtained by two of the student

co-authors, Washat Roxanne Ware and Candyce Collins, who were CHRNS SURF students during the summer of 2019. In lieu of facility visits during this past year, CHRNS representatives (Patrick Quarterman, Katie Weigandt and Yimin Mao) gave virtual seminars for FSU students and professors that highlighted the capabilities of neutron scattering. In a similar vein, CHRNS is engaged in a partnership with California State University, San Bernardino within the NSF CREST (Centers of Research Excellence in Science and Technology) program as part of their new Phase II Center for Advanced Functional Materials (HRD-1914777). Activities to date include a virtual tutorial for students on reflectivity data reduction.

Education and Outreach

CHRNS sponsors a variety of educational programs and activities tailored to specific student groups and professions. One of the premier outreach activities is the annual neutron summer school. During the past few years, the school has continued to attract graduate students, post-docs, and junior professors with a wide range of expertise in areas such as chemistry, engineering, physics, materials science, and biology. Recently we have adapted to the travel restrictions imposed by COVID-19 and developed a successful virtual school. The 26th Center for High Resolution Neutron Scattering (CHRNS) "School on Methods and Applications of Small Angle Neutron Scattering and Neutron Reflectometry," originally planned for June 1-5, 2020, was held virtually February 3-19, 2021. It was attended by 36 students affiliated with North American universities and US industry located in 22 US states, the District of Columbia, and Mexico. Students came from a diverse set of backgrounds including Chemical Engineering, Materials Science and Engineering, Chemistry, Physics, Biochemistry, Biomolecular Engineering, Energy, Mechanical Engineering, Aerospace & Nuclear Engineering, Polymer Science, and Electrical and Computer Engineering.

This school had many unique features due to its virtual venue. It included introductory lectures along with hands-on data analysis which simulated the work of a researcher after collecting neutron reflectivity and SANS neutron data. While the lectures were provided via a conventional video-conference platform, the students' poster sessions, coffee hours, and small-group tutorial sessions were held in GatherTown, an online platform that allows participants to move their avatars around a virtual conference center, providing an atmosphere for the school more like an in-person setting. As a final project, the students were asked to write a beam time proposal on a subject of their choice, either related to their own research or based on one of the school experiments that they did. The best SANS and neutron reflectivity proposals were awarded certificates and coffee mugs featuring CHRNS SANS data. Lessons learned from this undertaking are currently being applied to other events and will potentially open new opportunities even after travel returns to normal.



FIGURE 3: Guangcui Yuan and Sushil Satija teaching small groups during a polymer neutron reflectometry experiment. Parts of the Gathertown virtual room are seen in the background.

CHNRNS scientists also participated in teaching courses and giving lectures at universities or as part of workshops on topics including scattering theory and techniques. Ben Trump (NCNR Post-doctoral Scientist) organized and led lectures and tutorials for the Powder Diffraction Workshop held virtually on May 6 - 9, 2020 for over a dozen students in the University of Delaware Chemistry Department. In May of 2021 CHNRNS ran an online “Contributing to SasView” training workshop, with a follow up workshop scheduled for later in 2021. Significantly, a very popular CHNRNS Online Scattering Course with University Credit Option will be offered again in the fall of 2021 with Yun Liu as the primary lecturer. The registration limit of 400 was reached quickly with 63 students taking the course for credit and 360 students auditing the course.

William Ratcliff (NCNR Instrument Scientist) was featured as a lecturer at the virtual “Magnetic Structure Determination from Neutron Diffraction Data” which was organized by scientists from Oak Ridge National Laboratory and held on September 28 - October 2, 2020. In mid-June 2020 and late July 2021, Chuck Majkrzak (NIST Fellow and NCNR Team Leader) and Kathryn Krycka (CHNRNS vSANS Instrument Scientist) gave lectures on the fundamentals of reflectivity and on polarized neutrons, respectively, at the virtual National School on Neutron and X-ray Scattering which is co-sponsored by Argonne National Laboratory and Oakridge National Laboratory.

As part of its expanding education and outreach effort, CHNRNS allows university-based research groups with BTAC-approved experimental proposals to request travel support for an additional graduate student to participate in the experiment. This support is intended to enable new graduate students, for example, to acquire first-hand experience with a technique that they may later use in their own research. Announcements of this program are sent to all university

groups whose experimental proposals receive beam time from the BTAC. Recipients of the announcement are encouraged to consider graduate students from under-represented groups for this opportunity. The program is also advertised on the NCNR’s website at <https://www.nist.gov/ncnr/chnrns/travel-support>. As a new initiative in the CHNRNS renewal, this opportunity will be expanded to include a limited number of travel awards to enable graduate students or post-docs to attend workshops or related CHNRNS-sponsored events, once travel to NIST is opened again to users.

CHNRNS supports universities seeking an NSF INTERN supplemental grant that allows them to station graduate students at NIST for an extended period of time to help educate them on neutron scattering and become successful facility users. There have been four recent recipients. Donghui Zhang from LSU obtained the supplemental grant for her research on structures in amphiphilic coil-comb block copolymers, and her student was at NIST in 2020. Marcus Foston from Washington University in St Louis won an award to work on catalyzing lignin depolymerization. Dario Arena from the University of South Florida will send a student in September 2021 to investigate magnetic coupled heterostructures. In addition, Carol Korzeniewski at Texas Tech and Shelly Minter from the University of Utah were successful in obtaining funding for their student to apply neutron reflectometry to polymer electrolytes.

For 11 weeks in the summer of 2021, CHNRNS participated in NIST’s Summer Undergraduate Research Fellowship (SURF) program by hosting 10 SURF students, including two previous Summer High school Internship Program (SHIP) students. Though the program was virtual due to NIST-site access restrictions, it featured a variety of group instructional activities such as the Sketchnote Workshop given by Rob Dimeo (NCNR Director) in July 2021. The students performed

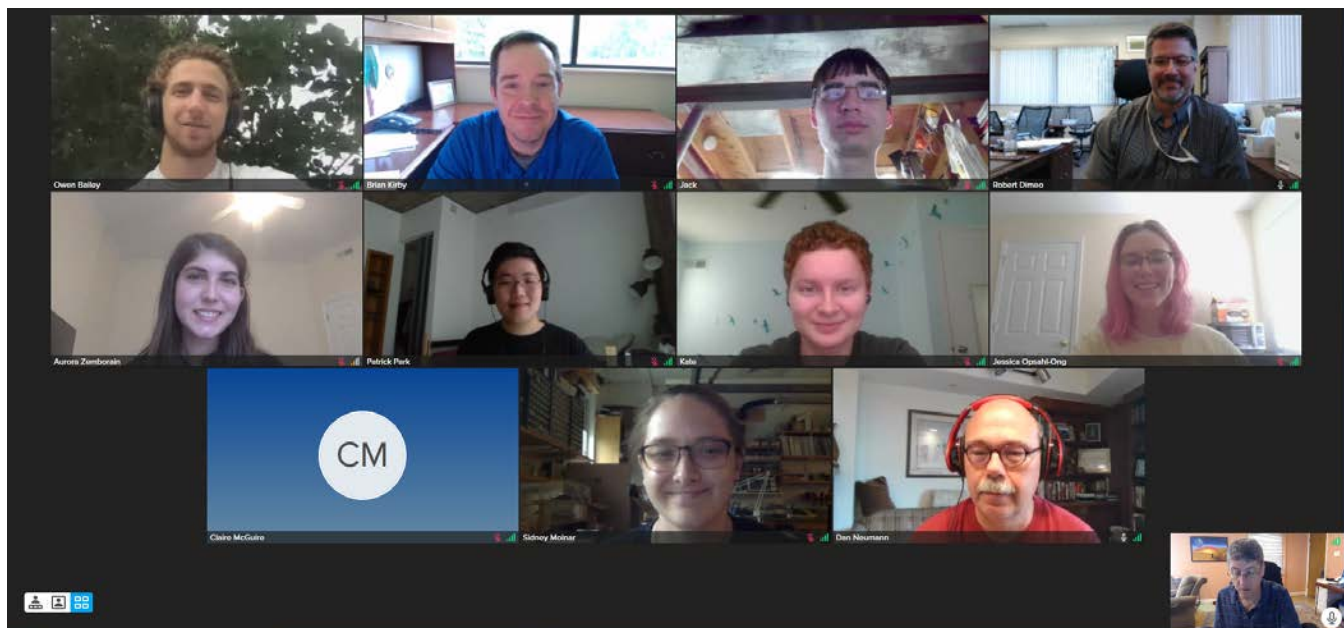


FIGURE 4: CHRNS SURF students interact virtually with NCNR managers (Rob Dimeo, Brian Kirby and Dan Neumann) during the “Meet the Director” lunch event.

research on topics ranging from assessing particle orientation from 2D SANS scattering patterns to exploring organic cation dynamics of hybrid vacancy-ordered halide perovskites. The students gave oral presentations describing their work at the virtual NIST SURF colloquium in early August 2021 moderated by programming officers from the National Science Foundation. The colloquium featured a plenary talk by Claire Lamberti from the University of Texas at Tyler on broad spectrum antibiotic glasses characterization.

CHRNS initiated a Research Experiences for Teachers (RET) program in 2010. Unfortunately, CHRNS was unable to host RET participants on-site during the summer of 2021 due to access restrictions.

The Summer High School Intern Program (SHIP) is a successful, competitive NIST-wide program for students who are interested in performing scientific research. In the summer of 2021 CHRNS hosted four SHIP interns from local high schools in a completely virtual format. The students developed a methodology for neutron field profiling for activation analysis, used AI to classify neutron diffraction patterns in Bravais lattices, and authored an analysis program for prompt gamma activation spectra. The results of the students’ summer investigations were highlighted in a NIST-wide virtual poster session, as well as in a well-attended symposium at the NCNR. Aaron Tian from Poolesville High School was honored as a finalist in the Outstanding Poster Award competition from NIST’s chapter of Sigma Xi for his work entitled “Data-Driven Traceability of Reagents and Stock Solutions.”

Despite access restrictions due to COVID-19, CHRNS was able to provide specialized tours and activities for high school and university students, all of them virtual unless otherwise noted. Chuck Majkrzak (Surfaces and Interfaces Team Leader) and Przemek Klosowski (NCNR Staff Scientist) mentored the FIRST Robotics Club at St. Johns High School during

the 2020-21 academic year. Steven Dewey (Health Physics Team Leader) gave a lecture on basic Health Physics to over 160 chemical engineering undergraduates at Pennsylvania State University. Craig Brown (Structure and Dynamics of Materials Team Leader) was a guest lecturer for a University of Delaware graduate chemistry class in November of 2020.

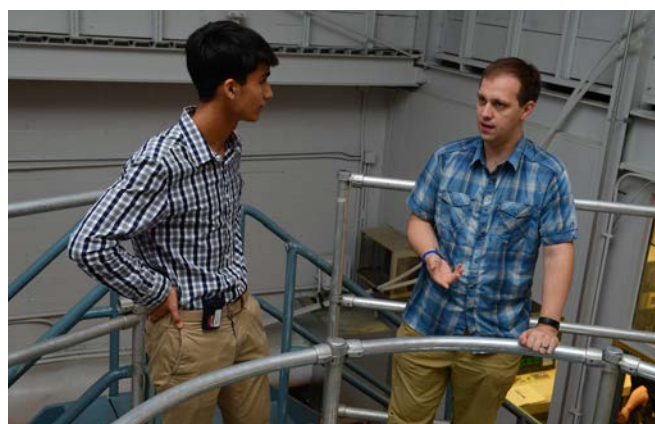


FIGURE 5: CHRNS SHIP student, Rafael Virador, and his mentor, Nick Sharp, perform an experiment at the University of Maryland Reactor

William Ratcliff (NCNR Staff Scientist) described opportunities at NIST for students, postdocs, and faculty as a panel member at the National Society of Black Physicists Conference, also in November. In January 2021 Rob Dimeo (NCNR Director) spoke at the Career Month event at Harford Technical High School in Bel Air, MD. Craig Brown gave another lecture to an undergraduate Chemistry class, in March of 2021, this time for Colgate University. In April, Yun Liu (vSANS Instrument Scientist) participated in the National Lab. Career Panel at U. Texas Austin. Julie Borchers (CHRNS Associate Director) along with William Ratcliff discussed Careers with students at the virtual NIST booth at the IGEN Networking Fair at IGEN National Meeting in June 2021.

2021 Awards



George Baltic received the **2020 NIST Distinguished Career Award** for “creating and sustaining a world-class construction and maintenance program at the NIST Center for Neutron Research”. The Distinguished Career Award recognizes NIST employees who have made positive, lasting, long-term, quality contributions to accomplishing NIST goals



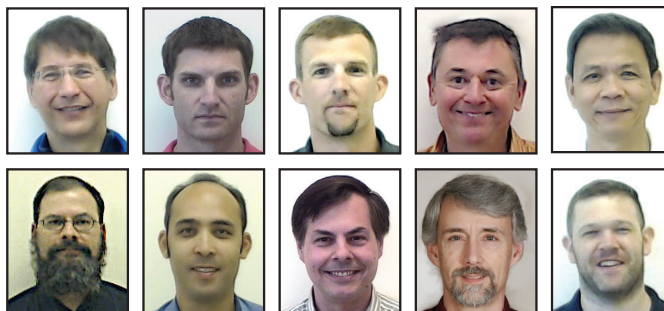
Nick Butch received the **2020 NIST Samuel Wesley Stratton Award** for “pioneering research into the exotic physics and extremely high-field re-entrant superconductivity in uranium ditelluride”. The Stratton Award recognizes outstanding scientific or engineering achievements in support of NIST objectives.



Tanya Dax received the **2020 NIST Colleagues Choice Award** for “exemplary support of NCNR sample environment equipment and invaluable assistance to hundreds of facility users and staff”. The Colleagues Choice Award recognizes outstanding non-supervisory NIST employees who, in the eyes of their colleagues, have made significant contributions that broadly advance the NIST mission and strategic goals or notably contribute to the overall health and effectiveness of NIST.



The NCNR’s **Antonio Faraone** received the **2020 Department of Commerce Bronze Medal Award**. He was recognized “for rigorous neutron spin-echo measurements that reveal the role of nanoparticles in tailoring the properties of polymer nanocomposites.



The NCNR team of **John Barker, Doug Ogg, Danny Ogg, Jim Moyer, Thuan Thai, Andrew Malone, Phil Chabot, Nick Maliszewskyj, Steve Kline, and Steve Pheiffer** received the **2020 Department of Commerce Gold Medal** for “the development of a very small angle neutron scattering instrument giving unprecedented structural information on the nano to meso length scales.”



An NCNR team composed of **Sam MacDavid, Dan Keyser, Andrew Main, Tony Norbedo, Dagistan Sahin, Brian Wright, and Justin Hudson** have been awarded the **2020 Department of Commerce Silver Medal** for “the flawless planning and execution of a never-before-attempted complete replacement of an obsolete, 50-year old, nuclear safety relay system.”



Scott Dewey of NIST's PML received the **2020 NIST Bronze Medal Award** for his work in "developing and carrying out the world's most precise measurement of the antineutrino-electron correlation coefficient in neutron beta decay."



Dan Hussey of NIST's Physical Measurement Laboratory has been elected a **Fellow of the American Physical Society** for "novel developments in neutron radiography and tomography leading to significant advances in lithium-ion batteries, hydrogen fuel cells, concretes, and additive manufacturing; and for the invention of simultaneous neutron/x-ray imaging for analysis of complex natural and engineered materials."



Fred Wietfeldt, Professor of Physics at Tulane University has been elected a **Fellow of the American Physical Society**, for "contributions to precision measurements using free neutrons, in particular, studies of neutron beta decay and investigations employing neutron interferometry." He is a Guest Researcher in PML's Neutron Physics Group which is located at the NCNR.



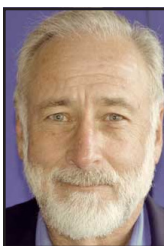
Gordon Jones, the Stone Professor of Natural History at Hamilton College has been awarded the **2021 Prize for a Faculty Member for Research in an Undergraduate Institution** by the American Physical Society. Gordon was recognized for "outstanding contributions to fundamental neutron physics, development of neutron polarizers using optically polarized helium-3, and extraordinary engagement and education of undergraduate students." Gordon was a post-doc at NIST and has remained active in neutron programs at the NCNR including the successful development of neutron spin filters.



John Doyle, the Henry B. Silsbee Professor of Physics at Harvard University was awarded the **2021 Herbert P. Broida Prize** by the American Physical Society for "pioneering work in the field of cold molecules, and for wide-ranging studies of these molecular systems, especially laser cooling, high-precision spectroscopy, and searches for permanent electric dipole moments, providing insight into possible new physics." John and his students have worked for many years at the NCNR, demonstrating the magnetic trapping of ultracold neutrons.



Wangchun Chen, Ross Erwin, and Shannon Watson of the NCNR were awarded the **2020 Department of Commerce Bronze Medal Award** "for development and application of the world's best polarized neutron capabilities using polarized helium-3 spin filters."



Geoffrey Greene, Professor Emeritus of the Department of Physics and Astronomy at the University of Tennessee was awarded the **2021 Tom W. Bonner Prize in Nuclear Physics** by the American Physical Society for "foundational work establishing the field of fundamental neutron physics in the US, for developing experimental techniques for in-beam measurements of the neutron lifetime and other experiments, and for realizing a facility for the next generation of fundamental neutron physics measurements." While at NIST, Geoffrey helped start the fundamental physics program, and has been a collaborator ever since.



Robert Cava of Princeton University was awarded the **2021 David Adler Lectureship Award in in the Field of Materials Physics** by the American Physical Society for "enabling significant advances in the field of topological materials by recognizing, discovering and fabricating novel compounds, and demonstrating with collaborators that such materials show the expected exotic topological properties." Robert is the Russell Wellman Moore Professor of Chemistry at Princeton University and has been a long-time user of the NCNR facilities.



Eric Bloch, Assistant Professor of Chemistry and Biochemistry at the University of Delaware, was named a **2020 Emerging Investigator** by the Royal Society of Chemistry. Eric is a member of the Center for Neutron Science at the University of Delaware and his group regularly uses NCNR facilities.



Greg Newbloom, founder and CEO of Membrion, was recognized as one of **AIChE's "35 Under 35"**, recognizing young professionals for their work with the Institute and within the chemical engineering profession. Membrion is a start-up company that manufactures membranes for water purification and other applications. In just four years and with a dozen team members, Membrion has raised \$7.5 million and generated more than \$2 million in revenue, and it has helped save 400,000 gallons of water through its various applications. Greg used the NCNR facilities extensively during his graduate research.



Yuyin Xi is the 2021 recipient of the **University of Delaware College of Engineering Award** for Post-Doctoral Researcher Excellence. This award recognizes a postdoctoral fellow who has demonstrated excellence in research, teaching, mentoring, service, and/or leadership. Yuyin has also been recognized with a **2021 PEAR Postdoc Technical Accolade** from NIST for "the breakthrough discovery of a novel type of thermal reversible colloidal gel systems with exceptional optical properties and precise structure reproducibility that can be used in a wide range of applications such as smart windows, temperature sensors, and filters." Yuyin is a post-doc in the Center for Neutron Science at the University of Delaware. He is stationed at the NCNR where he is advised by Yun Liu.



Professor **Karen Fleming** (Johns Hopkins University) is the recipient of the **Carl Brändén Award** from the Protein Society. The award honors an outstanding protein scientist who makes "exceptional contributions" in the areas of education or service. Dr. Fleming is cited for her work on thermodynamic measurements of membrane protein folding. Karen is a long-time collaborator and NCNR user.



Alannah Hallas, an Assistant Professor in the Department of Physics and Astronomy at the University of British Columbia has been named a **CIFAR Azrieli Global Scholar**. The CIFAR Azrieli Global Scholars program supports outstanding early-career researchers through mentorship, a global network, professional skills development, and \$100,000 in unrestricted research support for two years. CIFAR Azrieli Global Scholars join CIFAR research programs for 24 months where they collaborate with fellows and contribute new approaches toward the most important questions facing science and humanity. Alannah's research makes extensive use of the NCNR facilities.



Mitchell DiPasquale, a doctoral candidate in the Department of Chemistry and Biochemistry at the University of Windsor, was awarded the **Frederick Banting and Charles Best Canada Graduate Scholarships Doctoral Award** from the Canadian Institutes of Health Research (CIHR). The award provides special recognition and support to students who are pursuing a doctoral degree in a health-related field in Canada. Mitchell has used the NCNR facilities to study E-cigarette or Vaping use-Associated Lung Injury, highlighted in this year's report.



Roisin Donnelly received a **Langmuir Poster Award** winner at the 95th ACS Colloid and Surface Science Symposium held in June 2021. Roisin's poster was titled "Exploring the relationship between temperature activated hydrogen-deuterium exchange and protein stability with SANS". She is currently a PhD student in the Center for Neutron Science at the University of Delaware and is co-advised by Prof. Norm Wagner and the NCNR's Yun Liu.



Julia Mundy, an Assistant Professor of Physics at Harvard University has been awarded a **Packard Fellowship**. The fellowship citation reads: "In some materials, quantum mechanics transcends from the microscopic length scales to the macroscopic and in doing so can produce spectacular effects. Mundy's group combines atomically-precise thin film synthesis with picoscale electron microscopy imaging to design, construct, and probe new quantum materials." Julia has used the NCNR facilities for many years.

Publications: August 1, 2020 to July 31, 2021

- Abir, M., Hussey, D.S., Khaykovich, B., "Design of Neutron Microscopes Equipped with Wolter Mirror Condenser and Objective Optics for High-Fidelity Imaging and Beam Transport," *J. Imaging* **6**(10), 100 (2020).
- Addazi, A., Anderson, K., Ansell, S., Babu, K.S., Barrow, J.L., Baxter, D.V., Bentley, P.M., Bereziani, Z., Bevilacqua, R., Biondi, R., Bohm, C., Brooijmans, G., Broussard, L.J., Cedercäll, J., Crawford, C., Dev, P.S.B., DiJulio, D.D., Dolgov, A.D., Dunne, K., Fierlinger, P., Fitzsimmons, M.R., Fomin, A., Frost, M.J., Gardiner, S., Gardner, S., Galindo-Uribarri, A., Geltenbort, P., Girmohanta, S., Golubev, P., Golubeva, E., Greene, G.L., Greenshaw, T., Gudkov, V., Hall-Wilton, R., Heilbronn, L., Herrero-Garcia, J., Holley, A., Ichikawa, G., Ito, T.M., Iverson, E., Johansson, T., Jönsson, L., Jwa, Y.-J., Kamyshkov, Y., Kanaki, K., Kearns, E., Kokai, Z., Kerbikov, B., Kitaguchi, M., Kittelmann, T., Klinkby, E., Kobakhidze, A., Koerner, L.W., Kopeliovich, B., Kozela, A., Kudryavtsev, V., Kupsc, A., Lee, Y.T., Lindroos, M., Makkinje, J., Marquez, J.I., Meirose, B., Miller, T.M., Milstead, D., Mohapatra, R.N., Morishima, T., Muhrer, G., Mumm, H.P., Nagamoto, K., Nepomuceno, A., Nesti, F., Nesvizhevsky, V.V., Nilsson, T., Oskarsson, A., Paryev, E., Pattie, Jr., R.W., Penttil, S., Perrey, H., Pokotilovski, Y.N., Potashnikov, I., Ramic, K., Redding, C., Richard, J.-M., Ries, D., Rinaldi, E., Rizzi, N., Rossi, N., Ruggles, A., Rybolt, B., Santoro, V., Sarkar, U., Saunders, A., Senjanovic, G., Serebrov, A.P., Shimizu, H.M., Shrock, R., Silverstein, S., Silvermyr, D., Snow, W.M., Takibayev, A., Tkachev, I., Townsend, L., Tureanu, A., Varriano, L., Vainshtein, A., de Vries, J., Wagner, R., Woracek, R., Yamagata, Y., Yiu, S., Young, A.R., Zanini, L., Zhang, Z., Zimmer, O., "New High-Sensitivity Searches for Neutrons Converting into Antineutrons and/or Sterile Neutrons at the HIBEAM/NNBAR Experiment at the European Spallation Source," *J. Phys. G Nucl. Partic.* **48**(7), 070501 (2021).
- Agrawal, N.R., Omarova, M., Burni, F., John, V.T., Raghavan, S.R., "Spontaneous Formation of Stable Vesicles and Vesicle Gels in Polar Organic Solvents," *Langmuir* **37**(26), 7955 (2021).
- Al Hasan, M.A., Wang, J., Shin, S., Gilbert, D.A., Liaw, P.K., Tang, N., Liyanage, W.L.N.C., Santodonato, L., DeBeer-Schmitt, L., Butch, N.P., "Effects of Aluminum Content on Thermoelectric Performance of $\text{Al}_x\text{CoCrFeNi}$ High-Entropy Alloys," *J. Alloy Compd.*, in press.
- Aleksenskii, A., Bleuel, M., Bosak, A., Chumakova, A., Dideikin, A., Dubois, M., Korobkina, E., Lychagin, E., Muzychka, A., Nekhaev, G., Nesvizhevsky, V., Nezvanov, A., Schweins, R., Shvidchenko, A., Strelkov, A., Turlybekuly, K., Vul', A., Zhernenkov, K., "Clustering of Diamond Nanoparticles, Fluorination and Efficiency of Slow Neutron Reflectors," *Nanomaterials-Basel* **11**(8), 1945 (2021). [CHRNS]
- Andersson, M.S., Grinderslev, J.B., Chen, X.-M., Chen, X., Häussermann, U., Zhou, W., Jensen, T.R., Karlsson, M., Udovic, T.J., "Interplay between the Reorientational Dynamics of the B_3H_8^- Anion and the Structure in KB_3H_8 ," *J. Phys. Chem. C* **125**(7), 3716 (2021). [CHRNS]
- Andersson, M.S., Stavila, V., Skripov, A.V., Dimitrievska, M., Psurek, M.T., Leão, J.B., Babanova, O.A., Skoryunov, R.V., Soloninin, A.V., Karlsson, M., Udovic, T.J., "Promoting Persistent Superionic Conductivity in Sodium Monocarba-Closo-Dodecaborate $\text{NaCB}_{11}\text{H}_{12}$ via Confinement within Nanoporous Silica," *J. Phys. Chem. C*, in press. [CHRNS]
- Andersson, M.S., Grinderslev, J.B., Jensen, T.R., García Sakai, V., Häussermann, U., Udovic, T.J., Karlsson, M., "Interplay of NH_4^+ and BH_4^- Reorientational Dynamics in NH_4BH_4 ," *Phys. Rev. Mater.* **4**(8), 085002 (2020).
- Andriamirado, M., Balantekin, A.B., Band, H.R., Bass, C.D., Bergeron, D.E., Bowden, N.S., Bryan, C.D., Classen, T., Conant, A.J., Deichert, G., Diwan, M.V., Dolinski, M.J., Erickson, A., Foust, B.T., Gaison, J.K., Galindo-Uribarri, A., Gilbert, C.E., Hans, S., Hansell, A.B., Heeger, K.M., Heffron, B., Jaffe, D.E., Jayakumar, S., Ji, X., Jones, D.C., Koblanski, J., Kzylova, O., Lane, C.E., Langford, T.J., LaRosa, J., Littlejohn, B.R., Lu, X., Maricic, J., Mendenhall, M.P., Meyer, A.M., Milincic, R., Mueller, P.E., Mumm, H.P., Napolitano, J., Neilson, R., Nikkel, J.A., Nour, S., Palomino, J.L., Pushin, D.A., Qian, X., Rosero, R., Surukuchi, P.T., Tyra, M.A., Varner, R.L., Venegas-Vargas, D., Weatherly, P.B., White, C., Wilhelm, J., Woolverton, A., Yeh, M., Zhang, C., Zhang, X., "Limits on Sub-GeV Dark Matter from the PROSPECT Reactor Antineutrino Experiment," *Phys. Rev. D* **104**(1), 012009 (2021).

- Andriamirado, M., Balantekin, A.B., Band, H.R., Bass, C.D., Bergeron, D.E., Berish, D., Bowden, N.S., Brodsky, J.P., Bryan, C.D., Classen, T., Conant, A.J., Deichert, G., Diwan, M.V., Dolinski, M.J., Erickson, A., Foust, B.T., Gaison, J.K., Galindo-Uribarri, A., Gilbert, C.E., Goddard, B.W., Hackett, B.T., Hans, S., Hansell, A.B., Heeger, K.M., Jaffe, D.E., Ji, X., Jones, D.C., Kyzylva, O., Lane, C.E., Langford, T.J., LaRosa, J., Littlejohn, B.R., Lu, X., Maricic, J., Mendenhall, M.P., Meyer, A.M., Milincic, R., Mitchell, I., Mueller, P.E., Mumm, H.P., Napolitano, J., Nave, C., Neilson, R., Nikkel, J.A., Norcini, D., Nour, S., Palomino, J.L., Pushin, D.A., Qian, X., Romero-Romero, E., Rosero, R., Surukuchi, P.T., Tyra, M.A., Varner, R.L., Venegas-Vargas, D., Weatherly, P.B., White, C., Wilhelmi, J., Woolverton, A., Yeh, M., Zhang, A., Zhang, C., Zhang, X., "Improved Short-Baseline Neutrino Oscillation Search and Energy Spectrum Measurement with the PROSPECT Experiment at HFIR," *Phys. Rev. D* **103**(3), 032001 (2021).
- Anovitz, L.M., Cheshire, M.C., Hermann, R.P., Gu, X., Sheets, J.M., Brantley, S.L., Cole, D.R., Ilton, E.S., Mildner, D.F.R., Gagnon, C., Allard, L.F., Littrell, K.C., "Oxidation and Associated Pore Structure Modification during Experimental Alteration of Granite," *Geochim. Cosmochim. Ac.* **292**, 532 (2021). [CHRNS]
- Armstrong, C.L., Mang, J.T., "Thermally-Driven Changes to Porosity in TATB-Based High Explosives," *Propell. Explos. Pyrot.*, in press. [CHRNS]
- Astete, C.E., De Mel, J.U., Gupta, S., Noh, Y., Bleuel, M., Schneider, G.J., Sabliov, C.M., "Lignin-Graft-Poly(lactic-co-glycolic) Acid Biopolymers for Polymeric Nanoparticle Synthesis," *ACS Omega* **5**(17), 9892 (2020). [CHRNS]
- Babu, S.K., Spornjak, D., Mukundan, R., Hussey, D.S., Jacobson, D.L., Chung, H.T., Wu, G., Steinbach, A.J., Litster, S., Borup, R.L., Zelenay, P., "Understanding Water Management in Platinum Group Metal-Free Electrodes using Neutron Imaging," *J. Power Sources* **472**, 228442 (2020).
- Bae, S., Kim, H., Eo, Y.S., Ran, S., Liu, I.-L., Fuhrman, W.T., Paglione, J., Butch, N.P., Anlage, S.M., "Anomalous Normal Fluid Response in a Chiral Superconductor UTe_2 ," *Nat. Commun.* **12**(1), 2644 (2021).
- Bailey, E.J., Tyagi, M., Winey, K.I., "Correlation between Backbone and Pyridine Dynamics in Poly(2-Vinyl Pyridine)/Silica Polymer Nanocomposites," *J. Polym. Sci.* **58**(20), 2906 (2020). [CHRNS]
- Bao, X.-N., Zhang, W.-D., Gang, H.-Z., Yang, S.-Z., Li, Y.-C., Mu, B.-Z., "Formation of Viscoelastic Micellar Solutions by a Novel Cationic Surfactant and Anionic Salt System," *Colloid Surface. A* **611**, 125795 (2021).
- Barker, J.G., Cook, J.C., Chabot, J.P., Kline, S.R., Zhang, Z., Gagnon, C., "Mitigating Background caused by Extraneous Scattering in Small-Angle Neutron Scattering Instrument Design," *J. Appl. Crystallogr.* **54**(2), 461 (2021). [CHRNS]
- Beaucage, P.A., van Dover, R.B., DiSalvo, F.J., Gruner, S.M., Wiesner, U., "Superconducting Quantum Metamaterials from Convergence of Soft and Hard Condensed Matter Science," *Adv. Mater.* **33**(26), 2006975 (2021).
- Bell, R.T., Beaucage, P.A., Murphy, M.J., Connolly, A.B., Wiesner, U., Ginley, D., Van Dover, R.B., Thompson, M.O., "Rapid Identification of Synthetic Routes to Functional Metastable Phases using X-ray Probed Laser Anneal Mapping (XPLAM) Time-Temperature Quench Maps," *Chem. Mater.* **33**(12), 4328 (2021).
- Bethune, K., St-Pierre, J., LaManna, J.M., Hussey, D.S., Jacobson, D.L., "Contamination Mechanisms of Proton Exchange Membrane Fuel Cells - Mass Transfer Overpotential Origin," *J. Phys. Chem. C* **124**(44), 24052 (2020).
- Bhartiya, V.K., Hayashida, S., Povarov, K.Y., Yan, Z., Qiu, Y., Raymond, S., Zheludev, A., "Inelastic Neutron Scattering Determination of the Spin Hamiltonian for $BaCdVO(PO_4)_2$," *Phys. Rev. B* **103**(14), 144402 (2021). [CHRNS]
- Bhatnagar-Schöffmann, T., Kentzinger, E., Sarkar, A., Schöffmann, P., Lan, Q., Jin, L., Kovács, A., Grutter, A.J., Kirby, B.J., Beerwerth, R., Waschke, M., Stelhorn, A., Rücker, U., Dunin-Borkowski, R.E., Brückel, T., "Differentiation between Strain and Charge Mediated Magnetoelectric Coupling in $La_{0.7}Sr_{0.3}MnO_3/Pb(Mg_{1/3}Nb_{2/3})_{0.7}Ti_{0.3}O_3(001)$," *New J. Phys.* **23**(6), 063043 (2021).
- Bichler, K.J., Jakobi, B., Schneider, G.J., "Dynamical Comparison of Different Polymer Architectures-Bottlebrush vs Linear Polymer," *Macromolecules* **54**(4), 1829 (2021).
- Bone, A.N., Widener, C.N., Moseley, D.H., Liu, Z., Lu, Z., Cheng, Y., Daemen, L.L., Ozerov, M., Telsler, J., Thirunavukkuarasu, K., Smirnov, D., Greer, S.M., Hill, S., Krzystek, J., Holldack, K., Aliabadi, A., Schnegg, A., Dunbar, K.R., Xue, Z.-L., "Applying Unconventional Spectroscopies to the Single-Molecule Magnets, $Co(PPh_3)_2X_2$ (X = Cl, Br, I): Unveiling Magnetic Transitions and Spin-Phonon Coupling," *Chem.-Eur. J.*, in press.
- Bordelon, M.M., Liu, C., Posthuma, L., Kenney, E., Graf, M.J., Butch, N.P., Banerjee, A., Calder, S., Balents, L., Wilson, S.D., "Frustrated Heisenberg J_1 - J_2 Model within the Stretched Diamond Lattice of $LiYbO_2$," *Phys. Rev. B* **103**(1), 014420 (2021).

- Borger, A., Wang, W., O'Connor, T.C., Ge, T., Grest, G.S., Jensen, G.V., Ahn, J., Chang, T., Hassager, O., Mortensen, K., Vlassopoulos, D., Huang, Q., "Threading-Unthreading Transition of Linear-Ring Polymer Blends in Extensional Flow," *ACS Macro Lett.* **9**(10), 1452 (2020). [CHRNS]
- Browe, M.A., Landers, J., Tovar, T.M., Mahle, J.J., Balboa, A., Gordon, W.O., Fukuto, M., Karwacki, C.J., "Laponite-Incorporated UiO-66-NH₂-Polyethylene Oxide Composite Membranes for Protection against Chemical Warfare Agent Simulants," *ACS Appl. Mater. Inter.* **13**(8), 10500 (2021). [CHRNS]
- Burdette-Trofimov, M.K., Armstrong, B.L., Murphy, R.P., Heroux, L., Doucet, M., Rogers, A.M., Veith, G.M., "Probing Clustering Dynamics between Silicon and PAA or LiPAA Slurries under Processing Conditions," *ACS Appl. Polym. Mater.* **3**(5), 2447 (2021). [CHRNS]
- Burdette-Trofimov, M.K., Armstrong, B.L., Murphy, R.P., Heroux, L., Doucet, M., Trask, S.E., Rogers, A.M., Veith, G.M., "Role of Low Molecular Weight Polymers on the Dynamics of Silicon Anodes during Casting," *ChemPhysChem* **22**(11), 1049 (2021). [CHRNS]
- Cai, C., Nie, Z., Robinson, J.P., Hussey, D.S., LaManna, J.M., Jacobson, D.L., Koenig, Jr., G.M., "Thick Sintered Electrode Lithium-Ion Battery Discharge Simulations: Incorporating Lithiation-Dependent Electronic Conductivity and Lithiation Gradient due to Charge Cycle," *J. Electrochem. Soc.* **167**(14), 140542 (2020).
- Čajko, K.O., Dimitrievska, M., Sekulić, D.L., Petrović, D.M., Lukć-Petrović, S.R., "Ag-Doped As-S-Se Chalcogenide Glasses: a Correlative Study of Structural and Dielectrical Properties," *J. Mater. Sci.-Mater. El.* **32**(5), 6688 (2021).
- Callaghan-Patrachar, N., Peyronel, F., Pink, D.A., Marangoni, A.G., Adams, C.P., "USANS and SANS Investigations on the Coagulation of Commercial Bovine Milk: Microstructures Induced by Calf and Fungal Rennet," *Food Hydrocolloid.*, **116**, 106622 (2021). [CHRNS]
- Campbell, D.J., Collini, J., Sławińska, J., Autieri, C., Wang, L., Wang, K., Wilfong, B., Eo, Y.S., Neves, P., Graf, D., Rodriguez, E.E., Butch, N.P., Buongiorno Nardelli, M., Paglione, J., "Topologically Driven Linear Magnetoresistance in Helimagnetic FeP," *NPJ Quantum Mater.* **6**(1), 38 (2021).
- Cao, Y., Lin, K., Khmelevskiy, S., Avdeev, M., Taddei, K.M., Zhang, Q., Huang, Q., Li, Q., Kato, K., Tang, C.C., Gibbs, A., Wang, C.-W., Deng, J., Chen, J., Zhang, H., Xing, X., "Ultrawide Temperature Range Super-Invar Behavior of R₂(Fe,Co)₁₇ Materials (R = Rare Earth)," *Phys. Rev. Lett.* **127**(5), 055501 (2021).
- Cao, Z., Li, Z., Zhang, S., Galuska, L., Li, T., Do, C., Xia, W., Hong, K., Gu, X., "Decoupling Poly(3-Alkylthiophenes) Backbone and Side-Chain Conformation by Selective Deuteration and Neutron Scattering," *Macromolecules* **53**(24), 11142 (2020).
- Capaccioli, S., Zheng, L., Kyritsis, A., Paciaroni, A., Vogel, M., Ngai, K.L., "The Dynamics of Hydrated Proteins are the Same as those of Highly Asymmetric Mixtures of Two Glass-Formers," *ACS Omega* **6**(1), 340 (2021). [CHRNS]
- Cappelletti, R.L., Vinson, J., "Photons, Orbital Angular Momentum, and Neutrons," *Phys. Status Solidi B*, in press.
- Carmichael, J.R., Polsky, Y., An, K., Anovitz, L.M., Bingham, P., Dessieux, L., Ekici, K., Frost, M., Pemberton, S., "A High-Pressure Flow through Test Vessel for Neutron Imaging and Neutron Diffraction-Based Strain Measurement of Geological Materials," *Rev. Sci. Instrum.* **91**(8), 084502 (2020).
- Cascos, V.A., Roberts-Watts, J., Skingle, C., Levin, I., Zhang, W., Halasyamani, P.S., Stennett, M.C., Hyatt, N.C., Bousquet, E., McCabe, E.E., "Tuning between Proper and Hybrid-Improper Mechanisms for Polar Behavior in CsLn₂Ti₂NbO₁₀ Dion-Jacobson Phases," *Chem. Mater.* **32**(19), 8700 (2020).
- Chadda, R., Bernhardt, N., Kelley, E.G., Teixeira, S.C.M., Griffith, K., Gil-Ley, A., Öztürk, T.N., Hughes, L.E., Forsythe, A., Krishnamani, V., Faraldo-Gómez, J.D., Robertson, J.L., "Membrane Transporter Dimerization Driven by Differential Lipid Solvation Energetics of Dissociated and Associated States," *eLife* **10**, e63288 (2021). [CHRNS]
- Chakraborty, S., Doktorova, M., Molugu, T.R., Herberle, F.A., Scott, H.L., Dzikovski, B., Nagao, M., Stingaciu, L.-R., Standaert, R.F., Barrera, F.N., Katsaras, J., Khelashvili, G., Brown, M.F., Ashkar, R., "How Cholesterol Stiffens Unsaturated Lipid Membranes," *P. Natl. A. Sci. USA* **117**(36), 21896 (2020). [CHRNS]
- Chen, W.C., Erwin, R., Tsai, P., Hassan, M.T., Hadad, N., Majkrzak, C.F., "A Large Beam High Efficiency Radio Frequency Neutron Spin Flipper," *Rev. Sci. Instrum.* **92**(6), 063906 (2021).
- Chen, W.C., Hassan, M.T., Erwin, R., Watson, S.M., Gentile, T.R., Jones, G.L., "Optimizing Magnetically Shielded Solenoids," *Rev. Sci. Instrum.* **91**(10), 105102 (2020).
- Chen, X.C., Sacci, R.L., Osti, N.C., Tyagi, M., Wang, Y., Keum, J.K., Dudney, N.J., "Study of the Segmental Dynamics and Ion Transport of Solid Polymer Electrolytes in the Semi-Crystalline State," *Front. Chem.* **8**, 592604 (2021). [CHRNS]

- Chen, Y., Gaudet, J., Dasgupta, S., Marcus, G.G., Lin, J., Chen, T., Tomita, T., Ikhlas, M., Zhao, Y., Chen, W.C., Stone, M.B., Tchernyshyov, O., Nakatsuji, S., Broholm, C., "Antichiral Spin Order, its Soft Modes, and their Hybridization with Phonons in the Topological Semimetal Mn_3Ge ," *Phys. Rev. B* **102**(5), 054403 (2020).
- Cheng, D., Shimizu, R., Weaver, J., Meng, Y.S., "Unveiling the Stable Nature of LiPON-Associated Electrode/Electrolyte Interphases via Cryogenic Electron Microscopy," *Microsc. Microanal.*, in press.
- Chiang, W.-S., Chen, J.-H., Jacobi, D., Yildirim, T., Turkoglu, D., Althaus, S., Liu, Y., "Structural Properties of Kerogens with Different Maturities," *Energ. Fuel* **34**(10), 12354 (2020). [CHRNS]
- Chorażewski, M., Zajdel, P., Feng, T., Luo, D., Lowe, A.R., Brown, C.M., Leão, J.B., Li, M., Bleuel, M., Jensen, G., Li, D., Faik, A., Grosu, Y., "Compact Thermal Actuation by Water and Flexible Hydrophobic Nanopore," *ACS Nano* **15**(5), 9048 (2021). [CHRNS]
- Christovam, D.S., Freitas, G.S., Piva, M.M., Souza, J.C., Malcolms, M.O., Canton, O.L., Leão, J.B., Ratcliff, W., Lynn, J.W., Adriano, C., Pagliuso, P.G., "Evolution of the Magnetic Properties in the Antiferromagnet Ce_2RhIn_8 Simultaneously Doped with Cd and Ir," *Phys. Rev. B* **102**(19), 195137 (2020).
- Chu, S., Lin, K., Yang, T., Yu, C., Cao, Y., Zhang, Y., Sun, Y., Li, Z., Jiang, X., Lin, Z., Li, Q., Chen, J., Kato, K., Wu, H., Huang, Q., Xing, X., "Large Nonlinear Optical Effect in Tungsten Bronze Structures via Li/Na Cross-Substitutions," *Chem. Commun.* **56**(60), 8384 (2020).
- Chuang, P.-Y.A., Rahman, M.A., Mojica, F., Hussey, D.S., Jacobson, D.L., LaManna, J.M., "The Interactive Effect of Heat and Mass Transport on Water Condensation in the Gas Diffusion Layer of a Proton Exchange Membrane Fuel Cell," *J. Power Sources* **480**, 229121 (2020).
- Cleveland, IV, T., Blick, E., Krueger, S., Leung, A., Darwish, T., Butler, P., "Direct Localization of Detergents and Bacteriorhodopsin in the Lipidic Cubic Phase by Small-Angle Neutron Scattering," *IUCrJ* **8**(Part 1), 22 (2021). [CHRNS]
- Comert, F., Heinrich, F., Chowdhury, A., Schoeneck, M., Darling, C., Anderson, K.W., Libardo, M.D.J., Angeles-Boza, A.M., Silin, V., Cotten, M.L., Mihailescu, M., "Copper-Binding Anticancer Peptides from the Piscidin Family: an Expanded Mechanism that Encompasses Physical and Chemical Bilayer Disruption," *Sci. Rep.* **11**(1), 12620 (2021).
- Converse, E.S., Li, J., Mullins, A.C., LaBarre, P.G., Ramirez, A.P., Subramanian, M.A., "Influence of Alkaline-Earth-Metal Substitutions on the Bismuth Ruthenate Structure: $Bi_{2-x}A'_xRu_2O_6O'_{1-y}$ ($A' = Mg, Ca, Sr$)," *Inorg. Chem.* **59**(19), 14141 (2020).
- Corona, P.T., Silmore, K.S., Adkins, R., Lang, C., Lettinga, M.P., Swan, J.W., Leal, L.G., Helgeson, M.E., "Bayesian Estimations of Orientation Distribution Functions from Small-Angle Scattering Enable Direct Prediction of Mechanical Stress in Anisotropic Materials," *Phys. Rev. Mater.* **5**(6), 065601 (2021). [CHRNS]
- D'Agostino, G., Di Luzio, M., Sharp, N.E., Oddone, M., "A New Measurement of the ^{122}Sb Half-Life," *J. Radioanal. Nucl. Ch.* **329**(1), 411 (2021).
- Dahlman, C.J., Venkatesan, N.R., Corona, P.T., Kennard, R.M., Mao, L., Smith, N.C., Zhang, J., Seshadri, R., Helgeson, M.E., Chabiny, M.L., "Structural Evolution of Layered Hybrid Lead Iodide Perovskites in Colloidal Dispersions," *ACS Nano* **14**(9), 11294 (2020). [CHRNS]
- Dally, R.L., Lynn, J.W., Ghimire, N.J., Michel, D., Siegfried, P., Mazin, I.I., "Chiral Properties of the Zero-Field Spiral State and Field-Induced Magnetic Phases of the Itinerant Kagome Metal YMn_6Sn_6 ," *Phys. Rev. B* **103**(9), 094413 (2021).
- Dally, R.L., Phelan, D., Bishop, N., Ghimire, N.J., Lynn, J.W., "Isotropic Nature of the Metallic Kagome Ferromagnet Fe_3Sn_2 at High Temperatures," *Crystals* **11**(3), 307 (2021).
- De Hoe, G.X., Mao, J., Jiang, Z., Darling, S.B., Tirrell, M.V., Chen, W., "Probing Diffuse Polymer Brush Interfaces using Resonant Soft X-ray Scattering," *Synchrotron Radiat. News* **33**(4), 24 (2020). [CHRNS]
- De Mel, J.U., Gupta, S., Harmon, S., Stingaciu, L., Roth, E.W., Siebenbuerger, M., Bleuel, M., Schneider, G.J., "Acetaminophen Interactions with Phospholipid Vesicles Induced Changes in Morphology and Lipid Dynamics," *Langmuir*, in press. [CHRNS]
- De Mel, J.U., Gupta, S., Perera, R.M., Ngo, L., Zolnierczuk, P., Bleuel, M., Pingali, S.V., Schneider, G.J., "Influence of External NaCl Salt on Membrane Rigidity of Neutral DOPC Vesicles," *Langmuir* **36**(32), 9356 (2020). [CHRNS]
- De Mel, J.U., Gupta, S., Willner, L., Allgaier, J., Stingaciu, L.R., Bleuel, M., Schneider, G.J., "Manipulating Phospholipid Vesicles at the Nanoscale: A Transformation from Unilamellar to Multilamellar by an *n*-Alkyl-Poly(Ethylene Oxide)," *Langmuir* **37**(7), 2362 (2021). [CHRNS]

- DiPasquale, M., Gbadamosi, O., Nguyen, M.H.L., Castillo, S.R., Rickeard, B.W., Kelley, E.G., Nagao, M., Marquardt, D., "A Mechanical Mechanism for Vitamin E Acetate in E-Cigarette/Vaping-Associated Lung Injury," *Chem. Res. Toxicol.* **33**(9), 2432 (2020). [CHRNS]
- DiPasquale, M., Nguyen, M.H.L., Rickeard, B.W., Cesca, N., Tannous, C., Castillo, S.R., Katsaras, J., Kelley, E.G., Heberle, F.A., Marquardt, D., "The Antioxidant Vitamin E as a Membrane Raft Modulator: Tocopherols do not Abolish Lipid Domains," *Biochim. Biophys. Acta, Biomembr.* **1862**(8), 183189 (2020). [CHRNS]
- Dieterich, S., Prévost, S., Dargel, C., Sottmann, T., Giesselmann, F., "Synergistic Structures in Lyotropic Lamellar Gels," *Soft Matter* **16**(45), 10268 (2020).
- Dietz, T.C., Thompson, A., Al-Sheikhly, M., Sterniczuk, M., Bartels, D.M., "H₂ Production in the ¹⁰B(n,α)⁷Li Reaction in Water," *Radiat. Phys. Chem.* **180**, 109319 (2021).
- Dimeo, R., "Sketchnoting Science: How to Make Sketchnotes from Technical Content," *NIST Spec. Publ.* **1265**, 1 (2021). [CHRNS]
- Dimitrievska, M., Wu, H., Stavila, V., Babanova, O.A., Skoryunov, R.V., Soloninin, A.V., Zhou, W., Trump, B.A., Andersson, M.S., Skripov, A.V., Udovic, T.J., "Structural and Dynamical Properties of Potassium Dodecahydro-Monocarba-Closo-Dodecaborate: KCB₁₁H₁₂," *J. Phys. Chem. C* **124**(33), 17992 (2020). [CHRNS]
- Domhoff, A., Martin, T.B., Silva, M.S., Saberi, M., Creager, S., Davis, E.M., "Enhanced Proton Selectivity in Ionomer Nanocomposites Containing Hydrophobically Functionalized Silica Nanoparticles," *Macromolecules* **54**(1), 440 (2021).
- Dong, D., Kancharla, S., Hooper, J., Tsianou, M., Bedrov, D., Alexandridis, P., "Controlling the Self-Assembly of Perfluorinated Surfactants in Aqueous Environments," *Phys. Chem. Chem. Phys.* **23**(16), 10029 (2021). [CHRNS]
- Duell, B.A., Li, J., LaBarre, P.G., Zhang, J.J., Hermann, R.P., Ramirez, A.P., Subramanian, M.A., "Structure and Electronic Properties of CaAl_{12-x}Fe_xO₁₉ Hiconites," *J. Solid State Chem.* **291**, 121650 (2020).
- Dun, Z., Bai, X., Paddison, J.A.M., Hollingworth, E., Butch, N.P., Cruz, C.D., Stone, M.B., Hong, T., Demmel, F., Mourigal, M., Zhou, H., "Quantum Versus Classical Spin Fragmentation in Dipolar Kagome Ice Ho₃Mg₂Sb₃O₁₄," *Phys. Rev. X* **10**(3), 031069 (2020).
- Dun, Z., Daum, M., Baral, R., Fischer, H.E., Cao, H., Liu, Y., Stone, M.B., Rodriguez-Rivera, J.A., Choi, E.S., Huang, Q., Zhou, H., Mourigal, M., Frandsen, B.A., "Neutron Scattering Investigation of Proposed Kosterlitz-Thouless Transitions in the Triangular-Lattice Ising Antiferromagnet TmMgGaO₄," *Phys. Rev. B* **103**(6), 064424 (2021). [CHRNS]
- Dyatkin, B., Osti, N.C., Smith, R.W., Tyagi, M., Butler, T., Laskoski, M., "Chemical Structure and Curing Dynamics of Bisphenol S, PEEK™-like, and Resveratrol Phthalonitrile Thermoset Resins," *J. Polym. Sci.* **58**(24), 3419 (2020). [CHRNS]
- Ede, S.R., Poasada, C., Guffie, J., Ratcliff, W., Wu, H., Han, S., Luo, Z., "Synthesis and Characterization of Sr₂Co_{2-x}Fe_xO_{5+d} Perovskite Oxides," *Microsc. Microanal.*, in press. [CHRNS]
- Ede, S.R., Collins, C.N., Poasada, C.D., George, G., Wu, H., Ratcliff, W.D., Lin, Y., Wen, J., Han, S., Luo, Z., "Intermediate Sr₂Co_{1.5}Fe_{0.5}O_{6.6} Tetragonal Structure between Perovskite and Brownmillerite as a Model Catalyst with Layered Oxygen Deficiency for Enhanced Electrochemical Water Oxidation," *ACS Catal.* **11**(7), 4327 (2021). [CHRNS]
- Episcopo, N., Chang, P.-H., Heitmann, T.W., Wangmo, K., Guthrie, J.M., Fitta, M., Klein, R.A., Poudel, N., Gofryk, K., Zope, R.R., Brown, C.M., Nair, H.S., "Magnetic Structure, Excitations and Short-Range order in Honeycomb Na₂Ni₂TeO₆," *J. Phys.: Condens. Mat.* **33**(37), 375803 (2021).
- Erfani, A., Hanna, A., Zarrintaj, P., Manouchehri, S., Weigandt, K., Aichele, C.P., Ramsey, J.D., "Biodegradable Zwitterionic Poly(Carboxybetaine) Microgel for Sustained Delivery of Antibodies with Extended Stability and Preserved Function," *Soft Matter* **17**(21), 5349 (2021).
- Evans, H.A., Mao, L., Seshadri, R., Cheetham, A.K., "Layered Double Perovskites," *Ann. Rev. Mater. Res.* **51**, 351, (2021).
- Fallarino, L., Kirby, B.J., Fullerton, E.E., "Graded Magnetic Materials," *J. Phys. D Appl. Phys.* **54**(30), 303002 (2021).
- Fan, Y., Finley, J., Han, J., Holtz, M.E., Quarterman, P., Zhang, P., Safi, T.S., Hou, J.T., Grutter, A.J., Liu, L., "Resonant Spin Transmission Mediated by Magnons in a Magnetic Insulator Multilayer Structure," *Adv. Mater.* **33**(22), 2008555 (2021).
- Feng, J., Yuan, G., Mao, L., Leão, J.B., Bedell, R., Ramic, K., de Stefanis, E., Zhao, Y., Vidal, J., Liu, L., "Probing Layered Structure of Inconel 625 Coatings Prepared by Magnetron Sputtering," *Surf. Coat. Tech.* **405**, 126545 (2021).

- Foglia, F., Clancy, A.J., Berry-Gair, J., Lisowska, K., Wilding, M.C., Suter, T.M., Miller, T.S., Smith, K., Demmel, F., Appel, M., Garcia Sakai, V., Sella, A., Howard, C.A., Tyagi, M., Corà, F., McMillan, P.F., "Aquaporin-like Water Transport in Nanoporous Crystalline Layered Carbon Nitride," *Sci. Adv.* **6**(39), eabb6011 (2020). [CHRNS]
- Freitas, G.S., Piva, M.M., Grossi, R., Jesus, C.B.R., Souza, J.C., Christovam, D.S., Oliveira, Jr., N.F., Leão, J.B., Adriano, C., Lynn, J.W., Pagliuso, P.G., "Tuning the Crystalline Electric Field and Magnetic Anisotropy along the CeCuBi_{2-x}Sb_x Series," *Phys. Rev. B* **102**(15), 155129 (2020).
- Friberg, B.R., Glynos, E., Sakellariou, G., Tyagi, M., Green, P.F., "Effect of Molecular Stiffness on the Physical Aging of Polymers," *Macromolecules* **53**(18), 7684 (2020). [CHRNS]
- Fuhrman, W.T., Sidorenko, A., Hänel, J., Winkler, H., Prokofiev, A., Rodriguez-Rivera, J.A., Qiu, Y., Blaha, P., Si, Q., Broholm, C.L., Paschen, S., "Pristine Quantum Criticality in a Kondo Semimetal," *Sci. Adv.* **7**(21), eabf9134 (2021). [CHRNS]
- Ganeshan, K., Shin, Y.K., Osti, N.C., Sun, Y., Prenger, K., Naguib, M., Tyagi, M., Mamontov, E., Jiang, D.-E., van Duin, A.C.T., "Structure and Dynamics of Aqueous Electrolytes Confined in 2D-TiO₂/Ti₃C₂T₂ MXene Heterostructures," *ACS Appl. Mater. Inter.* **12**(52), 58378 (2020). [CHRNS]
- Gann, E., Crofts, T., Holland, G., Beaucage, P., McAfee, T., Kline, R.J., Collins, B.A., McNeill, C.R., Fischer, D.A., DeLongchamp, D.M., "A NIST Facility for Resonant Soft X-ray Scattering Measuring Nano-Scale Soft Matter Structure at NSLS-II," *J. Phys.: Condens. Mat.* **33**(16), 164001 (2021).
- Gao, J., Cai, Y., Qian, X., Liu, P., Wu, H., Zhou, W., Liu, D.-X., Li, L., Lin, R.-B., Chen, B., "A Microporous Hydrogen-Bonded Organic Framework for the Efficient Capture and Purification of Propylene" *Angew. Chem. Int. Edit.*, in press.
- Gao, Q., Shi, X., Venier, A., Carnera, A., Huang, Q., Wu, H., Chen, J., Sanson, A., Liang, E., "Effect of H₂O Molecules on Thermal Expansion of TiCo(CN)₆," *Inorg. Chem.* **59**(20), 14852 (2020).
- Gao, Q., Sun, Y., Shi, N., Milazzo, R., Pollastri, S., Olivi, L., Huang, Q., Liu, H., Sanson, A., Sun, Q., Liang, E., Xing, X., Chen, J., "Large Isotropic Negative Thermal Expansion in Water-Free Prussian Blue Analogues of ScCo(CN)₆," *Scripta Mater.* **187**, 119 (2020).
- Gaudet, J., Yang, H.-Y., Baidya, S., Lu, B., Xu, G., Zhao, Y., Rodriguez-Rivera, J.A., Hoffmann, C.M., Graf, D.E., Torchinsky, D.H., Nikolić, P., Vanderbilt, D., Tafti, F., Broholm, C.L., "Weyl-Mediated Helical Magnetism in NdAlSi," *Nat. Mater.*, in press. [CHRNS]
- Gehring, P., Helgeson, M., Louca, D., Olsen, B., Ross, K.A., Ross, N., Saunders, C., Xi, Y., "The 10th American Conference on Neutron Scattering," *Neutron News* **32**(1), 2 (2021).
- Ghimire, N.J., Dally, R.L., Poudel, L., Jones, D.C., Michel, D., Thapa Magar, N., Bleuel, M., McGuire, M.A., Jiang, J.S., Mitchell, J.F., Lynn, J.W., Mazin, I.I., "Competing Magnetic Phases and Fluctuation-Driven Scalar Spin Chirality in the Kagome Metal YMn₆Sn₆," *Sci. Adv.* **6**(51), eabe2680 (2020).
- Gilbert, P.H., Zhang, Z., Qian, K.K., Allen, D.P., Wagner, N.J., Liu, Y., "Preservative Induced Polysorbate 80 Micelle Aggregation," *J. Pharm. Sci.* **110**(6), 2395 (2021). [CHRNS]
- Gordon, M.B., Kloxin, C.J., Wagner, N.J., "Structural and Rheological Aging in Model Attraction-Driven Glasses by Rheo-SANS," *Soft Matter* **17**(4), 924 (2021). [CHRNS]
- Grinderslev, J.B., Andersson, M.S., Trump, B.A., Zhou, W., Udovic, T.J., Karlsson, M., Jensen, T.R., "Neutron Scattering Investigations of the Global and Local Structures of Ammine Yttrium Borohydrides," *J. Phys. Chem. C* **125**(28), 15415 (2021).
- Gu, X., Mavko, G., Ma, L., Oakley, D., Accardo, N., Carr, B.J., Nyblade, A.A., Brantley, S.L., "Seismic Refraction Tracks Porosity Generation and Possible CO₂ Production at Depth under a Headwater Catchment," *P. Natl. A. Sci. USA* **117**(32), 18991 (2020). [CHRNS]
- Gui, X., Klein, R.A., Brown, C.M., Xie, W., "Chemical Bonding Governs Complex Magnetism in MnPt₅P," *Inorg. Chem.* **60**(1), 87 (2021).
- Gui, X., Marshall, M., Dissanayaka Mudiyansele, R.S., Klein, R.A., Chen, Q., Zhang, Q., Shelton, W., Zhou, H., Brown, C.M., Cao, H., Greenblatt, M., Xie, W., "Spin Reorientation in Antiferromagnetic Layered FePt₅P," *ACS Appl. Electron. Mater.*, in press.
- Gundogdu, S., Clancy, J.P., Xu, G., Zhao, Y., Dube, P.A., Karalar, T.C., Cho, B.K., Lynn, J.W., Ramazanoglu, M., "Magnetic Order and Competition with Superconductivity in (Ho-Er) Ni₂B₂C," *Mater. Res. Express* **7**(11), 116002 (2020).

- Gupta, S., Ashkar, R., "The Dynamic Face of Lipid Membranes," *Soft Matter*, in press. [CHRNS]
- Habibi, N., Christau, S., Ochyl, L.J., Fan, Z., Hassani Najafabadi, A., Kuehnhammer, M., Zhang, M., Helgeson, M., von Klitzing, R., Moon, J.J., Lahann, J., "Engineered Ovalbumin Nanoparticles for Cancer Immunotherapy," *Adv. Ther.* **3**(10), 2000100 (2020). [CHRNS]
- Hadad, N., Anderson, D.C., Désert, S., Olsen, S.R., Sutton, I., Vehres, G., Adler, D., Ogg, B., Pierce, D., "8th Design and Engineering of Neutron Instruments Meeting in North Bethesda," *J. Neutron Res.* **22**(4), 371 (2020).
- Hameed, S., El-Khatib, S., Olson, K.P., Yu, B., Williams, T.J., Hong, T., Sheng, Q., Yamakawa, K., Zang, J., Uemura, Y.J., Zhao, G.Q., Jin, C.Q., Fu, L., Gu, Y., Ning, F., Cai, Y., Kojima, K.M., Freeland, J.W., Matsuda, M., Leighton, C., Greven, M., "Nature of the Ferromagnetic-Antiferromagnetic Transition in $Y_{1-x}La_xTiO_3$," *Phys. Rev. B* **104**(2), 024410 (2021).
- Han, B., Ding, X., Yu, B., Wu, H., Zhou, W., Liu, W., Wei, C., Chen, B., Qi, D., Wang, H., Wang, K., Chen, Y., Chen, B., Jiang, J., "Two-Dimensional Covalent Organic Frameworks with Cobalt(II)-Phthalocyanine Sites for Efficient Electrocatalytic Carbon Dioxide Reduction," *J. Am. Chem. Soc.* **143**(18), 7104 (2021).
- Han, J., Zhai, Y., Wang, Z., Bleuel, M., Liu, T., Yin, R., Wu, W., Hakem, I.F., Karim, A., Matyjaszewski, K., Bockstaller, M.R., "Nanosized Organo-Silica Particles with 'Built-in' Surface-Initiated Atom Transfer Radical Polymerization Capability as a Platform for Brush Particle Synthesis," *ACS Macro Lett.* **9**(9), 1218 (2020). [CHRNS]
- Han, Y., Wu, M., Gui, C., Zhu, C., Sun, Z., Zhao, M.-H., Savina, A.A., Abakumov, A.M., Wang, B., Huang, F., He, L., Chen, J., Huang, Q., Croft, M., Ehrlich, S., Khalid, S., Deng, Z., Jin, C., Grams, C.P., Hemberger, J., Wang, X., Hong, J., Adem, U., Ye, M., Dong, S., Li, M.-R., "Data-Driven Computational Prediction and Experimental Realization of Exotic Perovskite-Related Polar Magnets," *NPJ Quantum Mater.* **5**, 92 (2020).
- Hao, Y., Wo, H., Gu, Y., Zhang, X., Gu, Y., Zheng, S., Zhao, Y., Xu, G., Lynn, J.W., Nakajima, K., Murai, N., Wang, W., Zhao, J., "Field-Tuned Magnetic Structure and Phase Diagram of the Honeycomb Magnet $YbCl_3$," *Sci. China Phys. Mech. Astron.* **64**(3), 237411 (2021).
- Haque, M.A., Feric, T.G., Hamilton, S.T., Park, A.-H.A., Dadmun, M.D., "Structure and Dispersion of Free and Grafted Polymer in Nanoparticle Organic Hybrid Materials-Based Solutions by Small-Angle Neutron Scattering," *J. Phys. Chem. C* **125**(9), 5327 (2021).
- Hassan, M.T., Byron, W.A., Darius, G., DeAngelis, C., Wietfeldt, F.E., Collett, B., Jones, G.L., Komives, A., Noid, G., Stephenson, E.J., Bateman, F., Dewey, M.S., Gentile, T.R., Mendenhall, M.P., Nico, J.S., "Measurement of the Neutron Decay Electron-Antineutrino Angular Correlation by the aCORN Experiment," *Phys. Rev. C* **103**(4), 045502 (2021).
- Hayes, I.M., Wei, D.S., Metz, T., Zhang, J., Eo, Y.S., Ran, S., Saha, S.R., Collini, J., Butch, N.P., Agterberg, D.F., Kapitulnik, A., Paglione, J., "Multicomponent Superconducting Order Parameter in UTe_2 ," *Science*, in press.
- He, Z., Huang, R., Zhou, K., Liu, Y., Guo, S., Song, Y., Guo, Z., Hu, S., He, L., Huang, Q., Li, L., Zhang, J., Wang, S., Guo, J., Xing, X., Chen, J., "Superconductivity in Co-Layered $LaCoSi$," *Inorg. Chem.* **60**(9), 6157 (2021).
- He, Z., Song, Y., Zhou, K., Guo, S., Wu, J., Yin, C., Guo, Z., He, L., Huang, Q., Li, L., Huang, R., Guo, J., Xing, X., Chen, J., "Correlation of Tunable $CoSi_4$ Tetrahedron with the Superconducting Properties of $LaCoSi$," *Inorg. Chem.*, in press.
- Heacock, B., Sarenac, D., Cory, D.G., Huber, M.G., MacLean, J.P.W., Miao, H., Wen, H., Pushin, D.A., "Neutron Sub-Micrometre Tomography from Scattering Data," *IUCrJ* **7**(Part 5), 893 (2020).
- Heinrich, F., Van, Q.N., Jean-Francois, F., Stephen, A.G., Lösche, M., "Membrane-Bound KRAS Approximates an Entropic Ensemble of Configurations," *Biophys. J.*, in press.
- Henderson, D., Zhang, X., Mao, Y., Hu, L., Briber, R.M., Wang, H., "Cellulose Nanocomposites of Cellulose Nanofibers and Molecular Coils," *J. Compos. Sci.* **5**(8), 200 (2021).
- Hesse, S.A., Fritz, K.E., Beaucage, P.A., Thedford, R.P., Yu, F., DiSalvo, F.J., Suntivich, J., Wiesner, U., "Materials Combining Asymmetric Pore Structures with Well-Defined Mesoporosity for Energy Storage and Conversion," *ACS Nano* **14**(12), 16897 (2020).
- Hester, G., DeLazzer, T.N., Lim, S.S., Brown, C.M., Ross, K.A., "Néel Ordering in the Distorted Honeycomb Pyrosilicate: $C-Er_2Si_2O_7$," *J. Phys.: Condens. Mat.* **33**(12), 125804 (2021).
- Hester, G., DeLazzer, T.N., Yahne, D.R., Sarkis, C.L., Zhao, H.D., Rodriguez Rivera, J.A., Calder, S., Ross, K.A., "Magnetic Properties of the Ising-like Rare Earth Pyrosilicate: $D-Er_2Si_2O_7$," *J. Phys.: Condens. Mat.*, in press. [CHRNS]
- Higashi, K., Ochi, M., Nambu, Y., Yamamoto, T., Murakami, T., Yamashina, N., Tassel, C., Matsumoto, Y., Takatsu, H., Brown, C.M., Kageyama, H., "Enhanced Magnetic Interaction by Face-Shared Hydride Anions in $6H-BaCrO_2H$," *Inorg. Chem.*, in press.

- Higginbotham Duque, A.L., Patterson, B.M., Kuettner, L.A., Robillard, S.R., Mang, J.T., Perry, W.L., "Novel PBX Formulations Containing Thermally-Expandable Microspheres for On-Demand Control of Explosive Behavior," *AIP Conf. Proc.* **2272**(1), 100006 (2020).
- Hipp, J.B., Richards, J.J., Wagner, N.J., "Direct Measurements of the Microstructural Origin of Shear-Thinning in Carbon Black Suspensions," *J. Rheol.* **65**(2), 145 (2021). [CHRNS]
- Hoogerheide, D.P., Rostovtseva, T.K., Bezrukov, S.M., "Exploring Lipid-Dependent Conformations of Membrane-Bound α -Synuclein with the VDAC Nanopore," *BBA-Biomembranes*, in press.
- Hoogerheide, D.P., Rostovtseva, T.K., Jacobs, D., Gurnev, P.A., Bezrukov, S.M., "Tunable Electromechanical Nanopore Trap Reveals Populations of Peripheral Membrane Protein Binding Conformations," *ACS Nano* **15**(1), 989 (2021).
- Horkay, F., Chremos, A., Douglas, J.F., Jones, R., Lou, J., Xia, Y., "Comparative Experimental and Computational Study of Synthetic and Natural Bottlebrush Polyelectrolyte Solutions," *J. Chem. Phys.*, in press.
- Hu, X., Pajeroski, D.M., Zhang, D., Podlesnyak, A.A., Qiu, Y., Huang, Q., Zhou, H., Klich, I., Kolesnikov, A.I., Stone, M.B., Lee, S.-H., "Freezing of a Disorder Induced Spin Liquid with Strong Quantum Fluctuations," *Phys. Rev. Lett.* **127**(1), 017201 (2021).
- Hussey, D.S., Abir, M., Cook, J.C., Jacobson, D.L., LaManna, J.M., Kilaru, K., Ramsey, B.D., Khaykovich, B., "Design of a Neutron Microscope Based on Wolter Mirrors," *Nucl. Instrum. Meth. A* **987**, 164813 (2021).
- Hwang, I.Y., Lee, K.H., Chung, J.-H., Ikeuchi, K., Ovidiu Garlea, V., Yamauchi, H., Akatsu, M., Shamoto, S.-I., "Spin Wave Excitations in Honeycomb Antiferromagnet MnTiO_3 ," *J. Phys. Soc. Jpn.* **90**(6), 064708 (2021).
- Ishida, K., Tassel, C., Watabe, D., Takatsu, H., Brown, C.M., Nilsen, G.J., Kageyama, H., "Spin Frustration in Double Perovskite Oxides and Oxynitrides: Enhanced Frustration in $\text{La}_2\text{MnTaO}_5\text{N}$ with a Large Octahedral Rotation," *Inorg. Chem.* **60**(11), 8252 (2021).
- Janas, S., Lass, J., Ţuţueanu, A.-E., Haubro, M.L., Niedermayer, C., Stuhr, U., Xu, G., Prabhakaran, D., Deen, P.P., Holm-Dahlin, S., Lefmann, K., "Classical Spin Liquid or Extended Critical Range in h-YMnO_3 ?" *Phys. Rev. Lett.* **126**(10), 107203 (2021).
- Jaramillo, D.E., Jiang, H.Z.H., Evans, H.A., Chakraborty, R., Furukawa, H., Brown, C.M., Head-Gordon, M., Long, J.R., "Ambient-Temperature Hydrogen Storage via Vanadium(II)-Dihydrogen Complexation in a Metal-Organic Framework," *J. Am. Chem. Soc.* **143**(16), 6248 (2021).
- Jau, Y.-Y., Hussey, D.S., Gentile, T.R., Chen, W., "Electric Field Imaging using Polarized Neutrons," *Phys. Rev. Lett.* **125**(11), 110801 (2020).
- Jhalaria, M., Huang, Y., Ruzicka, E., Tyagi, M., Zorn, R., Zamponi, M., Garcia Sakai, V., Benicewicz, B., Kumar, S., "Activated Transport in Polymer Grafted Nanoparticle Melts," *Macromolecules* **54**(14), 6968 (2021). [CHRNS]
- Jiang, F., Zhang, X., Hwang, W., Nishiyama, Y., Briber, R.M., Wang, H., "Oligocellulose from Acid Hydrolysis: A Revisit," *Appl. Surf. Sci.* **537**, 147783 (2021).
- Jiang, S., Peng, R.L., Hegedűs, Z., Gnäupel-Herold, T., Moverare, J.J., Lienert, U., Fang, F., Zhao, X., Zuo, L., Jia, N., "Micromechanical Behavior of Multilayered Ti/Nb Composites Processed by Accumulative Roll Bonding: An *In-Situ* Synchrotron X-ray Diffraction Investigation," *Acta Mater.* **205**, 116546 (2021).
- Jing, Z., Tan, K.C., He, T., Yu, Y., Pei, Q., Wang, J., Wu, H., Chen, P., "Synthesis, Characterization, and Crystal Structure of Lithium Pyrrolide," *Acta Phys.-Chim. Sin.* **37**(11), 2009039 (2021).
- Jo, K.-I., Oh, Y., Kim, T.-H., Bang, J., Yuan, G., Satija, S.K., Sung, B.J., Koo, J., "Position-Dependent Diffusion Dynamics of Entangled Polymer Melts Nanoconfined by Parallel Immiscible Polymer Films," *ACS Macro Lett.* **9**(10), 1483 (2020).
- Jo, S., Xu, A., Curtis, J.E., Somani, S., MacKerell, Jr., A.D., "Computational Characterization of Antibody-Excipient Interactions for Rational Excipient Selection using the Site Identification by Ligand Competitive Saturation-Biologics Approach," *Mol. Pharmaceut.* **17**(11), 4323 (2020).
- Jørgensen, M., Zhou, W., Wu, H., Udovic, T.J., Paskevicius, M., Černý, R., Jensen, T.R., "Polymorphism of Calcium Decahydro-*Closo*-Decaborate and Characterization of its Hydrates," *Inorg. Chem.*, in press.
- Jung, B.T., Lim, M., Jung, K., Li, M., Dong, H., Dube, N., Xu, T., "Designing Sub-20 nm Self-Assembled Nanocarriers for Small Molecule Delivery: Interplay Among Structural Geometry, Assembly Energetics, and Cargo Release Kinetics," *J. Control. Release* **329**, 538 (2021). [CHRNS]
- Kancharla, S., Dong, D., Bedrov, D., Tsianou, M., Alexandridis, P., "Structure and Interactions in Perfluorooctanoate Micellar Solutions Revealed by Small-Angle Neutron Scattering and Molecular Dynamics Simulations Studies: Effect of Urea," *Langmuir* **37**(17), 5339 (2021). [CHRNS]
- Kancharla, S., Jahan, R., Bedrov, D., Tsianou, M., Alexandridis, P., "Role of Chain Length and Electrolyte on the Micellization of Anionic Fluorinated Surfactants in Water," *Colloid Surface. A*, in press. [CHRNS]

- Kancharla, S., Zoyhofski, N.A., Bufalini, L., Chatelais, B.F., Alexandridis, P., "Association between Nonionic Amphiphilic Polymer and Ionic Surfactant in Aqueous Solutions: Effect of Polymer Hydrophobicity and Micellization," *Polymers-Basel* **12**(8), 1831 (2020). [CHRNS]
- Karabanova, A., Knudsen, K.D., Berdiyeva, P., Cavalcanti, L.P., Liu, Y., van der Pal, M., Deledda, S., Blanchard, D., "Small-Angle Neutron Scattering Characterization of SrCl₂-ENG Composites for Thermochemical Heat Storage," *ACS Appl. Mater. Inter.* **13**(29), 34213 (2021). [CHRNS]
- Karimi, F., Pranzas, P.K., Puszkiel, J.A., Castro Riglos, M.V., Milanese, C., Vainio, U., Pistidda, C., Gizer, G., Klassen, T., Schreyer, A., Dornheim, M., "A Comprehensive Study on Lithium-Based Reactive Hydride Composite (Li-RHC) as a Reversible Solid-State Hydrogen Storage System Toward Potential Mobile Applications," *RSC Adv.* **11**(37), 23122 (2021).
- Kelley, E.G., Butler, P.D., Nagao, M., "Collective Dynamics in Lipid Membranes Containing Transmembrane Peptides," *Soft Matter* **17**(23), 5671 (2021). [CHRNS]
- Kelley, E.G., Butler, P.D., Ashkar, R., Bradbury, R., Nagao, M., "Scaling Relationships for the Elastic Moduli and Viscosity of Mixed Lipid Membranes," *P. Natl. A. Sci. USA* **117**(38), 23365 (2020). [CHRNS]
- Kelley, E.G., Nagao, M., Butler, P.D., Porcar, L., Farago, B., "Enhanced Dynamics in the Anomalous Melting Regime of DMPG Lipid Membranes," *Struct. Dynam.-US* **7**(5), 054704 (2020). [CHRNS]
- Khadka, D., Thapaliya, T.R., Hurtado Parra, S., Han, X., Wen, J., Need, R.F., Khanal, P., Wang, W., Zang, J., Kikkawa, J.M., Wu, L., Huang, S.X., "Kondo Physics in Antiferromagnetic Weyl Semimetal Mn_{3+x}Sn_{1-x} Films," *Sci. Adv.* **6**(35), eabc1977 (2020).
- Kim, M.G., Ratcliff, II, W., Pajerowski, D.M., Kim, J.-W., Yan, J.-Q., Lynn, J.W., Goldman, A.I., Kreyssig, A., "Magnetic Ordering and Structural Distortion in a PrFeAsO Single Crystal Studied by Neutron and X-ray Scattering," *Phys. Rev. B* **103**(17), 174405 (2021).
- Kim, Y., Kim, D., Lee, S., Kim, J., Hussey, D.S., Lee, S.W., "Neutron Grating Interferometer with an Analyzer Grating based on a Light Blocker," *Opt. Express* **28**(16), 23284 (2020).
- Klein, R.A., Evans, H.A., Trump, B.A., Udovic, T.J., Brown, C.M., "Neutron Scattering Studies of Materials for Hydrogen Storage," in "Comprehensive Inorganic Chemistry III," edited by Reedjik, J. and Poepelmeier, K., (Elsevier, Ltd., Amsterdam, Netherlands), in press.
- Kline, S.R., "2020 NIST Center for Neutron Research Accomplishments and Opportunities," *NIST Spec. Publ.* **1257**, 1 (2020).
- Knott, R., Dutta, N.K., Choudhury, N.R., "Molecular Structure Development in Silsesquioxane-Urethane Thin Film Hybrids: A Small-Angle Neutron Scattering Investigation," *J. Appl. Polym. Sci.* **137**(33), 48772 (2020).
- Krueger, S., Curtis, J.E., Scott, D.R., Grishaev, A., Glenn, G., Smith, G., Ellingsworth, L., Borisov, O., Maynard, E.L., "Structural Characterization and Modeling of a Respiratory Syncytial Virus Fusion Glycoprotein Nanoparticle Vaccine in Solution," *Mol. Pharmaceut.* **18**(1), 359 (2021). [CHRNS]
- Kruger, A.G., Brucks, S.D., Yan, T., Cárcarmo-Oyarce, G., Wei, Y., Wen, D.H., Carvalho, D.R., Hore, M.J.A., Ribbeck, K., Schrock, R.R., Kiessling, L.L., "Stereochemical Control Yields Mucin Mimetic Polymers," *ACS Central Sci.* **7**(4), 624 (2021). [CHRNS]
- Krzysko, A.J., Nakouzi, E., Zhang, X., Graham, T.R., Rosso, K.M., Schenter, G.K., Ilavsky, J., Kuzmenko, I., Frith, M.G., Ivory, C.F., Clark, S.B., Weston, J.S., Weigandt, K.M., De Yoreo, J.J., Chun, J., Anovitz, L.M., "Correlating Inter-Particle Forces and Particle Shape to Shear-Induced Aggregation/Fragmentation and Rheology for Dilute Anisotropic Particle Suspensions: A Complementary Study via Capillary Rheometry and *In-Situ* Small and Ultra-Small Angle X-ray Scattering," *J. Colloid Interf. Sci.* **576**, 47 (2020).
- Kumarage, T., Nguyen, J., Ashkar, R., "Neutron Spin Echo Spectroscopy as a Unique Probe for Lipid Membrane Dynamics and Membrane-Protein Interactions," *J. Visualized Exp.* (171), e62396 (2021). [CHRNS]
- Kumari, H., Wycoff, W.G., Mayhan, C.M., Kline, S.R., So, J.R., Deakynne, C.A., Adams, J.E., Atwood, J.L., "Solution Structure of Zinc-Seamed C-Alkylpyrogallol[4]arene Dimeric Nanocapsules," *RSC Adv.* **11**(6), 3342 (2021). [CHRNS]
- Kumari, P., Faraone, A., Kelley, E.G., Benedetto, A., "Stiffening Effect of the [Bmim][Cl] Ionic Liquid on the Bending Dynamics of DMPC Lipid Vesicles," *J. Phys. Chem. B* **125**(26), 7241 (2021). [CHRNS]
- Kupwade-Patil, K., Boul, P.J., Rasner, D.K., Lapidus, S.H., Leao, J.B., Johnson, K.D., Thaemlitz, C.J., Büyüköztürk, O., "In Situ Investigation of Phosphonate Retarder Interaction in Oil Well Cements at Elevated Temperature and Pressure Conditions," *J. Am. Ceram. Soc.* **103**(11), 6400 (2020).

- Kusano, T., Kumano, N., Yoshimune, W., Munekata, T., Matsunaga, T., Harada, M., "Interplay between Interparticle Potential and Adsorption Structure in Nanoparticle Dispersions with Polymer Addition as Displayed by Small-Angle Scattering," *Langmuir* **37**(24), 7503 (2021).
- Kushan, E., Demir, C., Senses, E., "Surfactant Driven Liquid to Soft Solid Transition of Cellulose Nanocrystal Suspensions," *Langmuir* **36**(32), 9551 (2020). [CHRNS]
- LaManna, J.M., Hussey, D.S., DiStefano, V.H., Baltic, E., Jacobson, D.L., "NIST NeXT: A System for Truly Simultaneous Neutron and X-ray Tomography," in "Hard X-Ray, Gamma-Ray, and Neutron Detector Physics XXII," edited by Burger, A.K, Payne, S.A., and Fiederle, M., (SPIE Optical Engineering & Applications, August 2020, online, CA) **11494**, (2020).
- Lane, H., Pachoud, E., Rodriguez-Rivera, J.A., Songvilay, M., Xu, G., Gehring, P.M., Attfield, J.P., Ewings, R.A., Stock, C., "Two-Dimensional Ferromagnetic Spin-Orbital Excitations in Honeycomb V_2O_3 ," *Phys. Rev. B* **104**(2), L020411 (2021). [CHRNS]
- Lanigan-Atkins, T., He, X., Krogstad, M.J., Pajeroski, D.M., Abernathy, D.L., Xu, G., Xu, Z., Chung, D.-Y., Kanatzidis, M.G., Rosenkranz, S., Osborn, R., Delaire, O., "Two-Dimensional Overdamped Fluctuations of the Soft Perovskite Lattice in CsPbBr_3 ," *Nat. Mater.* **20**, 977 (2021).
- Lavén, R., Häussermann, U., Perrichon, A., Andersson, M.S., Targama, M.S., Demmel, F., Karlsson, M., "Diffusional Dynamics of Hydride Ions in the Layered Oxyhydride SrVO_2H ," *Chem. Mater.* **33**(8), 2967 (2021). [CHRNS]
- Le Fer, G., Dilla, R.A., Wang, Z., King, J., Chuang, S.S.C., Becker, M.L., "Clustering and Hierarchical Organization of 3D Printed Poly(Propylene Fumarate)-*Block*-PEG-*Block*-Poly(Propylene Fumarate) ABA Triblock Copolymer Hydrogels," *Macromolecules* **54**(7), 3458 (2021). [CHRNS]
- LeMoine, J.-B., Halperin, C.T., "Comparing INAA and pXRF Analytical Methods for Ceramics: A Case Study with Classic Maya Wares," *J. Archaeol. Sci. Rep.* **36**, 102819 (2021).
- Lee, C.-H., Batsaikhan, E., Ma, M.-H., Li, W.-H., Wang, C.-W., Wu, C.-M., Yang, H.-D., Lynn, J.W., Berger, H., "Charge Transfer Enhanced Magnetic Correlations in Type-II Multiferroic Co_3TeO_6 ," *J. Chin. Chem. Soc.* **68**(3), 395 (2021).
- Lee, J.K., Lee, C., Fahy, K.F., Zhao, B., LaManna, J.M., Baltic, E., Jacobson, D.L., Hussey, D.S., Bazylak, A., "Critical Current Density as a Performance Indicator for Gas-Evolving Electrochemical Devices," *Cell Rep. Phys. Sci.* **1**(8), 100147 (2020).
- Lee, J.K., Lee, C., Fahy, K.F., Kim, P.J., Krause, K., LaManna, J.M., Baltic, E., Jacobson, D.L., Hussey, D.S., Bazylak, A., "Accelerating Bubble Detachment in Porous Transport Layers with Patterned Through-Pores," *ACS Appl. Energy Mater.* **3**(10), 9676 (2020).
- Lee, J.K., Lee, C., Fahy, K.F., Kim, P.J., LaManna, J.M., Baltic, E., Jacobson, D.L., Hussey, D.S., Stiber, S., Gago, A.S., Friedrich, K.A., Bazylak, A., "Spatially Graded Porous Transport Layers for Gas Evolving Electrochemical Energy Conversion: High Performance Polymer Electrolyte Membrane Electrolyzers," *Energ. Convers. Manage.* **226**, 113545 (2020).
- Lee, J.Y., Song, Y., Wessels, M.G., Jayaraman, A., Wooley, K.L., Pochan, D.J., "Hierarchical Self-Assembly of Poly(D-Glucose Carbonate) Amphiphilic Block Copolymers in Mixed Solvents," *Macromolecules* **53**(19), 8581 (2020). [CHRNS]
- Lee, Y.-F., Luo, Y., Bai, T., Velez, C., Brown, S.C., Wagner, N.J., "Microstructure and Rheology of Shear-Thickening Colloidal Suspensions with Varying Interparticle Friction: Comparison of Experiment with Theory and Simulation Models," *Phys. Fluids* **33**(3), 033316 (2021). [CHRNS]
- Leishman, A.W.D., Sokolova, A., Bleuel, M., Zhigadlo, N.D., Eskildsen, M.R., "Field Angle Dependent Vortex Lattice Phase Diagram in MgB_2 ," *Phys. Rev. B* **103**(9), 094516 (2021).
- Lenton, S., Wang, Q., Nylander, T., Teixeira, S., Holt, C., "Structural Biology of Calcium Phosphate Nanoclusters Sequestered by Phosphoproteins," *Crystals* **10**(9), 755 (2020).
- Li, S.S., Zhang, Q.H., Lin, S., Sang, X., Need, R.F., Roldan, M.A., Cui, W., Hu, Z., Jin, Q., Chen, S., Zhao, J., Wang, J.-O., Wang, J., He, M., Ge, C., Wang, C., Lu, H.-B., Wu, Z.P., Guo, H.Z., Tong, X., Zhu, T., Kirby, B., Gu, L., Jin, K.-J., Guo, E.-J., "Strong Ferromagnetism Achieved via Breathing Lattices in Atomically Thin Cobaltites," *Adv. Mater.* **33**(4), 2001324 (2021).
- Li, W.-H., Lee, C.-H., Ling, T.-Y., Ma, M.-H., Wei, P.-C., He, J.-H., Wu, C.-M., Peng, J.-C., Xu, G., Zhao, Y., Lynn, J.W., "Dual Lattice Incommensurabilities and Enhanced Lattice Perfection by Low-Temperature Thermal Annealing in Photoelectric $(\text{CH}_3\text{NH}_3)\text{PbBr}_3$," *Phys. Rev. Mater.* **5**(2), 025401 (2021).
- Li, Y., Zaki, N., Garlea, V.O., Savici, A.T., Fobes, D., Xu, Z., Camino, F., Petrovic, C., Gu, G., Johnson, P.D., Tranquada, J.M., Zaliznyak, I.A., "Electronic Properties of the Bulk and Surface States of $\text{Fe}_{1+y}\text{Te}_{1-x}\text{Se}_x$," *Nat. Mater.*, in press.

- Liang, B., Zhang, X., Xie, Y., Lin, R.-B., Krishna, R., Cui, H., Li, Z., Shi, Y., Wu, H., Zhou, W., Chen, B., "An Ultramicroporous Metal-Organic Framework for High Sieving Separation of Propylene from Propane," *J. Am. Chem. Soc.* **142**(41), 17795 (2020).
- Liang, K., Matsumoto, R.A., Zhao, W., Osti, N.C., Popov, I., Thapaliya, B.P., Fleischmann, S., Misra, S., Prenger, K., Tyagi, M., Mamontov, E., Augustyn, V., Unocic, R.R., Sokolov, A.P., Dai, S., Cummings, P.T., Naguib, M., "Engineering the Interlayer Spacing by Pre-Intercalation for High Performance Supercapacitor MXene Electrodes in Room Temperature Ionic Liquid," *Adv. Funct. Mater.*, in press. [CHRNS]
- Lin, B., Zhou, X., Zhao, H., Yuan, J., Zhou, K., Chen, K., Wu, H., Guo, R., Scheel, M.A., Chumakov, A., Roth, S.V., Mao, Y., Wang, L., Tang, Z., Müller-Buschbaum, P., Ma, W., "Balancing the Pre-Aggregation and Crystallization Kinetics Enables High Efficiency Slot-Die Coated Organic Solar Cells with Reduced Non-Radiative Recombination Losses," *Energ. Environ. Sci.* **13**(8), 2467 (2020).
- Lin, W.-C., Campbell, D.J., Ran, S., Liu, I.-L., Kim, H., Nevidomskyy, A.H., Graf, D., Butch, N.P., Paglione, J., "Tuning Magnetic Confinement of Spin-Triplet Superconductivity," *NPJ Quantum Mater.* **5**(1), 68 (2020).
- Lin, Y.-J., Horner, J., Illie, B., Lynch, M.L., Furst, E.M., Wagner, N.J., "Molecular Engineering of Thixotropic, Sprayable Fluids with Yield Stress using Associating Polysaccharides," *J. Colloid Interf. Sci.* **580**, 264 (2020). [CHRNS]
- Liu, I.-L., Heikes, C., Yildirim, T., Eckberg, C., Metz, T., Kim, H., Ran, S., Ratcliff, W.D., Paglione, J., Butch, N.P., "Quantum Oscillations from Networked Topological Interfaces in a Weyl Semimetal," *NPJ Quantum Mater.* **5**(1), 62 (2020).
- Liu, P., Klemm, M.L., Tian, L., Lu, X., Song, Y., Tam, D.W., Schmalzl, K., Park, J.T., Li, Y., Tan, G., Su, Y., Bourdarot, F., Zhao, Y., Lynn, J.W., Birgeneau, R.J., Dai, P., "In-plane Uniaxial Pressure-Induced Out-of-Plane Antiferromagnetic Moment and Critical Fluctuations in BaFe_2As_2 ," *Nat. Commun.* **11**(1), 5728 (2020).
- Liu, S., Kasbe, P.S., Yang, M., Shen, N., Duan, L., Mao, Y., Xu, W., "Intimately Bonded 2D Materials and Responsive Polymer Brushes for Adaptive Nanocomposites," *Polymer* **210**, 123033 (2020). [CHRNS]
- Liu, S., Tyagi, M., Akcora, P., "Polymer-Coupled Local Dynamics Enhances Conductivity of Ionic Liquids," *Macromolecules* **53**(15), 6538 (2020). [CHRNS]
- Liu, T., Wu, Z., Lu, C., Martin, R.P., "A Best Estimate Plus Uncertainty Safety Analysis Framework based on RELAP5-3D and RAVEN Platform for Research Reactor Transient Analyses," *Prog. Nucl. Eng.* **132**, 103610 (2021).
- Liu, Y., Kelley, E.G., Batchu, K.C., Porcar, L., Perez-Salas, U., "Creating Asymmetric Phospholipid Vesicles via Exchange with Lipid-Coated Silica Nanoparticles," *Langmuir* **36**(30), 8865 (2020). [CHRNS]
- Lopez, C.G., Horkay, F., Mussel, M., Jones, R.L., Richtering, W., "Screening Lengths and Osmotic Compressibility of Flexible Polyelectrolytes in Excess Salt Solutions," *Soft Matter* **16**(31), 7289 (2020). [CHRNS]
- López-Barrón, C.R., Vargas-Lara, F., Kang, S., "Single-Chain Conformation of Poly(α -olefins) in Dilute Solutions at the Crossover between Linear and Bottlebrush Architectures," *Macromolecules* **54**(14), 6854 (2021).
- Lorzing, G.R., Balto, K.P., Antonio, A.M., Trump, B.A., Brown, C.M., Bloch, E.D., "Elucidating the Structure of the Metal-Organic Framework Ru-HKUST-1," *Chem. Mater.* **32**(18), 7710 (2020).
- Luo, P., Jaiswal, A., Zhai, Y., Cai, Z., Walter, N.P., Zhou, L., Ding, D., Liu, M., Mills, R., Podlesynak, A., Ehlers, G., Faraone, A., Bai, H., Wang, W., Z., Y., "Atomic Dynamics of Metallic Glass Melts $\text{La}_{50}\text{Ni}_{15}\text{Al}_{35}$ and $\text{Ce}_{70}\text{Cu}_{19}\text{Al}_{11}$ Studied by Quasielastic Neutron Scattering," *Phys. Rev. B* **103**(22), 224104 (2021).
- Luo, P., Zhai, Y., Leao, J.B., Kofu, M., Nakajima, K., Faraone, A., Z, Y., "Neutron Spin-Echo Studies of the Structural Relaxation of Network Liquid ZnCl_2 at the Structure Factor Primary Peak and Prepeak," *J. Phys. Chem. Lett.* **12**(1), 392 (2021). [CHRNS]
- Luo, P., Zhai, Y., Senses, E., Mamontov, E., Xu, G., Z., Y., Faraone, A., "Influence of Kosmotrope and Chaotrope Salts on Water Structural Relaxation," *J. Phys. Chem. Lett.* **11**(21), 8970 (2020).
- Luzin, V., Spiridonov, P., Spencer, K., Gnaupel-Herold, T., "Neutron Diffraction Study of Macrostress and Microstress in $\text{Al-Al}_2\text{O}_3$ -Based Corrosion Protection Coating Obtained by Cold Spray (Dynamic Metallization)," *J. Therm. Spray Tech.* **29**(6), 1437 (2020).
- Lynn, J.W., Keimer, B., "Magnetic Scattering," in "Handbook of Magnetism and Magnetic Materials," edited by Coey, M. and Parkin, S. (Springer Nature, Switzerland), 1 (2021).

- Ma, L., Pollard, T.P., Zhang, Y., Schroeder, M.A., Ding, M.S., Cresce, A.V., Sun, R., Baker, D.R., Helms, B.A., Maginn, E.J., Wang, C., Borodin, O., Xu, K., "Functionalized Phosphonium Cations Enable Zinc Metal Reversibility in Aqueous Electrolytes," *Angew. Chem. Int. Edit.* **60**(22), 12438 (2021). [CHRNS]
- Mang, J.T., Hjelm, R.P., "Preferred Void Orientation in Uniaxially Pressed PBX 9502," *Propell. Explos. Pyrot.* **46**(1), 67 (2021). [CHRNS]
- Marcon, V., Hoagland, B., Gu, X., Liu, W., Kaye, J., DiBiase, R.A., Brantley, S.L., "How the Capacity of Bedrock to Collect Dust and Produce Soil Affects Phosphorus Bioavailability in the Northern Appalachian Mountains of Pennsylvania," *Earth Surf. Proc. Land.*, in press.
- Marx, D.C., Leblanc, M.J., Plummer, A.M., Krueger, S., Fleming, K.G., "Domain Interactions Determine the Conformational Ensemble of the Periplasmic Chaperone SurA," *Protein Sci.* **29**(10), 2043 (2020). [CHRNS]
- Marx, D.C., Plummer, A.M., Faustino, A.M., Devlin, T., Roskopf, M.A., Leblanc, M.J., Lessen, H.J., Amann, B.T., Fleming, P.J., Krueger, S., Fried, S.D., Fleming, K.G., "SurA is a Cryptically Grooved Chaperone that Expands Unfolded Outer Membrane Proteins," *P. Natl. A. Sci. USA* **117**(45), 28026 (2020). [CHRNS]
- Masud, A., Longanecker, M., Bhadauriya, S., Singh, M., Wu, W., Sharma, K., Terlier, T., Al-Enizi, A.M., Satija, S., Douglas, J.F., Karim, A., "Ionic Liquid Enhanced Parallel Lamellar Ordering in Block Copolymer Films," *Macromolecules* **54**(10), 4531 (2021).
- Mauws, C., Hiebert, N., Rutherford, M.L., Zhou, H.D., Huang, Q., Stone, M.B., Butch, N.P., Su, Y., Choi, E.S., Yamani, Z., Wiebe, C.R., "Magnetic Ordering in the Ising Antiferromagnetic Pyrochlore $\text{Nd}_2\text{ScNbO}_7$," *J. Phys.: Condens. Mat.* **33**, 245802 (2021).
- McCalla, E., Levin, E.E., Douglas, J.E., Barker, J.G., Frontzek, M., Tian, W., Fernandes, R.M., Seshadri, R., Leighton, C., "Understanding Magnetic Phase Coexistence in $\text{Ru}_2\text{Mn}_{1-x}\text{Fe}_x\text{Sn}$ Heusler Alloys: A Neutron Scattering, Thermodynamic, and Phenomenological Analysis," *Phys. Rev. Mater.* **5**(6), 064417 (2021).
- McCull, K., Griffith, K.J., Dally, R.L., Li, R., Douglas, J.E., Poepelmeier, K.R., Corà, F., Levin, I., Butala, M.M., "Energy Storage Mechanisms in Vacancy-Ordered Wadsley-Roth Layered Niobates," *J. Mater. Chem. A*, in press.
- McConville, C.A., Tao, Y., Evans, H.A., Trump, B.A., Lefton, J.B., Xu, W., Yakovenko, A.A., Kraka, E., Brown, C.M., Runčevski, T., "Peritectic Phase Transition of Benzene and Acetonitrile into a Cocrystal Relevant to Titan, Saturn's Moon," *Chem. Commun.* **56**(88), 13520 (2020).
- McFarlane, J., Anovitz, L.M., Cheshire, M.C., DiStefano, V.H., Bilheux, H.Z., Bilheux, J.-C., Daemen, L.L., Hale, R.E., Howard, R.L., Ramirez-Cuesta, A., Santodonato, L.J., Bleuel, M., Hussey, D.S., Jacobson, D.L., LaManna, J.M., Perfect, E., Qualls, L.M., "Water Migration and Swelling in Engineered Barrier Materials for Radioactive Waste Disposal," *Nucl. Technol.* **207**(8), 1237 (2021). [CHRNS]
- McTaggart, M., Li, X., Groves, M., Shah, V., Jugroot, M., Malardier-Jugroot, C., "Impact of Dimensionality and Confinement on Reaction Dynamics and Thermodynamics within 1D and 2D Nanostructures," *J. Chem. Phys.* **154**(17), 174903 (2021).
- Medina, E., Pathirana, V.H., Li, J., Ramirez, A.P., Subramanian, M.A., "Tetrahedral Mn^{4+} as Chromophore in Sillenite-Type Compounds," *J. Solid State Chem.* **289**, 121463 (2020).
- Méndez, R., Gómez-Ros, J.M., Thomas, D.J., Thompson, A.K., Bedogni, R., "Revision of the ^{252}Cf and D_2O -Moderated ^{252}Cf Reference Neutron Fields for use in Radiation Protection Dosimetry," *Radiat. Phys. Chem.* **184**, 109433 (2021).
- Miao, P., Tan, Z., Lee, S., Ishikawa, Y., Torii, S., Yonemura, M., Koda, A., Komatsu, K., Machida, S., Sano-Furukawa, A., Hattori, T., Lin, X., Li, K., Mochiku, T., Kikuchi, R., Kawashima, C., Takahashi, H., Huang, Q., Itoh, S., Kadono, R., Wang, Y., Pan, F., Yamauchi, K., Kamiyama, T., "Origin of Magnetovolume Effect in a Cobaltite," *Phys. Rev. B* **103**(9), 094302 (2021).
- Michalak, D.J., Lösche, M., Hoogerheide, D.P., "Charge Effects Provide Ångström-Level Control of Lipid Bilayer Morphology on Titanium Dioxide Surfaces," *Langmuir* **37**(13), 3970 (2021).
- Mills, J.N., Wagner, N.J., Mondal, P., "Relating Chemical Composition, Structure, and Rheology in Alkali-Activated Aluminosilicate Gels," *J. Am. Ceram. Soc.* **104**(1), 572 (2021). [CHRNS]
- Mirzamani, M., Dawn, A., Aswal, V.K., Jones, R.L., Smith, E.D., Kumari, H., "Investigating the Effect of a Simplified Perfume Accord and Dilution on the Formation of Mixed-Surfactant Microemulsions," *RSC Adv.* **11**(42), 25858 (2021).
- Mohammed, S., Liu, M., Gadikota, G., "Resolving the Organization of CO_2 Molecules Confined in Silica Nanopores using *In Situ* Small-Angle Neutron Scattering and Molecular Dynamics Simulations," *Environ. Sci.: Nano* **8**(7), 2006 (2021).
- Mohammed, S., Liu, M., Liu, Y., Gadikota, G., "Probing the Core-Shell Organization of Nanoconfined Methane in Cylindrical Silica Pores using *In Situ* Small-Angle Neutron Scattering and Molecular Dynamics Simulations," *Energ. Fuel.* **34**(12), 15246 (2020).

- Mojica, F., Rahman, M.A., Sarker, M., Hussey, D.S., Jacobson, D.L., LaManna, J.M., Chuang, P.-Y.A., "Study of Converging-Diverging Channel Induced Convective Mass Transport in a Proton Exchange Membrane Fuel Cell," *Energ. Convers. Manage.* **237**, 114095 (2021).
- Mueller, E., Himbert, S., Simpson, M.J., Bleuel, M., Rheinstadter, M.C., Hoare, T., "Cationic, Anionic, and Amphoteric Dual pH/Temperature-Responsive Degradable Microgels via Self-Assembly of Functionalized Oligomeric Precursor Polymers," *Macromolecules* **54**(1), 351 (2021). [CHRNS]
- Murray, P.D., Jensen, C.J., Quintana, A., Zhang, J., Zhang, X., Grutter, A.J., Kirby, B.J., Liu, K., "Electrically Enhanced Exchange Bias via Solid-State Magneto-Ionics," *ACS Appl. Mater. Interfaces*, in press.
- Nagao, M., Bradbury, R., Ansar, S.M., Kitchens, C.L., "Effect of Gold Nanoparticle Incorporation into Oil-Swollen Surfactant Lamellar Membranes," *Struct. Dynam.-US* **7**(6), 065102 (2020). [CHRNS]
- Nagao, M., Kelley, E.G., Faraone, A., Saito, M., Yoda, Y., Kurokuzu, M., Takata, S., Seto, M., Butler, P.D., "Relationship between Viscosity and Acyl Tail Dynamics in Lipid Bilayers," *Phys. Rev. Lett.*, in press. [CHRNS]
- Naidjonoka, P., Hernandez, M.A., Pålsson, G.K., Heinrich, F., Stålbrand, H., Nylander, T., "On the Interaction of Softwood Hemicellulose with Cellulose Surfaces in Relation to Molecular Structure and Physicochemical Properties of Hemicellulose," *Soft Matter* **16**(30), 7063 (2020).
- Nakada, A., Kato, D., Nelson, R., Takahira, H., Yabuuchi, M., Higashi, M., Suzuki, H., Kirsanova, M., Kakudou, N., Tassel, C., Yamamoto, T., Brown, C.M., Dronskowski, R., Saeki, A., Abakumov, A., Kageyama, H., Abe, R., "Conduction Band Control of Oxyhalides with a Triple-Fluorite Layer for Visible Light Photocatalysis," *J. Am. Chem. Soc.* **143**(6), 2491 (2021).
- Nakagawa, H., Saio, T., Nagao, M., Inoue, R., Sugiyama, M., Ajito, S., Tominaga, T., Kawakita, Y., "Conformational Dynamics of a Multidomain Protein by Neutron Scattering and Computational Analysis," *Biophys. J.*, in press. [CHRNS]
- Nakajima, Y., Metz, T., Eckberg, C., Kirshenbaum, K., Hughes, A., Wang, R., Wang, L., Saha, S.R., Liu, I.-L., Butch, N.P., Campbell, D., Eo, Y.S., Graf, D., Liu, Z., Borisenko, S.V., Zavalij, P.Y., Paglione, J., "Quantum-Critical Scale Invariance in a Transition Metal Alloy," *Comm. Phys.* **3**(1), 181 (2020).
- Nakatani, A.I., Mohler, C.E., Hughes, S., "Chain Conformation of Polymers Adsorbed to Clay Particles: Effects of Charge and Concentration," *Soft Matter* **17**(28), 6848 (2021).
- Neil, C.W., Mehana, M., Hjelm, R.P., Hawley, M.E., Watkins, E.B., Mao, Y., Viswanathan, H., Kang, Q., Xu, H., "Reduced Methane Recovery at High Pressure due to Methane Trapping in Shale Nanopores," *Commun. Earth Environ.* **1**(1), 49 (2020).
- Neves, P.M., Gilbert, D.A., Ran, S., Liu, I.-L., Saha, S., Collini, J., Bleuel, M., Paglione, J., Borchers, J.A., Butch, N.P., "Effect of Chemical Substitution on the Skyrmion Phase in Cu_2OSeO_3 ," *Phys. Rev. B* **102**(13), 134410 (2020). [CHRNS]
- Newton, T., Turkoglu, D., Diamond, D., Cheng, L.-Y., "Comparison of LEU Fuel Designs for the NBSR and a Replacement Reactor Concept," *T. Am. Nucl. Soc.* **123**(1), 319 (2020).
- Newton, T., Flynn, D., Williams, R., "The National Bureau of Standards Reactor at the NIST Center for Neutron Research," in "Encyclopedia of Nuclear Energy, Vol. 4," edited by Greenspan, E., (Elsevier, Amsterdam, Netherlands) **74** (2021).
- Nguyen, M.H.L., DiPasquale, M., Rikeard, B.W., Yip, C.G., Greco, K.N., Kelley, E.G., Marquardt, D., "Time-Resolved SANS Reveals Pore-Forming Peptides Cause Rapid Lipid Reorganization," *New J. Chem.* **45**(1), 447 (2021). [CHRNS]
- Nichols, N.S., Prisk, T.R., Warren, G., Sokol, P., Del Maestro, A., "Dimensional Reduction of Helium-4 Inside Argon-Plated MCM-41 Nanopores," *Phys. Rev. B* **102**(14), 144505 (2020).
- Nie, Z., Parai, R., Cai, C., Michaelis, C., LaManna, J.M., Hussey, D.S., Jacobson, D.L., Ghosh, D., Koenig, Jr., G.M., "Pore Microstructure Impacts on Lithium Ion Transport and Rate Capability of Thick Sintered Electrodes," *J. Electrochem. Soc.* **168**(6), 060550 (2021).
- Niedziela, J.L., Bansal, D., Ding, J., Lanigan-Atkins, T., Li, C., May, A.F., Wang, H., Lin, J.Y.Y., Abernathy, D.L., Ehlers, G., Huq, A., Parshall, D., Lynn, J.W., Delaire, O., "Controlling Phonon Lifetimes via Sublattice Disorder in AgBiSe_2 ," *Phys. Rev. Mater.* **4**(10), 105402 (2020).
- Osti, N.C., Thapaliya, B.P., Dai, S., Tyagi, M., Mamontov, E., "Strong Enhancement of Nanoconfined Water Mobility by a Structure Breaking Salt," *J. Phys. Chem. Lett.* **12**(16), 4038 (2021). [CHRNS]
- Ozaki, D., Suzuki, H., Ogawa, K., Sakamoto, R., Inaguma, Y., Nakashima, K., Tomita, O., Kageyama, H., Abe, R., "Synthesis, Band Structure and Photocatalytic Properties of Sillén-Aurivillius Oxychlorides $\text{BaB}_5\text{T}_3\text{O}_{14}\text{Cl}$, $\text{Ba}_2\text{B}_{15}\text{T}_{14}\text{O}_{17}\text{Cl}$ and $\text{Ba}_3\text{B}_{15}\text{T}_{15}\text{O}_{20}\text{Cl}$ with Triple-, Quadruple- and Quintuple-Perovskite Layers," *J. Mater. Chem. A* **9**(13), 8332 (2021).

- Pan, B.Y., Xu, H.C., Liu, Y., Sutarto, R., He, F., Shen, Y., Hao, Y.Q., Zhao, J., Harriger, L., Feng, D.L., "Anomalous Helimagnetic Domain Shrinkage due to the Weakening of the Dzyaloshinskii-Moriya Interaction in CrAs," *Phys. Rev. B* **102**(10), 104432 (2020).
- Pan, L., Grutter, A., Zhang, P., Che, X., Nozaki, T., Stern, A., Street, M., Zhang, B., Casas, B., He, Q.L., Choi, E.S., Disseler, S.M., Gilbert, D.A., Yin, G., Shao, Q., Deng, P., Wu, Y., Liu, X., Kou, X., Masashi, S., Han, X., Binek, C., Chambers, S., Xia, J., Wang, K.L., "Observation of Quantum Anomalous Hall Effect and Exchange Interaction in Topological Insulator/Antiferromagnet Heterostructure," *Adv. Mater.* **32**, 2001460 (2020).
- Paris, E.H., Bishop, R.L., López Bravo, R., Sullivan, T.D., "Imitation Games: The Exchange and Emulation of Fine Orange Pottery in Central Chiapas, Mexico," *J. Anthropol. Archaeol.* **62**, 101306 (2021).
- Park, C.B., Shin, K.W., Chun, S.H., Lee, J.H., Oh, Y.S., Disseler, S.M., Heikes, C.A., Ratcliff, W.D., Noh, W.-S., Park, J.-H., Kim, K.H., "Control of Magnetoelectric Coupling in the Co₂Y-Type Hexaferrites," *Phys. Rev. Mater.* **5**(3), 034412 (2021).
- Pathirana, V.H., LaBarre, P.G., Li, J., Ramirez, A.P., Subramanian, M.A., "Ambient Pressure Synthesis and Characterization of Layered Honeycomb Li₂PdO₃," *Solid State Commun.* **319**, 114011 (2020).
- Peng, J., Cantillo, N.M., Nelms, K.M., Roberts, L.S., Goenaga, G., Imel, A., Barth, B.A., Dadmun, M., Heroux, L., Hayes, D.G., Zawodzinski, T., "Electron Transfer in Microemulsion-Based Electrolytes," *ACS Appl. Mater. Inter.* **12**(36), 40213 (2020). [CHRNS]
- Peng, K., Preisig, N., Sottmann, T., Stubenrauch, C., "Formulation of Gelled Non-Toxic Bicontinuous Microemulsions Stabilized by Highly Efficient Alkanoyl Methylglucamides," *Langmuir* **36**(42), 12692 (2020).
- Peng, S., "Advanced Understanding of Gas Flow and the Klinkenberg Effect in Nanoporous Rocks," *J. Petrol. Sci. Eng.*, in press.
- Peng, S., Zhu, D., Li, W., Wu, H., Grutter, A.J., Gilbert, D.A., Lu, J., Xiong, D., Cai, W., Shafer, P., Wang, K.L., Zhao, W., "Exchange Bias Switching in an Antiferromagnet/Ferromagnet Bilayer Driven by Spin-Orbit Torque," *Nat. Electron.* **3**(12), 757 (2020).
- Pełowski, P.N., Yokley, Z.W., Liebel, M., Cheng, S., Elphic, R.C., Hoogerheide, S.F., Lawrence, D.J., Nico, J.S., "Position-Dependent Neutron Detection Efficiency Loss in ³He Gas Proportional Counters," *Nucl. Instrum. Meth. A* **982**, 164574 (2020).
- Perera, R.M., Gupta, S., Li, T., Bleuel, M., Hong, K., Schneider, G.J., "Influence of NaCl on Shape Deformation of Polymersomes," *Soft Matter* **17**(16), 4452 (2021). [CHRNS]
- Perry, W.L., Duque, A.L., Mang, J.T., Culp, D.B., "Computing Continuum-Level Explosive Shock and Detonation Response over a Wide Pressure Range from Microstructural Details," *Combust. Flame*, in press.
- Perticaroli, S., Herzberger, J., Sun, Y., Nickels, J.D., Murphy, R.P., Weigandt, K., Ray, P.J., "Multiscale Microstructure, Composition, and Stability of Surfactant/Polymer Foams," *Langmuir* **36**(48), 14763 (2020).
- Plymale, A.E., Wells, J.R., Pearce, C.I., Brislaw, C.J., Graham, E.B., Cheeke, T.E., Allen, J.L., Fansler, S.J., Arey, B.W., Bowden, M.E., Saunders, D.L., Danna, V.G., Tyrrell, K.J., Weaver, J.L., Sjöblom, R., Paul, R., McCloy, J.S., Hjörthner-Holdar, E., Englund, M., Ogenhall, E., Peeler, D.K., Kruger, A.A., "Niche Partitioning of Microbial Communities at an Ancient Vitrified Hillfort: Implications for Vitrified Radioactive Waste Disposal," *Geomicrobiol. J.* **38**(1), 36 (2021).
- Potashnikov, D., Caspi, E.N., Pesach, A., Kota, S., Sokol, M., Hanner, L.A., Barsoum, M.W., Evans, H.A., Eyal, A., Keren, A., Rivin, O., "Magnetic Properties of (Fe_{1-x}Mn_x)₂AlB₂ and the Impact of Substitution on the Magnetocaloric Effect," *Phys. Rev. Mater.* **4**(8), 084404 (2020).
- Prabhu, V.M., Ali, S., Bleuel, M., Mao, Y., Ma, Y., "Ultra-Small Angle Neutron Scattering to Study Droplet Formation in Polyelectrolyte Complex Coacervates," in "Methods in Enzymology, Vol. 646," edited by Keating, C.D., (Academic Press, Imprint of Elsevier, Cambridge, MA) Chap. **9**, 261 (2021). [CHRNS]
- Prisk, T.R., Hanna, S., Azuah, R.T., "Self-Diffusion of Liquid Hydrogen: A Quasi-Elastic Neutron Scattering Study," *J. Low Temp. Phys.* **201**(3), 451 (2020). [CHRNS]
- Pritchard, K., Chabot, J.P., Robucci, R., Choa, F.S., Osovizky, A., Ziegler, J., Binkley, E., Tsai, P., Hadad, N., Jackson, M., Hurlbut, C., Baltic, G.M., Majkrzak, C.F., Maliszewskij, N.C., "Real-Time Signal Processing for Mitigating SiPM Dark Noise Effects in a Scintillating Neutron Detector," *IEEE T. Nucl. Sci.* **68**(7), 1519 (2021).
- Pritchard, K., Chabot, J.P., Tsai, P., Robucci, R., Choa, F.S., Osovizky, A., Ziegler, J., Binkley, E., Hadad, N., Jackson, M., Hurlbut, C., Baltic, G.M., Majkrzak, C.F., Maliszewskij, N.C., "Measuring Deadtime and Double-Counts in a Non-Paralyzable Scintillating Neutron Detector using Arrival Time Statistics," *Nucl. Instrum. Meth. A* **1001**, 165270 (2021).

- Pritchard, K., Hussey, D., Osovizky, A., Ziegler, J., Binkley, E., Tsai, P., Hadad, N., Jackson, M., Hurlbut, C., Baltic, G.M., Majkrzak, C.F., Maliszewskij, N.C., "Cold Neutron Radiation Dose Effects on a $^6\text{LiF:ZnS(Ag)}$ Neutron Detector with Wavelength Shifting Fibers and SiPM Photodetector," *Nucl. Instrum. Meth. A* **986**, 164808 (2021).
- Qian, Q.-L., Gu, X.-W., Pei, J., Wen, H.-M., Wu, H., Zhou, W., Li, B., Qian, G., "A Novel Anion-Pillared Metal-Organic Framework for Highly Efficient Separation of Acetylene from Ethylene and Carbon Dioxide," *J. Mater. Chem. A* **9**(14), 9248 (2021).
- Qiu, J., Chen, X., López-Barrón, C.R., Rohde, B.J., Robertson, M.L., Krishnamoorti, R., "Effect of Copolymer Composition on Thermodynamic Interactions in Blends Containing a Diene-Olefin Copolymer and a Polyolefin," *Macromolecules* **53**(21), 9491 (2020). [CHRNS]
- Queralt-Martín, M., Hoogerheide, D.P., Noskov, S.Y., Berezhkovskii, A.M., Rostovtseva, T.K., Bezrukov, S.M., "VDAC Gating Thermodynamics, but Not Gating Kinetics, Are Virtually Temperature Independent," *Biophys. J.* **119**(12), 2584 (2020).
- Qviller, A.J., Frommen, C., Hauback, B.C., Magnus, F., Kirby, B.J., Hjörvarsson, B., "Direct Observation of Magnetic Proximity Effects in Amorphous Exchange-Spring Magnets by Neutron Reflectometry," *Phys. Rev. Mater.* **4**(10), 104404 (2020).
- Ran, S., Liu, I.-L., Saha, S.R., Saraf, P., Paglione, J., Butch, N.P., "Comparison of Two Different Synthesis Methods of Single Crystals of Superconducting Uranium Ditelluride," *J. Visualized Exp.* (173), e62563 (2021).
- Rostom, S., White, B.T., Yuan, G., Saito, T., Dadmun, M.D., "Polymer Chain Diffusion in All-Polymer Nanocomposites: Confinement vs Chain Acceleration," *J. Phys. Chem. C* **124**(34), 18834 (2020).
- Rostovtseva, T.K., Bezrukov, S.M., Hoogerheide, D.P., "Regulation of Mitochondrial Respiration by VDAC is Enhanced by Membrane-Bound Inhibitors with Disordered Polyanionic C-Terminal Domains," *Int. J. Mol. Sci.* **22**(14), 7358 (2021).
- Rubinson, K.A., "Why Proteins are Big: Length Scale Effects on Equilibria and Kinetics," *Protein J.* **38**(2), 95 (2019). [CHRNS]
- Saaun, P., Zhao, Y., Piyawongwathana, P., Sato, T.J., Chou, F.C., Avdeev, M., Gitgeatpong, G., Matan, K., "Magnetic Properties and Magnetic Structure of the Frustrated Quasi-One-Dimensional Antiferromagnet $\text{SrCuTe}_2\text{O}_6$," *Phys. Rev. B* **102**(13), 134407 (2020).
- Saini, A., Borchers, J.A., George, S., Maranville, B.B., Krycka, K.L., Dura, J.A., Theis-Bröhl, K., Wolff, M., "Layering of Magnetic Nanoparticles at Amorphous Magnetic Templates with Perpendicular Anisotropy," *Soft Matter* **16**(33), 7676 (2020). [CHRNS]
- Saini, A., Theis-Bröhl, K., Koutsioubas, A., Krycka, K.L., Borchers, J.A., Wolff, M., "Magnetic Particle Self-Assembly at Functionalized Interfaces," *Langmuir* **37**(14), 4064 (2021). [CHRNS]
- Sala, G., Stone, M.B., Rai, B.K., May, A.F., Laurell, P., Garlea, V.O., Butch, N.P., Lumsden, M.D., Ehlers, G., Pokharel, G., Podlesnyak, A., Mandrus, D., Parker, D.S., Okamoto, S., Halász, G.B., Christianson, A.D., "Van Hove Singularity in the Magnon Spectrum of the Antiferromagnetic Quantum Honeycomb Lattice," *Nat. Commun.* **12**(1), 171 (2021).
- Samant, S., Basutkar, M., Singh, M., Masud, A., Grabowski, C.A., Kisslinger, K., Strzalka, J., Yuan, G., Satija, S., Apata, I., Raghavan, D., Durstock, M., Karim, A., "Effect of Molecular Weight and Layer Thickness on the Dielectric Breakdown Strength of Neat and Homopolymer Swollen Lamellar Block Copolymer Films," *ACS Appl. Polym. Mater.* **2**(8), 3072 (2020).
- Sanchez-Fernandez, A., Leung, A.E., Kelley, E.G., Jackson, A.J., "Complex by Design: Hydrotrope-Induced Micellar Growth in Deep Eutectic Solvents," *J. Colloid Interf. Sci.* **581**(Part A), 292 (2021). [CHRNS]
- Sang, G., Liu, S., Elsworth, D., Zhang, R., Bleuel, M., "Pore-Scale Water Vapor Condensation Behaviors in Shales: An Experimental Study," *Transport Porous Med.* **135**(3), 713 (2020). [CHRNS]
- Sapkota, A., Li, Y., Winn, B.L., Podlesnyak, A., Xu, G., Xu, Z., Ran, K., Chen, T., Sun, J., Wen, J., Wu, L., Yang, J., Li, Q., Gu, G.D., Tranquada, J.M., "Electron-Phonon Coupling and Superconductivity in the Doped Topological Crystalline Insulator $(\text{Pb}_{0.5}\text{Sn}_{0.5})_{1-x}\text{In}_x\text{Te}$," *Phys. Rev. B* **102**(10), 104511 (2020).
- Sarkis, C.L., Rau, J.G., Sanjeeva, L.D., Powell, M., Kolis, J., Marbey, J., Hill, S., Rodriguez-Rivera, J.A., Nair, H.S., Yahne, D.R., Säubert, S., Gingras, M.J.P., Ross, K.A., "Unravelling Competing Microscopic Interactions at a Phase Boundary: A Single-Crystal Study of the Metastable Antiferromagnetic Pyrochlore $\text{Yb}_2\text{Ge}_2\text{O}_7$," *Phys. Rev. B* **102**(13), 134418 (2020). [CHRNS]
- Sarte, P.M., Cruz-Kan, K., Ortiz, B.R., Hong, K.H., Bordelon, M.M., Reig-i-Plessis, D., Lee, M., Choi, E.S., Stone, M.B., Calder, S., Pajerowski, D.M., Mangin-Thro, L., Qiu, Y., Atfield, J.P., Wilson, S.D., Stock, C., Zhou, H.D., Hallas, A.M., Paddison, J.A.M., Aczel, A.A., Wiebe, C.R., "Dynamical Ground State in the XY Pyrochlore $\text{Yb}_2\text{GaSbO}_7$," *NPJ Quantum Mater.* **6**(1), 42 (2021).

- Schafer, B.C., Byron, W.A., Chen, W.C., Collett, B., Dewey, M.S., Gentile, T.R., Hassan, M.T., Jones, G.L., Komives, A., Wietfeldt, F.E., "Neutron Polarimetry using a Polarized ^3He Cell for the aCORN Experiment," *Nucl. Instrum. Meth. A* **988**, 164862 (2021).
- Scheie, A., Kindervater, J., Zhang, S., Changlani, H.J., Sala, G., Ehlers, G., Heinemann, A., Tucker, G.S., Koohpayeh, S.M., Broholm, C., "Multiphase Magnetism in $\text{Yb}_2\text{Ti}_2\text{O}_7$," *P. Natl. A. Sci. USA* **117**(44), 27245 (2020).
- Schneeloch, J.A., Tao, Y., Duan, C., Matsuda, M., Aczel, A.A., Fernandez-Baca, J.A., Xu, G., Neuefeind, J.C., Yang, J., Louca, D., "Evolution of the Structural Transition in $\text{Mo}_{1-x}\text{W}_x\text{Te}_2$," *Phys. Rev. B* **102**(5), 054105 (2020).
- Schneider, K., Verkoyen, P., Krappel, M., Gardiner, C., Schweins, R., Frey, H., Sottmann, T., "Efficiency Boosting of Surfactants with Poly(Ethylene Oxide)-Poly(Alkyl Glycidyl Ether)s: A New Class of Amphiphilic Polymers," *Langmuir* **36**(33), 9849 (2020).
- Senses, E., Kitchens, C.L., Faraone, A., "Viscosity Reduction in Polymer Nanocomposites: Insights from Dynamic Neutron and X-ray Scattering," *J. Polym. Sci.*, in press. [CHRNS]
- Sepulveda-Medina, P.I., Tyagi, M., Wang, C., Vogt, B.D., "Water Dynamics within Nanostructured Amphiphilic Statistical Copolymers from Quasielastic Neutron Scattering," *J. Chem. Phys.* **154**(15), 154903 (2021). [CHRNS]
- Shafaque, H.W., Lee, C., Fahy, K.F., Lee, J.K., LaManna, J.M., Baltic, E., Hussey, D.S., Jacobson, D.L., Bazylak, A., "Boosting Membrane Hydration for High Current Densities in Membrane Electrode Assembly CO_2 Electrolysis," *ACS Appl. Mater. Inter.* **12**(49), 54585 (2020).
- Sharma, V.K., Hayes, D.G., Urban, V.S., O'Neill, H., Tyagi, M., Mamontov, E., "Melittin Exerts Opposing Effects on Short- and Long-Range Dynamics in Bicontinuous Microemulsions," *J. Colloid Interf. Sci.* **590**, 94 (2021).
- Sharma, V.K., Mukhopadhyay, R., Mohanty, A., Tyagi, M., Embs, J.P., Sarma, D.D., "Contrasting Behaviors of FA and MA Cations in APbBr_3 ," *J. Phys. Chem. Lett.* **11**(22), 9669 (2020). [CHRNS]
- Sharma, V.K., Mukhopadhyay, R., Mohanty, A., García Sakai, V., Tyagi, M., Sarma, D.D., "Contrasting Effects of FA Substitution on MA/FA Rotational Dynamics in $\text{FA}_x\text{MA}_{1-x}\text{PbI}_3$," *J. Phys. Chem. C* **125**(24), 13666 (2021). [CHRNS]
- Shen, F., Zhou, H., Hu, F., Wang, J.-T., Wu, H., Huang, Q., Hao, J., Yu, Z., Gao, Y., Lin, Y., Wang, Y., Zhang, C., Yin, Z., Wang, J., Deng, S., Chen, J., He, L., Liang, T., Sun, J.-R., Zhao, T., Shen, B., "A Distinct Spin Structure and Giant Baromagnetic Effect in MnNiGe Compounds with Fe-Doping," *J. Am. Chem. Soc.* **143**(18), 6798 (2021).
- Shen, J., Pan, X., Bhatia, S.R., "Self-Assembly and Thermoreversible Rheology of Perfluorocarbon Nanoemulsion-Based Gels with Amphiphilic Copolymers," *Colloid Surface. B* **202**, 111641 (2021).
- Shrestha, U.M., Han, L., Saito, T., Schweizer, K.S., Dadmun, M.D., "Mechanism of Soft Nanoparticle Diffusion in Entangled Polymer Melts," *Macromolecules* **53**(17), 7580 (2020).
- Sieber, J., Marlow, A., Paul, R., Barber, C., Wood, L., Yu, L., Rieke, A., Carl, R., Kutnerian, A., McCandless, J., Wallace, C., "Quantitative Analysis of Zirconium Alloys using Borate Fusion and Wavelength Dispersive X-ray Fluorescence Spectrometry," *X-ray Spectrom.* **50**(3), 210 (2021).
- Silin, V.I., Hoogerheide, D.P., "pH Dependent Electrical Properties of the Inner- and Outer- Leaflets of Biomimetic Cell Membranes," *J. Colloid Interf. Sci.* **594**, 279 (2021).
- Sinha, N.J., Kloxin, C.J., Saven, J.G., Jensen, G.V., Kelman, Z., Pochan, D.J., "Recombinant Expression of Computationally Designed Peptide-Bundlers in *Escherichia Coli*," *J. Biotechnol.* **330**, 57 (2021).
- Skripov, A.V., Majer, G., Babanova, O.A., Skoryunov, R.V., Soloninin, A.V., Ley, M.B., Jensen, T.R., Orimo, S., Udovic, T.J., "Lithium-Ion Diffusivity in Complex Hydrides: Pulsed-Field-Gradient NMR Studies of $\text{LiLa}(\text{BH}_4)_3\text{Cl}$, $\text{Li}_3(\text{NH}_2)_2\text{I}$ and $\text{Li-1-CB}_9\text{H}_{10}$," *Solid State Ion.* **362**, 115585 (2021).
- Skripov, A.V., Soloninin, A.V., Valeeva, A.A., Gusev, A.I., Rempel, A.A., Wu, H., Udovic, T.J., "Hydrogen in Nonstoichiometric Cubic Titanium Monoxides: X-ray and Neutron Diffraction, Neutron Vibrational Spectroscopy and NMR Studies," *J. Alloy Compd.*, in press.
- Skripov, A.V., Majer, G., Babanova, O.A., Skoryunov, R.V., Soloninin, A.V., Dimitrievska, M., Udovic, T.J., "Na⁺ Diffusivity in Carbon-Substituted *Nido*- and *Closo*-Hydroborate Salts: Pulsed-Field-Gradient NMR Studies of $\text{Na-7-CB}_{10}\text{H}_{13}$ and $\text{Na}_2(\text{CB}_9\text{H}_{10})(\text{CB}_{11}\text{H}_{12})$," *J. Alloy Compd.* **850**, 156781 (2021).
- Ślebarski, A., Fijałkowski, M., Maška, M.M., Deniszczyk, J., Zajdel, P., Trump, B., Yakovenko, A., "Enhancing Superconductivity of $\text{Lu}_5\text{Rh}_6\text{Sn}_{18}$ by Atomic Disorder," *Phys. Rev. B* **103**(15), 155133 (2021).

- Smith, G.N., "Revisiting Neutron Scattering Data from Deuterated Milk," *Food Hydrocolloid*. **113**, 106511 (2021). [CHRNS]
- Soles, C.L., Burns, A.B., Ito, K., Chan, E., Liu, J., Yee, A.F., Tyagi, M., "Importance of Sub-Nanosecond Fluctuations on the Toughness of Polycarbonate Glasses," *Macromolecules* **53**(15), 6672 (2020). [CHRNS]
- Soles, C.L., Burns, A.B., Ito, K., Chan, E.P., Douglas, J.F., Wu, J., Yee, A.F., Shih, Y.-T., Huang, L., Dimeo, R.M., Tyagi, M., "Why Enhanced Subnanosecond Relaxations are Important for Toughness in Polymer Glasses," *Macromolecules* **54**(5), 2518 (2021). [CHRNS]
- Song, Y., Wang, W., Cao, C., Yamani, Z., Xu, Y., Sheng, Y., Löser, W., Qiu, Y., Yang, Y.-F., Birgeneau, R.J., Dai, P., "High-Energy Magnetic Excitations from Heavy Quasiparticles in CeCu_2Si_2 ," *NPJ Quantum Mater.* **6**(1), 60 (2021). [CHRNS]
- Song, Y., Huang, R., Liu, Y., Zhang, Z., Huang, Q., Jiang, Y., Wang, S., Li, L., Xing, X., Chen, J., "Magnetic-Field-Induced Strong Negative Thermal Expansion in $\text{La}(\text{Fe,Al})_{13}$," *Chem. Mater.* **32**(17), 7535 (2020).
- Song, Y., Huang, R., Zhang, J., Zhang, S., Huang, Q., Wang, S., Jiang, Y., Li, L., Xing, X., Chen, J., "The Critical Role of Spin Rotation in the Giant Magnetostriction of $\text{La}(\text{Fe,Al})_{13}$," *Sci. China Mater.* **64**(5), 1238 (2021).
- Songvilay, M., Petit, S., Damay, F., Roux, G., Qureshi, N., Walker, H.C., Rodriguez-Rivera, J.A., Gao, B., Cheong, S.-W., Stock, C., "From One- to Two-Magnon Excitations in the $S = 3/2$ Magnet $\beta\text{-CaCr}_2\text{O}_4$," *Phys. Rev. Lett.* **126**(1), 017201 (2021). [CHRNS]
- Songvilay, M., Robert, J., Petit, S., Rodriguez-Rivera, J.A., Ratcliff, W.D., Damay, F., Balédent, V., Jiménez-Ruiz, M., Lejay, P., Pachoud, E., Hadj-Azzem, A., Simonet, V., Stock, C., "Kitaev Interactions in the Co Honeycomb Antiferromagnets $\text{Na}_3\text{Co}_2\text{SbO}_6$ and $\text{Na}_2\text{Co}_2\text{TeO}_6$," *Phys. Rev. B* **102**(22), 224429 (2020). [CHRNS]
- Soubias, O., Pant, S., Heinrich, F., Zhang, Y., Roy, N.S., Li, J., Jian, X., Yohe, M.E., Randazzo, P.A., Lösche, M., Tajkhorshid, E., Byrd, R.A., "Membrane Surface Recognition by the ASAP1 PH Domain and Consequences for Interactions with the Small GTPase Arf1," *Sci. Adv.* **6**(40), eabd1882 (2020).
- Srivastava, A., Zhao, Y., Meyerhofer, J., Jia, L., Foster, M.D., "Design of Interfacial Crowding for Elastomeric Reinforcement with Nanocrystals," *ACS Appl. Mater. Inter.* **13**(8), 10349 (2021).
- Su, L., Weaver, J.L., Groenenboom, M., Nakamura, N., Rus, E., Anand, P., Jha, S.K., Okasinski, J.S., Dura, J.A., Rees-Jayan, B., "Tailoring Electrode-Electrolyte Interfaces in Lithium-Ion Batteries using Molecularly Engineered Functional Polymers," *ACS Appl. Mater. Inter.* **13**(8), 9919 (2021).
- Sun, M., Zhao, X., Liu, Q., Ukaomah, C.F., Jiang, S., Hu, Q., Wang, Q., Blach, T.P., Yu, B., Cheng, G., "Investigation of Microwave Irradiation Stimulation to Enhance the Pore Connectivity of Shale," *Energ. Fuel.* **35**(4), 3240 (2021).
- Sun, R., Melton, M., Safaie, N., Ferrier, Jr., R.C., Cheng, S., Liu, Y., Zuo, X., Wang, Y., "Molecular View on Mechanical Reinforcement in Polymer Nanocomposites," *Phys. Rev. Lett.* **126**(11), 117801 (2021). [CHRNS]
- Sunday, D.F., Chremos, A., Martin, T.B., Chang, A.B., Burns, A.B., Grubbs, R.H., "Concentration Dependence of the Size and Symmetry of a Bottlebrush Polymer in a Good Solvent," *Macromolecules* **53**(16), 7132 (2020).
- Syed, A., Tanino, Y., LaManna, J.M., Jacobson, D.L., Hussey, D.S., Baltic, E., Burca, G., "A Portable Triaxial Cell for Beamline Imaging of Rocks under Triaxial State of Stress," *Meas. Sci. Technol.* **32**(9), 095403 (2021).
- Tan, L., Elkins, J.G., Davison, B.H., Kelley, E.G., Nickels, J., "Implementation of a Self-Consistent Slab Model of Bilayer Structure in the *SasView* Suite," *J. Appl. Crystallogr.* **54**(1), 363 (2021). [CHRNS]
- Thorsen, M.K., Lai, A., Lee, M.W., Hoogerheide, D.P., Wong, G.C.L., Freed, J.H., Heldwein, E.E., "Highly Basic Clusters in the HSV-1 Nuclear Egress Complex Drive Membrane Budding by Inducing Lipid Ordering," *mBio*, in press.
- Tortora, M., Zajdel, P., Lowe, A.R., Chorążewski, M., Leão, J.B., Jensen, G.V., Bleuel, M., Giacomello, A., Casciola, C.M., Meloni, S., Grosu, Y., "Giant Negative Compressibility by Liquid Intrusion into Superhydrophobic Flexible Nanoporous Frameworks," *Nano Lett.* **21**(7), 2848 (2021). [CHRNS]
- Trainer, C., Songvilay, M., Qureshi, N., Stunault, A., Yim, C.M., Rodriguez, E.E., Heil, C., Tsurkan, V., Green, M.A., Loidl, A., Wahl, P., Stock, C., "Magnetic Surface Reconstruction in the van der Waals Antiferromagnet Fe_{1+x}Te ," *Phys. Rev. B* **103**(2), 024406 (2021).
- Turkoglu, D.J., Chen-Mayer, H.H., "Chopped Cold Neutron Beam Activation Analysis (March 2021)," *IEEE T. Nucl. Sci.* **68**(7), 1505 (2021).
- Usuda, H., Hishida, M., Nagao, M., "Effect of *n*-Alkane on Bilayer Structure and Dynamics in Nanoscales Observed by Neutron Scattering," *Acc. Mater. Surf. Res.* **5**(5), 171 (2020). [CHRNS]

- Uzan, L., Leão, J.B., Brocker, C., Mattes, D., Dax, T., "Heat Transfer Analysis Study for the Design of the New Polychromatic Beam Neutron Reflectometer CANDOR (Chromatic Analysis Neutron Diffractometer Or Reflectometer)," *J. Neutron Res.* **22**(4), 417 (2020). [CHRNS]
- Valadez-Pérez, N.E., Liu, Y., Castañeda-Priego, R., "Cluster Morphology of Colloidal Systems with Competing Interactions," *Front. Phys.* **9**, 637138 (2021). [CHRNS]
- Valentine, M.E., Higo, T., Nambu, Y., Chaudhuri, D., Wen, J., Broholm, C., Nakatsuji, S., Drichko, N., "Impact of the Lattice on Magnetic Properties and Possible Spin Nematicity in the $S = 1$ Triangular Antiferromagnet NiGa_2S_4 ," *Phys. Rev. Lett.* **125**(19), 197201 (2020). [CHRNS]
- Van, Q.N., López, C.A., Tonelli, M., Taylor, T., Niu, B., Stanley, C.B., Bhowmik, D., Tran, T.H., Frank, P.H., Messing, S., Alexander, P., Scott, D., Ye, X., Drew, M., Chertov, O., Lösche, M., Ramanathan, A., Gross, M.L., Hengartner, N.W., Westler, W.M., Markley, J.L., Simanshu, D.K., Nissley, D.V., Gillette, W.K., Esposito, D., McCormick, F., Gnanakaran, S., Heinrich, F., Stephen, A.G., "Uncovering a Membrane-Distal Conformation of KRAS Available to Recruit RAF to the Plasma Membrane," *P. Natl. A. Sci. USA* **117**(39), 24258 (2020).
- van Ravensteijn, B.G.P., Zerdan, R.B., Hawker, C.J., Helgeson, M.E., "Role of Architecture on Thermorheological Properties of Poly(Alkyl Methacrylate)-Based Polymers," *Macromolecules* **54**(12), 5473 (2021).
- Vedmedenko, E.Y., Kawakami, R.K., Sheka, D.D., Gambardella, P., Kirilyuk, A., Hirohata, A., Binek, C., Chubykalo-Fesenko, O., Sanvito, S., Kirby, B.J., Grollier, J., Everschor-Sitte, K., Kampfrath, T., You, C.-Y., Berger, A., "The 2020 Magnetism Roadmap," *J. Phys. D Appl. Phys.* **53**(45), 453001 (2020).
- Villanueva-Valencia, J.R., Guo, H., Castañeda-Priego, R., Liu, Y., "Concentration and Size Effects on the Size-Selective Particle Purification Method using the Critical Casimir Force," *Phys. Chem. Chem. Phys.* **23**(7), 4404 (2021). [CHRNS]
- Vivanco, H.K., Trump, B.A., Brown, C.M., McQueen, T.M., "Competing Antiferromagnetic-Ferromagnetic States in d^7 Kitaev Honeycomb Magnet," *Phys. Rev. B* **102**(22), 224411 (2020).
- Vogt, B.D., Weiss, R.A., "Hydrophobically Associating Hydrogels with Microphase-Separated Morphologies," in "Self-Healing and Self-Recovering Hydrogels. Advances in Polymer Science, Vol. 285," edited by Creton, C. and Okay, O., (Springer Nature Switzerland, Cham, Switzerland) Chap. **5**, 165 (2020). [CHRNS]
- Wang, B.-X., Zheng, H., Krivyakina, E., Chmaissem, O., Lopes, P.P., Lynn, J.W., Gallington, L.C., Ren, Y., Rosenkranz, S., Mitchell, J.F., Phelan, D., "Synthesis and Characterization of Bulk $\text{Nd}_{1-x}\text{Sr}_x\text{NiO}_2$ and $\text{Nd}_{1-x}\text{Sr}_x\text{NiO}_3$," *Phys. Rev. Mater.* **4**(8), 084409 (2020).
- Wang, B., Zhang, X., Huang, H., Zhang, Z., Yildirim, T., Zhou, W., Xiang, S., Chen, B., "A Microporous Aluminum-Based Metal-Organic Framework for High Methane, Hydrogen, and Carbon Dioxide Storage," *Nano Res.* **14**(2), 507 (2021).
- Wang, F., Evans, H.A., Kim, K., Yin, L., Li, Y., Tsai, P.-C., Liu, J., Lapidus, S.H., Brown, C.M., Siegel, D.J., Chiang, Y.-M., "Dynamics of Hydroxyl Anions Promotes Lithium Ion Conduction in Antiperovskite Li_2OHCl ," *Chem. Mater.* **32**(19), 8481 (2020). [CHRNS]
- Wang, Q., Neubauer, K.J., Duan, C., Yin, Q., Fujitsu, S., Hosono, H., Ye, F., Zhang, R., Chi, S., Krycka, K., Lei, H., Dai, P., "Field-Induced Topological Hall Effect and Double-Fan Spin Structure with a c -Axis Component in the Metallic Kagome Antiferromagnetic Compound YMn_6Sn_6 ," *Phys. Rev. B* **103**(1), 014416 (2021).
- Wang, Y., Wang, W., Hong, K., Liu, Y., "Quantification of Deformation-Induced Concentration Fluctuations in Polymeric Liquids by Small-Angle Neutron Scattering," *Macromolecules* **54**(7), 3531 (2021). [CHRNS]
- Wang, Y., Reeder, T., Karaki, Y., Kindervater, J., Halloran, T., Maliszewskyj, N., Qiu, Y., Rodriguez, J.A., Gladchenko, S., Koohpayeh, S.M., Nakatsuji, S., Broholm, C., "Monopolar and Dipolar Relaxation in Spin Ice $\text{Ho}_2\text{Ti}_2\text{O}_7$," *Sci. Adv.* **7**(25), eabg0908 (2021). [CHRNS]
- Wang, Z.-C., Thanabalasingam, K., Scheifers, J.P., Streeter, A., McCandless, G.T., Gaudet, J., Brown, C.M., Segre, C.U., Chan, J.Y., Tafti, F., "Antiferromagnetic Order and Spin-Canting Transition in the Corrugated Square Net Compound $\text{Cu}_3(\text{TeO}_4)(\text{SO}_4)\cdot\text{H}_2\text{O}$," *Inorg. Chem.* **60**(14), 10565 (2021).
- Wang, Z.-B., Mao, Y.-M., Li, X.-K., Li, Y.-G., Jarumaneeroj, C., Thitisak, B., Tiyapiboonchaiya, P., Rungswang, W., Hsiao, B.S., "The Influence of Ethyl Branch on Formation of Shish-Kebab Crystals in Bimodal Polyethylene under Shear at Low Temperature," *Chinese J. Polym. Sci.*, in press.
- Ware, W., Wright, T., Mao, Y., Han, S., Guffie, J., Danilov, E.O., Rech, J., You, W., Luo, Z., Gautam, B., "Aggregation Controlled Charge Generation in Fullerene Based Bulk Heterojunction Polymer Solar Cells: Effect of Additive," *Polymers-Basel* **13**(1), 115 (2021). [CHRNS]

- Weadock, N.J., Gehring, P.M., Gold-Parker, A., Smith, I.C., Karunadasa, H.I., Toney, M.F., "Test of the Dynamic-Domain and Critical Scattering Hypotheses in Cubic Methylammonium Lead Triiodide," *Phys. Rev. Lett.* **125**(7), 075701 (2020).
- Weaver, J., Job, A., "Adjustment to the Light Element Areal Concentration Calculation for Neutron Depth Profiles," *Microsc. Microanal.*, in press.
- Weaver, J.L., DePriest, P.T., Plymale, A.E., Pearce, C.I., Arey, B., Koestler, R.J., "Microbial Interactions with Silicate Glasses," *NPJ Mater. Degrad.* **5**(1), 11 (2021).
- Weber, J., Cheshire, M.C., Bleuel, M., Mildner, D., Chang, Y.-J., Ilev, A., Littrell, K.C., Ilavsky, J., Stack, A.G., Anovitz, L.M., "Influence of Microstructure on Replacement and Porosity Generation during Experimental Dolomitization of Limestones," *Geochim. Cosmochim. Ac.* **303**, 137 (2021). [CHRNS]
- Wei, Y., Lang, X., Hore, M.J.A., "A Correspondence between the Flory-Rehner Theory for Microgels and the Daoud-Cotton Model for Polymer-Grafted Nanoparticles," *J. Appl. Phys.* **128**(21), 214701 (2020). [CHRNS]
- Wen, H.-M., Shao, K., Zhou, W., Li, B., Chen, B., "A Novel Expanded Metal-Organic Framework for Balancing Volumetric and Gravimetric Methane Storage Working Capacities," *Chem. Commun.* **56**(86), 13117 (2020).
- Wilson, S., Bordelon, M.M., "Quantum Disorder and Unconventional Magnetism in AlN_xX_2 ($A = \text{Alkali}$; $Ln = \text{Lanthanide}$; $X = \text{Chalcogen}$) Materials," *Neutron News* **32**(1), 19 (2021).
- Winslow, S.W., Liu, Y., Swan, J.W., Tisdale, W.A., "Repulsive, Densely Packed Ligand-Shells Mediate Interactions between PbS Nanocrystals in Solution," *J. Phys. Chem. C* **125**(14), 8014 (2021). [CHRNS]
- Wolf, C.M., Guio, L., Scheiwiller, S.C., O'Hara, R.P., Luscombe, C.K., Pozzo, L.D., "Blend Morphology in Polythiophene-Polystyrene Composites from Neutron and X-ray Scattering," *Macromolecules* **54**(6), 2960 (2021). [CHRNS]
- Wong-Ng, W., Laws, W., Huang, Q., Hou, J., Lapidus, S.H., Ribaud, L., Kaduk, J.A., "Crystal Chemistry and Phase Equilibria of the $CaO\text{-}\frac{1}{2}Ho_2O_3\text{-}CoO_2$ System at 885 °C in Air," *Solid State Sci.* **107**, 106348 (2020).
- Wu, H., Wang, Z., Zhang, Y., Mo, W., Bai, P., Song, K., Zhang, Z., Wang, Z., Hussey, D.S., Liu, Y., Wang, Z., Wang, X., "Demonstration of Small-Angle Neutron Scattering Measurements with a Nested Neutron-Focusing Supermirror Assembly," *Nucl. Instrum. Meth. A* **972**, 164072 (2020). [CHRNS]
- Wu, J., Xu, S., Han, C.C., Yuan, G., "Controlled Drug Release: On the Evolution of Physically Entrapped Drug inside the Electrospun Poly(Lactic-Co-Glycolic Acid) Matrix," *J. Control. Release* **331**, 472 (2021). [CHRNS]
- Wu, W., Singh, M., Masud, A., Wang, X., Nallapaneni, A., Xiao, Z., Zhai, Y., Wang, Z., Terlier, T., Bleuel, M., Yuan, G., Satija, S.K., Douglas, J.F., Matyjaszewski, K., Bockstaller, M.R., Karim, A., "Control of Phase Morphology of Binary Polymer Grafted Nanoparticle Blend Films via Direct Immersion Annealing," *ACS Nano* **15**(7), 12042 (2021).
- Wu, Y., Yin, G., Pan, L., Grutter, A.J., Pan, Q., Lee, A., Gilbert, D.A., Borchers, J.A., Ratcliff, II, W., Li, A., Han, X.-D., Wang, K.L., "Large Exchange Splitting in Monolayer Graphene Magnetized by an Antiferromagnet," *Nat. Electron.* **3**(10), 604 (2020).
- Xi, Y., Lankone, R.S., Sung, L.-P., Liu, Y., "Tunable Thermo-Reversible Bicontinuous Nanoparticle Gel Driven by the Binary Solvent Segregation," *Nat. Commun.* **12**(1), 910 (2021). [CHRNS]
- Xi, Y., Leão, J.B., Ye, Q., Lankone, R.S., Sung, L.-P., Liu, Y., "Controlling Bicontinuous Structures through a Solvent Segregation-Driven Gel," *Langmuir* **37**(6), 2170 (2021). [CHRNS]
- Xie, S., Zhang, B., Bates, F.S., Lodge, T.P., "Phase Behavior of Salt-Doped A/B/AB Ternary Polymer Blends: The Role of Homopolymer Distribution," *Macromolecules* **54**(14), 6990 (2021).
- Xie, S., Zhang, B., Mao, Y., He, L., Hong, K., Bates, F.S., Lodge, T.P., "Influence of Added Salt on Chain Conformations in Poly(Ethylene Oxide) Melts: SANS Analysis with Complications," *Macromolecules* **53**(16), 7141 (2020). [CHRNS]
- Xie, Y., Li, Y., Yin, Z., Zhang, R., Wang, W., Stone, M.B., Cao, H., Abernathy, D.L., Harriger, L., Young, D.P., DiTusa, J.F., Dai, P., "Magnetic Order and Fluctuations in the Quasi-Two-Dimensional Planar Magnet $Sr(Co_{1-x}Ni_x)_2As_2$," *Phys. Rev. B* **102**(21), 214431 (2020).
- Xie, Y., Cui, H., Wu, H., Lin, R.-B., Zhou, W., Chen, B., "Electrostatically Driven Selective Adsorption of Carbon Dioxide over Acetylene in an Ultramicroporous Material," *Angew. Chem. Int. Edit.* **60**(17), 9604 (2021).
- Xu, S., Lyu, Y., Noda, I., Mao, Y., Fairbrother, A., Gu, X., "Two-Dimensional Correlation Spectroscopy Studies on Degradation of Photovoltaic Backsheets from Indoor to Outdoor," *Polym. Degrad. Stabil.* **181**, 109341 (2020).

- Yadav, A., Panda, D.K., Zhang, S., Zhou, W., Saha, S., "Electrically Conductive 3D Metal–Organic Framework Featuring π -Acidic Hexaazatriphenylene Hexacarbonitrile Ligands with Anion– π Interaction and Efficient Charge-Transport Capabilities," *ACS Appl. Mater. Inter.* **12**(36), 40613 (2020).
- Yamamoto, T., Chikamatsu, A., Kitagawa, S., Izumo, N., Yamashita, S., Takatsu, H., Ochi, M., Maruyama, T., Namba, M., Sun, W., Nakashima, T., Takeiri, F., Fujii, K., Yashima, M., Sugisawa, Y., Sano, M., Hirose, Y., Sekiba, D., Brown, C.M., Honda, T., Ikeda, K., Otomo, T., Kuroki, K., Ishida, K., Mori, T., Kimoto, K., Hasegawa, T., Kageyama, H., "Strain-Induced Creation and Switching of Anion Vacancy Layers in Perovskite Oxynitrides," *Nat. Commun.* **11**(1), 5923 (2020).
- Yang, C.-Y., Pan, L., Grutter, A.J., Wang, H., Che, X., He, Q.L., Wu, Y., Gilbert, D.A., Shafer, P., Arenholz, E., Wu, H., Yin, G., Deng, P., Borchers, J.A., Ratcliff, II, W., Wang, K.L., "Termination Switching of Antiferromagnetic Proximity Effect in Topological Insulator," *Sci. Adv.* **6**(33), eaaz8463 (2020).
- Yang, H.-Y., Singh, B., Gaudet, J., Lu, B., Huang, C.-Y., Chiu, W.-C., Huang, S.-M., Wang, B., Bahrami, F., Xu, B., Franklin, J., Sochnikov, I., Graf, D.E., Xu, G., Zhao, Y., Hoffman, C.M., Lin, H., Torchinsky, D.H., Broholm, C.L., Bansil, A., Tafti, F., "Noncollinear Ferromagnetic Weyl Semimetal with Anisotropic Anomalous Hall Effect," *Phys. Rev. B* **103**(11), 115143 (2021).
- Yao, H., Olsen, B.D., "SANS Quantification of Bound Water in Water-Soluble Polymers across Multiple Concentration Regimes," *Soft Matter* **17**(21), 5303 (2021).
- Yao, Y., Huang, Z., Hughes, L.A., Gao, J., Li, T., Morris, D., Zeltmann, S.E., Savitzky, B.H., Ophus, C., Finrock, Y.Z., Dong, Q., Jiao, M., Mao, Y., Chi, M., Zhang, P., Li, J., Minor, A.M., Shahbazian-Yassar, R., Hu, L., "Extreme Mixing in Nanoscale Transition Metal Alloys," *Matter* **4**(7), 2340 (2021).
- Yoshimune, W., Harada, M., "Nanostructure of a Catalyst Ink Investigated by Contrast-Variation Small-Angle Neutron Scattering," *ECS Transactions* **98**(9), 447 (2020).
- Yoshimune, W., Harada, M., "Temperature-Induced Shear-Thinning in Catalyst Inks," *Electrochem. Commun.*, in press.
- Yoshimune, W., Harada, M., Akimoto, Y., "Small-Angle Neutron Scattering Studies on the Distribution of Polytetrafluoroethylene within Microporous Layers for Polymer Electrolyte Fuel Cells," *Compos. Part C-Open Access* **2**, 100015 (2020).
- Yu, B., Li, L., Liu, S., Wang, H., Liu, H., Lin, C., Liu, C., Wu, H., Zhou, W., Li, X., Wang, T., Chen, B., Jiang, J., "Robust Biological Hydrogen-Bonded Organic Framework with Post-Functionalized Rhenium(I) Sites for Efficient Heterogeneous Visible-Light-Driven CO₂ Reduction," *Angew. Chem. Int. Edit.* **60**(16), 8983 (2021).
- Yuan, B., Butch, N.P., Xu, G., Winn, B., Clancy, J.P., Kim, Y.-J., "Neutron Scattering Study of Magnetic Anisotropy in the Tetragonal Antiferromagnet Bi₂CuO₄," *Phys. Rev. B* **103**(13), 134436 (2021).
- Yuan, G., Kienzle, P.A., Satija, S.K., "Salting Up and Salting Down of Bovine Serum Albumin Layers at the Air-Water Interface," *Langmuir* **36**(50), 15240 (2020).
- Yuan, X., Krueger, S., Sztucki, M., Jones, R.L., Curtis, J.E., Shalaev, E., "Phase Behavior of Pluronic 188 Aqueous Solutions at Subzero Temperatures: A Neutron and X-ray Scattering Study," *J. Phys. Chem. B* **125**(5), 1476 (2021).
- Yuan, Y.D., Dong, J., Liu, J., Zhao, D., Wu, H., Zhou, W., Gan, H.X., Tong, Y.W., Jiang, J., Zhao, D., "Porous Organic Cages as Synthetic Water Channels," *Nat. Commun.* **11**(1), 4927 (2020).
- Yusuf, M., LaManna, J., Paul, P., Agyeman-Budu, D., Toney, M., Weker, J., "Ex-Situ Li Plating Detection on Graphite Anodes in Extremely Fast-Charged Lithium-Ion Batteries using Simultaneous Neutron and X-ray Tomography," *Microsc. Microanal.*, in press.
- Zajdel, P., Chorążewski, M., Leão, J.B., Jensen, G.V., Bleuel, M., Zhang, H.-F., Feng, T., Luo, D., Li, M., Lowe, A.R., Geppert-Rybczynska, M., Li, D., Grosu, Y., "Inflation Negative Compressibility during Intrusion-Extrusion of a Non-Wetting Liquid into a Flexible Nanoporous Framework," *J. Phys. Chem. Lett.* **12**(20), 4951 (2021). [CHRNS]
- Zangmeister, C.D., Radney, J.G., Staymates, M.E., Vicenzi, E.P., Weaver, J.L., "Hydration of Hydrophilic Cloth Face Masks Enhances the Filtration of Nanoparticles," *ACS Appl. Nano Mater.* **4**(3), 2694 (2021).
- Zeisler, R., Turkoglu, D., Sharp, N., Chen-Mayer, H., "Determination of Aluminum in Bovine Liver SRM 1577 c by Instrumental Cold Neutron Activation Analysis," *J. Radioanal. Nucl. Ch.* **326**(3), 1879 (2020).
- Zhai, Y., Martys, N.S., George, W.L., Curtis, J.E., Nayem, J., Z, Y., Liu, Y., "Intermediate Scattering Functions of a Rigid Body Monoclonal Antibody Protein in Solution Studied by Dissipative Particle Dynamic Simulation," *Struct. Dynam.-US* **8**(2), 024102 (2021). [CHRNS]

- Zhai, Y., Luo, P., Nagao, M., Nakajima, K., Kikuchi, T., Kawakita, Y., Kienzle, P.A., Z, Y., Faraone, A., "Relevance of Hydrogen Bonded Associates to the Transport Properties and Nanoscale Dynamics of Liquid and Supercooled 2-Propanol," *Phys. Chem. Chem. Phys.* **23**(12), 7220 (2021). [CHRNS]
- Zhang, B., Xie, S., Lodge, T.P., Bates, F.S., "Phase Behavior of Diblock Copolymer-Homopolymer Ternary Blends with a Compositionally Asymmetric Diblock Copolymer," *Macromolecules* **54**(1), 460 (2021).
- Zhang, H., Zhu, Y.L., Qiu, Y., Tian, W., Cao, H.B., Mao, Z.Q., Ke, X., "Field-Induced Magnetic Phase Transitions and the Resultant Giant Anomalous Hall Effect in the Antiferromagnetic Half-Heusler Compound DyPtBi," *Phys. Rev. B* **102**(9), 094424 (2020). [CHRNS]
- Zhang, J., Phelan, D., Botana, A.S., Chen, Y.-S., Zheng, H., Krogstad, M., Wang, S.G., Qiu, Y., Rodriguez-Rivera, J.A., Osborn, R., Rosenkranz, S., Norman, M.R., Mitchell, J.F., "Intertwined Density Waves in a Metallic Nickelate," *Nat. Mater.* **11**(1), 6003 (2020). [CHRNS]
- Zhang, X., He, Z., Hao, Y., Shen, Y., Shen, S., Feng, Y., Xu, G., Butch, N.P., Nilsen, G.J., Wang, W., Zhao, J., "Quantum Phase Transitions in a Quasi-One-Dimensional Ising Quantum Magnet in Transverse Fields," *Phys. Rev. B* **103**(14), 144405 (2021).
- Zhang, X., Wang, J.-X., Li, L., Pei, J., Krishna, R., Wu, H., Zhou, W., Qian, G., Chen, B., Li, B., "A Rod-Packing Hydrogen-Bonded Organic Framework with Suitable Pore Confinement for Benchmark Ethane/Ethylene Separation," *Angew. Chem. Int. Edit.* **60**(18), 10304 (2021).
- Zhang, Z., Woys, A.M., Hong, K., Grapentin, C., Khan, T.A., Zarraga, I.E., Wagner, N.J., Liu, Y., "Adsorption of Non-Ionic Surfactant and Monoclonal Antibody on Siliconized Surface Studied by Neutron Reflectometry," *J. Colloid Interf. Sci.* **584**, 429 (2021). [CHRNS]
- Zhao, J., Gao, J., Li, W., Qian, Y., Shen, X., Wang, X., Shen, X., Hu, Z., Dong, C., Huang, Q., Cao, L., Li, Z., Zhang, J., Ren, C., Duan, L., Liu, Q., Yu, R., Ren, Y., Weng, S.-C., Lin, H.-J., Chen, C.-T., Tjeng, L.-H., Long, Y., Deng, Z., Zhu, J., Wang, X., Weng, H., Yu, R., Greenblatt, M., Jin, C., "A Combinatory Ferroelectric Compound Bridging Simple ABO_3 and A-Site-Ordered Quadruple Perovskite," *Nat. Commun.* **12**(1), 747 (2021).
- Zheng, B., Zheng, B., Carr, A.J., Yu, X., McClements, D.J., Bhatia, S.R., "Emulsions Stabilized by Inorganic Nanoclays and Surfactants: Stability, Viscosity, and Implications for Applications," *Inorg. Chim. Acta* **508**, 119566 (2020). [CHRNS]
- Zheng, J., Wahiduzzaman, M., Barpaga, D., Trump, B.A., Gutiérrez, O.Y., Thallapally, P., Ma, S., McGrail, B.P., Maurin, G., Motkuri, R.K., "Porous Covalent Organic Polymers for Efficient Fluorocarbon-Based Adsorption Cooling," *Angew. Chem. Int. Edit.*, in press.
- Zheng, Y., Colón, L.N.I., Ul Hassan, N., Williams, E.R., Stefik, M., LaManna, J.M., Hussey, D.S., Mustain, W.E., "Effect of Membrane Properties on the Carbonation of Anion Exchange Membrane Fuel Cells," *Membranes* **11**(2), 102 (2021).
- Zic, M.P., Fuhrman, W.T., Wang, K., Ran, S., Paglione, J., Butch, N.P., "Coupled Spin Waves and Crystalline Electric Field Levels in Candidate Multiferroic $ErFeO_3$," *J. Appl. Phys.* **130**(1), 014102 (2021).
- Zoghlin, E., Schmehr, J., Holgate, C., Dally, R., Liu, Y., Laurita, G., Wilson, S.D., "Evaluating the Effects of Structural Disorder on the Magnetic Properties of $Nd_2Zr_2O_7$," *Phys. Rev. Mater.*, in press.

Instruments and Contacts

(name, tel. 301-975-xxxx, email)

High resolution powder diffractometer (BT-1):

- H. Wu, 2387, hui.wu@nist.gov
- Q. Z. Huang, 6164, qing.huang@nist.gov
- C. M. Brown, 5134, craig.brown@nist.gov

Engineering diffractometer (BT-8):

- T. Gnaeupel-Herold, 5380, thomas.gnaeupel-herold@nist.gov

vSANS instrument (NG-3) (CHRNS):

- E. Kelley, 8584, elizabeth.kelley@nist.gov
- Y. Liu, 6235, yun.liu@nist.gov
- J. Gaudet, 5010, jonathon.gaudet@nist.gov
- R. P. Murphy, 8544, ryan.murphy@nist.gov
- C. Gagnon, 2020, cedric.gagnon@nist.gov

30-m SANS instrument (NG-B) (CHRNS):

- P. D. Butler, 2028, paul.butler@nist.gov
- S. Krueger, 6734, susan.krueger@nist.gov
- Y. Mao, 6017, yimin.mao@nist.gov
- M. Zhang, 5513, zhenhuan.zhang@nist.gov

10-m SANS instrument (NG-B) (nSoft):

- R. Jones, 4624, ronald.jones@nist.gov
- K. Weigandt, 8396, kathleen.weigandt@nist.gov
- T. Martin, 8866, tyler.martin@nist.gov
- M. Zhang, 5513, zhenhuan.zhang@nist.gov

uSANS, Perfect Crystal SANS (BT-5) (CHRNS):

- J. G. Barker, 6732, john.barker@nist.gov
- P. D. Butler, 2028, paul.butler@nist.gov

30-m SANS instrument (NG-7):

- S. Teixeira, 4404, susana.marujoteixeira@nist.gov
- J. G. Barker, 6732, john.barker@nist.gov
- J. Gaudet, 5010, jonathon.gaudet@nist.gov
- J. R. Krzywon, 6650, jkrzywon@nist.gov

CANDOR, White-beam reflectometer/diffractometer (CHRNS):

- A. Grutter, 4198, alexander.grutter@nist.gov
- D. Hoogerheide, 8839, david.hoogerheide@nist.gov
- B. Maranville, 6034, brian.maranville@nist.gov
- C. F. Majkrzak, 5251, charles.majkrzak@nist.gov

MAGIK, Off-Specular Reflectometer (NG-D):

- J. A. Dura, 6251, joseph.dura@nist.gov
- F. Heinrich, 4507, frank.heinrich@nist.gov

Polarized Beam Reflectometer/Diffractometer (NG-D):

- C. F. Majkrzak, 5251, cmajkrzak@nist.gov

Neutron reflectometer-horizontal sample (NG-7):

- S. K. Satija, 5250, satija@nist.gov

HFBS, High-flux backscattering spectrometer (NG-2) (CHRNS):

- M. Tyagi, 2046, madhusudan.tyagi@nist.gov
- R. Azuah, 5604, richard.azuah@nist.gov

NSE, Neutron spin echo spectrometer (NG-A) (CHRNS):

- A. Faraone, 5254, antonio.faraone@nist.gov
- M. Nagao, 5505, michihiro.nagao@nist.gov

MACS, Multi-angle crystal spectrometer (BT-9) (CHRNS):

- J. A. Rodriguez-Rivera, 6019, jose.rodriguez@nist.gov
- Y. Qiu, 3274, yiming.qiu@nist.gov

Double-focusing triple-axis Spectrometer (BT-7):

- Y. Zhao, 2164, yang.zhao@nist.gov
- R. Dally, 8369, rebecca.dally@nist.gov
- J. W. Lynn, 6246, jeff.lynn@nist.gov

SPINS, Spin-polarized triple-axis spectrometer (NG-5):

- G. Xu, 4144, guangyong.xu@nist.gov

Triple-axis spectrometer (BT-4):

- W. Ratcliff, 4316, william.ratcliff@nist.gov

FANS, Filter-analyzer neutron spectrometer (BT-4):

- C. M. Brown, 5134, craig.brown@nist.gov

DCS, Disk-chopper time-of-flight spectrometer (NG-4):

- N. Butch, 4863, nicholas.butch@nist.gov
- W. Zhou, 8169, wei.zhou@nist.gov
- C. M. Brown, 5134, craig.brown@nist.gov

Cold neutron depth profiling (NG-A):

- J. Weaver, 6311, jamie.weaver@nist.gov

Cold-neutron prompt-gamma neutron activation analysis (NG-D):

- R. L. Paul, 6287, rpaul@nist.gov
- H. H. Chen-Mayer, 5595, heather.chen-mayer@nist.gov

Thermal-neutron prompt-gamma activation analysis (VT-5):

- R. L. Paul, 6287, rpaul@nist.gov

Other activation analysis facilities:

- N. Sharp, 3926, nicholas.sharp@nist.gov
- R. L. Paul, 6287, rpaul@nist.gov

Thermal Neutron Imaging Facility (BT-2):

- J. LaManna, 6809, jacob.lamanna@nist.gov
- D. Jacobson, 6207, david.jacobson@nist.gov
- E. Baltic, 4842, eli.baltic@nist.gov
- D. Hussey, 6465, daniel.hussey@nist.gov

Cold Neutron Imaging Instrument (NG-6):

- D. Hussey, 6465, daniel.hussey@nist.gov
- E. Baltic, 4842, eli.baltic@nist.gov
- D. Jacobson, 6207, david.jacobson@nist.gov
- J. LaManna, 6809, jacob.lamanna@nist.gov

Neutron interferometer (NG-7):

- M. Huber, 5641, michael.huber@nist.gov
- S. Hoogerheide, 8582, shannon.hoogerheide@nist.gov

Quantum-based neutron interferometer facility (NG-7):

- M. Huber, 5641, michael.huber@nist.gov
- S. Hoogerheide, 8582, shannon.hoogerheide@nist.gov

Fundamental neutron physics station (NG-C):

- S. Hoogerheide, 8582, shannon.hoogerheide@nist.gov
- H. P. Mumm, 8355, hans.mumm@nist.gov
- M. S. Dewey, 4843, maynard.dewey@nist.gov
- J. Nico, 4663, jeffrey.nico@nist.gov

PhAND: Advanced Neutron Detector Development (NG-6a):

- H. P. Mumm, 8355, hans.mumm@nist.gov
- C. B. Shahi, 8194, chandra.shahi@nist.gov

 α - γ : absolute neutron counter (NG-6m):

- M. S. Dewey, 4843, maynard.dewey@nist.gov
- H. P. Mumm, 8355, hans.mumm@nist.gov
- C. Haddock, 5761, christopher.haddock@nist.gov

Grating interferometer for fundamental physics (NG-6u):

- M. G. Huber, 5641, michael.huber@nist.gov
- D. Hussey, 6465, daniel.hussey@nist.gov

Theory and modeling:

- J. E. Curtis, 3959, joseph.curtis@nist.gov
- T. Yildirim, 6228, taner@nist.gov

Neutron test station (PHADES):

- R. Erwin, 6245, ross.erwin@nist.gov
- S. Watson, 6232, shannon.watson@nist.gov

Instruments under development:**SPINS-II:**

- L. Harriger, 8360, leland.harriger@nist.gov

NIST Center for Neutron Research Contacts

Copies of annual reports, facility information, user information, and research proposal guidelines are available electronically.

Please visit our website: <http://www.ncnr.nist.gov>

For a paper copy of this report:

Steve Kline
301-975-6243
steven.kline@nist.gov

For general information on the facility:

Rob Dimeo
301-975-6210
robert.dimeo@nist.gov

Dan Neumann
301-975-5252
dan.neumann@nist.gov

For information on visiting the facility and/or user access questions:

Julie Keyser
301-975-8200
julie.keyser@nist.gov

Mary Ann FitzGerald
301-975-8200
maryann.fitzgerald@nist.gov

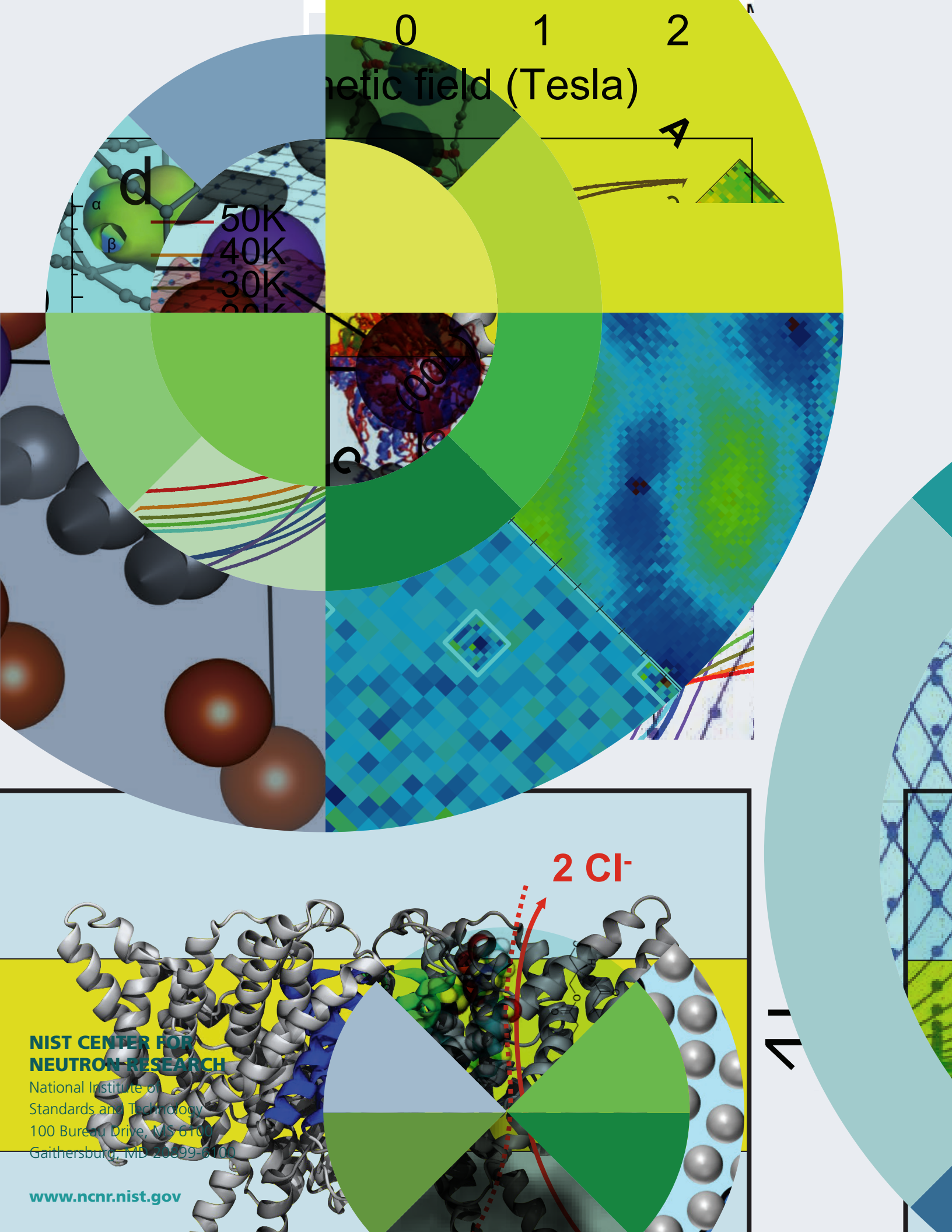
Becky Ogg
301-975-8200
rebecca.ogg@nist.gov

For information on performing research at the facility:

Yamali Hernandez
301-975-5295
yamali.hernandez@nist.gov

Facility address:

NIST Center for Neutron Research
National Institute of Standards and Technology
100 Bureau Drive, Mail Stop 6100
Gaithersburg, MD 20899-6100 USA



**NIST CENTER FOR
NEUTRON RESEARCH**

National Institute of
Standards and Technology
100 Bureau Drive, MS 6100
Gaithersburg, MD 20899-6100

www.ncnr.nist.gov